UNIVERSITY OF CALIFORNIA

Santa Barbara

AU AND CDSE NANOCRYSTAL ASSEMBLIES

A Dissertation submitted in partial satisfaction of the requirements for the Degree Doctor of Philosophy in Chemistry

by

Scott Lee Cumberland

Committee in charge:

Professor Geoffrey F. Strouse, Chair

Professor Peter C. Ford

Professor William C. Kaska

Professor Steven K. Buratto

December 2001

The dissertation of Scott Lee Cumberland is approved.

_____

Peter C. Ford

_____

William C. Kaska

_____

Steven K. Buratto

_____

Geoffrey F. Strouse, Committee Chair

October 2001

Au and CdSe Nanocrystal Assemblies

by

Scott Lee Cumberland

ACKNOWLEDGEMENTS

This work is dedicated to my mother, Dorthy Ann Cumberland, who always believed in me and whose love carried me through. I would like to acknowledge my father, Willard Lewis Cumberland, who taught me respect and to have the strength to endure. I would like to acknowledge my brothers Michael Shawn Cumberland, Brian Lewis Cumberland, Wayne Allen Cumberland, and Lance Jimmy Cumberland who have inspired me to succeed. I would like to acknowledge by wife, Brendi Mercedes Makepeace-Cumberland, whose love has supported my efforts and who has given me the greatest gifts a man could want: a wonderful son, Kevin John Macarthur, and a wonderful daughter, Isabella Lee Cumberland.

VITA OF SCOTT LEE CUMBERLAND
December 2001

EDUCATION

Bachelor of Science in Psychology, University of Texas, San Antonio, May 1985
Bachelor of Science in Chemistry, University of Texas, San Antonio, May 1997
Doctor of Philosophy in Chemistry, University of California, Santa Barbara, December 2001 (expected)

PROFESSIONAL EMPLOYMENT

1997-1999: Teaching Assistant, Department of Chemistry and Biochemistry, University of California, Santa Barbara.
1997-2001: Research Assistant, Department of Chemistry and Biochemistry.

PUBLICATIONS

"Au and CdSe nanocrystals and their assemblies," Unpublished thesis submitted in partial fulfillment of the requirements for the Degree Doctor of Philosophy in Chemistry, University of California, Santa Barbara, 2001.

"Colloidal Gold Superstructures: Effect of Ligand Length and Nanoparticle Size on the Forces Controlling Assembly." Cumberland, S.L.; Strouse, G.F. Langmuir, in prep.

"Analysis of the Nature of Oxyanion Adsorption on Gold Nanomaterial Surfaces." Cumberland, S.L.; Strouse, G.F. Langmuir, 2001, in press.

"Inorganic Clusters as Single Source Precursors for Preparation of CdSe, ZnSe, CdSe/ZnS Nanomaterials." Cumberland, S.L.; Hanif, K.M.; Javier, J.; Khitrov, G.A.; Strouse, G.F.; Woessner, S.M.; Yun, C.S., Chemistry of Materials, submitted.

"Nanoarchitectures: Building Composites from Noble Metal and Semiconducting Nanomaterials." Cumberland, S.L.; Strouse, G.F. Chemistry of Materials, submitted.

AWARDS

University of California - GOF Fellowship, UCSB (2000-2001)
Office of Naval Research Undergraduate research fellowship, UTSA (1993-1995)
Welch Foundation Fellowship, UTSA (1992)

FIELDS OF STUDY

Major Field: Materials and Inorganic Chemistry with Professor Geoffrey F. Strouse, University of California, Santa Barbara 1997-2001.
Organic Chemistry with Professor S. Tyagarajan, University of Texas, San Antonio, 1995-1997.

ABSTRACT

Au and CdSe Nanocrystal Assemblies

by

Scott Lee Cumberland

The organization of nanomaterials into 2- and 3-dimensional structures are interesting materials due to the potential for combined collective properties of the individual nanomaterials in both homogeneous and heterogeneous architectures. The electronic structure of these nanoparticle assemblies should be determined by the interaction of individual nanoparticle wave functions and the particle separation distance allowing for potential manipulation of the ensemble electronic properties by control of the nanoparticle size, separation distance, and connectivity of the nanomaterials. The forces controlling these assemblies include electrostatic interactions of the nanoparticle surface charge, steric repulsion energy terms arising from the surface passivating ligands, Van der Waals dispersion forces arising from core interactions between particles, and covalent binding energy forces arising from the binding affinities of functional groups for the nanoparticle surface. Careful manipulation these forces by controlling the size, dispersity, and surface passivating ligands allows for the assembly of tailored homogeneous and heterogeneous nanoparticle architectonic structures.

TABLE OF CONTENTS

List of Figures

List of Tables

Peak assignments for amine stretching frequencies for octylamine and Au-octylamine. 221 Chapter 1 Assembly of Nanomaterials.

1.1 Introduction.

Nanomaterials are considered to be materials in the intermediate size range between that of molecular (>10Å) and bulk materials (<100Å) that exhibit unique size-dependent optical, electrical, and chemical properties.[1-6] Recent advances in synthesis of metal and semiconductor quantum dots have resulted in an increased interest in organization of these materials into macroscopic assemblies that take advantage of the unique individual properties and the potential combined collective properties of the assembled nanomaterials.[4,7-18] These assemblies offer the potential for novel hybrid systems that exhibit interesting and useful properties with prospective applications in nanoelectronics, memory storage devices, nonlinear optics, sensor science, catalysis, and light energy conversion systems.[1,9,10,19-27] The properties of such constructs can potentially be tuned by manipulation of the size, ratio, type, and connectivity of the nanomaterials.

Individually, the quantum dots exhibit size-dependent properties due to quantum confinement effects, which induce quantization of the bulk band structure and confines the electronic excitation states of the material to within the volume of the dot. In a quantum dot lattice where the quantum dots are organized in such a way as to cause an overlap of the wave functions of the individual units, an enhancement in the optical nonlinearity is expected due to the propagation of a Frenkel type exciton throughout the lattice via exciton transfer.[28] In such a case the excitonic state in the quantum dot is no longer localized within each individual quantum dot, but is extended over the entire lattice. The coupling of the wave functions of the neighboring quantum dots increases the exciton coherence length of the exciton and results in an increase of the oscillator strength of the exciton thus increasing the nonlinear optical properties of the material.

Organization of nanomaterials of different types and sizes has proven to be a daunting task due to the nature of the forces controlling the assembly of the individual materials. Forces controlling the assembly of nanomaterials include electrostatic forces between oppositely charged species (E_{elec}), steric forces due to the passivants on the nanomaterial surface (E_{steric}), Van der Waals attractive forces of nanoparticle cores (E_{VdW}), and covalent forces dealing with the binding affinity of functionalized surface passivating groups

to other nanoparticle surfaces (E_{cov}). The total force (E_{total}) governing these assemblies comes from a contribution of all these terms with the degree of contribution depending on the physical and chemical properties of the nanomaterial and surface passivant (eqn 1). Illustrations of assemblies governed by the forces outlined in equation 1 are shown in Figures 1-1, 1-2, and 1-3.

$$E_{total} = E_{elec} + E_{steric} + E_{VdW} + E_{cov} \quad \text{(eqn 1)}$$

Figure 1-1. Illustration of evaporative self-assembly. The dominant forces controlling these assemblies are E_{VdW} and E_{steric}, where $d \leq 2l$.

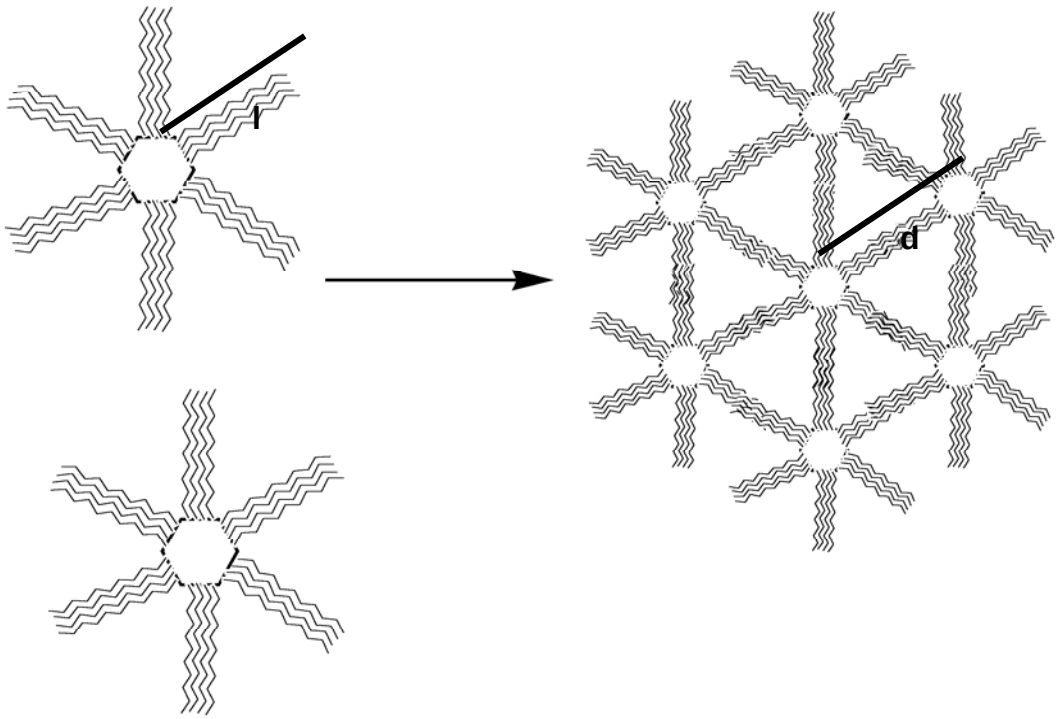

Figure 1-2. Illustration of electrostatic assembly. The dominant force governing these assemblies is E_{elec}, where $d \sim l_1 + l_2$.

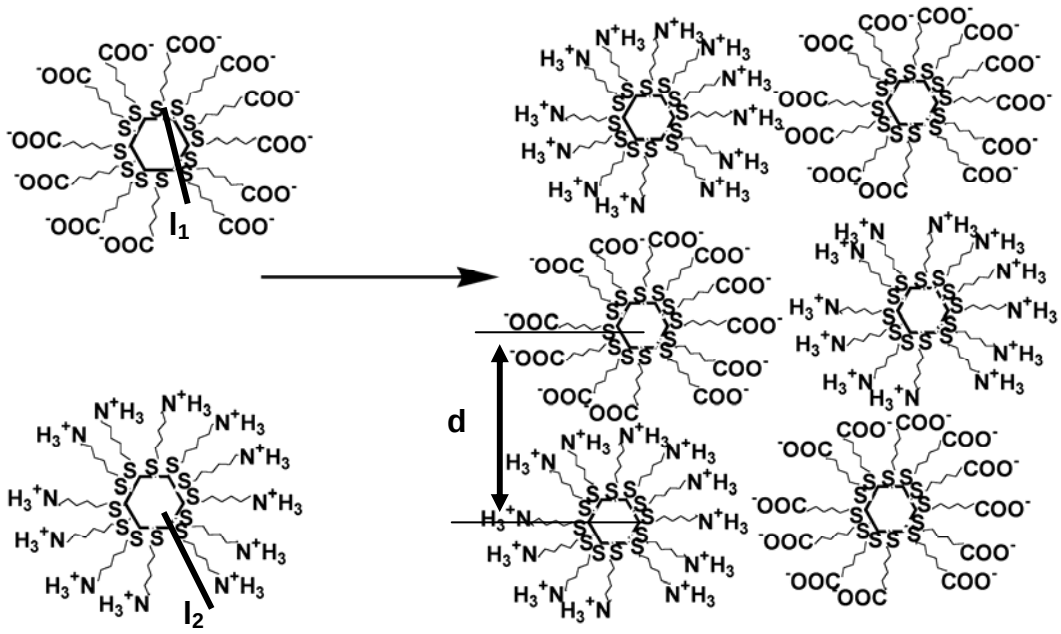

Figure 1-3. Illustration of a covalent assembly. The dominant force governing these assemblies is E_{cov}, where d = l.

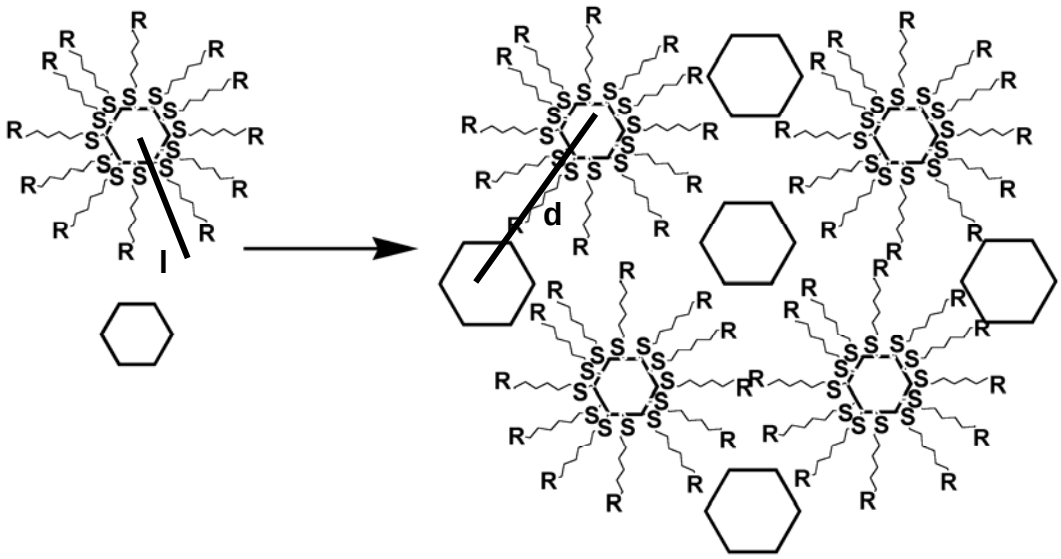

Several methods have been employed which take advantage of one or more of these forces controlling assembly in attempts to form 2 and 3 dimensional nanoparticle thin films and superstructures. These methods rely on self-assembly techniques such as evaporative self-assembly and Langmuir-Blodgett assembly and ligand-directed assemblies utilizing bifunctional ligands for electrostatic and covalently linked networks, as outlined below.

1.2 Evaporative Self-Assembly.

Superstructures of nanoparticles on the micrometer length scale have been achieved in 2 and 3 dimensional networks by allowing organically modified, surface-stabilized nanoparticles to slowly evaporate producing monolayer thin films or fcc single crystals.[13,15-17,23,29-34] The packing of nanocrystals into 3-dimensional arrays is analogous to the hard sphere packing of polystyrene spheres to produce photonic band gap materials.[35] The formation of such assemblies is strongly dependent upon the evaporation temperature and rate of evaporation of the solvent. The thermodynamically favored structure is face-centered-cubic (fcc) packing, but the difference in the Gibbs free energy between the fcc and hexagonally close-packed (hcp) phase is so small that many plane-stacking faults occur in the structure resulting in a polycrystalline material.[35]

Unlike the hard sphere packing of colloids, nanocrystals are surface-stabilized with long-chain alkyl groups, which extend their overall diameter beyond the core diameter and influence the forces controlling their assembly. Packing becomes governed by the total thermodynamic energy for assembly, involving the intermolecular forces of the individual nanoparticles and the surface mediated interactions of the passivant layer. In analogy to micelle models for soft-sphere packing, the thermodynamic interaction potentials for an evaporative assembly (E_{ea}) can be separated into ligand-ligand interactions (E_{steric}) and core-core interactions (E_{VdW}) between the nanomaterials, eqn 2.

$$E_{ea} \sim E_{steric} + E_{VdW} \qquad (2)$$

The strength of the steric energy term will be proportional to the ratio of the nanomaterial radius (R) and the distance of closest approach between the nanomaterial cores (C). The ligand length dictates the distance of closest approach and the intra-ligand interactions governed by δ_{SAM}, the brush thickness of the alkane chain, as well as σ_{thiol}, the diameter of the area occupied by the thiol on the particle surface. An illustration of these variables is given in Figure 1-4. The steric interaction potential (E_{steric}) can therefore be described as the thermodynamic energy for repulsion between two organically passivated nanoparticles as a surface dominated energy term (eqn 3).[8,36]

$$E_{steric} \approx \frac{100 R \delta_{SAM}^2}{\left(1 - 2\left(\frac{R}{C}\right)\right)\pi\sigma_{thiol}^3} kT \exp\left(\frac{-\pi\left(1 - 2\left(\frac{R}{C}\right)\right)}{\delta_{SAM}}\right) \qquad (3)$$

Figure 1-4. Illustration of the variables in equations 3 and 4.

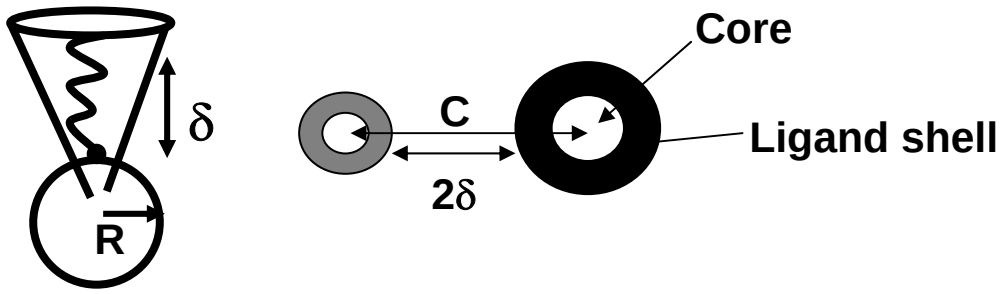

Competing with the ligand terms (E_{steric}), the core interactions between particles can be described in terms of a Van der Waals energy term, which is largely dictated by the square of the ratio of the radius (R) of the nanomaterial and distance of particle separation (C) (eqn 4).

For homogenous systems composed of individual nanomaterials the magnitude of E_{VdW} is a primary contributor to phase segregation of materials with a large polydispersity.

$$E_{vdW} \approx -\frac{A}{12}\left\{\frac{4\left(\frac{R}{C}\right)^2}{1-4\left(\frac{R}{C}\right)^2}+4\left(\frac{R}{C}\right)^2+2\ln\left[1-4\left(\frac{R}{C}\right)^2\right]\right\} \quad (4)$$

Figure 1-5 shows a plot of the energy as a function of separation distance between two 7.0 nm diameter silver nanoparticles (A = 1.95 eV) surface-stabilized with dodecanethiol using equation 3 (E_{steric}) and equation 4 (E_{VdW}).[8] Figure 1-6 illustrates a 3-dimensional representation of the interaction potential (E_{VdW} + E_{steric}) between two 10 nm Ag nanoparticles as a function of the length of the surface passivating ligands. This graph shows that as the chain length decreases there is an increased contribution from E_{VdW}, which leads to particle agglomeration. Figure 1-7 shows that there is also an increase in the E_{VdW} contribution as the particle size increases, for nanoparticles surface-stabilized with dodecanethiol ligands.

Figure 1-5. Plot of the energy as a function of separation distance.

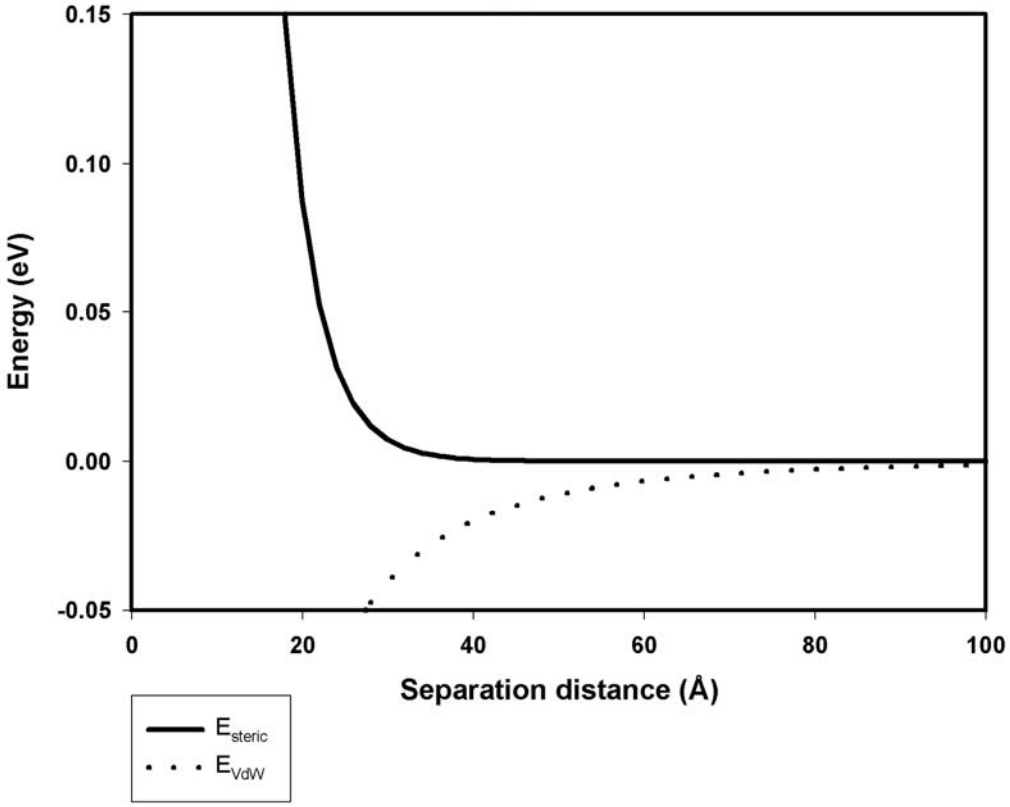

Figure 1-6. Interaction potential as a function of ligand length.

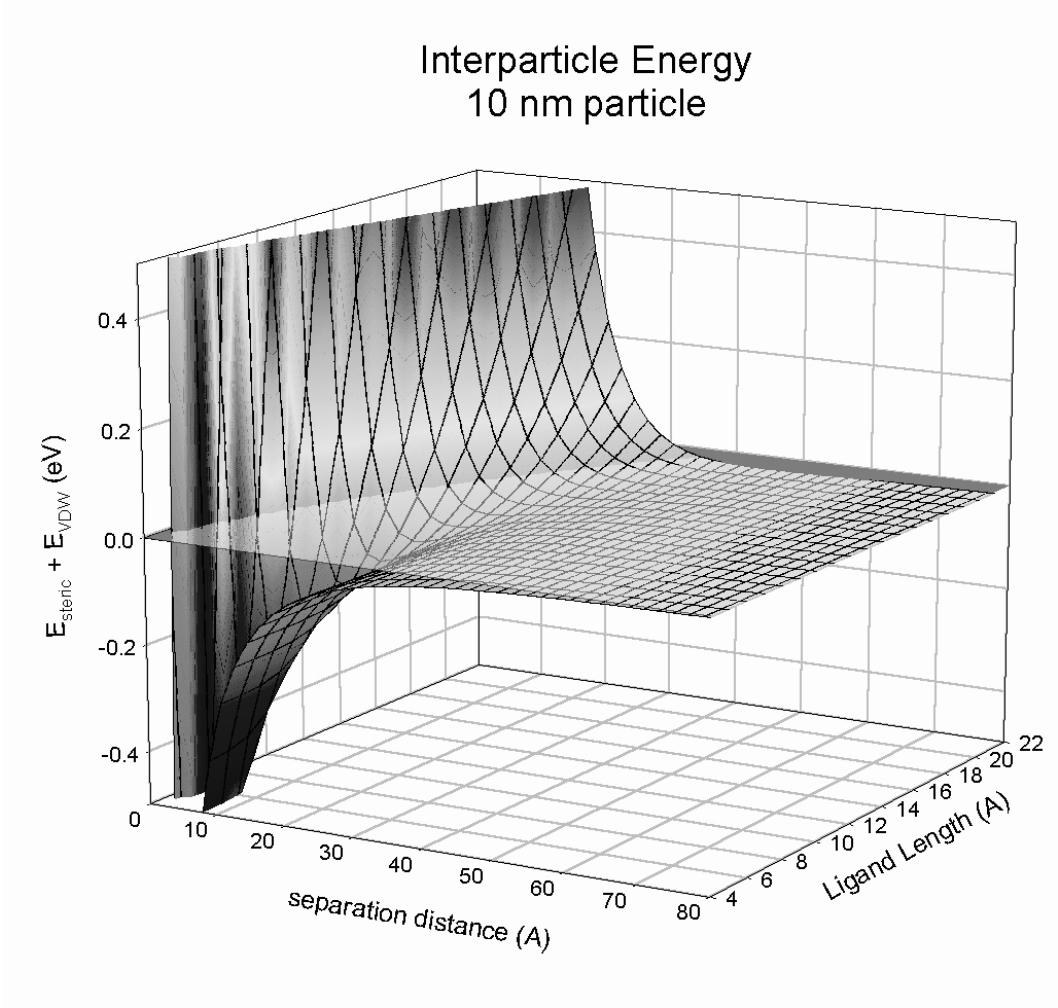

Figure 1-7. Interaction potential as a function of particle diameter.

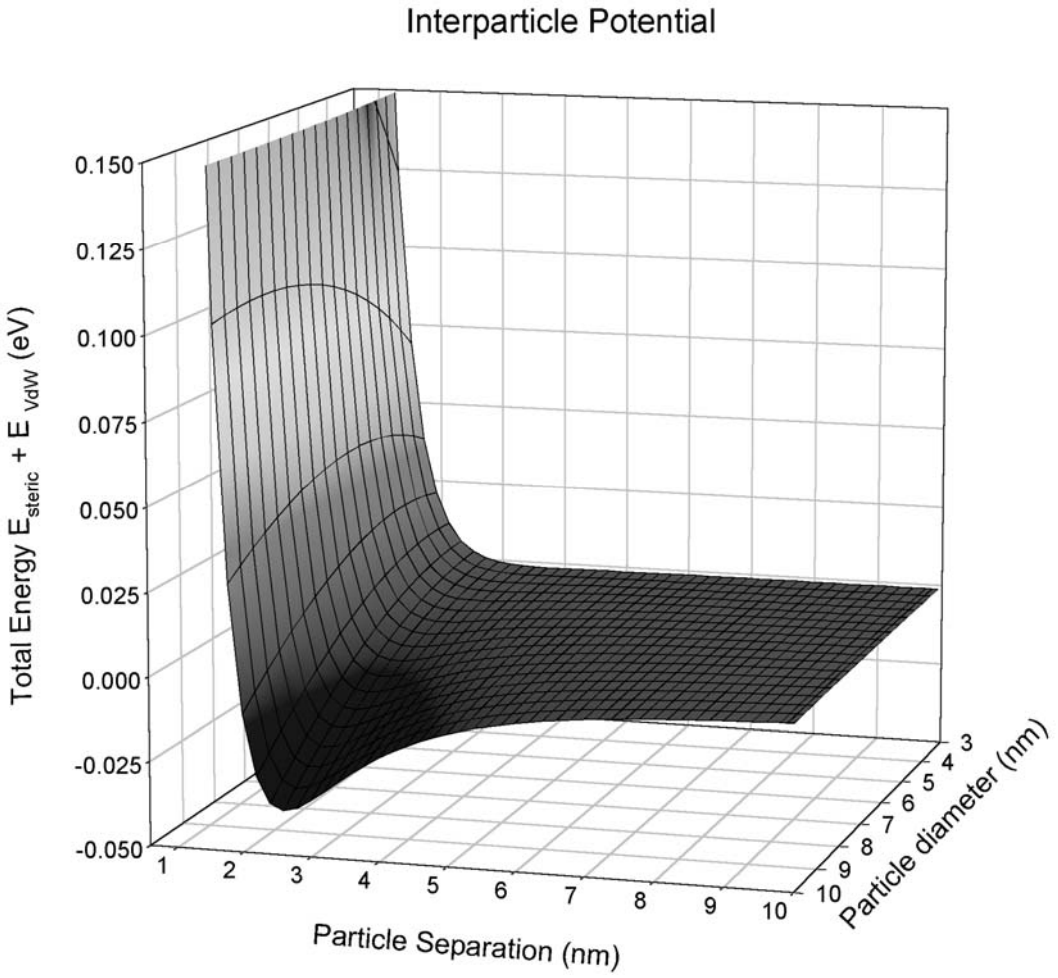

Phase segregation due to differences in the particle radius term (R) have been observed in systems for opal-like assemblies from poly disperse Au nanoparticles.[36,37] Similar to the stacking faults observed in opals, nanocrystal superstructures exhibit defects such as point defects, slip planes, and stacking faults due to strain and deformation in the solid material caused by differences particle radius and morphology.[27]

1.3 Langmuir-Blodgett Assembly.

Mono- and multilayers of semiconductor and metal nanoparticles have been fabricated utilizing Langmuir-Blodgett techniques, which depend on the same weak attractive interparticle dispersion forces controlling assembly of superstructures via evaporative self-assembly, as illustrated in Figure 1-8. This technique has been beneficial in elucidating the cooperative effects of quantum dot assemblies[21,26,38,39] such as inter-dot coupling, electron and energy transfer, and collective excitation, as well as the electrical properties of metal nanoparticles[9,40] by transference of monolayer assemblies onto solid substrates. Multi-layered assemblies of single and mixed component nanoparticles can be achieved by repeated transference of Langmuir-Blodgett monolayers onto solid substrates allowing for the study of cooperative effects between nanoparticles of different sizes and compositions.[20,41]

Figure 1-8. Illustration of a Langmuir-Blodgett assembly.

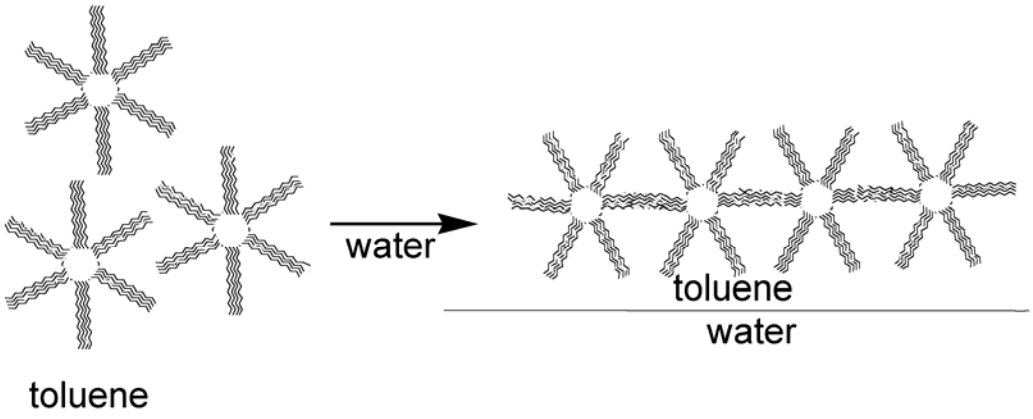

1.4 Electrostatic Assembly.

Electrostatic assemblies have been formed as both 2 and 3-dimensional assemblies on gold[42-46] and glass[24,47,48] substrates as well as 3-dimensional structures in solution[11,49] using nanoparticles surface-stabilized with ligands containing negatively charged carboxylate functionalities and positively charged ammonium functionalities or positively charged metal ions. These assemblies overcome many of the problems associated with the formation of superstructures using the evaporative assembly approach including chain-length dependence of the surface passivating groups and polydispersity of the nanoparticles. The charged nature of surface passivating groups on the nanoparticle surfaces allows for assemblies to be performed in polar media such as water and methanol and eliminates the E_{steric} term from equation 1. Likewise, electrostatic attractive forces tend to be stronger than van der Waals attractive forces reducing the size dispersity dependence on superstructure formation. Although single crystals are much more difficult to produce using electrostatic assemblies, many of the defects seen in evaporatively self-assembled single crystal superstructures, which may affect electron or energy transfer throughout the lattice, are eliminated from electrostatic and covalent assemblies due to their amorphous morphology.

A common methodology employed in the formation of electrostatic assemblies utilizes a technique developed by Whitesides for the formation of self-assembled monolayers (SAM) of alkanethiols on gold surfaces. Immersion of a cleaned gold substrate into a solution of carboxyl- or ammonium-functionalized thiols results in the formation of a monolayer of the thiols on the gold substrate with the functional groups extending out from the substrate. Glass substrates can be similarly prepared with functional groups by modification with functionalized silicates. Immersion of these substrates into solutions containing gold nanoparticles surface-passivated with oppositely charged ligands results in the formation of a monolayer of gold nanoparticles on the surface of the substrate. Adjusting the pH of the solution controls the electrostatic interactions giving greater control over the assembly of the nanoparticle monolayer.[44] Repeated immersion of this substrate into solutions containing oppositely charged nanoparticles[50] or charged metal ions[42,43] results in the buildup of 3-dimensional structures of nanoparticles. In this way single nanoparticle or mixed nanoparticle superstructures can be formed. Similarly, mixture of two aqueous solutions of nanoparticles functionalized with oppositely charges ligands results in the formation of electrostatically bound superstructures.

In the formation of these assemblies there is no indication of ligand exchange, which is expected due to the greater binding affinity of thiols to gold surfaces than ammonium or carboxylate groups. Although the strength of the adsorbed nanoparticles on the substrate is strong enough to withstand shear hydrodynamic forces used in the experiments, sonication of the substrates in water is enough to remove the adsorbed particles.[46] An additional drawback to this approach is that multiple layers may be formed after the first dipping cycle with the amount formed being dependent upon concentration and soaking time indicating that assembly using this methodology cannot be controlled.

1.5 Covalent Assembly.

The use of bifunctional ligands such as dithiols and aminoalkanethiols for the formation of 2- and 3-dimensional assemblies of single and mixed metal and semiconductor nanoparticles on gold or glass substrates have also been fabricated using similar dipping techniques as described above for electrostatic assemblies.[10,14,22,24,47,51-55] The use of ligands capable of covalent binding to nanoparticle surfaces offers the benefit of stronger binding between nanoparticles than that of electrostatic assemblies. Hetero-composite systems opens the possibilities for nano-electronics and solar conversion applications where individual materials are intimately connected allowing for

electron or energy transfer throughout the lattice network. Possibilities for covalent assembly arise from interactions of functionalized surface-passivating ligands with nanomaterial surfaces, metal ions, or proteins and DNA base pairs.

1.6 Overview.

The methodologies used to prepare the gold, silver, and CdSe nanoparticles and their optical and physical properties are outlined in Chapter 2. The colloidal metal nanoparticles were prepared either as organically soluble nanomaterials by $NaBH_4$ reduction of metal salts in toluene via a two-phase liquid-liquid methodology or as water-soluble metal nanoparticles by the reduction of an aqueous metal salt solution with sodium citrate and tannic acid. TEM images of the metal nanoparticles are presented as well as powder x-ray diffraction and selected-area electron diffraction (SAED) patterns of the gold nanoparticles illustrating the dominant faces of the nanocrystals. UV-vis absorbance of the metal solutions is presented illustrating the characteristic surface plasmon resonance (SPR).

CdSe nanocrystals were prepared using a modification of the lyothermal methodology in which a single source precursor is heated to high temperatures in a coordinating solvent. UV-vis absorbance is presented illustrating the control obtainable over the sizes of the materials produced as well as the

narrowing of the dispersity resulting from size-selected precipitation. TEM, powder x-ray diffraction, and selected-area electron diffraction (SAED) patterns of hexadecylamine-capped CdSe are shown illustrating the hexagonal-packing as well as the crystalline nature of the CdSe.

The optical and physical properties of water-soluble colloidal gold nanoparticles as a function of surface-passivating groups are explored in Chapter 3. Colloidal gold nanoparticles can be isolated from excess citric acid buffer by electrolyte-induced precipitation from water solutions through the addition of oxyanions. This allows the nanomaterials to be isolated as freely soluble powders that can be used for bio-labeling experiments. Analysis of UV-vis and FTIR spectroscopy allows direct analysis of the oxyanion interaction at the surface of the Au nanomaterial. These studies indicate the thermodynamic stability and nature of binding is dictated by the availability of d-orbitals for back bonding, while the SPR band frequency is largely modulated by the electrostatics of the ligand. Comparison of the extinction coefficient of the SPR band to Mie theory predictions further illustrates the affect of ligand interactions on the properties of the Au nanomaterials. For a series of oxyanions, the order of thermodynamic stability is $CO_3^{2-} < H_2PO_4^{1-} < SO_4^{2}$, while the shift in the SPR band follows the trend $H_2PO_4^{1-} > CO_3^{2-} > SO_4^{2-}$.

Assembly of gold superstructures via addition of aminoalkanethiol ligands to aqueous gold nanoparticle solutions is presented in Chapter 4. The influence of ligand chain length and nanoparticle size on assembly is discussed with regards to steric and Van der Waals packing forces. UV-vis, FTIR and TEM analysis of the structures is presented.

Formation of a uniform 3-D hetero-assembled "glassy" composite comprised of individual nano-scale Au and CdSe materials is presented in Chapter 5. This methodology presents a thermodynamically driven non-lithographic synthetic strategy for the preparation of a mixed nanoparticle composite, which utilizes a ligand modified CdSe nanomaterial to direct the assembly of weakly passivated Au nanoparticles into a hexagonally packed alternating 6:1 CdSe:Au composite structure. The assembly is believed to arise from a competition between steric repulsion terms, van der Waals attraction energies, and ligand directing covalent bond-forming interactions. Organization of these materials into 3- dimensional structures may provide a structural paradigm for developing nano-electronic composite architectures.

The physical properties of the composites were characterized by TEM, SEM, SAED, pXRD, and UV-vis spectroscopy. FTIR spectroscopy was used to support the theory that the composite arises from the formation of a Au-N bond. The crystallinity of the nanocomposite is examined as a function of pH

of the reaction solutions as well as the molar and size ratios of the nanomaterials.

1.7 References.

1) Zhang, J. Z. *Accounts of Chemical Research* **1997**, *30*, 423-429.

2) Stucky, G. D.; Macdougall, J. E. *Science* **1990**, *247*, 669-678.

3) Lorenz, J. K.; Ellis, A. B. *Journal of the American Chemical Society* **1998**, *120*, 10970-10975.

4) Heath, J. R.; Shiang, J. J. *Chemical Society Reviews* **1998**, *27*, 65-71.

5) Alivisatos, A. P. *Science* **1996**, *271*, 933-937.

6) Alivisatos, A. P. *Journal of Physical Chemistry* **1996**, *100*, 13226-13239.

7) Murray, C. B.; Norris, D. J.; Bawendi, M. G. *Journal of the American Chemical Society* **1993**, *115*, 8706-8715.

8) Korgel, B. A.; Fullam, S.; Connolly, S.; Fitzmaurice, D. *Journal of Physical Chemistry B* **1998**, *102*, 8379-8388.

9) Markovich, G.; Collier, C. P.; Henrichs, S. E.; Remacle, F.; Levine, R. D.; Heath, J. R. *Accounts of Chemical Research* **1999**, *32*, 415-423.

10) Brust, M.; Bethell, D.; Kiely, C. J.; Schiffrin, D. J. *Langmuir* **1998**, *14*, 5425-5429.

11) Galow, T. H.; Boal, A. K.; Rotello, V. M. *Advanced Materials* **2000**, *12*, 576-579.

12) Green, M.; O'Brien, P. *Chemical Communications* **1999**, 2235-2241.

13) Harfenist, S. A.; Wang, Z. L.; Whetten, R. L.; Vezmar, I.; Alvarez, M. M. *Advanced Materials* **1997**, *9*, 817+.

14) Nakanishi, T.; Ohtani, B.; Uosaki, K. *Journal of Physical Chemistry B* **1998**, *102*, 1571-1577.

15) Pileni, M. P. *Journal of Physical Chemistry B* **2001**, *105*, 3358-3371.

16) Sun, S. H.; Murray, C. B. *Journal of Applied Physics* **1999**, *85*, 4325-4330.

17) Wang, Z. L.; Harfenist, S. A.; Vezmar, I.; Whetten, R. L.; Bentley, J.; Evans, N. D.; Alexander, K. B. *Advanced Materials* **1998**, *10*, 808-812.

18) Whetten, R. L.; Shafigullin, M. N.; Khoury, J. T.; Schaaff, T. G.; Vezmar, I.; Alvarez, M. M.; Wilkinson, A. *Accounts of Chemical Research* **1999**, *32*, 397-406.

19) Kagan, C. R.; Murray, C. B.; Nirmal, M.; Bawendi, M. G. *Physical Review Letters* **1996**, *76*, 1517-1520.

20) Berfeld, M.; Samokhvalov, A.; Naaman, R.; Lahav, M. *Advanced Materials* **2001**, *13*, 584-587,541.

21) Cordero, S. R.; Carson, P. J.; Estabrook, R. A.; Strouse, G. F.; Buratto, S. K. *Journal of Physical Chemistry B* **2000**, *104*, 12137-12142.

22) Fishelson, N.; Shkrob, I.; Lev, O.; Gun, J.; Modestov, A. D. *Langmuir* **2001**, *17*, 403-412.

23) Heath, J. R.; Knobler, C. M.; Leff, D. V. *Journal of Physical Chemistry B* **1997**, *101*, 189-197.

24) Musick, M. D.; Pena, D. J.; Botsko, S. L.; McEvoy, T. M.; Richardson, J. N.; Natan, M. J. *Langmuir* **1999**, *15*, 844-850.

25) Taleb, A.; Petit, C.; Pileni, M. P. *Journal of Physical Chemistry B* **1998**, *102*, 2214-2220.

26) Torimoto, T.; Tsumura, N.; Miyake, M.; Nishizawa, M.; Sakata, T.; Mori, H.; Yoneyama, H. *Langmuir* **1999**, *15*, 1853-1858.

27) Wang, Z. L. *Advanced Materials* **1998**, *10*, 13+.

28) Takagahara, T. *Surface Science* **1992**, *267*, 310-314.

29) Martin, J. E.; Wilcoxon, J. P.; Odinek, J.; Provencio, P. *Journal of Physical Chemistry B* **2000**, *104*, 9475-9486.

30) Wang, Z. L.; Harfenist, S. A.; Whetten, R. L.; Bentley, J.; Evans, N. D. *Journal of Physical Chemistry B* **1998**, *102*, 3068-3072.

31) Gutierrez-Wing, C.; Santiago, P.; Ascencio, J. A.; Camacho, A.; Jose-Yacaman, M. *Applied Physics a-Materials Science & Processing* **2000**, *71*, 237-243.

32) Harfenist, S. A.; Wang, Z. L.; Alvarez, M. M.; Vezmar, I.; Whetten, R. L. *Journal of Physical Chemistry* **1996**, *100*, 13904-13910.

33) Motte, L.; Pileni, M. P. *Journal of Physical Chemistry B* **1998**, *102*, 4104-4109.

34) Kagan, C. R.; Murray, C. B.; Bawendi, M. G. *Physical Review B-Condensed Matter* **1996**, *54*, 8633-8643.

35) Ye, Y. H.; LeBlanc, F.; Hache, A.; Truong, V. V. *Applied Physics Letters* **2001**, *78*, 52-54.

36) Ohara, P. C.; Leff, D. V.; Heath, J. R.; Gelbart, W. M. *Physical Review Letters* **1995**, *75*, 3466-3469.

37) Kiely, C. J.; Fink, J.; Brust, M.; Bethell, D.; Schiffrin, D. J. *Nature* **1998**, *396*, 444-446.

38) Tian, Y. C.; Fendler, J. H. *Chemistry of Materials* **1996**, *8*, 969-974.

39) Dabbousi, B. O.; Murray, C. B.; Rubner, M. F.; Bawendi, M. G. *Chemistry of Materials* **1994**, *6*, 216-219.

40) Brust, m.; Stuhr-Hansen, N.; Norgaard, K.; Christensen, J. B.; Nielsen, L. K.; Bjornholm, T. *Nano Letters* **2001**, *1*, 189-191.

41) Kotov, N. A.; Meldrum, F. C.; Wu, C.; Fendler, J. H. *Journal of Physical Chemistry* **1994**, *98*, 2735-2738.

42) Zamborini, F. P.; Hicks, J. F.; Murray, R. W. *Journal of the American Chemical Society* **2000**, *122*, 4514-4515.

43) Templeton, A. C.; Zamborini, F. P.; Wuelfing, W. P.; Murray, R. W. *Langmuir* **2000**, *16*, 6682-6688.

44) Gole, A.; Sainkar, S. R.; Sastry, M. *Chemistry of Materials* **2000**, *12*, 1234-1239.

45) Auer, F.; Scotti, M.; Ulman, A.; Jordan, R.; Sellergren, B.; Garno, J.; Liu, G. Y. *Langmuir* **2000**, *16*, 7554-7557.

46) Tien, J.; Terfort, A.; Whitesides, G. M. *Langmuir* **1997**, *13*, 5349-5355.

47) Musick, M. D.; Keating, C. D.; Lyon, L. A.; Botsko, S. L.; Pena, D. J.; Holliway, W. D.; McEvoy, T. M.; Richardson, J. N.; Natan, M. J. *Chemistry of Materials* **2000**, *12*, 2869-2881.

48) Grabar, K. C.; Smith, P. C.; Musick, M. D.; Davis, J. A.; Walter, D. G.; Jackson, M. A.; Guthrie, A. P.; Natan, M. J. *Journal of the American Chemical Society* **1996**, *118*, 1148-1153.

49) Chen, S. H.; Kimura, K. *Chemistry Letters* **1999**, 233-234.

50) Kumar, A.; Mandale, A. B.; Sastry, M. *Langmuir* **2000**, *16*, 6921-6926.

51) He, H. X.; Zhang, H.; Li, Q. G.; Zhu, T.; Li, S. F. Y.; Liu, Z. F. *Langmuir* **2000**, *16*, 3846-3851.

52) Bethell, D.; Brust, M.; Schiffrin, D. J.; Kiely, C. *Journal of Electroanalytical Chemistry* **1996**, *409*, 137-143.

53) Colvin, V. L.; Goldstein, A. N.; Alivisatos, A. P. *Journal of the American Chemical Society* **1992**, *114*, 5221-5230.

54) Sarathy, K. V.; Thomas, P. J.; Kulkarni, G. U.; Rao, C. N. R. *Journal of Physical Chemistry B* **1999**, *103*, 399-401.

55) Miyake, M.; Matsumoto, H.; Nishizawa, M.; Sakata, T.; Mori, H.; Kuwabata, S.; Yoneyama, H. *Langmuir* **1997**, *13*, 742-746.

Chapter 2

Synthesis of Nanoparticles

2.1 Introduction.

Metal and semiconductor nanomaterials are of great interest due to their size dependant optical and electronic properties, as well as their potential applications in areas of catalysis, nanoelectronics, biolabeling, and surface enhanced Raman spectroscopy (SERS).[1-11] At sizes smaller than that for bulk materials, nanomaterials exhibit optical, electronic, and catalytic properties different from those of the bulk material. For semiconductor nanoparticles such as CdSe, these properties stem from quantum state effects (QSEs) due to a confinement of an electron-hole pair (exciton) within the nanocrystal.[6,12] The exciton comes from the excitation of an electron from the valence band into the conduction band of the nanocrystal, as illustrated in Figure 2-1. As the size of the nanocrystal increases, the band gap between the valence and conduction band decreases. This leads to a decrease in the energy (E_g) required to inject an electron from the valence to the conduction band and is evidenced by the shift in the absorbance band of the CdSe to higher wavelengths (or lower energy).

Figure 2-1. Illustration of band structure of CdSe.

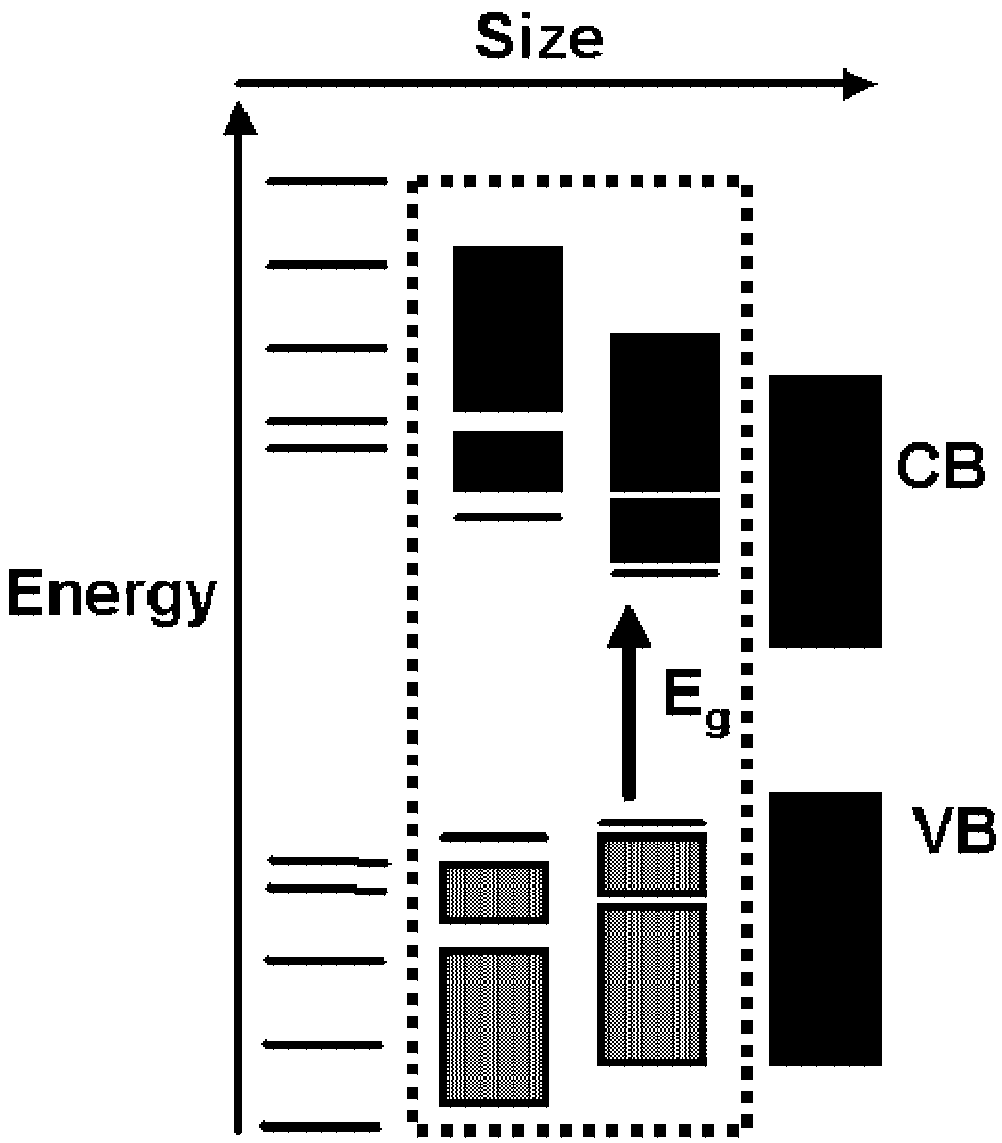

For noble metals, which have no band gap between the valence and conduction bands, there is a less pronounced influence of particle size on the optical properties of the material. Rather, as the particle size is decreased below the electron free mean path of the bulk material, the free electrons on the particle surface begin to oscillate with the electric field vector of the light giving rise to a strong absorption band referred to as the surface plasmon resonance band (SPR).[13] An increase in the size of the nanoparticle results in an increase in the intensity of the SPR rather than a shift in the absorption maximum.

Recent synthetic advances allow for the production of near monodisperse metal and semiconducting nanoparticles in organic as well as aqueous media, surface-stabilized with a variety of passivating ligands.[1,12,14-28] Size-selective precipitation allows for the dispersity of organically soluble nanoparticles to be narrowed further. Ligand exchange procedures allow for the tailoring of the reactivity and solubility of these materials.

2.2 Gold.

Among the metal nanoparticles that have been produced, colloidal gold nanoparticles are of great interest due to their ease of preparation and long-term stability in organic as well as aqueous media.[15-18,20,22,23,25,28] A

recent review by Handley describes many different methods of synthesis affording colloidal gold nanoparticles of various sizes and with varying degrees of stability.[29] The methodologies employed in this work were selected on the basis of producing colloidal gold nanoparticles with good monodispersity and long-term stability.

2.2.1 Two-Phase Organic Methodology for Au Preparation.

Colloidal gold nanoparticles prepared in organic media involve a two-phase liquid-liquid methodology developed by Brust, which produces gold nanoparticles from 2-14 nm with good monodispersity and which can be surface passivated with a variety of ligands containing amine or thiol moieties.[16] This method involves the phase transfer of $AuCl_4^-$ ions from an aqueous solution of hydrogen tetrachloroauric acid into an organic solvent, such as toluene or diethyl ether, using tetraoctylammonium bromide (TOABr) as the phase transfer catalyst. The Au^{2+} ions are then reduced by rapid mixing with an aqueous solution of sodium borohydride ($NaBH_4^-$). The source of electrons for the reduction of Au^{2+} to Au^0 is the BH_4^- and the possible side products include $H_{2(g)}$, sodium borate, and sodium chloride.[22] The size of the gold nanoparticles produced is dependent on the TOABr/Au and $NaBH_4$/Au ratio with the resulting gold nanoparticles weakly surface passivated by tetraoctylammonium bromide, which can then be exchanged for other ligands

containing amine of thiol functional groups by addition of the ligand to the organic phase. Addition of alkylamines or alkanethiols to the organic phase prior to the addition of the sodium borohydride solution allows for the preparation of already surface-passivated gold nanoparticles, with the ligand/Au ratio influencing the size of the nanoparticle. Surface passivation with long-chain alkyl groups allows for size-selective precipitation using a solvent/non-solvent combination, which further improves the monodispersity of the sample.[12]

In a typical synthesis, ~5.0 nm colloidal gold nanoparticles surface-passivated with hexadecanethiol (HDT) can be prepared by reaction of 0.354g of $HAuCl_4 \bullet 3H_2O$ in 30ml of deionized water, which results in a clear yellow 30mM gold solution, with a vigorously stirred toluene solution (80 ml) containing 2.187g of TOABr (50mM). Upon mixing the aqueous layer became clear and colorless and the organic layer obtained a dark yellow color. A freshly prepared solution containing 0.473g of $NaBH_4$ in 25 ml of deionized water (0.5M) was added with vigorous stirring resulting in a color change from dark yellow to dark purple. The resulting two-phase system was stirred at room temperature for 2 hours to insure complete reduction of the auric acid. The organic phase was separated from the aqueous phase and washed once with 30ml of a 0.1 M H_2SO_4 solution to insure complete oxidation of the

sodium borohydride. The organic phase was then washed twice with a 1M $NaCO_3$ solution and 5 times with deionized water, then dried over sodium sulfate and decanted. This produced 5.0 nm gold nanoparticles surface passivated with TOABr (Au-TOABr). Reduction of the concentration of $NaBH_4$ from 25ml of 0.5M $NaBH_4$ solution to 25ml of 0.4M $NaBH_4$ solution resulted in an increase in the size of the gold nanoparticles from 5.0 nm to 8.0 nm. Surface passivation of the gold nanoparticles was accomplished by addition of 170mg of HDT (65.76 mmol) to the toluene solution at room temperature and stirred overnight. The colloidal gold nanoparticles surface-passivated with HDT (Au-HDT) were size-selectively precipitated from the toluene solution by drop-wise addition of anhydrous methanol until a turbid solution resulted. The nanoparticles were then collected by centrifuge and decanted followed by washing with methanol and drying under vacuum. The size-selective precipitation procedure was repeated on the supernatant, with the minimal amount of methanol being added to produce a turbid solution, until all the nanoparticles had been collected and a clear organic solution remained. This resulted in near monodisperse 5.0 nm colloidal gold nanoparticles surface-passivated with hexadecanethiol as illustrated in Figure 2-2. Selected area electron diffraction of Au-HDT evaporatively self-assembled on a TEM grid is shown in Figure 2-3. A distribution curve taken from the SAED image is shown in Figure 2-4 and the matching powder x-ray

diffraction analysis is shown in Figure 2-5. Both indicate a strong peaks for the (111) lattice plane of the nanocrystals as well as moderate peaks for the (200), (220), and (311) lattice planes. The distribution curve was obtained from performing a line scan on the SAED image in Sigma Plot.

Figure 2-2. TEM image of 5.0 nm colloidal gold nanoparticles prepared by the two-phase methodology and surface-passivated with HDT. Images were obtained at a magnification of x100K.

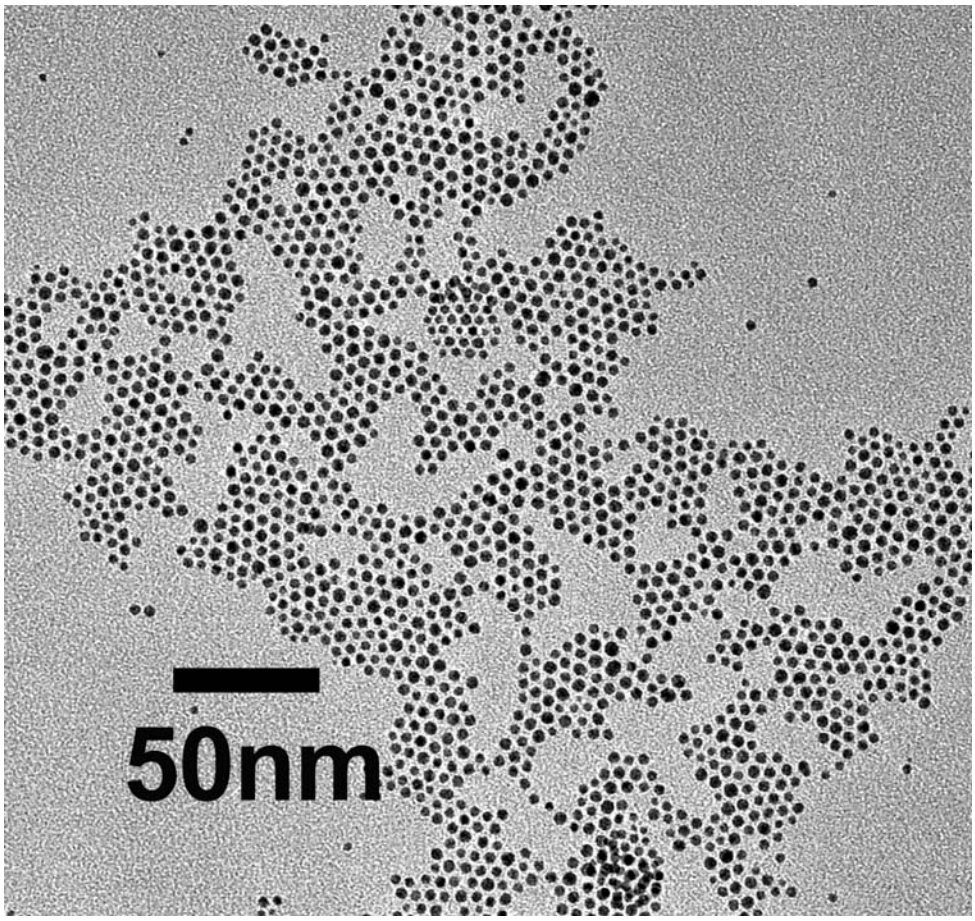

Figure 2-3. SAED pattern for the Au-HDT shown in Figure 2-1.

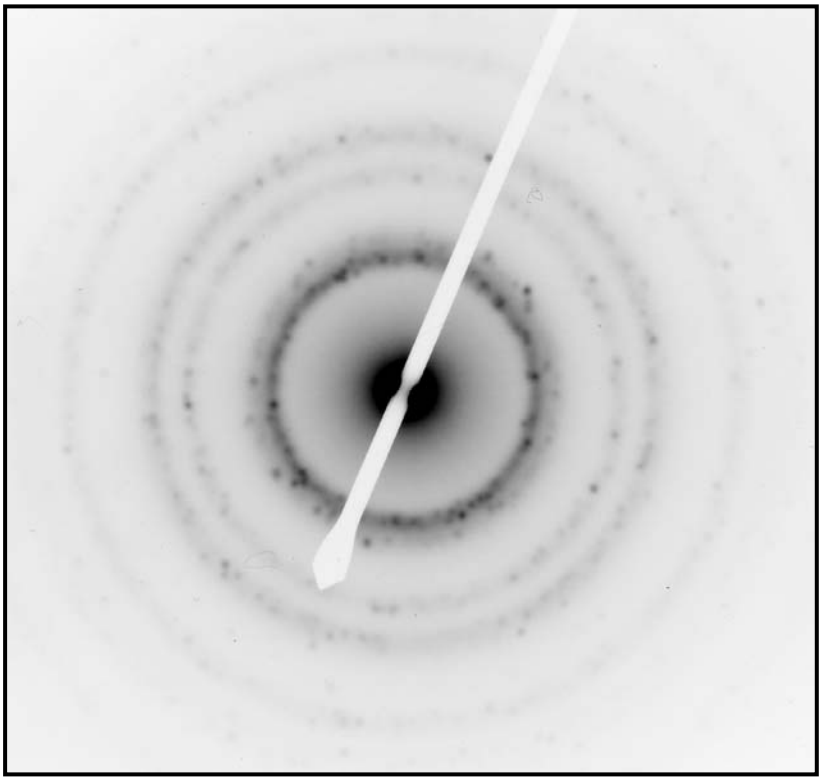

Figure 2-4. Distribution curve from SAED pattern in Figure 2-3.

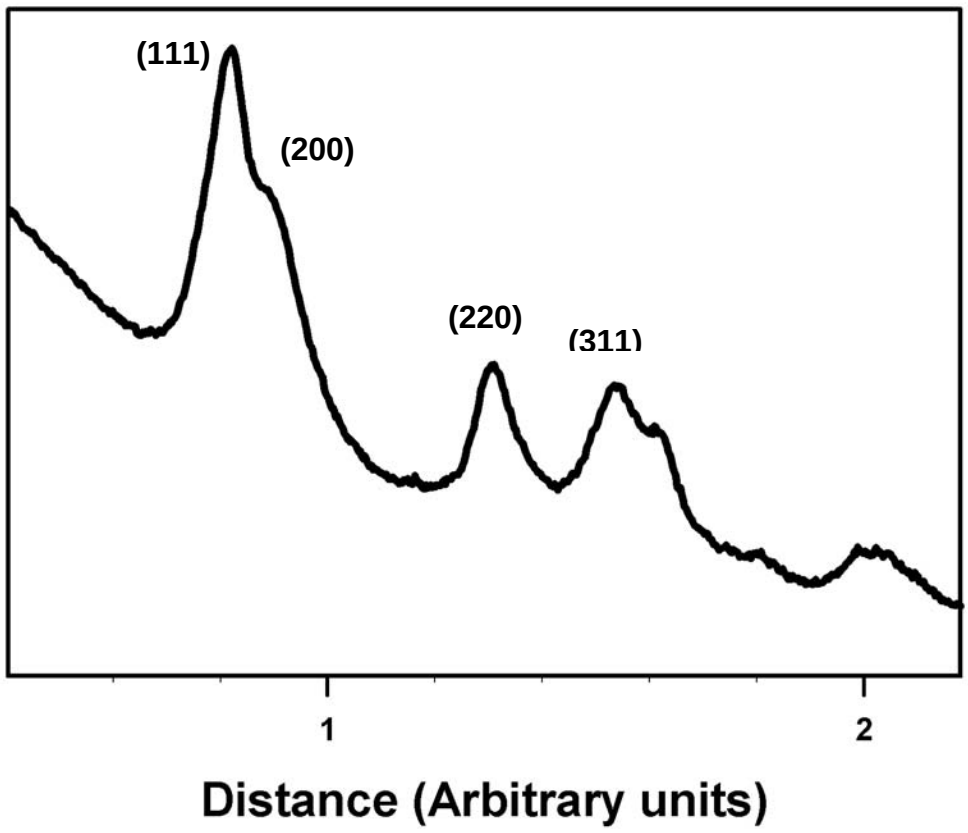

Figure 2-5. Powder x-ray diffraction of Au-HDT.

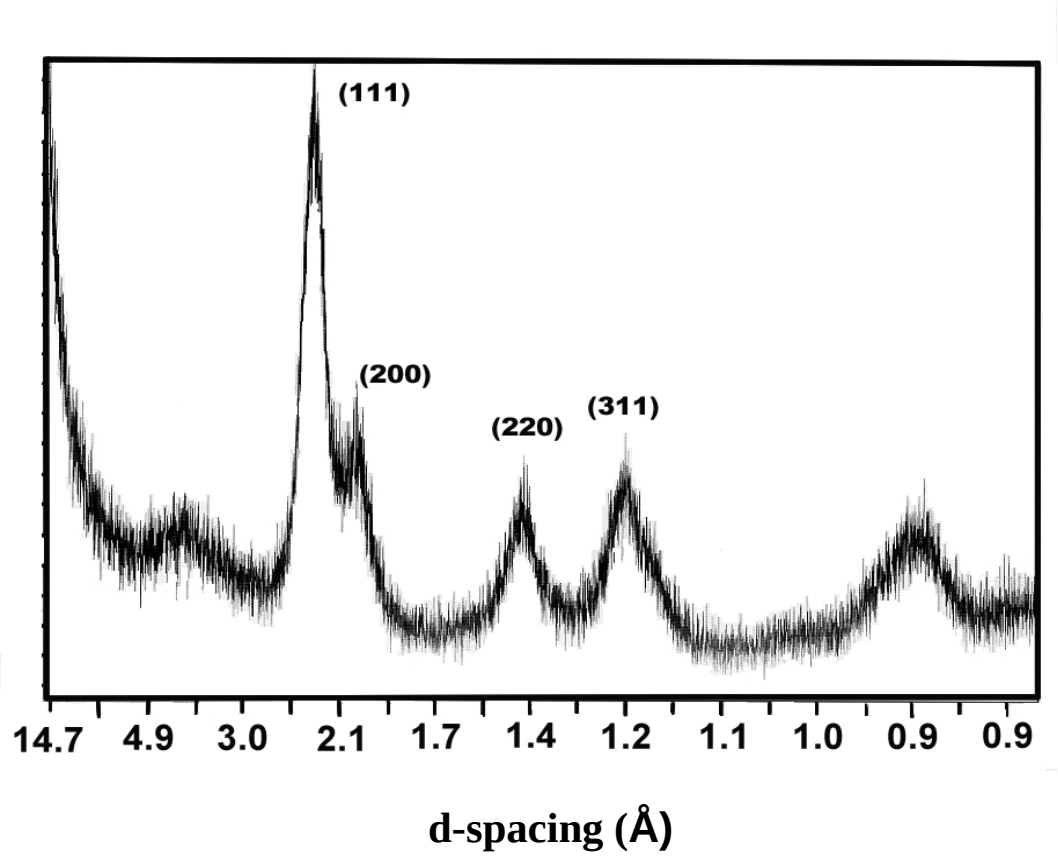

Colloidal gold nanoparticles exhibit a surface plasmon resonance (SPR) band around 520nm with the intensity and shape of the band dependent on the size of the nanoparticles, dispersity of the nanoparticles, the surface passivating group, and the dielectric constant of the medium in which the absorbance is measured.[26,30-32] Figure 2-6 shows the absorbance of (a) 5.0 nm Au-TOABr, (b) 5.0 nm Au-HDT, and (c) 8.0 nm colloidal gold nanoparticles surface passivated with n-octylamine (Au-OA). The Au-TOABr toluene solution exhibits a SPR at 518 nm. Surface passivation with HDT results in a slight broadening of the SPR without a shift in the peak location. By comparison, 8.0 nm Au-OA exhibits a SPR of greater intensity, due to the larger size, and red-shifted 6 nm.

2.2.2 Aqueous Methodology for Au Preparation.

2.2.2.1 10-30 nm Diameter Au Colloids.

Aqueous methodologies for the synthesis of colloidal gold nanoparticles do not allow for gold nanoparticles surface-passivated with long-chain alkyl groups due to the hydrophobic nature of the ligands. This limits the ability to size-select the Au nanomaterials. Nevertheless, water-soluble gold nanoparticles are essential in cytochemistry for biolabeling of proteins and DNA and can be synthesized with a dispersity of 15-20% with labile surface stabilizing groups that are easily displaced by water-soluble ligands.[23,27,32] Turkevich et al developed a methodology for the formation of 10-30 nm

colloidal gold nanoparticles using sodium citrate as the reductant of auric acid as well as serving as passivating groups on the gold surface (Au-cit).[32] The molar ratio of auric acid to citrate allows for the control of the size of the nanoparticles produced with a decrease in the Au/citrate ratio resulting in an increase the nanoparticle size.

In a typical synthesis of 15 nm Au-cit, 0.025g of $HAuCl_4$ was dissolved in 250ml of deionized water and brought to reflux. To this rapidly stirring solution was added 8.75ml of a 34mmol solution of sodium citrate. This resulted in a gradual change in color from a pale yellow to a wine red color. The solution was refluxed for an additional 15 minutes with rapid stirring followed by cooling to room temperature by swirling the flask under running water. This methodology produced 15.0 nm gold nanoparticles, surface-stabilized with citrate ions, and exhibiting good monodispersity, as illustrated in Figure 2-7. In this image gold nanoparticles can be identified as having spherical or truncated dodecahedral morphology. Figure 2-8 shows a TEM image of 18 nm Au-cit with arrows indicating staple faults common in metal nanoparticles. UV-vis absorbance of 15.0 nm Au-cit shown in Figure 2-9 indicates a strong SPR centered at 517nm. By comparison to the SPR of 6.0 and 8.0 nm Au nanoparticles in Figure 2-6, the SPR for the larger Au-cit nanoparticles is greater in intensity.

Figure 2-6. UV-vis absorbance of (a) 5.0 nm Au-TOABr, (b) 5.0 nm Au-HDT, and (c) 8.0 nm Au-OA. The lines have been offset for clarity.

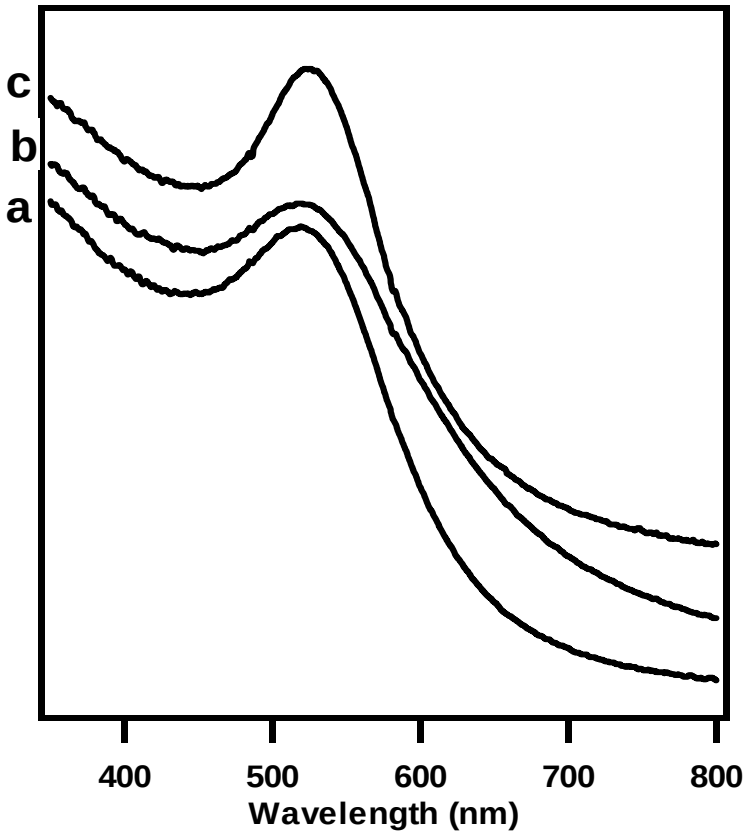

Figure 2-7. TEM image of 15 nm Au-cit nanoparticles taken at x100K magnification.

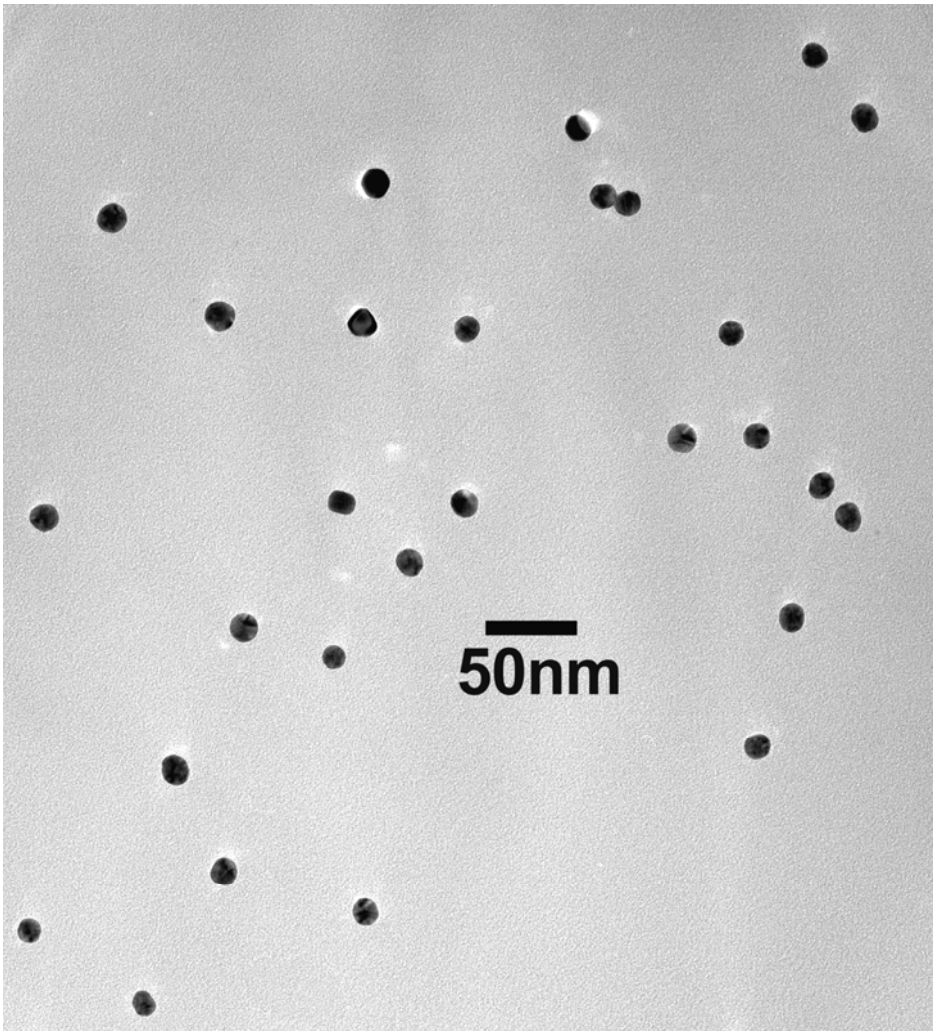

Figure 2-8. TEM image of 18 nm citrate-stabilized gold nanoparticles taken at x210K magnification with arrows indicating staple faults characteristic of metal nanoparticles.

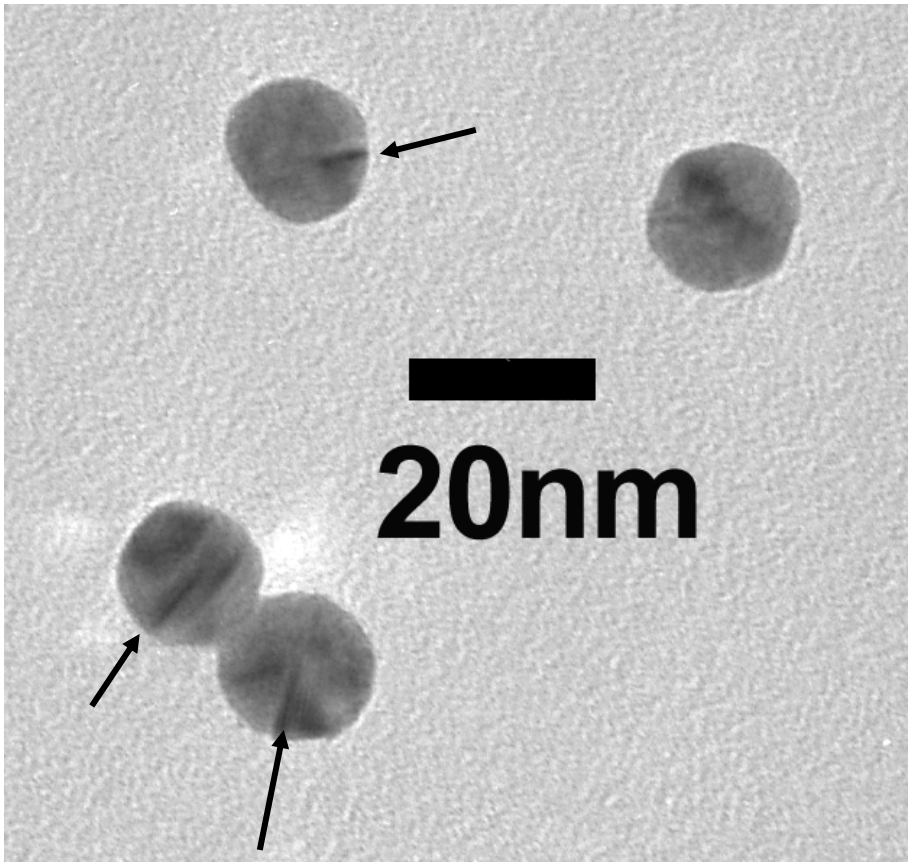

Figure 2-9. UV-vis absorbance of 15 nm Au-cit showing an intense SPR band centered at 518nm.

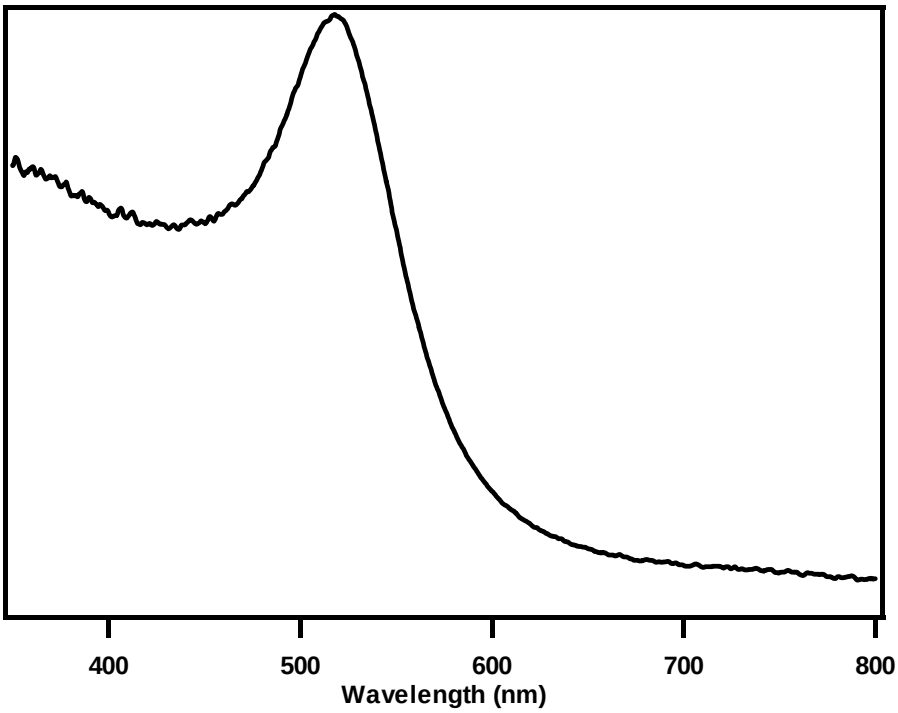

2.2.2.2 3-17 nm Diameter Au Colloids.

Sodium citrate, in comparison to $NaBH_4$, is a weak reducer of auric acid, as is illustrated by the longer reaction time required for the solutions to turn from a yellow to red color. The advantage of using sodium citrate as a reductant is that water-soluble gold nanoparticles can be prepared with good monodispersity and labile citrate ions serving as surface-passivating groups. A disadvantage is that gold nanoparticles smaller than 10 nm is difficult to achieve. It is believed that slower reaction times result in the formation of a fewer number of nuclei from which the gold nanoparticles grow, resulting in the growth of larger nanoparticles.[27] To overcome this, Mühlfordt developed a methodology using tannic acid in addition to sodium citrate, which causes a fast reduction of the gold resulting in the formation of more nuclei and smaller gold nanoparticles.[23,27] Slot and Geuze expanded on this procedure showing how varying the amount of tannic acid used allowed for size control of the nanoparticles. Decreasing the amount of 1% tannic acid from 5ml to 0.01ml resulted in an increase in the nanoparticle size from 3 to 17nm.[27]

In a typical synthesis of 6.0 nm Au-TA, 100ml of a freshly prepared 0.1% (w/v) $HAuCl_4$ solution was brought to reflux and to it was rapidly injected a solution containing 2ml of a 1% (w/v) sodium citrate dihydrate solution and

0.45ml of a 1% (w/v) tannic acid solution, with vigorous stirring. The solution immediately changed from a pale yellow to a wine red color. The resulting solution was refluxed for an additional 5 minutes then removed from heat and cooled to room temperature under running water. TEM analysis of the resulting gold nanoparticle solution, shown in Figure 2-10, indicates the formation of 6.0nm colloidal gold nanoparticles with good monodispersity. UV-vis absorbance of the gold nanoparticle, shown in Figure 2-11, shows the SPR band centered at 525nm. The absorbance peak around 360nm is due to polymerized tannic acid in solution.

2.2.2.3 2-3 nm Diameter Au Colloids.

Smaller gold nanoparticles ~3.0 nm in diameter (Au-SCN) were prepared by a method developed by Baschong et al using thiocyanate as the reductant.[33] In this method 0.3 ml of 1 M thiocyanate solution was added at room temperature with stirring to 50 ml of deionized water containing 0.5 ml of 1% (w/v) auric acid and 0.75 ml of 0.2 M K_2CO_3. The solution was let stir for 15 hours in the dark at 22 ^{o}C and used shortly after preparation. The resulting solution is yellowish in color without the wine red color characteristic in larger colloidal gold nanoparticles and due not exhibit any surface plasmon resonance absorption band due to their small size, as illustrated in Figure 2-12. At this size the gold colloids do not have the electron scattering ability of

larger nanoparticles and thus in the TEM images do not have an electron-dense profile, as illustrated in Figure 2-13.

Figure 2-10. TEM image of 6.0nm Au-TA taken at a magnification of x210K.

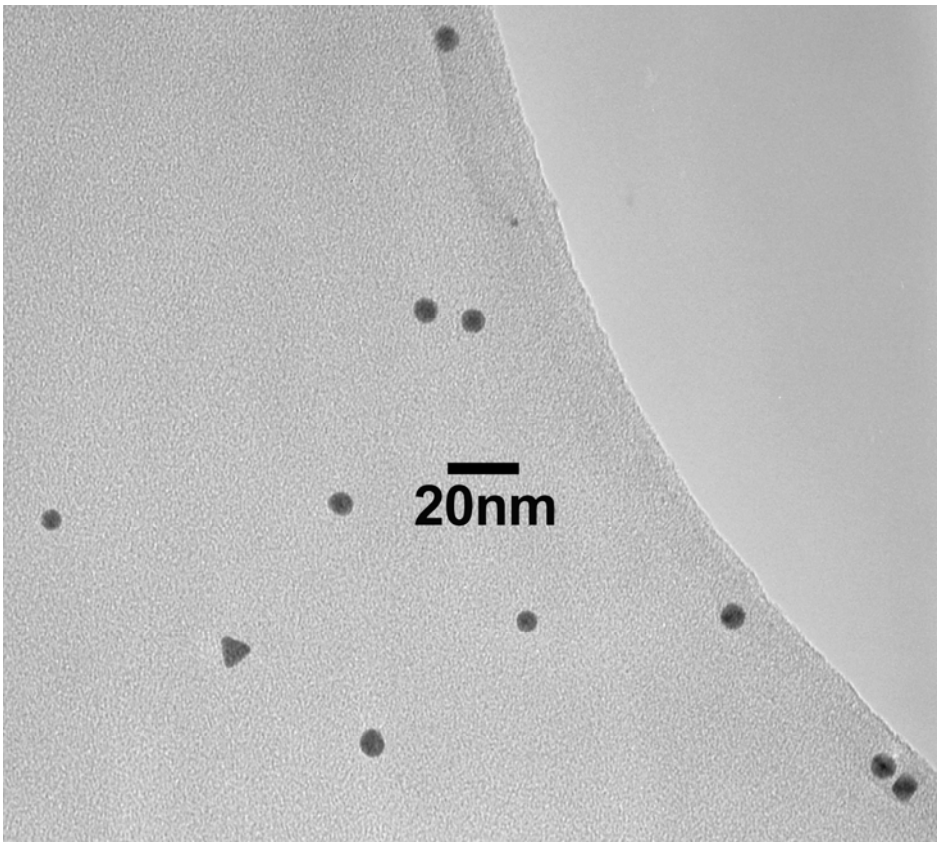

Figure 2-11. UV-vis absorbance of 6.0 nm Au-TA with the SPR centered at 525nm and the absorbance peak around 360 due to polymerized tannic acid in solution.

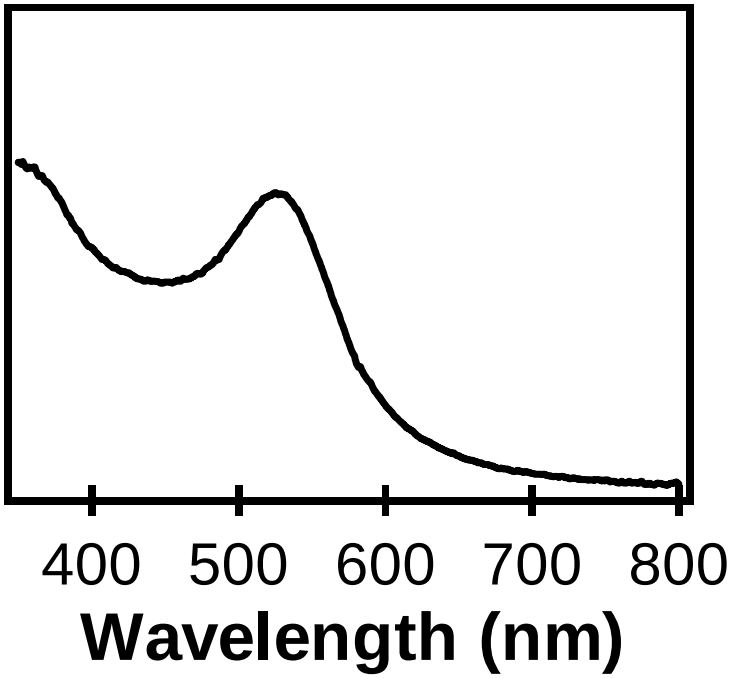

Figure 2-12. UV-vis absorbance of 3.0 nm Au-SCN showing the absence of a SPR band.

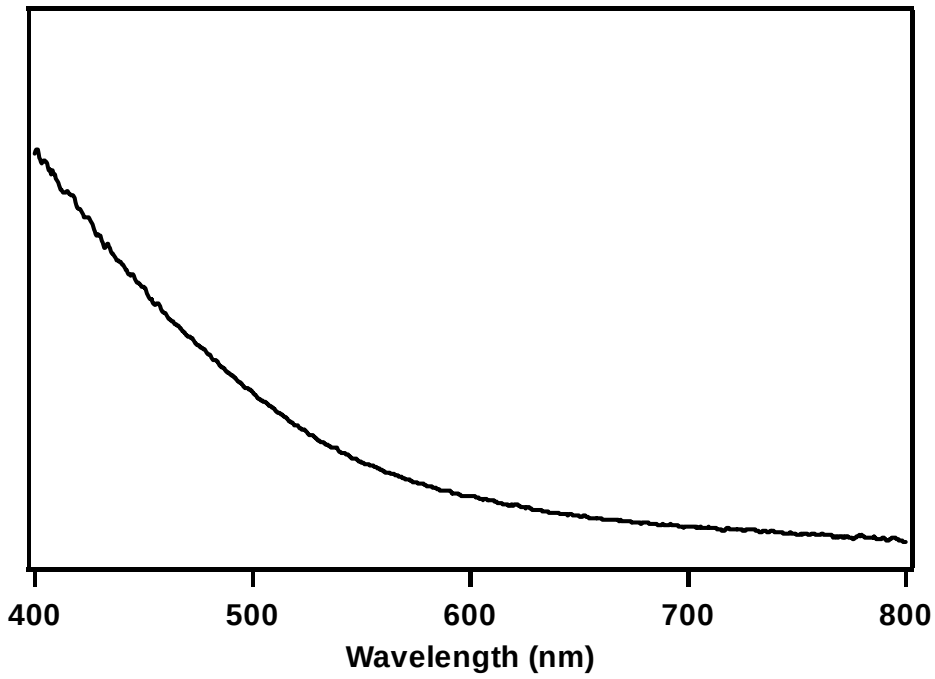

Figure 2-13. TEM image of 3.0nm Au-SCN taken at a magnification of x500K.

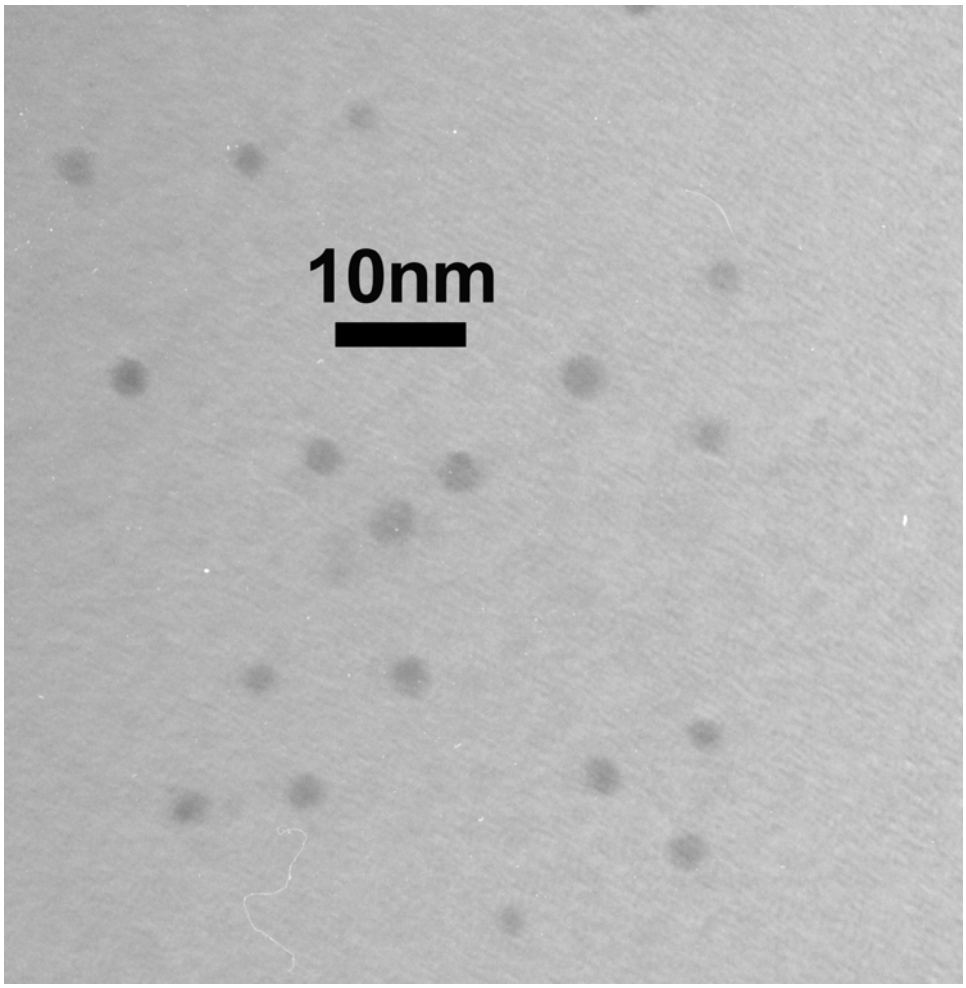

2.3 Silver.

Colloidal silver nanoparticles represent a second metal nanoparticle material that has been studied extensively for their potential use in nanoscale catalysis and optoelectronic devices.[11,22,34] Synthetic procedures follow very closely those outlined above for the synthesis of gold nanoparticles. Silver nanoparticles surface-stabilized with long-chain alkylamines or alkanethiols in the 2-10 nm size range have been synthesized following the two-phase procedure outlined by Brust for the synthesis of colloidal gold nanoparticles and used to form close packed superstructures.[11,16,25,34,35] Aqueous methods have used reductants such as sodium citrate, sodium borohydride, and N,N-dimethylformamide to reduce silver ions from $AgClO_4$ and $AgNO_3$.[19,24,36] Problems encountered in using silver nanoparticles in this research have been in obtaining monodisperse silver colloids and their instability in solution leading to large particle agglomerations. Silver nanoparticles react readily with oxygen in solution resulting in a loss of electrons leading to further complexation with surface groups and dissolution of the nanoparticle.[21] Silver nanoparticles were prepared following both the two-phase methodology in toluene using sodium borohydride as a reducer and

the aqueous methodology using sodium citrate and sodium borohydride as a combined reducer, similar to the methods stated above for gold nanoparticles.

2.3.1 Two-Phase Organic Methodology for Ag Preparation.

The silver nanoparticles surface passivated with dodecanethiol (Ag-DDT) synthesized via the two-phase methodology, shown in Figure 2-14, were prepared by vigorous mixing 50ml of a 59 mM solution of $AgNO_3$ with 100 ml of a toluene solution containing 2.41g of tetraoctylammonium bromide (TOABr). Following mixing for 1 hour, the toluene phase was separated and to it added 0.892g of dodecanethiol (DDT) with vigorous stirring. After the Ag/DDT solution was stirred for 15 minutes, 25 ml of a 0.36M solution of freshly prepared sodium borohydride was added with rapid stirring. After a few minutes the toluene layer becomes dark brown and the aqueous layer becomes clear and colorless. The organic layer was separated from the aqueous layer and washed 3 times with deionized water then dried over sodium sulfate. Size selective precipitation was accomplished by slow addition of methanol to the toluene until a cloudy solution results and the product collected by centrifuge. The product was then washed with methanol and dried under vacuum. UV-vis absorbance of the final product in toluene, shown in Figure 2-15, illustrates a strong surface plasmon resonance band for the silver nanoparticles centered at 465 nm.

Figure 2-14. TEM image of Ag-DDT. The image was taken at a magnification of x500K.

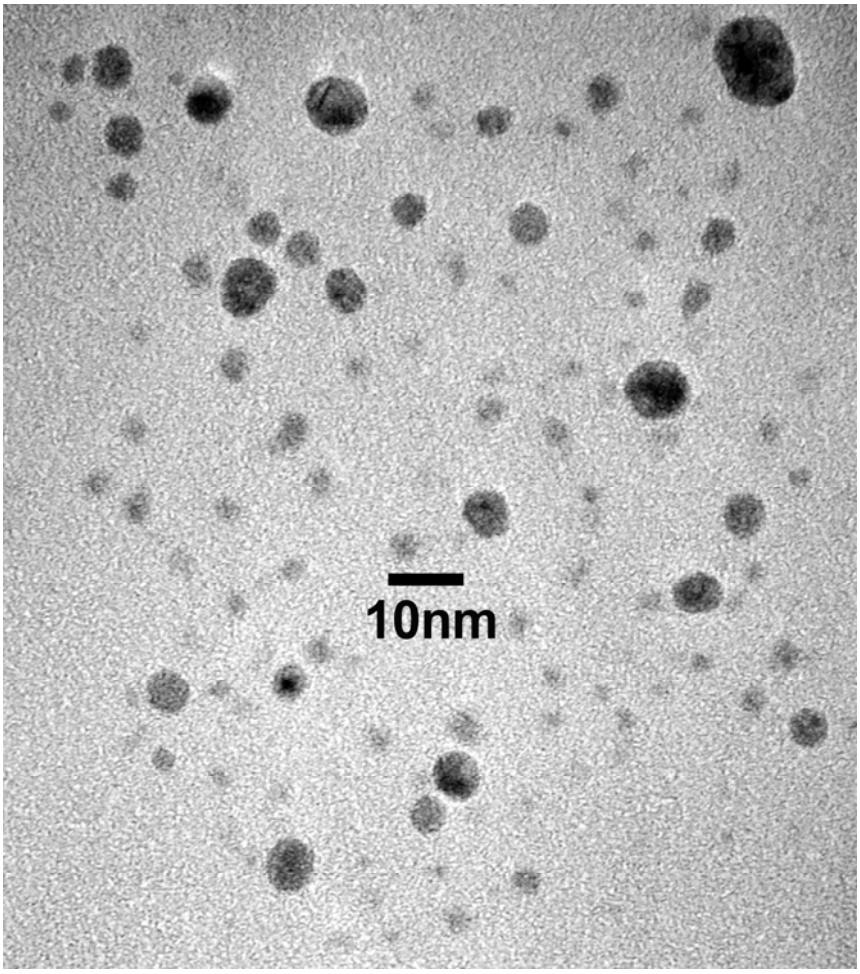

Figure 2-15. UV-vis absorption of the Ag-DDT nanoparticle product shown in Figure 2-14.

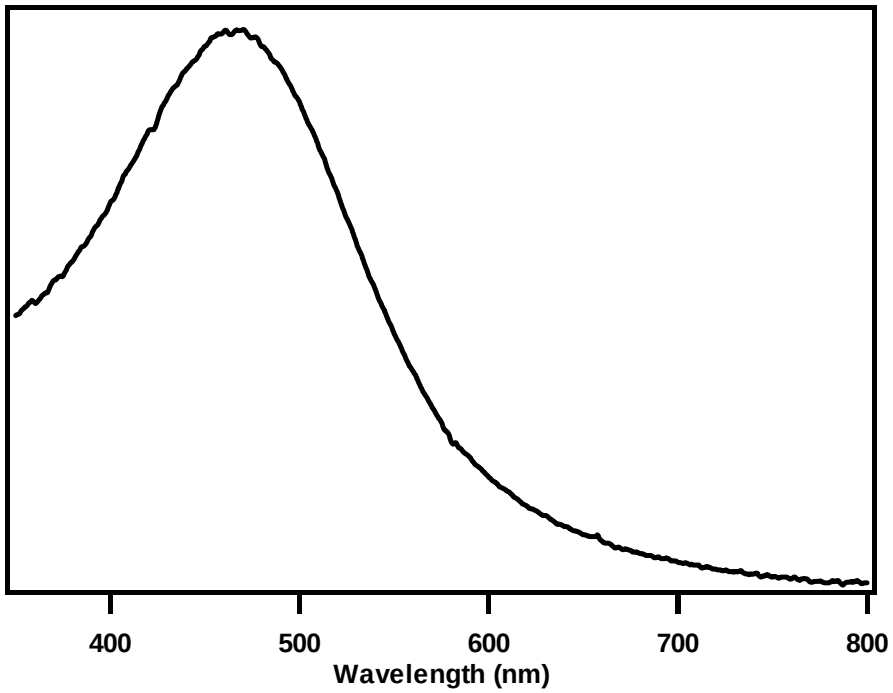

2.3.2 Aqueous Methodology for Ag Preparation

Silver nanoparticles prepared by the reduction of an aqueous solution of silver nitrate with sodium borohydride and sodium citrate produces larger citrate-stabilized water-soluble silver nanoparticles (Ag-cit), as shown in Figure 2-16. Comparison with Figure 2-14 illustrates the greater dispersity of sizes with this methodology. The sodium borohydride is the stronger of the two reducers with the citrate serving as the surface-stabilizing group. In this reaction 3.8mg of sodium borohydride and 8.8mg of sodium citrate were dissolved in 100ml of ice-cold Milli-Q water, degassed with N_2. To the rapidly stirring solution, in an ice bath, was added 1ml of a 0.01M $AgNO_3$ solution. This resulted in the formation of an aqueous solution with a rich yellow color. The UV-vis absorbance of water-soluble silver nanoparticles, shown in Figure 2-17, illustrates the SPR band of aqueous silver nanoparticles centered at 395 nm. Comparison of the SPR band of the larger water-soluble silver nanoparticles with that of the smaller organic-soluble silver nanoparticles illustrates the increase in the intensity of the SPR band as the particle size increases.

Figure 2-16. TEM image of Ag-cit. The image was taken at a magnification of x200K.

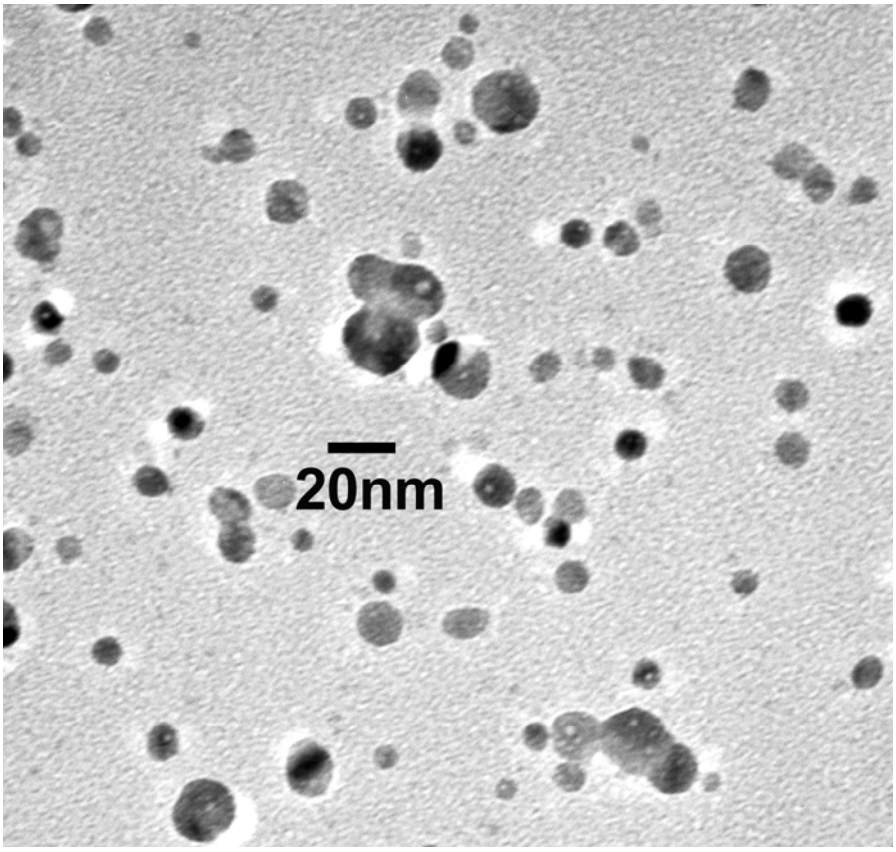

Figure 2-17. UV-vis absorption of the Ag-cit nanoparticle product shown in Figure 2-16 illustrating the SPR band of aqueous silver nanoparticles centered at 395 nm.

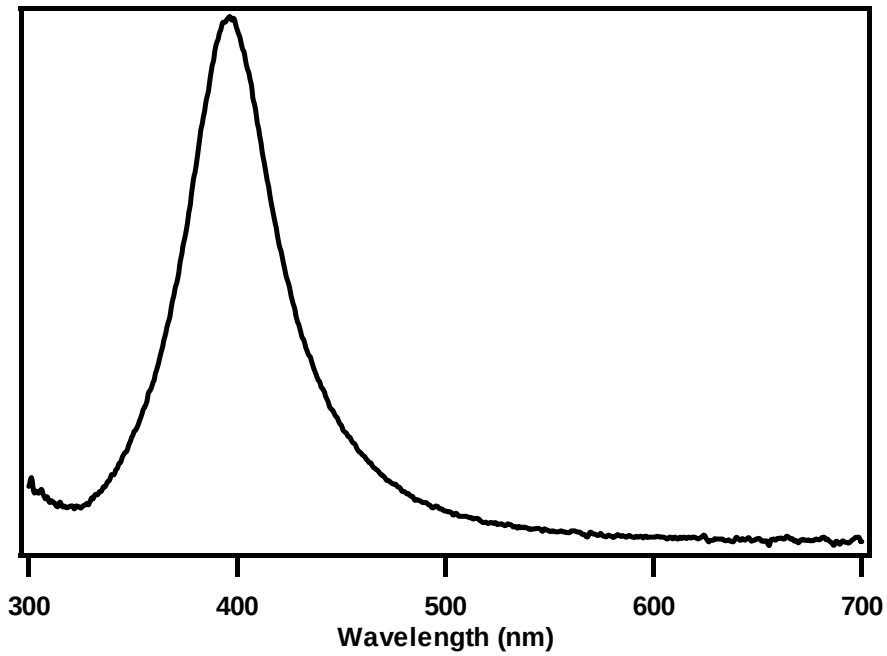

2.4 CdSe.

CdSe nanocrystals are of great interest due to their pronounced size dependent optical properties. Increasing the size of the nanocrystals from 2 to 10 nm spans the UV-vis range of 350 to 680 nm. Traditional routes for the synthesis of high quality, near monodisperse CdSe nanocrystals require lyothermal techniques involving the rapid injection of precursors into hot coordinating solvents, such as tri-n-octylphosphine oxide (TOPO), which initiates nucleation of CdSe seed crystals from which larger CdSe nanocrystals are grown.[12,37] Disadvantages with these methodologies include the use of highly air-sensitive and toxic precursors, which must be carefully handled under inert atmosphere, and difficulty in controlling the growth of the nanocrystal from the nucleating step at high temperatures.

The synthetic route to the production of high quality, monodisperse CdSe nanocrystals, surface-passivated with hexadecylamine (CdSe-HDA) used in this work involved an adaptation of the lyothermal approach. In this method, a single source precursor containing a pre-existing CdSe nucleus was heated in a coordinating solvent, which allowed for the growth of CdSe nanocrystals to any desired size. The single source precursor was the lithium salt of the $[Se_4Cd_{10}(SPh)_{16}]^{4-}$ cluster compound originally produced by Dance et al.[38]

This cluster contains a Se_4Cd_6 core in a tetrahedral adamantane-like structure with bridging and capping thiophenol ligands, which have been shown to be labile and easily displaced in solution, making it an ideal nucleus for growth of CdSe nanocrystals into larger structures. The general procedure involved the addition of 50 ml of hexadecylamine to a 3-neck round-bottom flask equipped with a Teflon stir bar. A thermometer adapter with a high-temperature thermometer (400 ^{o}C max) was connected to one side neck and the other was capped with a rubber septa through which aliquots of the reaction solution could be removed by syringe for UV-vis spectral analysis. The center neck was fixed with a condenser topped with a vacuum joint allowing for vacuum and purging of the flask with nitrogen. The hexadecylamine was heated to 120 ^{o}C under vacuum for 30 minutes then purged with nitrogen gas. Approximately 120 mg of $Li_4[Se_4Cd_{10}(SPh)_{16}]$ ($Cd_{10}Se_4$), in a nitrogen-purged addition funnel, was added to the hexadecylamine at 110-120 ^{o}C. The pale yellow compound dissolved immediately into the hexadecylamine giving a bright yellow solution. The reaction temperature was heated to 220 ^{o}C within one hour with removal of 0.25 to 0.5 ml aliquots of the reaction solution every 10 ^{o}C for UV-vis analysis. Once the temperature had reached 220 ^{o}C the rate of heating was decreased to 1 ^{o}C/min and the UV-vis absorbance was followed every 1 ^{o}C change in temperature. Once it was determined by UV-vis analysis that the

desired nanocrystal size had been achieved, the reaction flask was removed from heat and allowed to cool to 80 ^{o}C. At that point the reaction solution was poured into two 45ml centrifuge tubes containing 20ml of methanol. This resulted in the immediate flocculation of the product from solution, which was then collected by centrifuge. The supernatant was decanted and discarded.

The crude CdSe-HDA product was purified by size-selected precipitation using toluene and methanol as the solvent/non-solvent pair. To size selectively precipitate CdSe-HDA nanocrystals of different diameters, and to remove any excess HDA, the crude product was dissolved in a minimal amount of toluene necessary to afford a clear colored solution. Sonication of the mixture aided in the dispersion of the CdSe in the toluene. Anhydrous methanol was added drop wise until the solution became turbid. At this point the solution was centrifuged to isolate the aggregated nanocrystals. This was repeated 8-12 times on the supernatant liquid until a clear colorless solution was obtained. The isolated CdSe nanocrystals were washed two times with methanol then dried under vacuum to give near monodisperse CdSe-HDA nanocrystals with ~5-8% dispersity. The dried products were stored in vials under ambient conditions.

Figures 2-18 and 2-19 illustrate the growth of the CdSe nanocrystals from 2 to 10nm in the reaction solution with an increase in the rate of growth between

220 and 240 ^{o}C. At the larger sizes the first exciton peak becomes broadened considerably possibly due to greater dispersity in the sizes. Annealing the reaction at 170 ^{o}C overnight helps to narrow the absorbance peak and decrease the dispersity. Size-selected precipitation allows for the isolation of near monodisperse CdSe-HDA.

Figure 2-20 illustrates how the size-selected precipitation procedure can narrow the dispersity of the crude reaction mixture considerably. Figure 2-21 illustrates how repeating the procedure can further narrow the dispersity of one of the size-selectively precipitated products. Figure 2-22 compares the CdSe-HDA absorbance before and after size-selective precipitation illustrating a significant narrowing of the first exciton peak as well as the immergence of four separate absorbance peaks. Figure 2-23 presents a TEM image of the size-selectively precipitated 5.7 nm CdSe-HDA showing the hexagonal packing of the nanocrystals characteristic of nanoparticle samples with high monodispersity. Figure 2-24 shows a distribution curve for size-selected 5.7 nm CdSe-HDA with ~5% size dispersity.

Figure 2-18. UV-vis absorbance spectrum of the growth of the CdSe nanocrystals in solution from 2 to 10nm as a function of temperature.

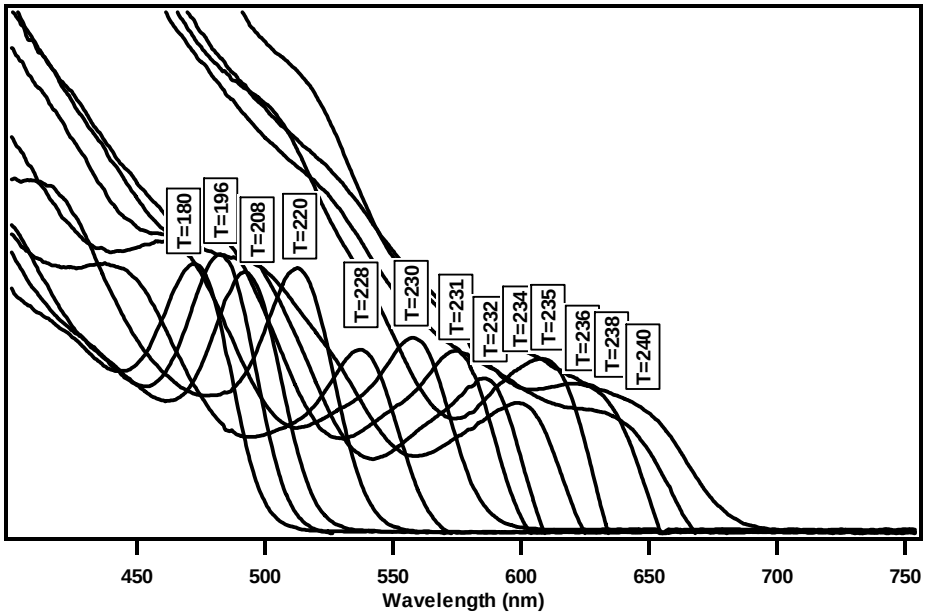

Figure 2-19. Graph of the first exciton peak location as a function of the reaction temperature indicating an increase in the growth rate between 230 and 240 ^{o}C.

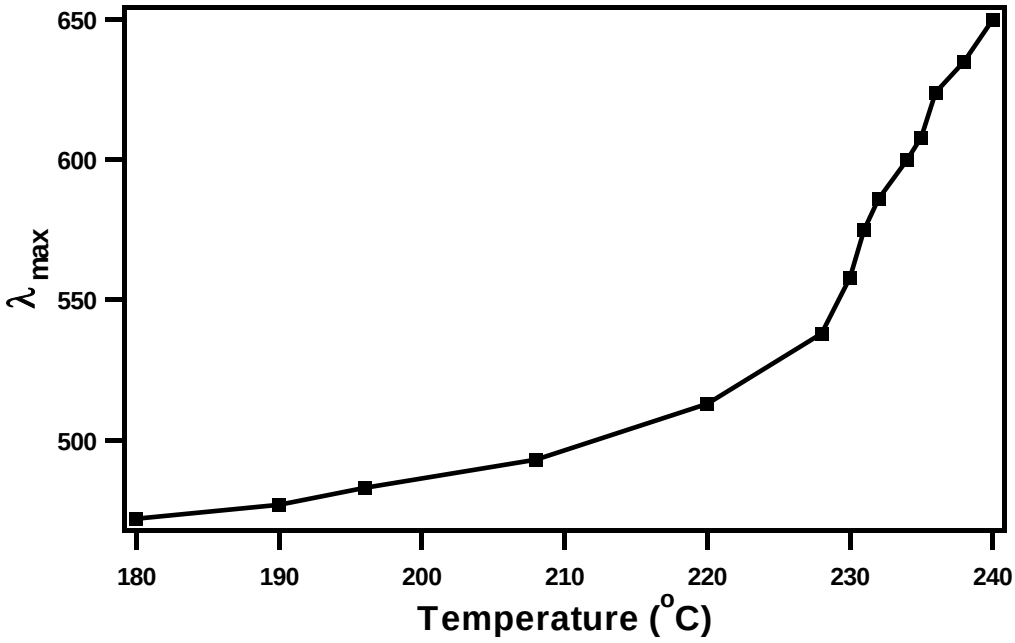

Figure 2-20. UV-vis absorption spectrum illustrating a narrowing of the first exciton peak of the CdSe-HDA with size-selective precipitation. Many of the fractions have been removed to enhance the clarity of the picture.

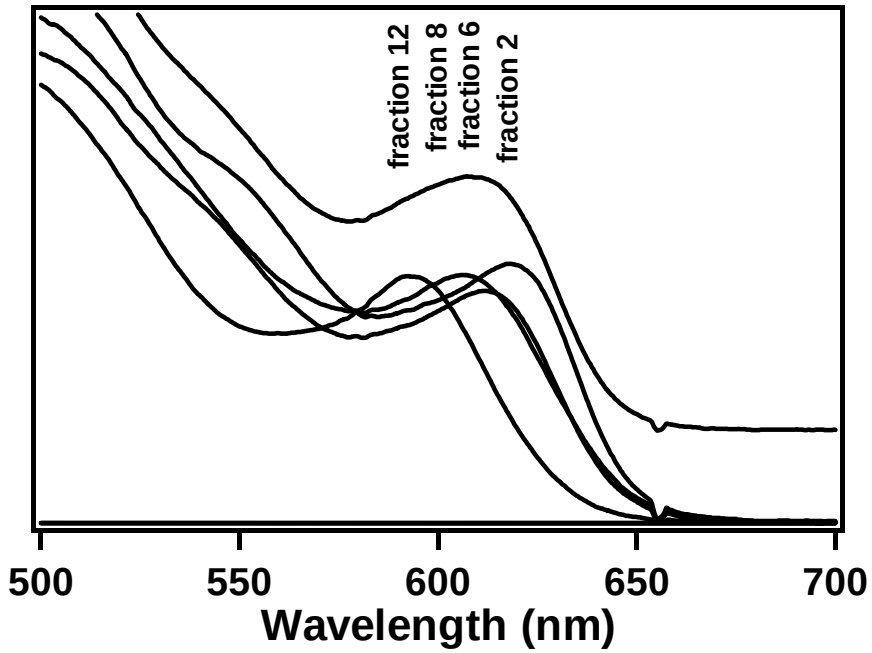

Figure 2-21. UV-vis absorption spectrum illustrating an increased narrowing of the first exciton peak of the CdSe-HDA with further size-selective precipitation of one of the fractions in Figure 2-20. Many of the fractions have been removed to enhance the clarity of the picture.

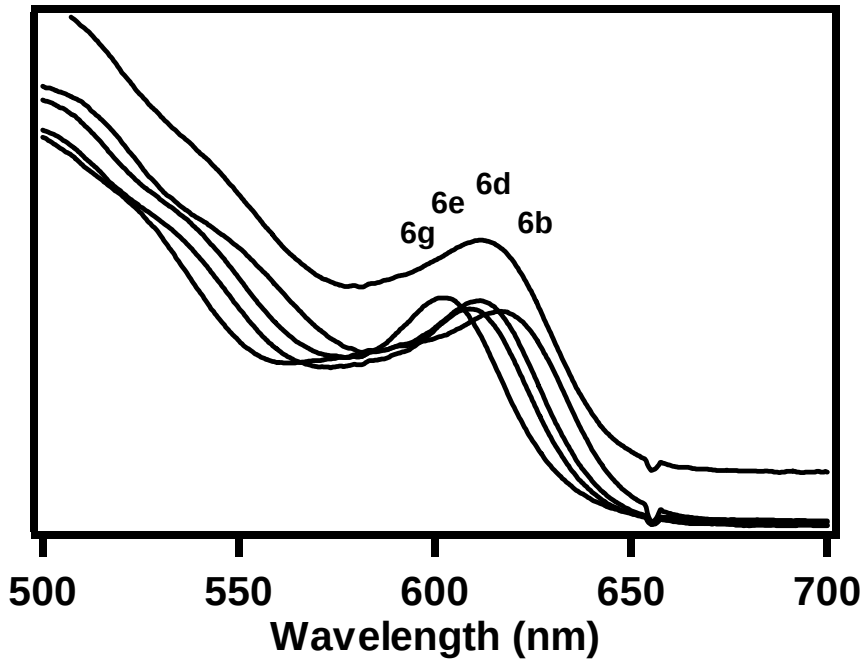

Figure 2-22. UV-vis absorbance spectrum of CdSe-HDA nanocrystals before and after size-selective precipitation.

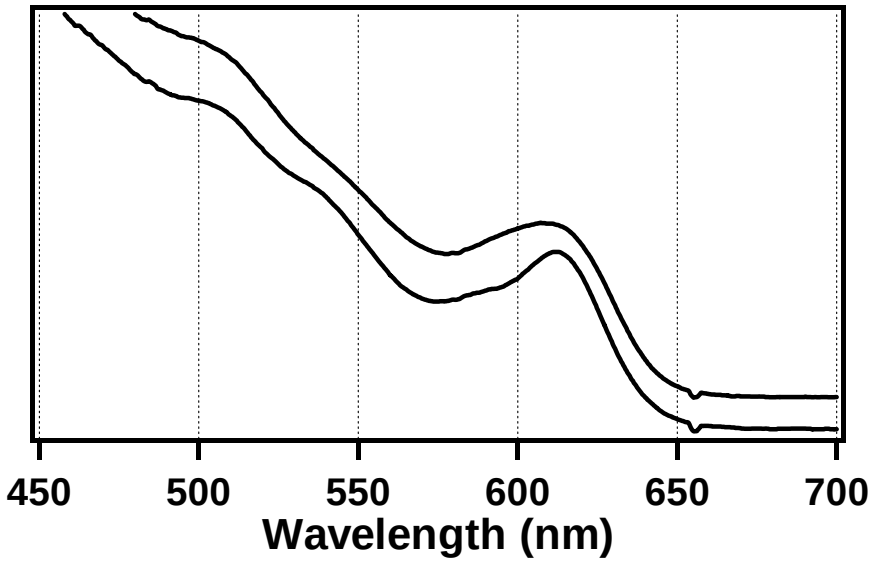

Figure 2-23. TEM image of size-selectively precipitated 5.7 nm CdSe-HDA. The image was taken at a magnification of x210K.

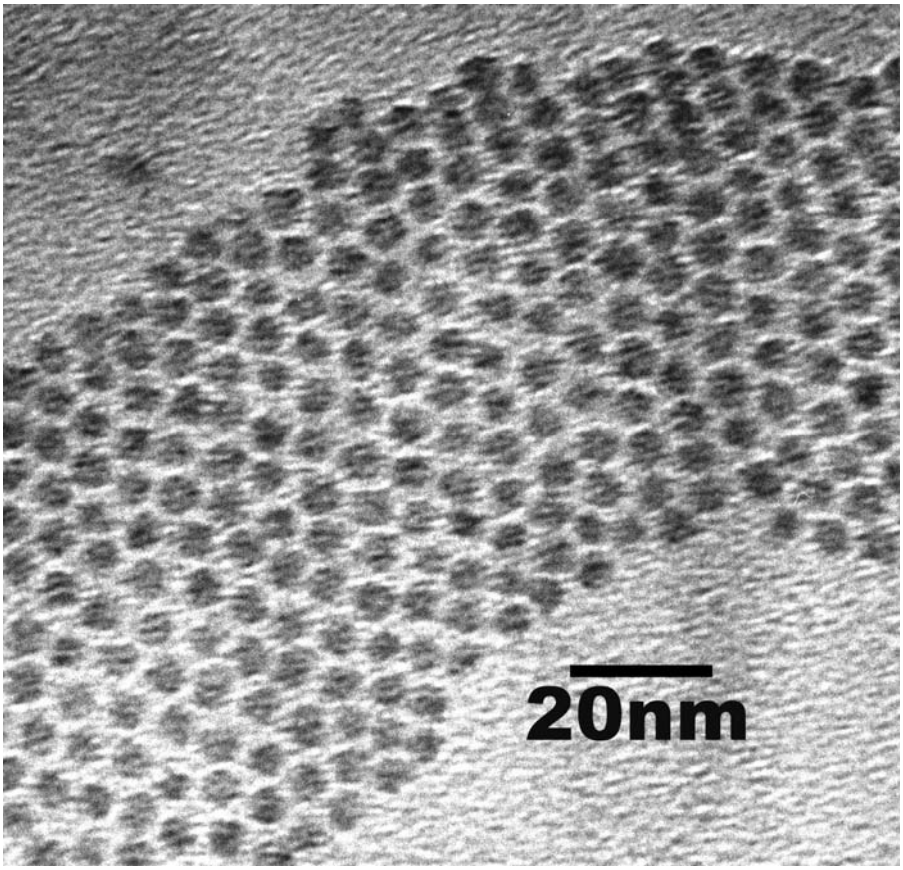

Figure 2-24. Size distribution curve for 5.7 nm CdSe-HDA with ~5% size dispersity.

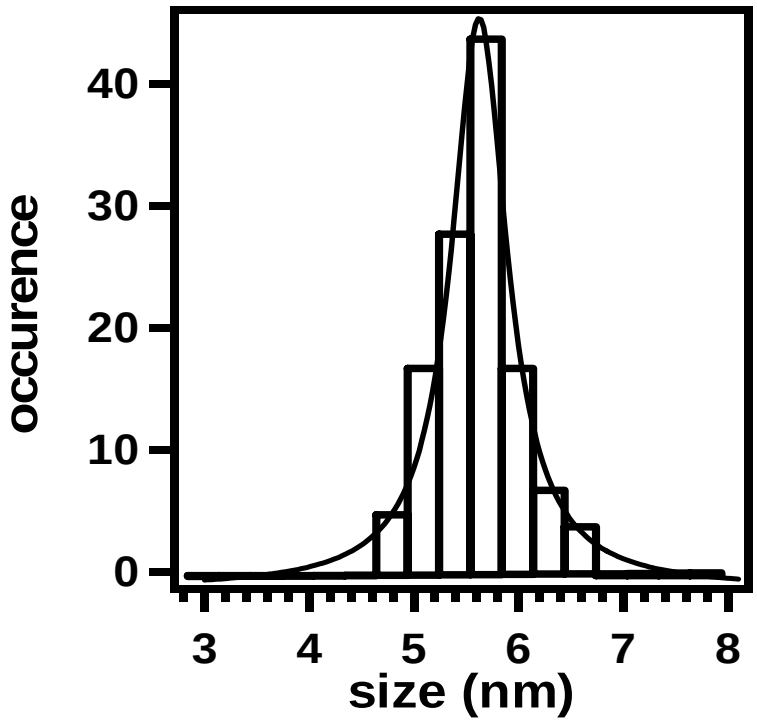

Figure 2-25 shows higher resolution image of 8.0 nm CdSe-HDA with arrows indicating the axis that is measured to determine the size of the nanocrystals for size dispersity measurements. The lines in the image reflect the characteristic fringe patterns of CdSe indicating the hexagonal lattice of the (002) wurtzite projection. Figure 2-26 shows a TEM image of 2 CdSe nanocrystals imaged parallel to (a) and perpendicular to (b) the (002) axis as evidenced by the hatched pattern in the image. An SAED pattern of the CdSe-HDA shown in Figure 2-23 is presented in Figure 2-27 with a corresponding intensity distribution curve obtained using Sigma plot shown in Figure 2-28. The greater intensity of the peak corresponding to the (110) lattice plane suggests preferential packing of the nanocrystals in the lattice. For comparison a powder x-ray diffraction pattern for CdSe-HDA is shown in Figure 2-29.

Figure 2-25. TEM image of 8.0 nm CdSe-HDA showing characteristic fringe patterns indicating the (002) wurtzite projection. Arrows in the image indicate the axis that is measured to determine the size of the nanocrystals. The image was taken at a magnification of x250K.

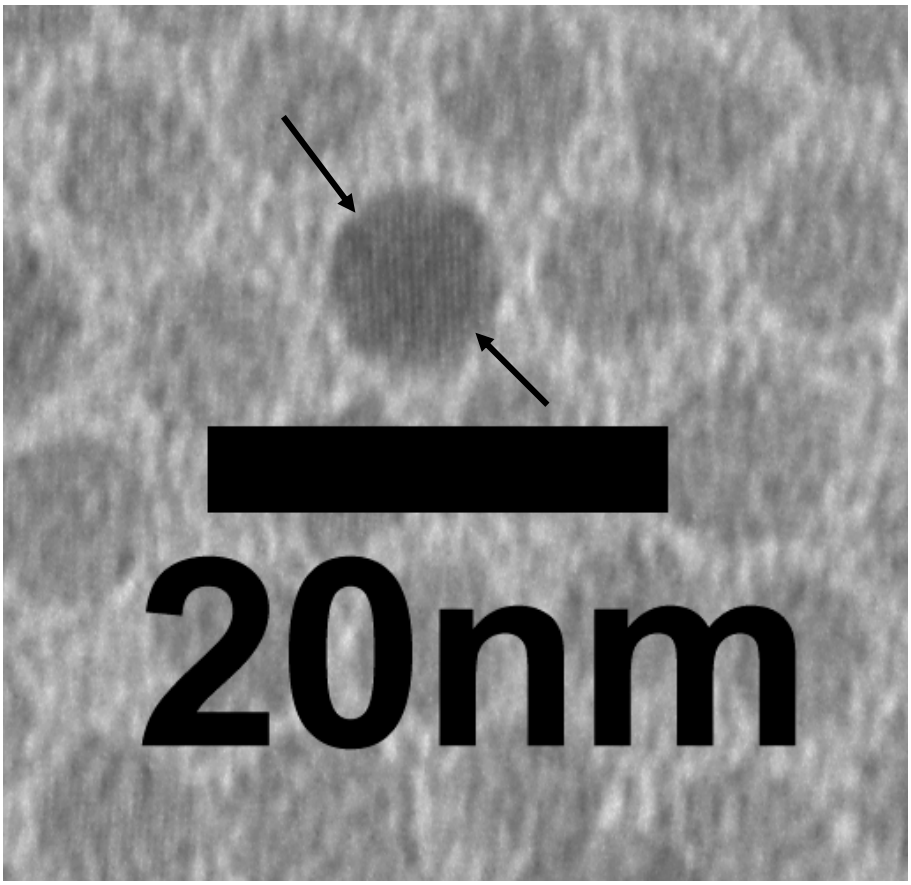

Figure 2-26. TEM image of 2 CdSe nanocrystals imaged parallel to (a) and perpendicular to (b) the (002) axis, as evidenced by the hatched pattern in the image. The image was taken at a magnification of x250K.

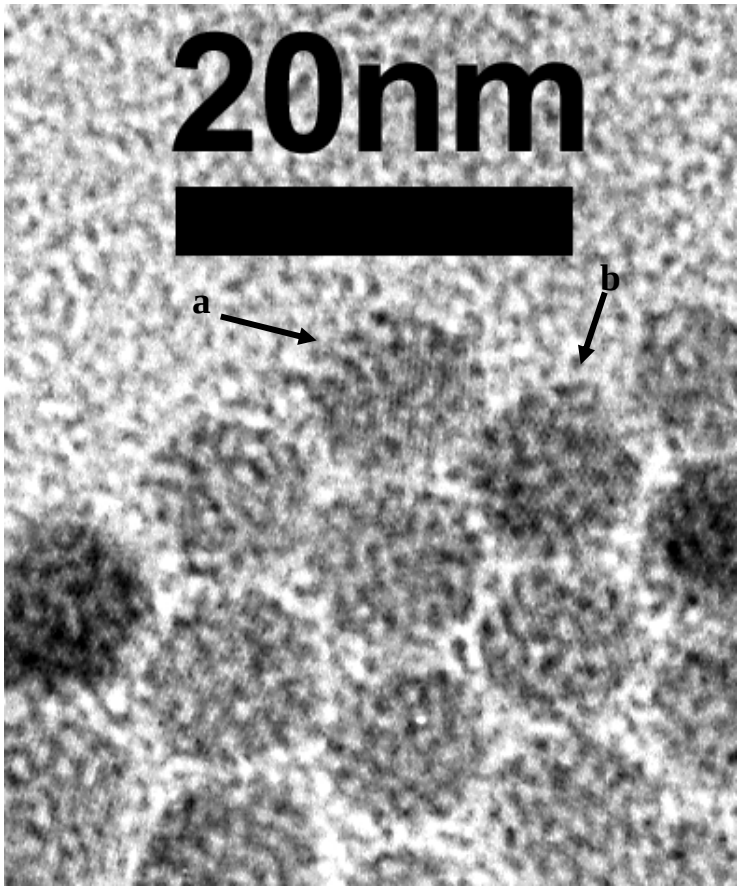

Figure 2-27. SAED pattern from CdSe-HDA shown in Figure 2-23. The pattern was taken at a camera length of 83.0 cm.

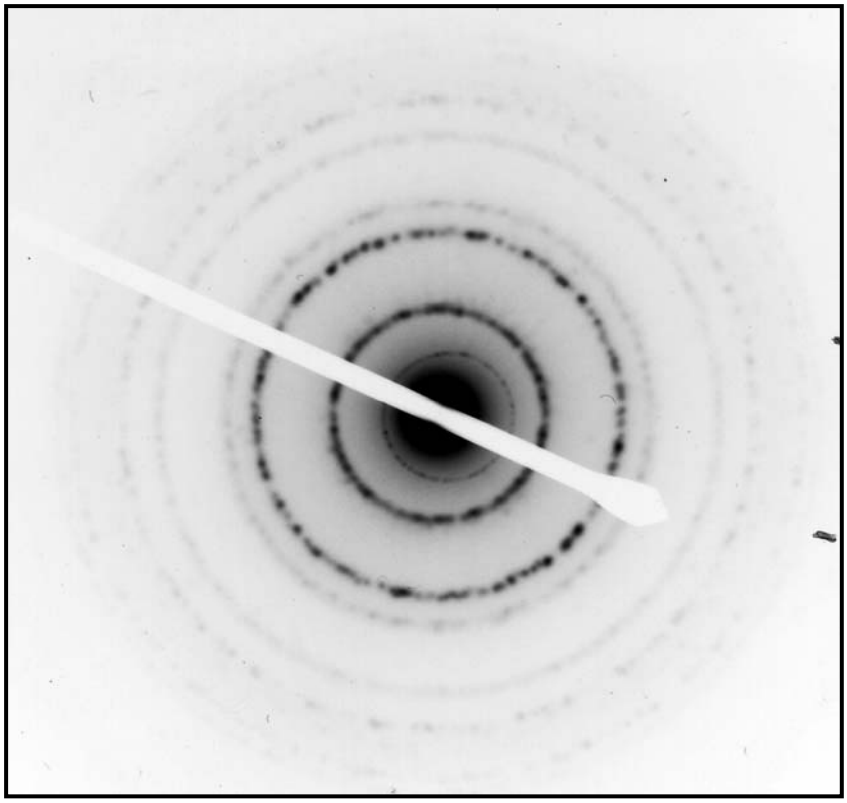

Figure 2-28. Intensity distribution curve taken from a line scan in Figure 2-27 using Sigma plot.

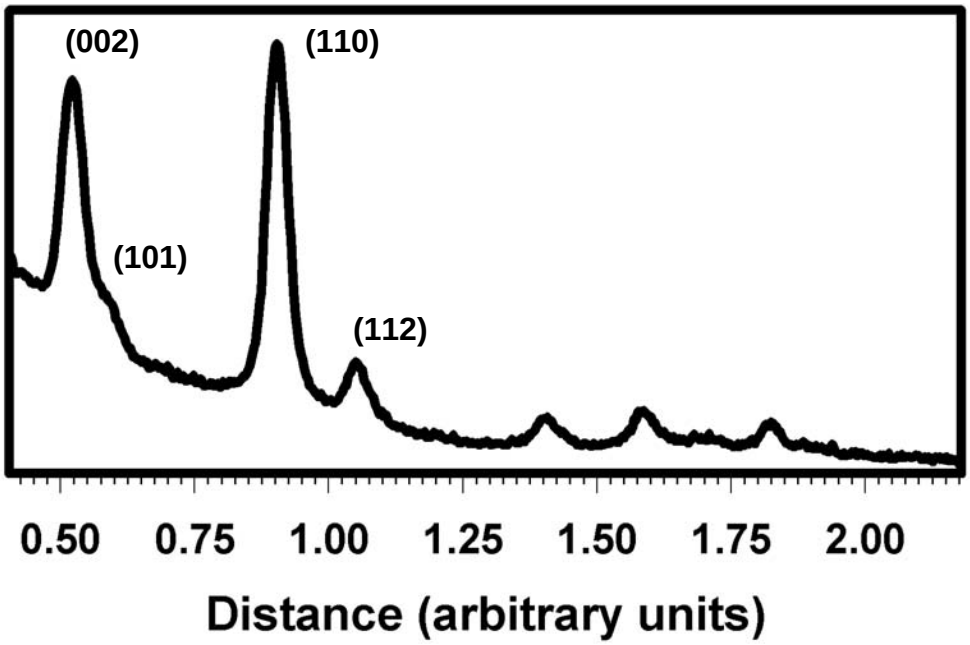

Figure 2-29. Powder x-ray diffraction analysis of CdSe-HDA showing the prominent lattice planes.

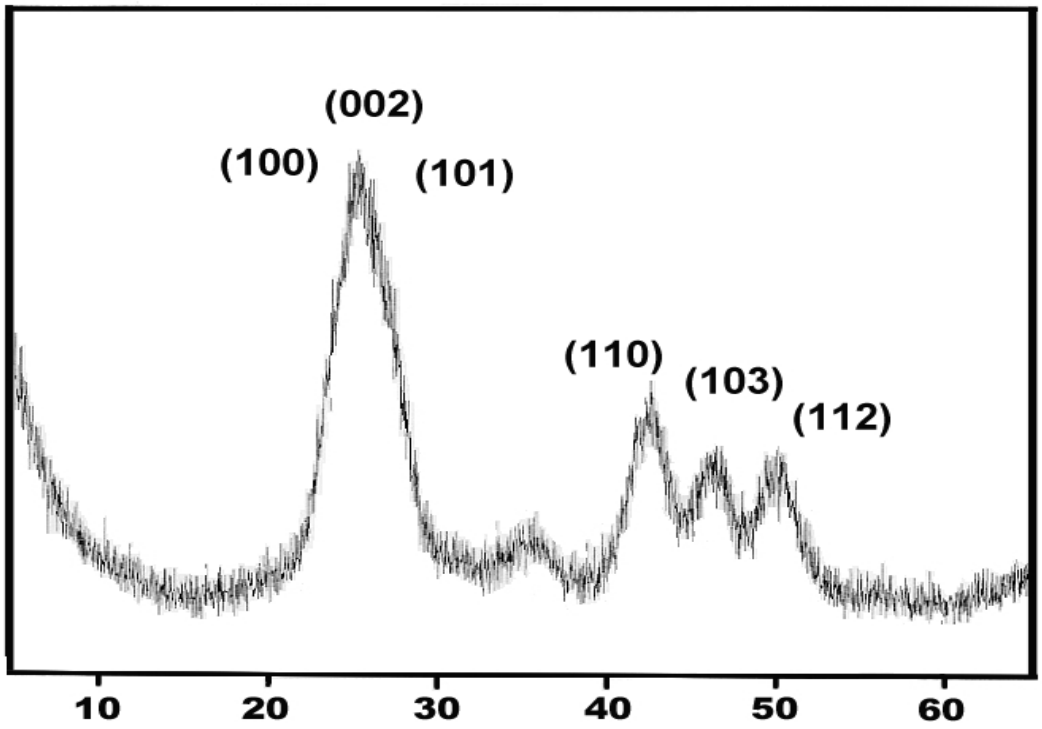

2.5 References.

1) Sun, S. H.; Murray, C. B. *Journal of Applied Physics* **1999**, *85*, 4325-4330.

2) Takagahara, T. *Surface Science* **1992**, *267*, 310-314.

3) Bigioni, T. P.; Harrell, L. E.; Cullen, W. G.; Guthrie, D. E.; Whetten, R. L.; First, P. N. *European Physical Journal D* **1999**, *6*, 355-364.

4) Harfenist, S. A.; Wang, Z. L.; Alvarez, M. M.; Vezmar, I.; Whetten, R. L. *Journal of Physical Chemistry* **1996**, *100*, 13904-13910.

5) Harfenist, S. A.; Wang, Z. L.; Whetten, R. L.; Vezmar, I.; Alvarez, M. M. *Advanced Materials* **1997**, *9*, 817.

6) Kagan, C. R.; Murray, C. B.; Nirmal, M.; Bawendi, M. G. *Physical Review Letters* **1996**, *76*, 1517-1520.

7) Mitchell, G. P.; Mirkin, C. A.; Letsinger, R. L. *Journal of the American Chemical Society* **1999**, *121*, 8122-8123.

8) Murray, C. B.; Kagan, C. R.; Bawendi, M. G. *Science* **1995**, *270*, 1335-1338.

9) Sun, S. H.; Murray, C. B.; Weller, D.; Folks, L.; Moser, A. *Science* **2000**, *287*, 1989-1992.

10) Wang, Z. L.; Harfenist, S. A.; Vezmar, I.; Whetten, R. L.; Bentley, J.; Evans, N. D.; Alexander, K. B. *Advanced Materials* **1998**, *10*, 808-812.

11) Korgel, B. A.; Fullam, S.; Connolly, S.; Fitzmaurice, D. *Journal of Physical Chemistry B* **1998**, *102*, 8379-8388.

12) Murray, C. B.; Norris, D. J.; Bawendi, M. G. *Journal of the American Chemical Society* **1993**, *115*, 8706-8715.

13) El-Sayed, M. A. *Accounts of Chemical Research* **2001**, *34*, 257-264.

14) Cumberland, S. L.; Hanif, K.; Khitrov, G. A.; Raola, O. E.; Simburger, J. T.; Yun, C. S.; Woessner, S.; Strouse, G. F. *submitted to Journal of Materials Chemistry* **2001**.

15) Brown, L. O.; Hutchison, J. E. *Journal of the American Chemical Society* **1997**, *119*, 12384-12385.

16) Brust, M.; Walker, M.; Bethell, D.; Schiffrin, D. J.; Whyman, R. *Journal of the Chemical Society-Chemical Communications* **1994**, 801-802.

17) Cliffel, D. E.; Zamborini, F. P.; Gross, S. M.; Murray, R. W. *Langmuir* **2000**, *16*, 9699-9702.

18) Green, M.; O'Brien, P. *Chemical Communications* **2000**, 183-184.

19) Henglein, A.; Giersig, M. *Journal of Physical Chemistry B* **1999**, *103*, 9533-9539.

20) Henglein, A. *Journal of Physical Chemistry B* **2000**, *104*, 2201-2203.

21) Kapoor, S. *Langmuir* **1998**, *14*, 1021-1025.

22) Leff, D. V.; Brandt, L.; Heath, J. R. *Langmuir* **1996**, *12*, 4723-4730.

23) Mühlfordt, H. *Experientia* **1982**, *38*, 1127-1128.

24) Pastoriza-Santos, I.; Liz-Marzan, L. M. *Langmuir* **1999**, *15*, 948-951.

25) Sarathy, K. V.; Kulkarni, G. U.; Rao, C. N. R. *Chemical Communications* **1997**, 537-538.

26) Schmitt, J.; Machtle, P.; Eck, D.; Mohwald, H.; Helm, C. A. *Langmuir* **1999**, *15*, 3256-3266.

27) Slot, J. W.; Geuze, H. J. *European Journal of Cell Biology* **1985**, *38*, 87-93.

28) Torigoe, K.; Esumi, K. *Journal of Physical Chemistry B* **1999**, *103*, 2862-2866.

29) Handley, D. A. *Colloidal Gold: Principles, Methods, and Applications.*; Academic Press: San Diego, 1989; Vol. 1.

30) Alvarez, M. M.; Khoury, J. T.; Schaaff, T. G.; Shafigullin, M. N.; Vezmar, I.; Whetten, R. L. *Journal of Physical Chemistry B* **1997**, *101*, 3706-3712.

31) Underwood, S.; Mulvaney, P. *Langmuir* **1994**, *10*, 3427-3430.

32) Turkevich, J.; Stevenson, P. S.; Hillier, J. *Journal of Physical Chemistry* **1951**, 58.

33) Baschong, W.; Lucocq, J. M.; Roth, J. *Journal of Histochemistry* **1985**, *83*, 409.

34) Kim, S. H.; Medeiros-Ribeiro, G.; Ohlberg, D. A. A.; Williams, R. S.; Heath, J. R. *Journal of Physical Chemistry B* **1999**, *103*, 10341-10347.

35) Heath, J. R.; Knobler, C. M.; Leff, D. V. *Journal of Physical Chemistry B* **1997**, *101*, 189-197.

36) Shirtcliffe, N.; Nickel, U.; Schneider, S. *Journal of Colloid and Interface Science* **1999**, *211*, 122-129.

37) Malik, M. A.; Revaprasadu, N.; O'Brien, P. *Chemistry of Materials* **2001**, *13*, 913-920.

38) Dance, I. G.; Choy, A.; Scudder, M. L. *Journal of the American Chemical Society* **1984**, *106*, 6285-6295.

Chapter 3

Oxyanion Adsorption on Gold Nanomaterial Surfaces

3.1 Introduction

Materials at the nanoscale have recently attracted much attention due to their size-dependent optical, non-linear optical, electronic, and chemical properties, as well as their potential for incorporation into electronic circuits at the nanoscale.[1-19] In particular, metal nanoparticles have been widely applied due to their ease of synthesis, stability, and potential for applications ranging form magnetic memory to electronics to catalysis.[1,7,8,13,20-32] Colloidal gold nanoparticles can be isolated with a variety of surface-stabilizing ligands that allow them to be tailored for specific reactions in both organic and aqueous media with relatively good monodispersity and stability. The unique optical properties of gold nanoparticles, arising from a strong surface plasmon resonance band (SPR), make them ideal for use as non-cytotoxic biolabeles, and in optical biosensors.[30,33-45] Water-soluble gold has recently been demonstrated to allow biolabeling via electrostatic interactions in DNA

assemblies.[17,24,30,40,43,45-50] In biolabeling applications, isolation of the water-soluble gold from buffers is essential for biocompatibility and is typically accomplished by dialysis, which often results in irreversible agglomeration of Au nanoparticles.[7] Water-soluble Au nanoparticles can be isolated from citrate buffers present from the reaction mixture by the addition of excess salt to the buffer producing re-dispersible Au nanomaterials.[51] The process of isolation of Au nanomaterials by electrolyte-induced precipitation has been referred to as a "salting-out" process. Precipitation of Au nanomaterials from solution proceeds by a competition between electrolyte induced coagulation and ligand exchange of the citrate passivating groups. Displacement of the citrate passivating ligand by a better Lewis base may allow isolation of the nanomaterials from the buffer and provide a convenient water-soluble species that can be readily recapped for bio-labeling experiments. The stability of Au nanomaterials, as well as the frequency and bandwidth of SPR band, is modulated by the magnitude of the Lewis basicity, the bonding symmetry, and the nature of the bonding to the metal particle surface.[36] As the electrolyte becomes more coordinating through stronger back bonding with the metal, the thermodynamic stability of the water-soluble Au nanomaterials should increase, improving the processability of the Au for biolabeling.

Oxyanions can be a convenient electrolyte for salting out Au nanomaterials.[51] In earlier studies, the addition of perchlorate leads to isolation of Au colloids that can be readily re-dispersed in water. Oxyanions have been shown to coordinate metal surfaces through both electrostatic interactions of the anion and coordination of the oxygen donor atoms. The nature of the bonding in oxyanions on metal surfaces depends on the symmetry of the anion, and the propensity for metal to oxygen back bonding from the metal. For a series of oxyanions, such as sulfate, phosphate, and carbonate, infrared analysis of the anion allows direct assignment of the nature of bonding due to changes in the molecular symmetry of the anion bound to the metal surface, which induces a change in the allowed vibrational modes, and can be observed by infrared spectroscopy.[36,52-68] The nature of the bonding has been shown to further depend on the crystallographic face of the metal, due to differences in the electronic interactions and atom packing. Since the location of the SPR is dependent on the electron density surrounding the gold nanoparticle, it is expected that the nature of the adsorbates on the gold surface would affect the SPR due to the greater or lesser electron withdrawing nature of the adsorbate.

By judicious choice of the surface passivating layer, Au colloids can be isolated from the reaction solution and re-dispersed in water for applications in bio-labeling. Presented here is an analysis of the nature of the binding for a

series of oxyanionic ligands on the surface of Au nanomaterials. The binding geometry of oxygen donor ligands on the surface of water-soluble colloidal gold nanoparticles are studied by means of UV-vis and FTIR spectroscopy as a function of the surface stabilizing groups on the gold surface. The ability to isolate Au from aqueous solution without buffer contamination, allows accurate determination of the extinction coefficient of these materials.

3.2 Experimental

3.2.1 Chemicals.

$HAuCl_4 \bullet H_2O$ (99.9+%), tannic acid, and sodium citrate were purchased form Aldrich. Sodium phosphate (monobasic), sodium carbonate, and sodium chloride were purchased from Fisher Scientific. Sodium sulfate was purchased from EM Science. Nitrogen-purged deionized water was used for the production of gold sols.

3.2.2 Optical Measurements.

FT-IR analysis was conducted using pressed KBr pellets on a Perkin-Elmer Spectrum GX FT-IR between 370 – 7000 cm^{-1} with a resolution of 4 cm^{-1}. UV/Vis spectra were recorded using an Ocean Optics S2000 CCD spectrometer (resolution 0.1 nm).

3.2.3 Electron Microscopy.

TEM analysis was performed on 400 mesh Cu grids coated with a ~5 nm layer of holey carbon (SPI). Images were obtained on a JEOL 2000 (Au-TA and

Au-Cl) or JEOL 2010 (Au-CO_3, Au-SO_4, and Au-PO_4) microscope operated at 200 kV in bright field mode.

3.2.4 Synthesis and Isolation of Colloidal Gold.

Colloidal gold was prepared by a method developed by Mühlfordt using sodium citrate and tannic acid as reducing agents of hydrogen tetrachloroauric acid.[31] Briefly, 100ml of a 0.001% (w/v) solution of freshly prepared tetrachloroauric acid was heated to reflux. A solution containing 2ml of a 1% (w/v) solution of sodium citrate and 0.45ml of a 1% (w/v) tannic acid solution was added to the rapidly stirred gold solution. The solution was stirred at reflux for an additional 5 minutes followed by cooling. This produces a colloidal gold solution with a pH of 4.5 that is stable for an indefinite period of time at room temperature on the bench top. The gold nanoparticles exhibit a mean diameter of 6.0 nm with a size distribution of ~15%, as determined by transmission electron microscopy (TEM).

3.2.5 Surface Passivation.

The gold nanoparticles were isolated from the excess citrate and tannic acid buffer solution by the addition of sodium chloride (NaCl) (Au-Cl), sodium carbonate (Na_2CO_3) (Au- CO_3), sodium sulfate (Na_2SO_4) (Au-SO_4), or sodium phosphate (NaH_2PO_4) (Au-PO_4) until the colloidal gold solution became opalescent to the eye. The solutions were centrifuged and the supernatant

liquid discarded. The collected gold nanoparticles were washed with a minimal amount of water to remove the excess salt, centrifuged and redissolved in deionized water for optical characterization or dried under vacuum for analysis by FTIR analysis.

3.2.6 Extinction Coefficient Calculations.

Extinction coefficients for the colloidal gold were calculated from the dried gold-salts dissolved in deionized water using the Beer Lambert law. The molecular weight of the gold nanoparticles was calculated based on the number of gold atoms in a 6.0 nm gold particle using equation 1, where N_A is

$$n = \frac{0.5\pi N_A d_m^3}{3V_m} \qquad (1)$$

Avogadros' number, d_m is the diameter of the nanoparticle measured by TEM analysis, and V_m is the molar volume of bulk gold (10.215 cm^3).[21] In these calculations it is assumed the mass of the surface-stabilizing salts is negligible compared to the mass of the gold. Using this equation, the molecular weight of 6.0 nm Au nanoparticles was calculated to be 1.313×10^{-10} grams per mole of nanoparticles.

3.3 Results

3.3.1 Reaction and Isolation of Colloidal Gold.

Upon addition of a sodium citrate and tannic acid solution to a rapidly stirred auric acid solution at reflux, an optically transparent wine-red solution is produced. In the citrate buffer solution, the Au nanomaterials are stable for an

extended period of time. Upon addition of sodium chloride, sodium sulfate, sodium carbonate, or monobasic sodium phosphate, electrolyte induced precipitation of the gold nanoparticles is observed, allowing the gold nanoparticles to be isolated from excess citrate buffer. The gold can then be redissolved in water to give a non-aggregated colloidal gold nanoparticle solution free from excess citrate and tannic acid. When the gold colloids were isolated by the addition of sodium chloride then dried under vacuum, the product was a black powder. In the cases where sodium carbonate, sodium sulfate, or sodium phosphate was used, the product obtains the appearance of gold metal upon complete drying.

3.3.2 UV-vis Absorption.

Figure 3-1 shows a comparison of the absorption properties of a 6.0 nm colloidal gold solution prepared from the reduction of auric acid with sodium citrate and tannic acid (3-1e) and the same gold colloid isolated from solution by the addition of sodium phosphate (3-1a), sodium carbonate (3-1b), sodium sulfate (3-1c), and sodium chloride (3-1d). The initial colloidal gold solution exhibits a SPR around 525 nm and a second band around 360 nm, which is attributable to the absorbance of tannic acid. Upon treatment with NaCl, the SPR band remains at 525 nm, while the tannic acid absorption band at 360 nm is observed to decrease in intensity. Upon treatment of the oxyanions, complete loss of the tannic acid band at 360 nm and shifts in the frequency of

the SPR Au band is observed in the UV-Vis spectra. For the Au-PO_4 the SPR is centered at 544 nm, the Au-CO_3 SPR is centered at 536 nm, the Au-SO_4 SPR is centered at 534 nm. Figure 3-2 shows a comparison of the absorption properties of 6.0 nm Au-TA and agglomerated citrate-stabilized gold colloids exhibiting an absorption band around 620 nm. Absence of this band in Figures 3-1a-d illustrate that the gold colloids are not agglomerated.

Assuming minimal mass contribution from the passivating layer on the Au surface, the extinction coefficients for 6.0 nm colloidal gold can be calculated from eqn 1. The calculated extinction coefficients are $4.05 \pm 0.81 \times 10^6$ $mol^{-1}cm^{-1}$ for Au-PO_4, $5.32 \pm 0.36 \times 10^6$ $mol^{-1}cm^{-1}$ for Au-SO_4, $6.54 \pm 0.96 \times 10^6$ $mol^{-1}cm^{-1}$ for Au-CO_3, and $9.93 \pm 0.48 \times 10^6$ $mol^{-1}cm^{-1}$ for Au-Cl. Table 3-1 illustrates the comparison of the surface plasmon absorption maximum and the extinction coefficients of the Au-salts.

Figure 3-1. Absorption spectra of 6.0nm colloidal gold surface-stabilized by (a) sodium phosphate, (b) sodium carbonate, (c) sodium sulfate, (d) and sodium chloride, and (e) citrate and tannic acid.

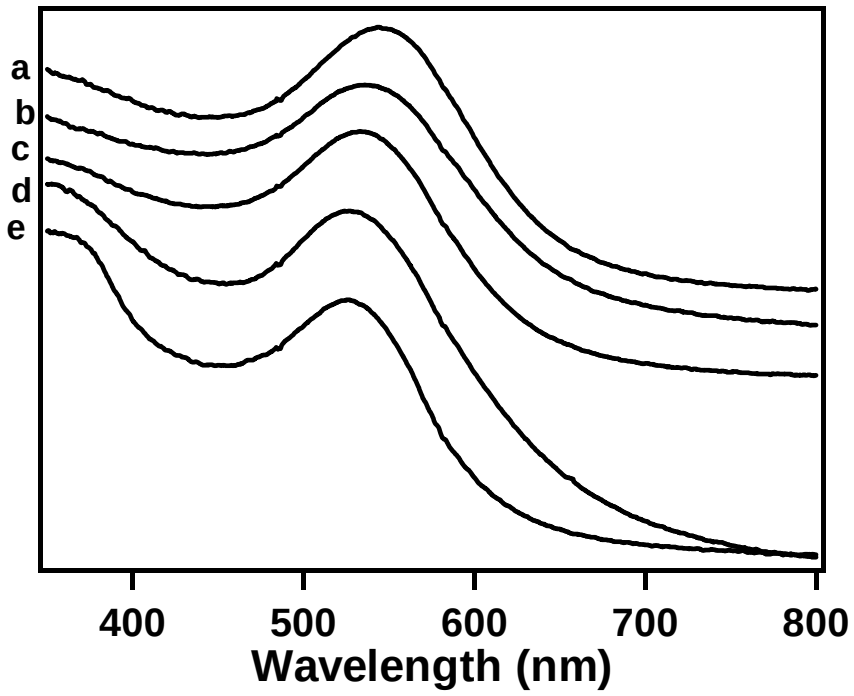

Table 3-1. Surface plasmon absorption maximum and extinction coefficients for the Au salts.

Au-salt	**λ_{max} (nm)**	**$\in$ ($x10^6$ $mol^{-1}cm^{-1}$)**
Au-PO_4	544	4.05 ± 0.81
Au-CO_3	536	6.54 ± 0.96
Au-SO_4	534	5.32 ± 0.36
Au-Cl	525	9.93 ± 0.48

Au-TA	525	

Figure 3-2. Absorption spectrum of 6.0 nm Au-TA in solution (a) and as dried agglomerates (b).

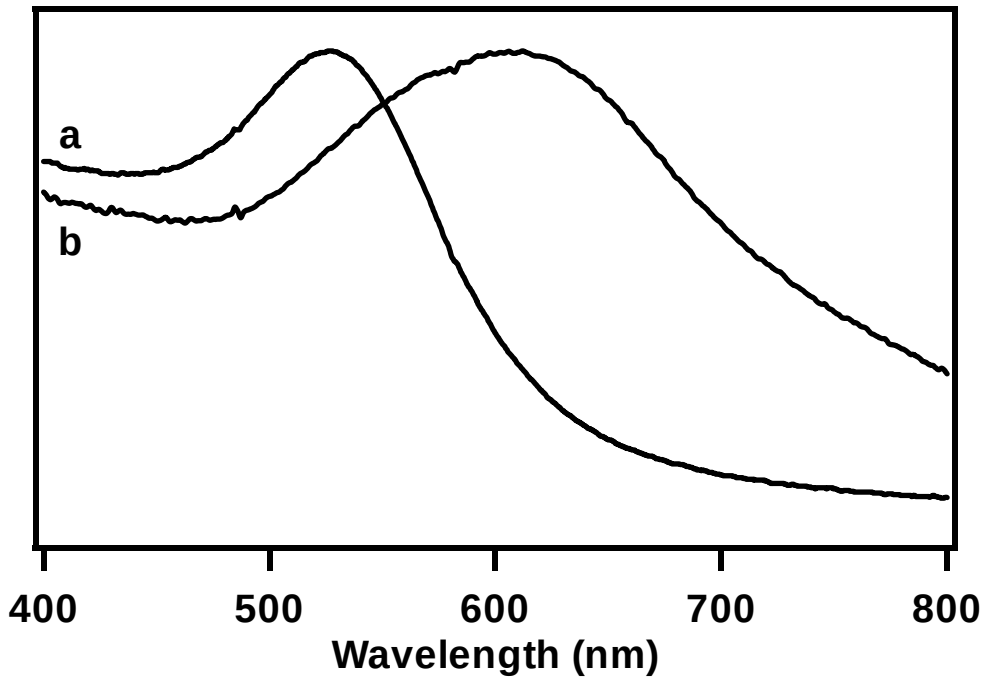

3.3.3 Infrared Spectroscopy.

Solid-state infrared spectra of the isolated Au nanomaterials are shown in Figures 3-3, 3-4, 3-5, and 3-6. Figure 3-3 compares the FTIR spectra of sodium citrate, tannic acid, and Au-Cl with the assignments given in Table 3-2. Figure 3-4 shows the FTIR spectra of sodium carbonate (4a) and Au-CO_3 (4b) with the assignments given in Table 3-3. Figure 3-5 shows the FTIR spectra of monobasic sodium phosphate (NaH_2PO_4) (5a) and Au-PO_4 (5b) with the assignments given in Table 3-4. Figure 3-6 shows the FTIR spectra of sodium sulfate (6a) and Au-SO_4 (6b) with the assignments given in Table 3-5. In Figure 3-4, the observation of a combination of peaks associated with carboxylate and carbonyl vibrations of sodium citrate and tannic acid in the Au-Cl spectrum is consistent with the presence of tannic acid/citrate at the nanomaterial surface. The absence of modes for citrate or tannic acid in Figures 3-4, 3-5, and 3-6 corroborates the isolation of gold from the citrate and tannic acid buffer for the oxyanion isolated Au nanomaterials.

Figure 3-3. FTIR spectra of (a) sodium citrate, (b) Au-Cl, and (c) and tannic acid.

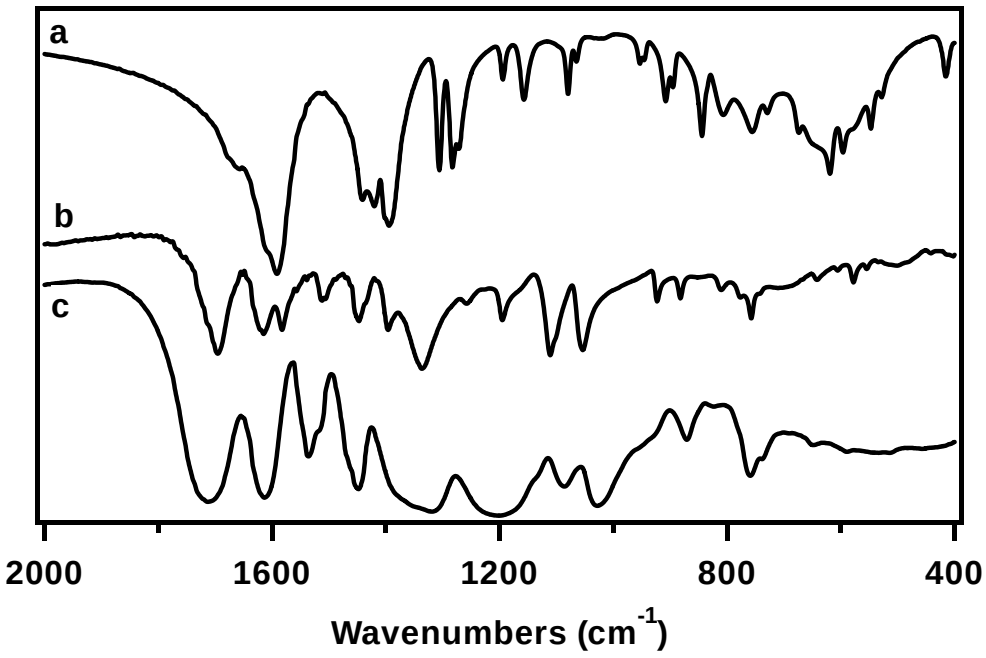

Table 3-2. Assignment of FTIR carboxylate and carbonyl modes for sodium citrate, tannic acid, and Au-Cl.

Assignment	sodium citrate	tannic acid	Au-Cl
$\nu_s(C(\underline{---}O)_2^-)$	1395 cm^{-1}		1396 cm^{-1}
$\nu_{as}(C(\underline{---}O)_2^-)$	1594 cm^{-1}		1583 cm^{-1}
ν(C-O)		1318 cm^{-1}	1335 cm^{-1}
ν(C=O)		1713 cm^{-1}	1697 cm^{-1}
$\delta(C\text{-}O\text{-}H)_{op}$		872 cm^{-1}	882 cm^{-1}

$\delta(C\text{-}O\text{-}H)_{ip}$		1447 cm^{-1}	1445 cm^{-1}

op = out of plane bend, in = in plane bend

Figure 3-4. FTIR spectra of (a) sodium carbonate and (b) and Au-CO_3.

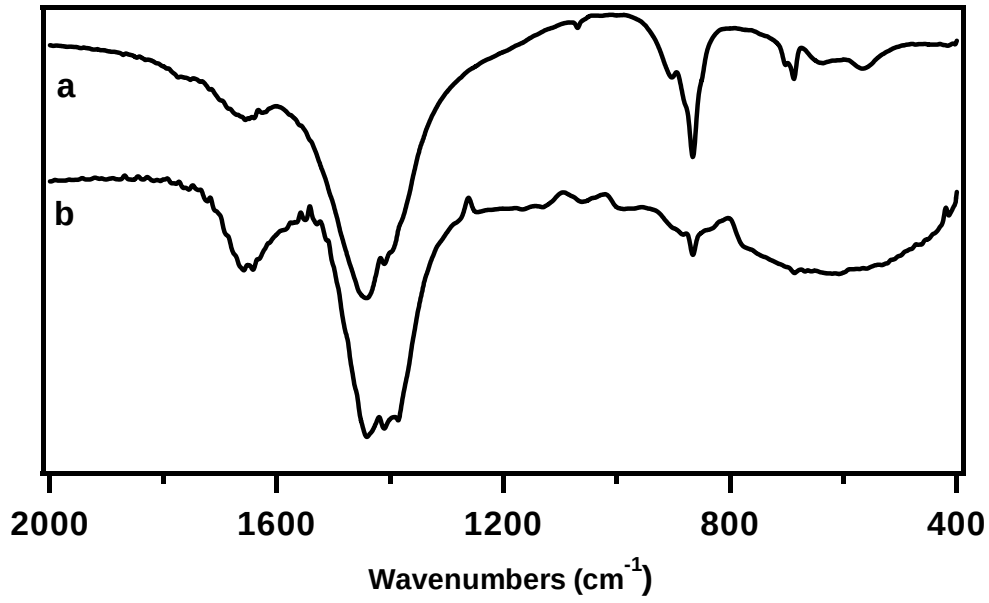

Table 3-3. FTIR assignments for $NaCO_3$ and Au-CO_3.

mode	**$NaCO_3$**	**Au-CO_3**
v_3	1386 cm^{-1}	1385 cm^{-1}
v_2	880 cm^{-1}	880 cm^{-1}
v_4	687 cm^{-1}	687 cm^{-1}

Figure 3-5. FTIR spectra of (a) NaH_2PO_4 and (b) Au-PO_4.

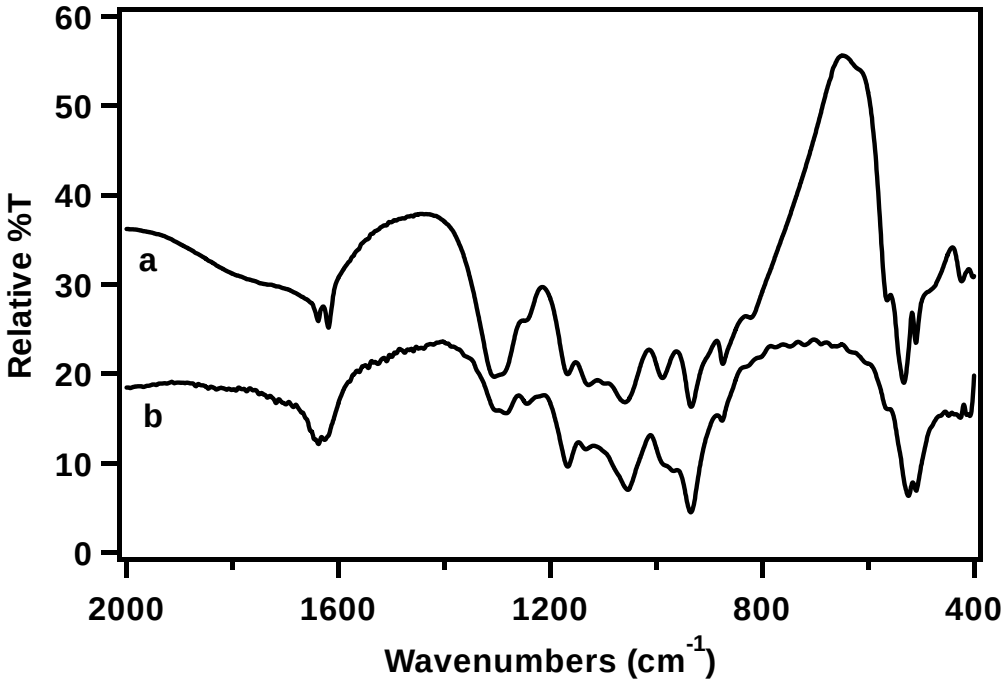

Table 3-4. FTIR assignment for NaH_2PO_4 and Au-PO_4.

mode	**NaH_2PO_4**	**Au-PO_4**
ν_s(P-OH) (A_1)	874 cm^{-1}	876 cm^{-1}
ν_{as}(P-OH) (B_2)	934 cm^{-1}	935 cm^{-1}
ν_s(P(---O)$_2^-$) (B_1)	1061 cm^{-1}	1055 cm^{-1}
ν_{as}(P(---O)$_2^-$) (A_1)	1169 cm^{-1}	1168 cm^{-1}

δ(P-O-H)	1245 cm^{-1}	1243 cm^{-1}

Figure 3-6. FTIR spectra of (a) sodium sulfate and (b) Au-SO_4.

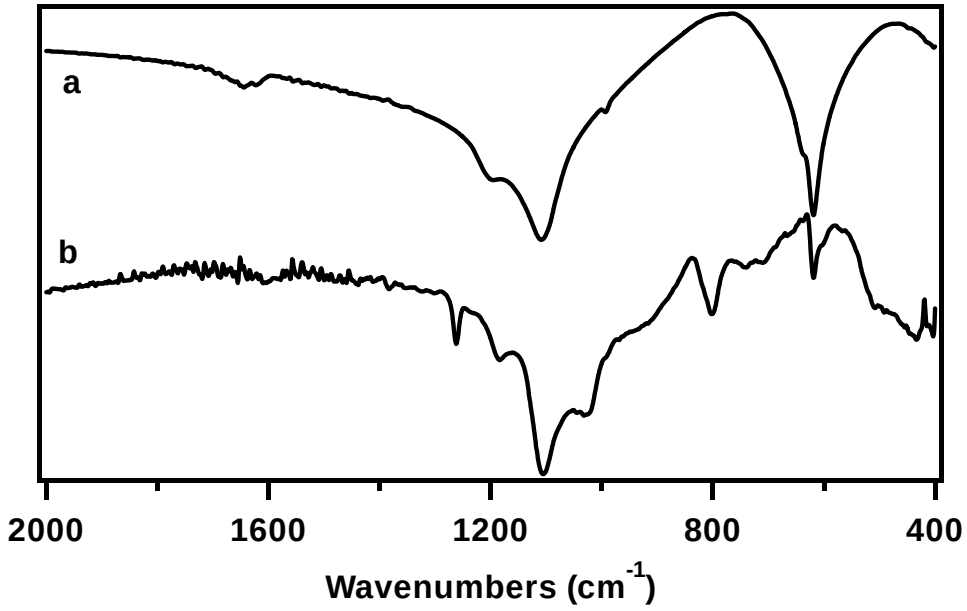

Table 3-5. FTIR assignments for Na_2SO_4 and Au-SO_4.

mode (SO_4)	**Na_2SO_4**	**Au-SO_4**	**mode (Au-SO_4)**
		1262 cm^{-1}	ν_3 (C_{3v})
	1202 cm^{-1}	1184 cm^{-1}	ν_3 (C_{3v})
ν_3 (T_d)	1110 cm^{-1}	1106 cm^{-1}	ν_3 (C_{2v})
		1030 cm^{-1}	ν_3 (C_{2v})
ν_3 (C_{2v})	994 cm^{-1}	801 cm^{-1}	ν_3 (C_{2v})
		710 cm^{-1}	ν_4 (C_{2v})

v_4 (T_d)	620 cm^{-1}	619 cm^{-1}	v_4 (C_{2v})
		510 cm^{-1}	v_4 (C_{3v})
		435 cm^{-1}	v_4 (C_{3v})

3.3.4 Transmission Electron Microscopy.

Figure 3-7 shows a TEM image of the as-prepared Au-TA from solution. Figure 3-8 shows a TEM image of Au-TA agglomerated from solution by addition of 2-aminoethanethiol hydrochloride (AET). AET is a short-chain, bifunctional ligand that displaces the citrate and tannic acid surface-stabilizing groups bringing the gold nanoparticles into close proximity where the E_{VdW} forces become strong enough to fuse the particles together. It is the fusing of the nanoparticles that leads to a shift in the SPR band of the colloidal gold. This is discussed further in chapter 4. Figures 3-9, 3-10, 3-11, and 3-12 show TEM images of Au-Cl, Au-CO_3, Au-SO_4, and Au-PO_4, respectively. These images show the gold nanoparticles to be well differentiated from one another and not fused together as agglomerated particles.

Figure 3-7. TEM images of Au-TA from solution. The image was taken at a magnification of x250K.

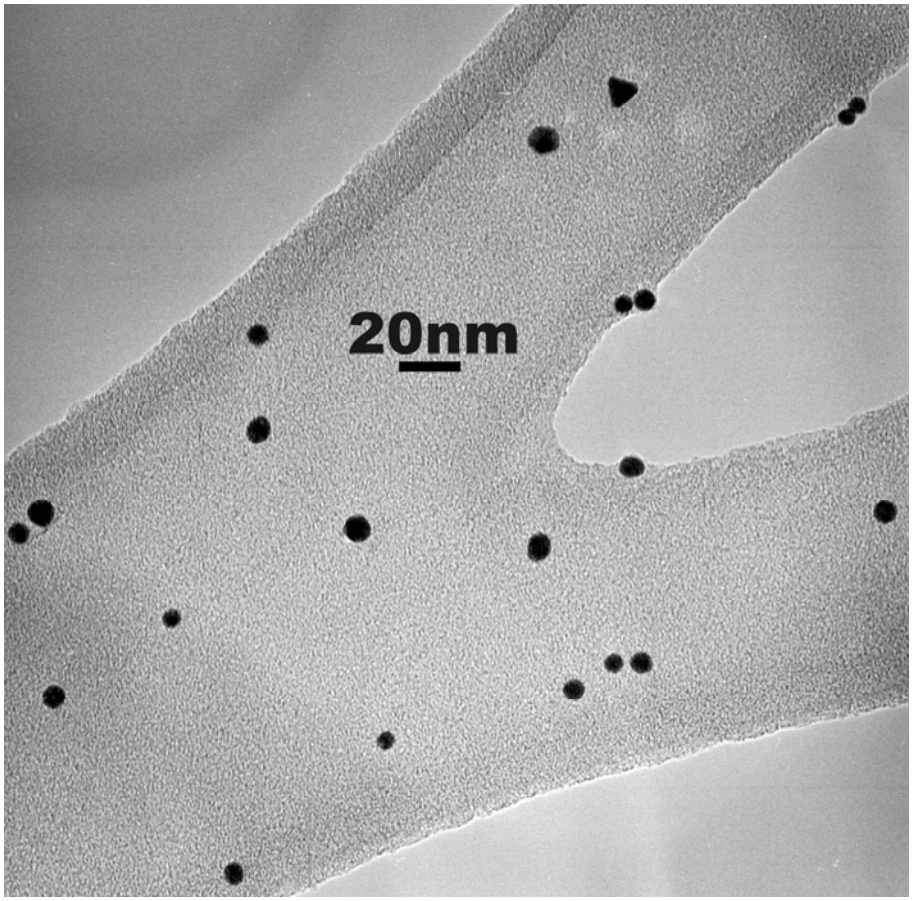

Figure 3-8. TEM image of Au-TA agglomerated from solution by the addition of 2-aminoethanethiol hydrochloride (AET). The image was taken at a magnification of x340K.

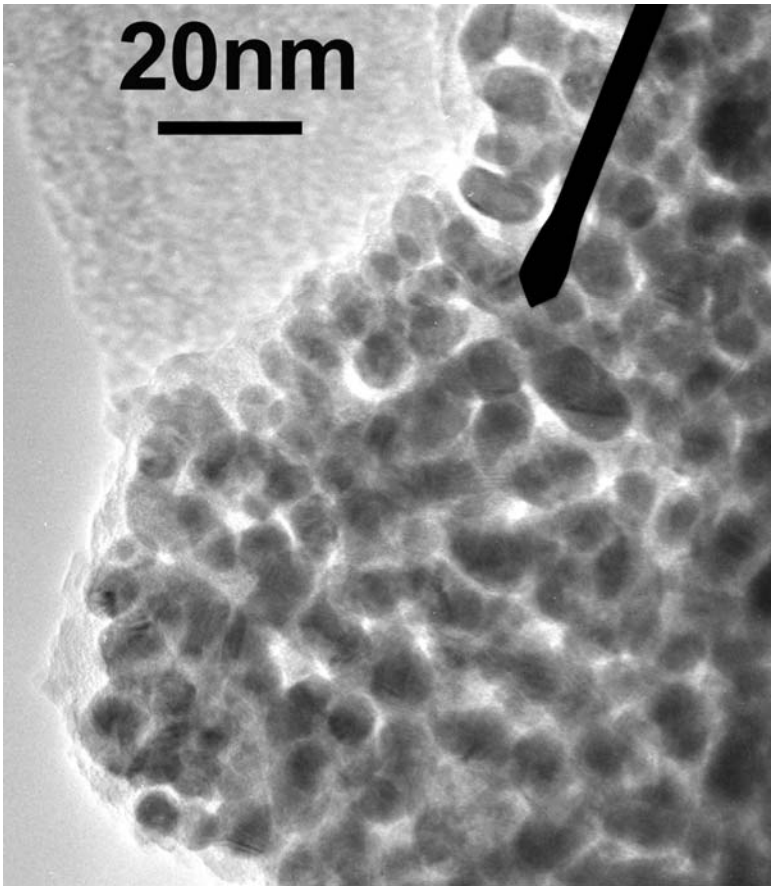

Figure 3-9. TEM image of Au-Cl taken at a magnification of x340K.

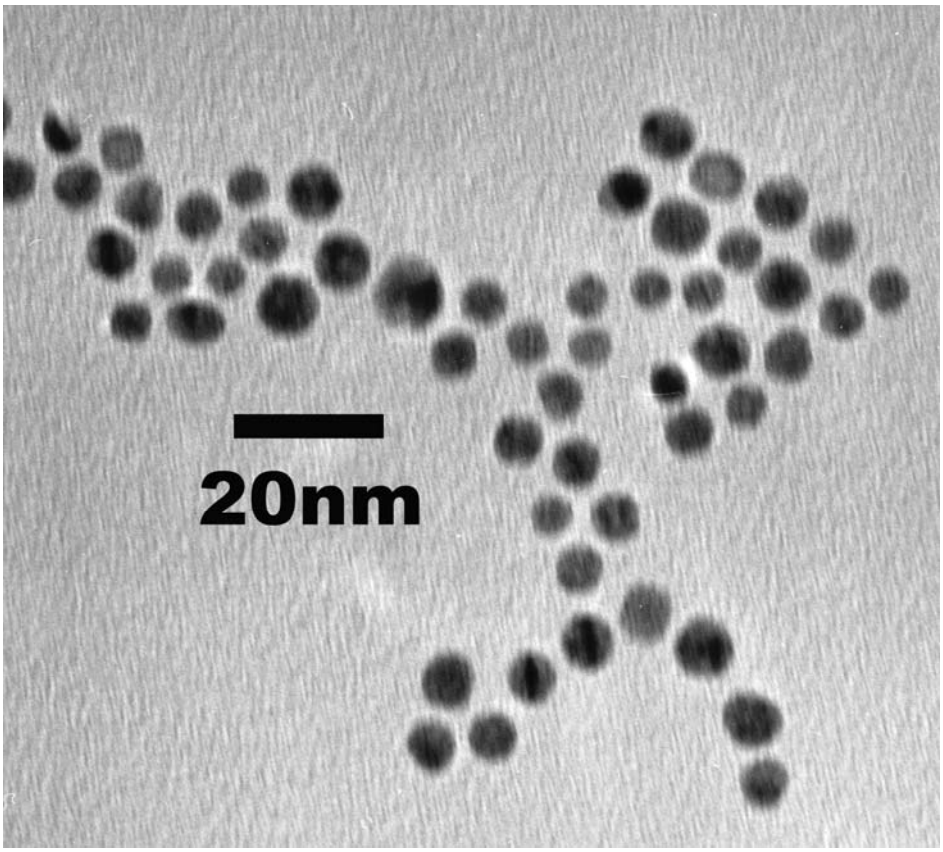

Figure 3-10. TEM image of Au-CO_3 taken at a magnification of x400K.

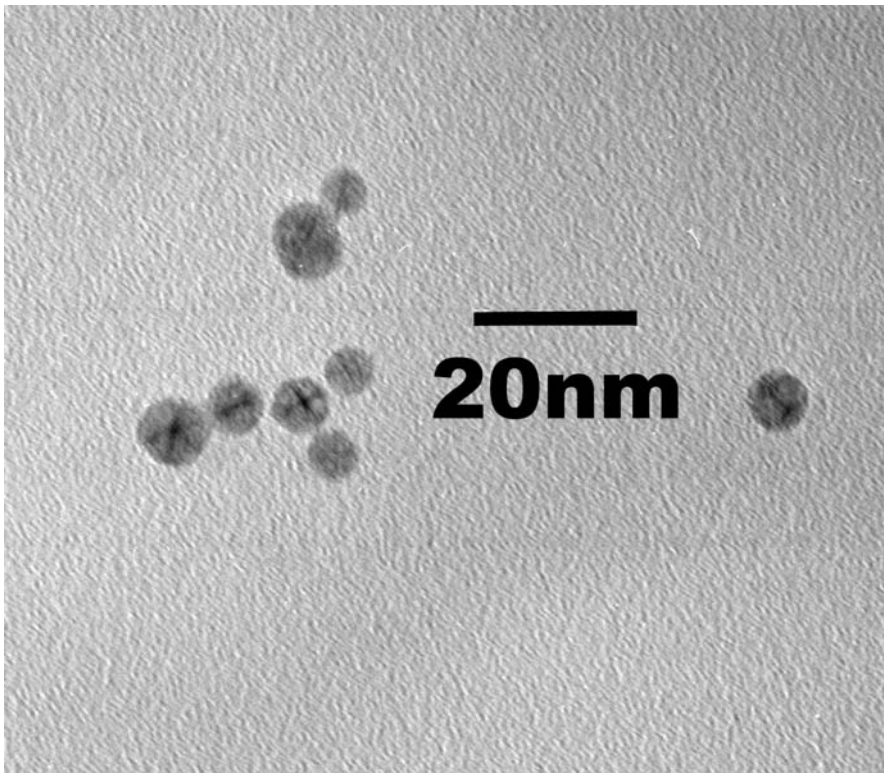

Figure 3-11. TEM image of Au-SO_4 taken at a magnification of x400K.

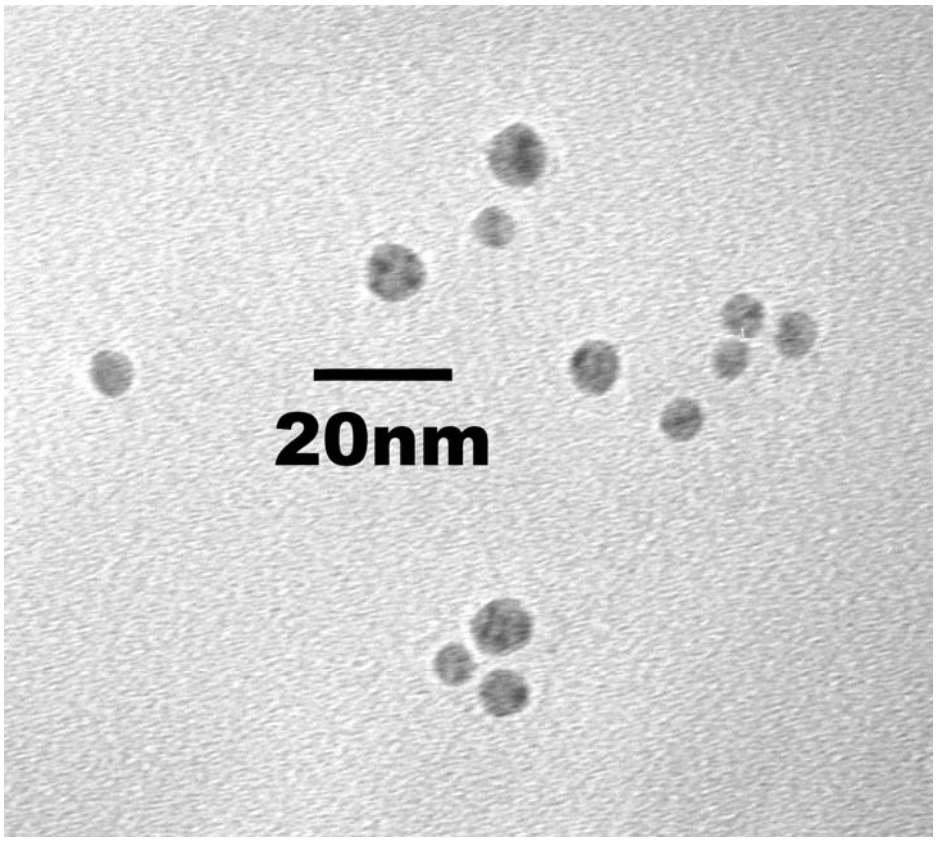

Figure 3-12. TEM image of Au-PO_4 taken at a magnification of x400K.

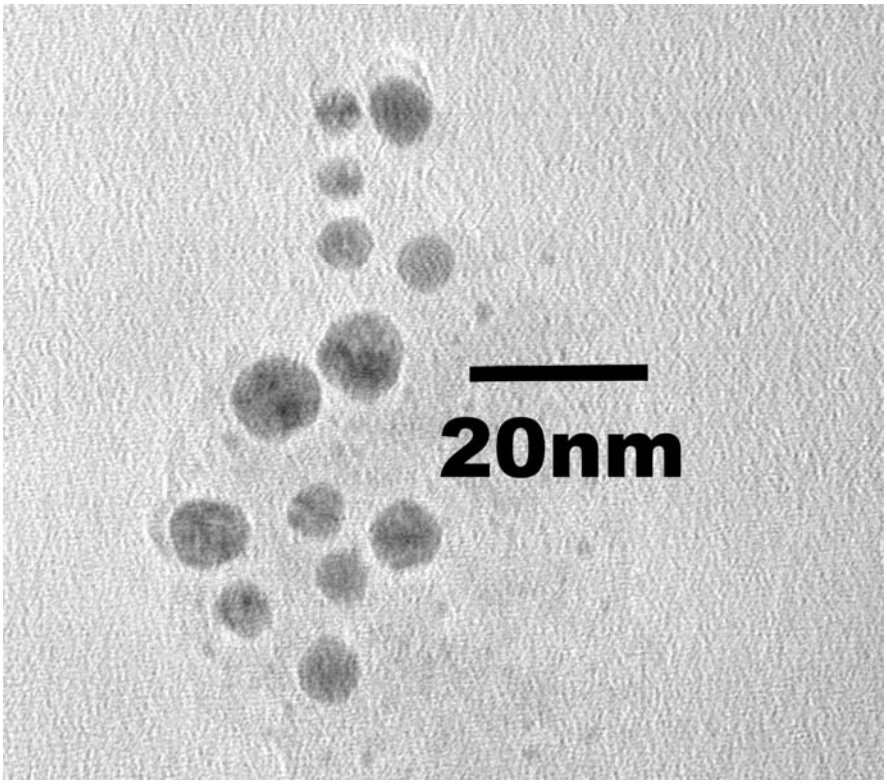

3.4 Discussion

Isolation of water-soluble nanomaterial gold from excess buffers allows a convenient method for preparation of 'de-salted' Au nanomaterials for bio-labeling experiments. The precipitation of the colloidal gold arises from a combination of electrolyte induced changes in the electrical double layer on the gold surface and by ligand interactions producing ligand exchange, as has been observed previously for colloids.[51] The ligand type and the metal-ligand interaction strength govern the importance of these interactions. For instance, addition of Cl^- ions to a colloidal solution should give rise to electrolyte-induced precipitation without significant interaction with the Au surface, due to the poor Lewis basicity of the ligand. In the case of the addition of oxyanions, the ability to accept charge from the metal surface is expected to result in ligand exchange and loss of the citrate and tannic acid passivating ligands from the Au nanomaterial surface. For addition of CO_3^{2-}, SO_4^{2-}, and H_2PO4^- salts, inspection of the absorption and IR data support the loss of the tannic acid peak indicating gold nanoparticles can be readily isolated from excess citrate and tannic acid. For the oxyanion series, the strength of the interaction depends on the ability for the oxyanion to allow back bonding from the metal, and the electronegativity of the central ion. Three possible

bonding interactions can be envisioned, purely ionic, weakly covalent, and strongly covalent. The strength of the interactions will control the thermodynamic stability of the nanomaterials, with less coagulation for more strongly interacting ligands. This can be seen by inspection of the TEM and SPR images, which indicate addition of chloride ion produces the least stable materials and evidence in the absorption spectrum for particle agglomeration; while SO_4^- produces insignificant agglomeration of the Au nanomaterials due to the strength of the interaction. The details of the interaction are discussed below.

3.4.1 Electrolyte-Induced Precipitation.

The addition of sodium chloride to the aqueous gold sol results in isolation of gold nanoparticles from solution producing a gold nanoparticle product (Au-Cl) that can be readily redissolved back into water. In analogy to precipitation of Au colloids with the addition of sodium perchlorate, at a critical concentration of added salt, changes in the double layer at the Au surface leads to rapid coagulation.[51] Changes in the microscopic double layer have been invoked to explain electrolyte-induced precipitation in latex beads and colloids. Based on the UV-Vis (Figure 3-1) and IR (Figure 3-3) analysis, the isolated Au-Cl product maintains the presence of tannic acid and citrate ions on the gold nanoparticles. This suggests the addition of NaCl does not induce

ligand exchange, but will allow removal of excess citrate and tannic acid from the reaction mixture.

In the Au-Cl absorption spectrum the absorption at 360 nm arises from tannic acid, consistent with the observation of a 360 nm tannic acid band in Au-TA (Figure 3-1). The observation of a decreased intensity of the tannic acid band in comparison to the SPR mode indicates the Cl^- anion acts mainly to remove excess tannic acid from the gold solution while maintaining the presence of tannic acid as a surface-stabilizing group. This is further supported by the observation of no significant shift in the SPR band position for the Au-Cl colloidal gold product compared to Au-TA. Drying the nanomaterials precipitated by addition of NaCl leads to re-dispersible materials with identical optical properties and non-agglomerated Au colloids as evidenced by the TEM image in Figure 3-9. Surprisingly, Au nanomaterials isolated by direct drying of Au-TA samples in an oven at 120 ^oC leads to particle agglomeration as evidenced in the TEM image in Figure 3-13 and the appearance of a new absorption band at 620 nm due to the fusing of Au nanoparticles (Figure 3-2). Based on the lack of the 620 nm band in freshly prepared Au-TA solutions, the fusing arises from isolation of Au-TA by drying. The observation of slight broadening in the bandwidth from 59 nm in Au-TA to 90 nm in Au-Cl may result either from participation of the Cl^- ion on the surface of the Au or more likely due to increased particle aggregation

in the absence of excess citrate and tannic acid ions as surface-stabilizing groups.[21] Similar optical changes are observed for citrate-stabilized gold colloids after extensive dialysis for long periods of time.[7]

Figure 3-13. TEM image of Au-TA agglomerated on a TEM grid by heating the sample in an oven at 120 ^{o}C. The image was taken at a magnification of x340K.

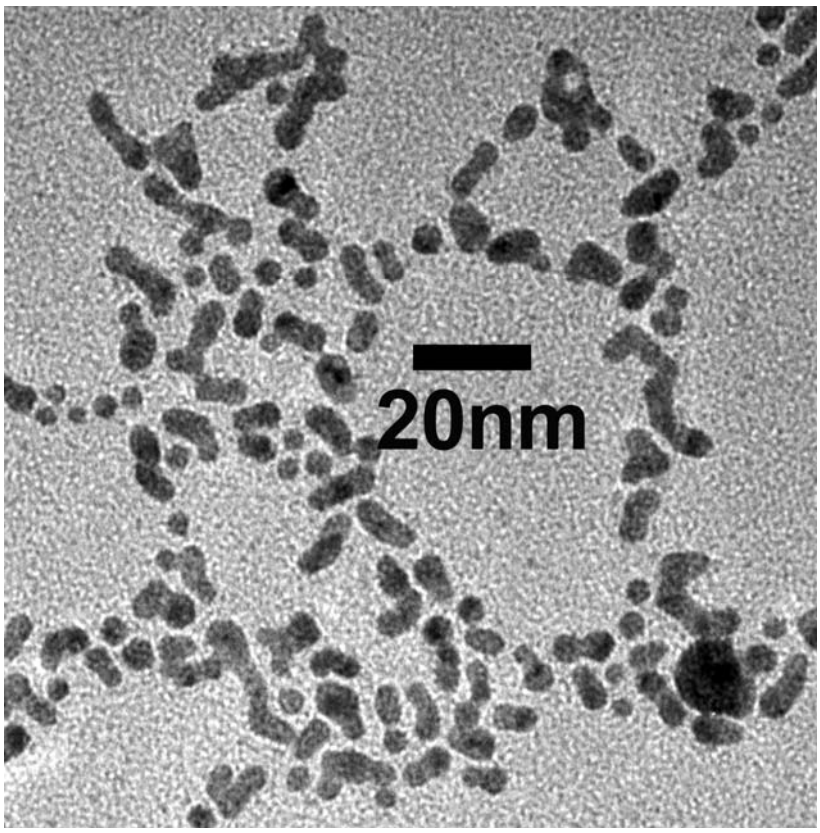

Comparison of the FTIR spectrum of the Au-Cl product with FTIR data from sodium citrate and tannic acid corroborates the presence of both citric acid and tannic acid at the surface of the Au nanomaterial (Figure 3-3). The FTIR spectrum of Au-Cl shows a characteristic carboxylate ion stretching mode at 1395 and 1594 cm^{-1} corresponding to the symmetric and asymmetric $C(\underline{---}O)_2^-$ stretching modes of the citrate functionality, respectively.[69] Comparison of the citrate spectrum to the Au-Cl spectrum indicates the asymmetric $C(\underline{---}O)_2$ band for citrate at 1594 cm^{-1} is shifted 11 cm^{-1} to 1583 cm^{-1} yet the band at 1396 cm^{-1} is maintained at 1396 cm^{-1}. It has been reported for alkanoic acids adsorbed onto silver and gold surfaces that a loss of the asymmetrical carboxylic stretch is indicative of symmetrically binding with both oxygen atoms to the surface.[70] In our case, a shift in the asymmetrical mode, while maintaining the position of the symmetrical mode, suggests that the citrate stabilizes the gold surface via bonding through one oxygen atom only. Further evidence for tannic acid binding through the acid functionality can be gained by comparison of the observed Au-Cl IR spectrum to the IR spectrum for Au-TA. The IR peaks observed at 1318 and 872 cm^{-1} correspond to the C-O stretch and the out of plane bending of the O-H on the acid functionality in tannic acid, respectively. The shift of the C-O stretch in the Au-Cl spectrum to 1335 cm^{-1} with a more narrow shape, and the shift in the OH out of plane bending mode to 882 cm^{-1} supports the assignment of tannic acid and citric

acid remaining on the Au surface. The FTIR spectrum of tannic acid exhibits a strong absorbance peak around 1712 cm^{-1}, typical of a dimeric carboxylate C=O stretch, which is shifted to 1697 cm^{-1} in the Au-Cl spectrum along with a shoulder at 1714 cm^{-1} indicating that free carboxyl groups are present in the Au-Cl sample. The small shift (2 cm^{-1}) in the IR absorbance corresponding to a C-O-H in plane bend of the hydroxyl groups in tannic acid at 1447 cm^{-1} indicates the C-O-H functionality on tannic acid does not significantly interact with the Au-surface. Based on the IR and UV-Vis data, the citrate and tannic acid groups remain bound to the surface through the acid functionality, with the Cl^- interacting purely as an ionic interaction.

3.4.2 Covalent Binding.

The nature of binding for the oxyanions to metal surfaces has been shown to depend on the crystallographic face of the metal, the nature of the metal and the oxyanion.[55,57,58,60,61,63,64,66,67,71] The trend in covalency of the metal-oxyanion interaction is governed largely by the electronegativity and the availability of empty d-orbitals on the central ion. In carbonate, the lack of d-orbitals for back bonding and the less electronegative *C* atom in comparison to sulfate results in more electron density on the O's in carbonate, and therefore more iconicity in the metal-oxyanion interaction. Stronger covalent bonding to the metal surface will arise in cases where empty d-orbitals are available for

back bonding, as in the case of phosphate and sulfate. The nature of the oxyanion-metal interaction is expected to perturb the thermodynamic stability, Au SPR band frequency, and change the IR frequency of the oxyanion upon binding to the surface of the Au nanomaterials.

Two regimes for covalent binding of the oxyanion can be imagined, the weak regime where the metal-oxygen interaction is predominately electrostatic in nature, and the strong binding limit, where a coordination bond possessing back donation form the Au to the O donor ligand arises at the metal-organic interface. In both cases, the oxyanion would displace the citric acid/tannic acid passivant from the Au surface. The weaker interaction should be dominated by a propensity for irreversible agglomeration, due to the weaker passivation strength, with little change in oxyanion symmetry and an insignificant shift in the IR modes for the oxyanion. On the other hand, greater thermodynamic stability and more significant changes in the oxyanion group symmetry and the IR is expected for a stronger interaction. In the series CO_3^{2-}, $H_2PO_4^{1-}$, and SO_4^{2-}, the CO_3^{2-} anion is expected to exhibit weak interactions with the surface due to the lack of back bonding in carbonate. The trend for sulfate and phosphate will be governed by a competition between electronegativity and back-bonding ability. Due to the greater electronegativity, the sulfate is expected to have the strongest interaction with gold surface. This arises from the *S* ability to pull density from the O's

allowing greater electron density to be donated from the metal to the bound *O* orbitals. The SPR frequency on the other hand will be largely governed by the electronegativity of an anion only, rather than the strength of the coordination at the metal surface. This predicts a shift to lower energy for a less electronegative anion, due to the less perturbation of the oscillation of electric charge on the metal surface. This predicts the trend in the SPR band energy for the oxyanions will be $H_2PO_4^{1-} > CO_3^{2-} > SO_4^{2-}$. Based on TEM, IR, and absorption, the predicted trend in both the strength of the interaction, the nature of the binding, and the affect on the SPR band is observed as discussed below.

3.4.2.1 Au-CO_3.

The addition of sodium carbonate leads to CO_3^{2-} displacement of the citrate and tannic acid on the Au nanoparticle surface, allowing isolation of Au nanomaterials with a coordinated carbonate passivating layer (Au-CO_3). The lack of infrared absorbance bands indicative of carboxylate and carbonyl groups supports the complete displacement of the citrate and tannic acid passivating layer in the presence of carbonate. This is further supported by the absence of the tannic acid absorption peak at 360 nm. The carbonate-passivated materials are readily redissolved in water without the formation of

large agglomerates of gold, as indicated by UV-vis spectroscopy and TEM in Figures 3-1 and 3-10, respectively.

The binding motif of the carbonate on the Au surface is indicative of the strength of the metal-ligand interaction. The carbonate anion can bind either as a tridentate (D_{3h} symmetry), bidentate (C_{2v} symmetry) or unidentate (C_s symmetry) ligand, as indicated in Figure 3-14.[72] The unidentate and bidentate binding would be indicative of a strong metal ligand interaction, and can be differentiated based upon the shifts in the observed IR modes for the carbonate upon binding. The tridentate binding motif can either exist in the strong or weak limit, possessing more electrostatic or more covalent character. In the strong limit, the IR frequency for the C-O bond is expected to shift to lower frequency, and symmetry breaking from ideal D_{3h} to C_{3v} symmetry is predicted. On the other hand, in the weak limit, little symmetry breaking from D_{3h} is expected with small shifts in the C-O bond in conjunction with the small perturbation of the carbonate structure upon binding. The lack of back bonding in the carbonate due to the absence of available d-orbitals would be predicted to favor the D_{3h} binding motif with minimal metal-ligand interaction.

In the free ion state the carbonate ion has D_{3h} symmetry and possesses four allowed vibrational modes, three of which are IR active.[72] Upon binding as a

tridentate ligand, if the symmetry is maintained three modes of vibration should be observed. For bidentate or unidentate binding to the surface, the symmetry of the ion changes to C_s or C_{2v}. This change in symmetry results in six IR active modes arising from splitting of the doubly degenerate ν_3 and ν_4 vibrations. In the Au-CO_3, the carbonate appears to bind in D_{3h} symmetry, suggesting little perturbation of the anion upon binding, as predicted by the electronegativity and lack of d-orbitals in the carbonate ligand. This assignment is supported by the IR spectra in Figure 3-4, where 3 IR absorbance bands are observed at 1386 cm^{-1} (ν_3), 687 cm^{-1} (ν_4) and 880 cm^{-1} (ν_2) consistent with binding in D_{3h} symmetry. The position of the ν_3 band upon binding to the metal surface is in good agreement with the ν_3 mode in the free carbonate anion observed at 1385 cm^{-1}, which suggests the carbonate only weakly interacts with the metal surface. Assignment of a tridentate binding motif rather than a bidentate interaction is consistent with a lack of splitting of the ν_3 mode upon carbonate binding as has been observed for bidentate binding of carbonate on a ZrO_2 surface.[52] This suggests that there is no change in the geometry of the carbonate ion and is only weakly coordinating the gold surface due to delocalized charge on the carbonate species.

3.4.2.2 Au-PO_4.

As with CO_3^{2-} addition, the $H_2PO_4^{1-}$ displaces the citrate and tannic acid from the surface of the Au nanomaterials producing a water soluble Au nanomaterial that readily re-disperses without large particle agglomeration (Figures 3-1 and 3-12). As illustrated in Figure 3-15, phosphate can coordinate to the gold surface either in a bidentate coordination (C_{2v}) or monodentate coordination (C_s). Both symmetries will give rise to 4 P-O modes, however the shift in the P-O vibrations will reflect the strength of the interaction and the asymmetry of the binding to the surface.

Figure 3-14. Illustration of CO_3^{2-} binding on a gold nanoparticle surface as a monodentate, tridentate, or bidentate complex.

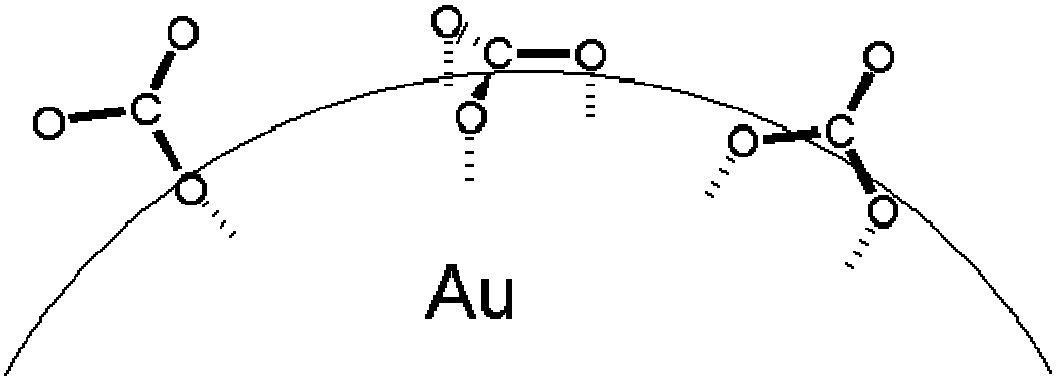

Phosphate ions have been reported to adsorb onto gold and platinum (111) and (100) electrodes in both C_{2v} and C_s symmetry depending on pH and applied voltage.[55,56,60-62] The dominant species in solution at pH ~5.0 is $H_2PO_4^-$, which would favor binding through the 2 non-protonated O's in C_2v symmetry at the gold nanomaterial surface. On gold and platinum electrode surfaces, C_{2v} binding is the dominant species and gives rise to the emergence of bands at 1120 and 1000 cm^{-1} for Au (100), 1100 and 980 cm^{-1} for Au(111), and 1110 and 1000 cm^{-1} for Pt (111) and Pt(100) faces. The shifts in the P-O bands have been correlated with differences in the strength of the metal-oxyanion interaction.

The spectrum of Au-PO_4 shown in Figure 3-5b, exhibits a series of peaks between 1250-800 cm^{-1} at 876 cm^{-1} (ν_sP-OH), 935 cm^{-1} (ν_{as}P-OH), 1055 cm^{-1} (ν_sPO-*M*), 1168 cm^{-1} (ν_{as}PO-*M*), 1243 cm^{-1} (δ P-OH), where PO-*M* indicates the O's bound at the metal surface. The observed bands are consistent with the phosphate maintaining C_2v symmetry upon binding to the gold surface through the two non-protonated oxygen atoms. The slight shift in the ν_s (P-O) band from 1061 cm^{-1} in the sodium salt arises from the possibility of asymmetry in the binding at the Au surface. Comparison of the peak positions on the gold nanomaterials to the Au electrode indicate the phosphate ligand is

less strongly interacting with the nanomaterial surface possibly due to increased surface energy or charge in these materials.

Figure 3-15. Illustration of $H_2PO_4^{2-}$ binding on a gold nanoparticle surface as a monodentate or bidentate complex.

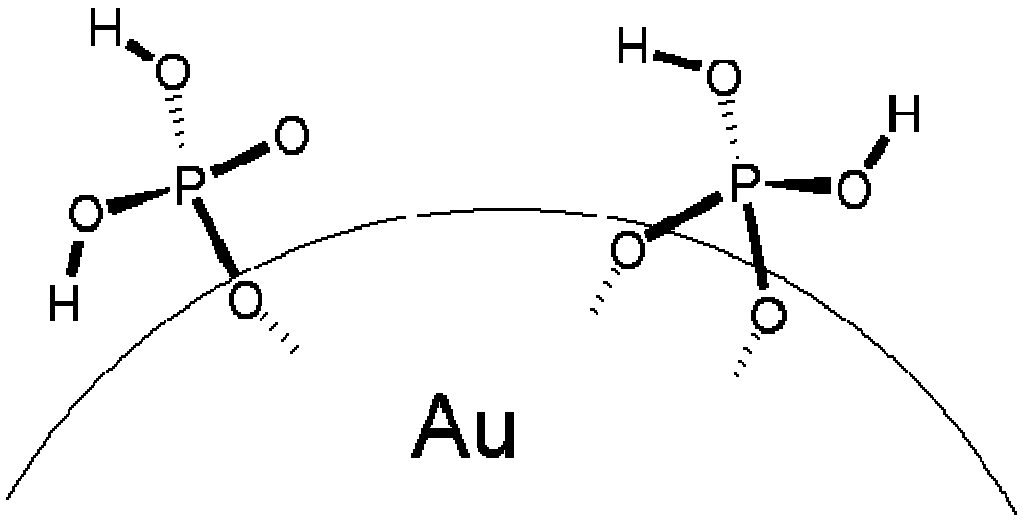

3.4.2.3 Au-SO_4.

Treatment of Au nanomaterials with sodium sulfate allows isolation of Au nanomaterials without the presence of citrate or tannic acid. Based on UV-vis and TEM analysis, the isolated Au nanomaterial product can be readily dissolved back into water without irreversible agglomeration of the gold nanoparticles or change in morphology or size dispersity (Figures 3-1 and 3-11). The Au-SO_4 materials exhibit greater long-term stability in concentrated solutions than either the carbonate or phosphate adsorbed anion, supporting a stronger interaction with the metal surface due to the differences in back bonding and electronegativity.

In sulfate adsorption to metal surfaces, there has been considerable debate in the literature as to the orientation of adsorbed sulfates on metal surfaces and to whether or not IR can determine the specific geometry.[53,55,57-59,63-68] As a free ion in solution SO_4^{2-} belongs to the high-symmetry tetrahedral point group, yet, as illustrated in figure 3-16, upon coordination with a metal surface through 3 oxygen atoms the symmetry changes to the lower symmetry C_{3v} point group.[72] The IR spectrum for sodium sulfate, in Figure 3-6a, exhibits a strong absorbance peak at 1110 cm^{-1} corresponding to the S-O stretch in the v_3 region and 620 cm^{-1} corresponding to the v_4 vibration of the

sulfate ion in T_d symmetry. Two additional peaks are observed at 1202 cm^{-1} and a weaker peak at 994 cm^{-1}, which are attributed to IR-inactive modes. In C_{3v} symmetry the v_1 and v_2 modes becomes IR active and the v_3 and v_4 vibrations arising from the *f* symmetry modes in T_d symmetry split into four total bands with a doubly degenerate E mode and a symmetric A_1 vibration. If the SO_4^{2-} coordinates as a bidentate complex through 2 oxygen atoms, the symmetry is lowered to C_{2v} in which case the double degenerate E mode in the v_3 and v_4 vibrations split further into two bands (B_1 and B_2).

Figure 3-16. Illustration of SO_4^{2-} binding on a gold nanoparticle surface as a bidentate or tridentate complex.

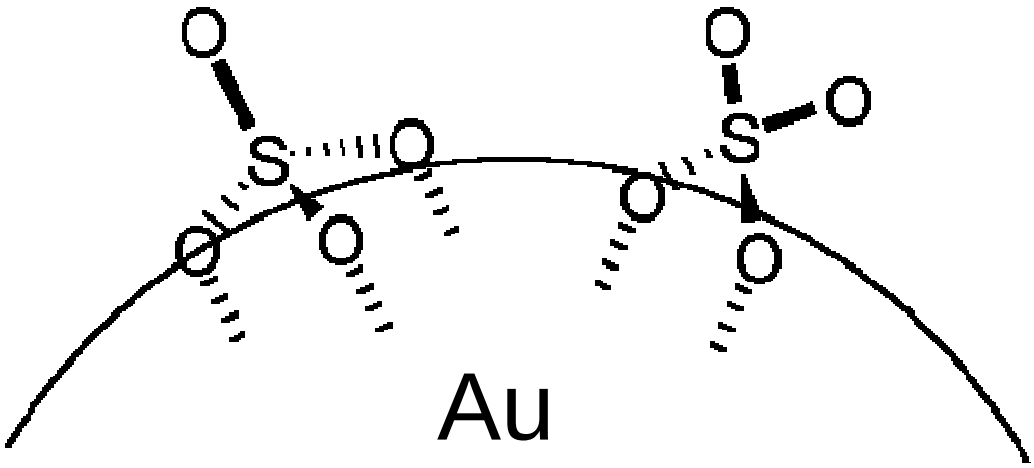

As illustrated in Figure 3-6b, the FTIR spectrum of Au-SO_4 exhibits four stretching vibrations at 1262, 1184, 1106, 1030 cm^{-1}. Based on studies of sulfate binding on Au and Pt electrodes, it is believed these four bands arise from the splitting of the ν_3 mode due to a combination of both tridentate (C_{3v}) and bidentate (C_{2v}) binding on Au nanomaterials.[53,59,64,65] The bands at 1262 and 1184 cm^{-1} are assignable to C_{3v} symmetry. The band a t 1262 cm^{-1} arises from the free S=O stretch. The IR bands at 1106 and 1030 cm^{-1} are assignable to S-O bands in C_{2v} symmetry. This may potentially arise from face-selectivity in the Au nanomaterials, as observed for selective sulfate binding on the (100) face of platinum and gold electrodes with C_{2v} symmetry via coordination through 2 oxygen atoms and binding to the (111) face with C_{3v} symmetry via coordination through 3 oxygen atoms. Inspection of the low frequency modes provides further support of face-selective binding. The emergence of several IR bands in the sulfate capped Au nanomaterials at 801, 619, and 435 cm^{-1} arise from splitting of the ν_4 mode at 620 cm^{-1}. The observation of 3 modes is consistent with C_{2v} symmetry. A series of weak peaks at ~710 cm^{-1} and 510 cm^{-1} may suggest C_{3v} binding is also present. The observation of sulfate stretching frequencies corresponding to C_{2v} and C_{3v} symmetry is similar to the reported binding motifs for sulfate on Au electrodes, and consistent with the observation in pXRD and SAED of the gold nanoparticles exhibiting prominent (111) and (100) faces.

3.4.3 Binding Influence on SPR Band.

Several researchers have indicated that the bandwidth and oscillator strength of the SPR band for Au nanomaterials scale with the particle size, while the frequency depends primarily on the electron density around the nanoparticle.[33-35,37,38,42,73] While thermodynamic stability and covalency of the interaction is largely dictated by back bonding, the shift in the SPR band should follow the electronegativity of the coordinating group.[73] As a result of metal-ligand interactions on passivated Au nanomaterials, the observed SPR frequency does not track the Mie theory exactly. This effect is observed upon surface exchange of citrate and tannic acid with carbonate, sulfate, and phosphate ions. As seen in Figure 3-1 the SPR of the Au-PO_4, Au-CO_3, and Au-SO_4 are observed at 545, 537, and 532 nm corresponding to shifts of 20, 12, and 7 nm from the SPR of Au-TA at 525 nm, respectively. The SPR of Au-Cl remains unchanged at 525 nm, which is to be expected since the addition of sodium chloride does not displace the citrate and tannic acid groups from the gold surface but rather causes coagulation of the colloidal gold due to a change in the electrolyte concentration. From this we see that the sulfate ions exhibit the least change in the SPR of the colloidal gold compared to the original solution and the phosphate groups exhibit the greatest change, although the Au-SO_4 shows the greatest long-term stability in

concentrated solutions and the greatest degree of coordination with the metal surface, as determined by the greatest change in the FTIR spectrum.

Damping of the oscillator strength for the Au SPR band is dependent on nanomaterial size, exhibiting a 1/r dependence, and the nature of the surface-capping group. Deviations from oscillator strength predictions in Mie theory have been observed to arise for strong back-donation, and a shift in the SPR due to a change in the refractive index at the nanoparticle surface.[42,73] Recapping of the Au nanomaterials with oxyanions allows the nanomaterials to be isolated from solution, providing a convenient opportunity to compare Mie theory to experimental data for the extinction coefficient of Au. The experimental extinction coefficients for the Au nanomaterials are $4.05 \pm 0.81 \times 10^6$ $M^{-1}cm^{-1}$ for Au-PO_4, $5.32 \pm 0.36 \times 10^6$ $M^{-1}cm^{-1}$ for Au-SO_4, $6.54 \pm 0.96 \times 10^6$ $M^{-1}cm^{-1}$ and for Au-CO_3. For the Au-Cl sample, the larger extinction coefficient, $9.93 \pm 0.48 \times 10^6$ $M^{-1}cm^{-1}$, arises from experimental assumptions which do not accurately correct for the mass of citrate and tannic acid on the Au surface. Conversion of the average measured extinction coefficient to units more typical of Mie theory yields an extinction coefficient of 800 $M^{-1}cm^{-1}$ per metal atom, assuming 6667 Au atoms in a 6.0 nm Au nanomaterial. Comparison of these values to estimates for the SPR extinction coefficient in 6 nm Au dots, indicate the extinction coefficients are in

reasonable agreement if ligand induced broadening is taken into account. The lowering of the extinction coefficient relative to Mie theory calculations was also seen for 19 and 20 nm Au nanomaterials.[39,74]

3.5 Conclusion.

The addition of sodium salts of carbonate, phosphate, and sulfate to aqueous solutions of colloidal gold nanoparticles allow for the isolation of the colloidal gold which can be washed free of excess citrate and tannic acid and redissolved in water to give any desired concentration of gold nanoparticle. The concentration of the gold nanoparticle solution can be calculated based on the extinction coefficients calculated in this experiment. The nature of the binding is dictated by the strength of back bonding, while the SPR frequency tracks the electronegativity of the central atom in the oxyanion. Therefore, this results in the order of thermodynamic stability is $CO_3^{2-} < H_2PO_4^{1-} < SO_4^{2-}$, while the shift in the SPR band follows the trend $H_2PO_4^{1-} > CO_3^{2-} > SO_4^{2-}$. Overall, this method produces gold colloidal nanoparticles with labile surface-stabilizing groups that maintain the integrity of the shape and size distribution of the original colloidal gold.

3.5 References.

1) Ahmadi, T. S.; Wang, Z. L.; Green, T. C.; Henglein, A.; El-Sayed, M. A. *Science* **1996**, *272*, 1924-1926.

2) Danek, M.; Jensen, K. F.; Murray, C. B.; Bawendi, M. G. *Journal of Crystal Growth* **1994**, *145*, 714-720.

3) Cumberland, S. L.; Hanif, K.; Khitrov, G. A.; Raola, O. E.; Simburger, J. T.; Yun, C. S.; Woessner, S.; Strouse, G. F. *submitted to Chem. Mater*.

4) Murray, C. B.; Norris, D. J.; Bawendi, M. G. *Journal of the American Chemical Society* **1993**, *115*, 8706-8715.

5) Murray, C. B.; Kagan, C. R.; Bawendi, M. G. *Annual Review of Materials Science* **2000**, *30*, 545-610.

6) Murthy, S.; Bigioni, T. P.; Wang, Z. L.; Khoury, J. T.; Whetten, R. L. *Materials Letters* **1997**, *30*, 321-325.

7) Slot, J. W., Geuze, H. J. *European Journal of Cell Biology* **1985**, *38*, 87-93.

8) Sun, S. H.; Murray, C. B. *Journal of Applied Physics* **1999**, *85*, 4325-4330.

9) Chen, S. W.; Murray, R. W. *Journal of Physical Chemistry B* **1999**, *103*, 9996-10000.

10) Bigioni, T. P.; Harrell, L. E.; Cullen, W. G.; Guthrie, D. E.; Whetten, R. L.; First, P. N. *European Physics Journal D* **1999**, *6*, 355-364.

11) Takagahara, T. *Surface Science* **1992**, *267*, 310-314.

12) Harfenist, S. A.; Wang, Z. L.; Whetten, R. L.; Vezmar, I.; Alvarez, M. M. *Advanced Materials* **1997**, *9*, 817+.

13) Harfenist, S. A.; Wang, Z. L.; Alvarez, M. M.; Vezmar, I.; Whetten, R. L. *Journal of Physical Chemistry* **1996**, *100*, 13904-13910.

14) Kagan, C. R.; Murray, C. B.; Nirmal, M.; Bawendi, M. G. *Physics Review Letters* **1996**, *76*, 1517-1520.

15) Korgel, B. A.; Fullam, S.; Connolly, S.; Fitzmaurice, D. *Journal of Physical Chemistry B* **1998**, *102*, 8379-8388.

16) Mitchell, G. P.; Mirkin, C. A.; Letsinger, R. L. *Journal of the American Chemical Society* **1999**, *121*, 8122-8123.

17) Mucic, R. C.; Storhoff, J. J.; Mirkin, C. A.; Letsinger, R. L. *Journal of the American Chemical Society* **1998**, *120*, 12674-12675.

18) Wang, Z. L.; Yin, J. S. *Materials Science and Engineering a* **2000**, *286*, 39-47.

19) Whetten, R. L.; Shafigullin, M. N.; Khoury, J. T.; Schaaff, T. G.; Vezmar, I.; Alvarez, M. M.; Wilkinson, A. *Accounts of Chemical Research* **1999**, *32*, 397-406.

20) Frens, G. *Kolloidn-Z. Z. Polym.* **1972**, *250*, 736-41.

21) Henglein, A.; Giersig, M. *Journal of Physical Chemistry B* **1999**, *103*, 9533-9539.

22) Leff, D. V.; Brandt, L.; Heath, J. R. *Langmuir* **1996**, *12*, 4723-4730.

23) Lin, X. M.; Sorensen, C. M.; Klabunde, K. J. *Chemistry of Materials* **1999**, *11*, 198-202.

24) Loweth, C. J.; Caldwell, W. B.; Peng, X. G.; Alivisatos, A. P.; Schultz, P. G. *Angewandte Chemie-International Edition* **1999**, *38*, 1808-1812.

25) Musick, M. D.; Keating, C. D.; Lyon, L. A.; Botsko, S. L.; Pena, D. J.; Holliway, W. D.; McEvoy, T. M.; Richardson, J. N.; Natan, M. J. *Chemistry of Materials* **2000**, *12*, 2869-2881.

26) Tian, F.; Klabunde, K. J. *New Journal of Chemistry* **1998**, *22*, 1275-1283.

27) Wang, Z. L.; Harfenist, S. A.; Vezmar, I.; Whetten, R. L.; Bentley, J.; Evans, N. D.; Alexander, K. B. *Advanced Materials* **1998**, *10*, 808-812.

28) Warner, M. G.; Reed, S. M.; Hutchison, J. E. *Chemistry of Materials* **2000**, *12*, 3316-3320.

29) Whetten, R. L.; Khoury, J. T.; Alvarez, M. M.; Murthy, S.; Vezmar, I.; Wang, Z. L.; Stephens, P. W.; Cleveland, C. L.; Luedtke, W. D.; Landman, U. *Advanced Materials* **1996**, *8*, 428.

30) Park, S. J.; Lazarides, A. A.; Mirkin, C. A.; Brazis, P. W.; Kannewurf, C. R.; Letsinger, R. L. *Angewandte Chemie-International Edition* **2000**, *39*, 3845-3848.

31) Mühlfordt, H. *Experientia* **1982**, *38*, 1127-1128.

32) Tejedor-Tejedor, M. I.; Anderson, M. A. *Langmuir* **1990**, *6*, 602-611.

33) Link, S.; El-Sayed, M. A. *Journal of Physical Chemistry B* **1999**, *103*, 8410-8426.

34) Link, S.; El-Sayed, M. A. *Journal of Physical Chemistry B* **1999**, *103*, 4212-4217.

35) Klar, T.; Perner, M.; Grosse, S.; von Plessen, G.; Spirkl, W.; Feldmann, J. *Physics Review Letters* **1998**, *80*, 4249-4252.

36) Eck, D.; Helm, C. A.; Wagner, N. J.; Vaynberg, K. A. *Langmuir* **2001**, *17*, 957-960.

37) Alvarez, M. M.; Khoury, J. T.; Schaaff, T. G.; Shafigullin, M. N.; Vezmar, I.; Whetten, R. L. *Journal of Physical Chemistry B* **1997**, *101*, 3706-3712.

38) Gluodenis, M.; Manley, C.; Foss, C. A. *Analytical Chemistry* **1999**, *71*, 4554-4558.

39) Mulvaney, P.; Giersig, M.; Henglein, A. *Journal of Physical Chemistry* **1992**, *96*, 10419-10424.

40) Lazarides, A. A.; Kelly, K. L.; Jensen, T. R.; Schatz, G. C. *Journal of Molecular Structure -Theochem* **2000**, *529*, 59-63.

41) He, L.; Musick, M. D.; Nicewarner, S. R.; Salinas, F. G.; Benkovic, S. J.; Natan, M. J.; Keating, C. D. *Journal of the American Chemical Society* **2000**, *122*, 9071-9077.

42) Mulvaney, P. *Langmuir* **1996**, *12*, 788-800.

43) Storhoff, J. J.; Lazarides, A. A.; Mucic, R. C.; Mirkin, C. A.; Letsinger, R. L.; Schatz, G. C. *Journal of the American Chemical Society* **2000**, *122*, 4640-4650.

44) Schmitt, J.; Machtle, P.; Eck, D.; Mohwald, H.; Helm, C. A. *Langmuir* **1999**, *15*, 3256-3266.

45) Taton, T. A.; Mirkin, C. A.; Letsinger, R. L. *Science* **2000**, *289*, 1757-1760.

46) Lazarides, A. A.; Schatz, G. C. *Journal of Physical Chemistry B* **2000**, *104*, 460-467.

47) Letsinger, R. L.; Mirkin, C. A.; Elghanian, R.; Mucic, R. C.; Storhoff, J. J. *Phosphorus Sulfur and Silicon and the Related Elements* **1999**, *146*, 359-362.

48) Mbindyo, J. K. N.; Reiss, B. D.; Martin, B. R.; Keating, C. D.; Natan, M. J.; Mallouk, T. E. *Advanced Materials* **2001**, *13*, 249-254,222.

49) Mirkin, C. A. *MRS Bulletin* **2000**, *25*, 43-54.

50) Taton, T. A.; Mucic, R. C.; Mirkin, C. A.; Letsinger, R. L. *Journal of the American Chemical Society* **2000**, *122*, 6305-6306.

51) Enustun, B. V.; Turkevick, J. *Journal of the American Chemical Society* **1963**, *85*, 3317-3328.

52) Dobson, K. D.; McQuillan, A. J. *Langmuir* **1997**, *13*, 3392-3396.

53) Parry, D. B.; Samant, M. G.; Seki, H.; Philpott, M. R.; Ashley, K. *Langmuir* **1993**, *9*, 1878-1887.

54) Nart, F. C.; Iwasita, T. *Journal of Electroanalytical Chemistry and Interference Electrochemistry* **1991**, *308*, 277-293.

55) Nart, F. C.; Iwasita, T. *Electrochimica Acta* **1992**, *37*, 385-391.

56) Nart, F. C.; Iwasita, T.; Weber, M. *Berichte Der Bunsen Gesellschaft Fur Physikalische Chemie-an International Journal of Physical Chemistry* **1993**, *97*, 737-738.

57) Nart, F. C.; Iwasita, T.; Weber, M. *Electrochimica Acta* **1994**, *39*, 961-968.

58) Nart, F. C.; Iwasita, T.; Weber, M. *Electrochimica Acta* **1994**, *39*, 2093-2096.

59) Weber, M.; Nart, F. C. *Langmuir* **1996**, *12*, 1895-1900.

60) Weber, M.; Nart, F. C. *Electrochimica Acta* **1996**, *41*, 653-659.

61) Weber, M.; Nart, F. C.; de Moraes, I. R.; Iwasita, T. *Journal of Physical Chemistry* **1996**, *100*, 19933-19938.

62) Weber, M.; de Moraes, I. R.; Motheo, A. J.; Nart, F. C. *Colloids and Surfaces a-Physicochemical and Engineering Aspects* **1998**, *134*, 103-111.

63) de Moraes, I. R.; Nart, F. C. *J. Electroanalytical Chemistry* **1999**, *461*, 110-120.

64) Shingaya, Y.; Ito, M. *Electrochimica Acta* **1998**, *44*, 745-751.

65) Ataka, K.; Osawa, M. *Langmuir* **1998**, *14*, 951-959.

66) Nart, F. C.; Iwasita, T. *J. Electroanalytical Chemistry and International Electrochemistry* **1992**, *322*, 289-300.

67) Edens, G. J.; Gao, X. P.; Weaver, M. J. *J. Electroanalytical Chemistry* **1994**, *375*, 357-366.

68) Degenhardt, J.; McQuillan, A. J. *Langmuir* **1999**, *15*, 4595-4602.

69) Silverstein, R. M.; Bassler, G. C.; Morrill, T. C. *Spectrometric identification of organic compounds*; 5th ed.; Wiley: New York, 1991.

70) Lin, S. Y.; Chen, C. H.; Chan, Y. C.; Lin, C. M.; Chen, H. W. *Journal of Physical Chemistry B* **2001**, *105*, 4951-4955.

71) Shingaya, Y.; Ito, M. *J. Electroanalytical Chemistry* **1999**, *467*, 299-306.

72) Nakamoto, K. *Infrared and Raman spectra of inorganic and coordination compounds*; 4th ed.; Wiley: New York, 1986.

73) Templeton, A. C.; Pietron, J. J.; Murray, R. W.; Mulvaney, P. *Journal of Physical Chemistry B* **2000**, *104*, 564-570.

74) Link, S.; Wang, Z. L.; El-Sayed, M. A. *Journal of Physical Chemistry B* **1999**, *103*, 3529-3533.

Chapter 4

Au Nanoparticle Superstructures

4.1 Introduction.

The potential to assemble 3-dimensional architectures of metal nanoparticles opens the possibility to both control and probe the onset of correlated electronic and optical properties arising from the quantum mechanical coupling of individual nanoparticle wavefunctions.[1-14] Nanoparticles of coinage metals can be prepared as near monodisperse materials with surface passivating ligands that act to stabilize the surface of the particle, lower surface energy, and maintain the separation distance between individual particles in a self-assembled structure.[15-30] The onset of collective electronic behavior in these metal nanoparticle assemblies are modulated by the oscillator strength of the oscillating dipole field for the metal nanoparticle, which is size dependent; and the particle separation, which is a function of both the ligand steric effects and the dispersional forces arising from Van der Walls contributions between particles.[4,31-38] The steric repulsion energy (E_{steric}) between two nanoparticles surface stabilized with alkyl ligands scales directly with the particle diameter and the square of the ligand length.[39,40] The Van der Waals attractive forces (E_{vdW}) between particles

increase with the square of the ratio of the particle radius and center-to-center separation distances.[39,40] The dependence of the steric term and the Van der Walls term on particle size and ligand length predicts as ligand length increases, the E_{steric} term dominates, driving particle separation; but increasing particle radius or decreasing particle separation leads to more dominant E_{vdW} contributions, pulling the particles together. The modulation of Van de Waals and steric interactions in these assemblies allow potential manipulation of the ensemble electronic properties by control of the nanoparticle size, separation distance, and connectivity of the nanomaterials. The observation of collective properties opens the potential to design nano-assemblies that respond to changes in particle spacing for applications in nanoelectronics, memory storage devices, nonlinear optics, sensor science, catalysis, and light energy conversion systems. As the interparticle spacing in a 2- or 3-dimensional lattice is reduced, collective interactions due to overlap of the wavefunctions give rise to a myriad of changes in the optical and electronic properties of the ensemble. The onset of collective electronic and optical properties occurs at different separation distances due to the nature of the quantum mechanical coupling process. Optical coupling arises from a dipolar exchange coupling with a $1/R^6$ distance dependence, while electronic coupling arises from a short-range spin-exchange coupling which has been described as a polaronic hopping model.[9,12,41] The polaronic model, in which phonon assisted electron transport arises in these assemblies, gives rise to a

discontinuity in the electrical properties consistent with a classical insulator-metal transition for Co, Ag, and Au nanoparticle assemblies.[1,2,4,5] The critical threshold is reached when the energy to repel electron density between the particles, arising from an electrical double layer, is exceeded by lowering of the total thermodynamic energy through delocalization of the free electrons over several particles.[42-44] This behavior can be envisioned as analogous to 1-D models of Peierls distortion, or the onset of superconducting behavior in 3-D high T_C cuprates.[45,46]

The polaronic nature of the I-M transition results in particle size dependent behavior for the assembly's conductivity associated with the energy of promoting an electron as a function of particle size. This energy barrier correlates with lattice order-disorder transitions arising partially from the formation of opal-like phase-segregation due to the contributions from Van der Waals dispersion forces, as well as contributions arising from the size-dependent nature of the charging energy, $Uc = e^2/(4\pi\varepsilon\varepsilon_o R)$.[5,41,47] Phase segregation effects in these assemblies can be largely minimized by use of bifunctional ligands that force assembly through the minimization of purely dispersional forces due to covalent bond formation on the Au surfaces.[48]

Changes in the optical properties of these assemblies occur due to the onset of long-range quantum mechanical coupling.[4,9] Based on models developed by

Brongersma et al, the interaction will scale as a dipole exchange problem, with a commensurate $1/R^6$ particle separation dependence and a ε^2 dependence, which is reflected in particle size.[49] Complicating the onset of optical coupling, changes in the local dielectric fields surrounding individual nanomaterials as particles assemble, will give rise to shifts in the SPR band and the observed oscillator strength of the transition based on Mie theory.[8,31-33,38] For a series of studies probing ligand dependent separation of Ag nanoparticles, the shift in the real part of the optical spectrum (Δ_{SPR}) follows a quasi linear dependence on D/2R (where D is observed separation distance and R is particle radius) behavior that has been attributed predominately to changes in the electrical field around the assembled particles as a function of particle separation distance. As the distance, decreases below ~1.2 nm, the collective oscillation gives rise to an apparent discontinuity that is attributable to the onset of dipolar coupling between individual particles based on the optical properties of the materials. The net effect is the onset of a correlated electronic motion, a plasmon, arising from coupling between the individual surface plasmon resonances.[50,51]

The size dependent properties of a series of gold nanoparticles assembled into 3-D aggregate structures covalently linked by hetero-functional ligands is probed in this Chapter. Hetero-functional ligands allow the slow formation of thermodynamically controlled structures that are readily analyzed by optical and

electron spectroscopy. Steric and Van der Waals effects can be assessed by analysis of TEM spacing and FTIR ligand packing analysis. Variation of the optical properties arising from the onset of quantum mechanical coupling is investigated as a function of the ligand length and the nanoparticle core size. With increasing core size and decreasing ligand lengths, E_{VdW} forces tend to lead to particle coalescence resulting in a loss of the surface plasmon resonance (SPR) of the nanoparticles at 525 nm and the emergence of a collective particle plasmon band around 650 nm. At longer ligand lengths and smaller core sizes E_{VdW} and $E_{covalent}$ compete to control assembly formation and smaller shifts in the SPR to lower energy are observed as a function of the interparticle spacing.

4.2 Experimental.

4.2.1 Chemicals.

$HAuCl_4 \bullet H_2O$ (99.9+%), tannic acid, sodium citrate, potassium carbonate, sodium thiocyanate, 2-aminoethanethiol hydrochloride, 10-undecenyl bromide, thioacetic acid, and hydrazine monohydrate were purchased form Aldrich. Nitrogen-purged deionized water was used for the production of gold sols.

4.2.2 Optical Measurements.

FT-IR analysis was conducted using pressed KBr pellets on a Perkin-Elmer Spectrum GX FT-IR between 370 – 7000 cm^{-1} with a resolution of 4 cm^{-1}. Analysis of the gold nanoparticles was accomplished by isolation of the

nanoparticles from solution by the addition of sodium chloride until the solution became opalescent to the eye and the precipitate collected by centrifuge. Analysis of the nanoparticle assemblies was accomplished by centrifuging the solution after the addition of the bifunctional ligands followed by washing with water, then methanol to remove the water, and then drying under vacuum. UV/Vis spectra were recorded using an Ocean Optics S2000 CCD spectrometer (resolution 0.1 nm). Temperature dependent measurements were obtained on a sample holder from Ocean Optics that allowed for the flow of water from a water bath with a Haake A80 temperature controller.

4.2.3 Electron Microscopy.

TEM analysis was performed on 400 mesh Cu grids coated with a ~5 nm layer of holey carbon (SPI). Images were obtained on a JEOL 2000 or JEOL 2010 microscope operated at 200 kV in bright field mode.

4.2.4 Preparation of Colloidal Gold.

4.2.4.1 3.0 nm Au

Colloidal gold nanoparticles ~3.0 nm in diameter (Au-SCN) were prepared by a method developed by Baschong et al.[52] Briefly, 0.3 ml of 1 M thiocyanate solution was added at room temperature with stirring to 50 ml of deionized water containing 0.5 ml of 1% (w/v) auric acid and 0.75 ml of 0.2 M K_2CO_3. The

solution was stirred for 15 hours in the dark at 22 ^{o}C and used shortly after preparation.

4.2.4.2 6.0 nm Au

Colloidal gold nanoparticles 6.0 nm in diameter surface-passivated with citrate and tannic acid groups (Au-TA) were prepared by a method developed by Mühlfordt using sodium citrate and tannic acid as reducing agents of hydrogen tetrachloroauric acid.[19] In this methodology 100 ml of a 0.001% (w/v) solution of freshly prepared auric acid was heated to reflux and a solution containing 2 ml of a 1% (w/v) solution of sodium citrate and 0.45 ml of a 1% (w/v) tannic acid solution was added with vigorous stirring. The solution was stirred at reflux for an additional 5 minutes followed by cooling to room temperature.

4.2.4.3 18.0 nm Au

Colloidal gold nanoparticles 18.0 nm in diameter were prepared by a method developed by Turkevich et al with sodium citrate serving as the reductant of auric acid as well as the passivating groups on the gold surface (Au-cit).[53] In a typical synthesis 0.025g of hydrogen tetrachloroauric acid was dissolved in 250 ml of deionized water and brought to reflux and 8.75 ml of a 34 mmol solution of sodium citrate was added with vigorous stirring. This resulted in a gradual change in color from a pale yellow to a wine red color. The solution was refluxed

for an additional 15 minutes with rapid stirring followed by cooling to room temperature. Detailed descriptions of the preparation of the nanoparticles are given in Chapter 2.

4.2.5 Preparation of (11-mercaptoundecyl)ammonium chloride.

The MUAm ligand was prepared by literature methods.[54] N-(10-undecenyl)phthalimide was prepared by mixing potassium phthalimide (18.5 g, 100 mmol) and 10-undecenyl bromide (28 g, 120 mmol) in 100 ml of DMF and refluxed for 20 h. The mixture was cooled to room temperature, diluted with deionized water, and extracted twice with Et_2O. The organic phase was washed with water, dried over Na_2SO_4, and evaporated to dryness. The N-(10-undecenyl)phthalimide product was recrystallized from methanol giving an off-white powder (23.7 g, 79% yield). NMR ($CDCl_3$): 1.21-1.42 (m, 12 H, CH_2), 1.58-1.75 (m, 2 H, C*H*$_2$CH$_2$N), 1.97-2.08 (m, 2 H, C*H*$_2$CH=CH$_2$), 3.68 (t, 8 Hz, 2 H, C*H*$_2$N), 4.88-5.04 (m, 2 H, CH=C*H*$_2$), 5.72-5.91 (m, 1 H, C*H*=CH$_2$), 7.67-7.90 (m, 4 H, arom.).

N-(11-thioacetylundecyl) phthalimide was prepared by irradiating N-(10-undecenyl)phthalimide (23.7 g, 79 mmol) and thioacetic acid (20 ml, 280 mmol) in CH_2Cl_2 (100 ml) for 16 h. The solvent was removed under vacuum and the product recrystallized twice from methanol (100 ml) (27.0 g, 91% yield). NMR ($CDCl_3$): 1.16-1.42 (m, 14 H, CH_2), 1.47-1.61 (m, 2 H, C*H*$_2$CH$_2$SAc), 1.61-1.74 (m, 2 H, C*H*$_2$CH$_2$N), 2.32 (s, 3 H, Ac), 2.85 (t, 8 Hz, 2 H, C*H*$_2$SAc), 3.68 (t, 8 Hz,

2 H, CH_2N), 7.65-7.88 (m, 4 H, arom.). GCMS (MeOH) m/z (relative abundance): 375 (M^+, 3), 332 (M^+ -C_2H_3O, 86), 300 (M^+ - C_2H_3OS, 14), 160 ($C_9H_6NO_2^+$, 100), 77 ($C_2H_5OS^+$, 10), 43 ($C_2H_3O^+$, 93).

(11-mercaptoundecyl)ammonium chloride was prepared by heating N-(11-thioacetylundecyl) phthalimide (13.5 g, 36 mmol) with H_2NNH_2 (4.0 ml, 125 mmol) in methanol (125 ml) at reflux for 3 h. The volatiles were removed in vacuum and the product was extracted with dilute HCl then dried and extracted with CH_2Cl_2/MeOH (10:1). The organic phase was evaporated to dryness and the residue recrystallized twice from CH_2Cl_2 by the addition of a minimal amount of MeOH to give a white powder (6.0 g, 82 %). NMR (DMSO): 1.20-1.42 (m, 16 H, CH_2), 1.46-1.62 (m, 2 H, C*H*$_2CH_2NH_3^+$), 2.28 (d, 8 Hz, 1 H, SH), 2.44 (q, 8 Hz, 2 H, C*H*$_2$SH), 2.65-2.81 (m, 8 Hz, 2 H, SH C*H*$_2NH_3^+$), 8.06 (s br, 3 H, NH_3^+). GCMS (CH_2Cl_2) m/z (relative abundance): 203 (M^+, 10), 170 (M^+ - SH, 100).

An FTIR spectrum of MUAm is shown in Figure 4-1 along with the FTIR spectrum of AET comparing the characteristic thiol, ammonium, and methylene peaks. Peak assignments are given in Table 4-1. These compounds are characterized by a broad absorbance band between 3200 and 1700 cm^{-1} arising from the symmetrical and asymmetrical stretching of the NH_3^+ group, a combination band of the asymmetrical bending and the torsional oscillation of the NH_3^+ around 2000 cm^{-1}, symmetrical and asymmetrical bending bands around

1550-1504 and 1600-1575 cm^{-1}, respectively, and an S-H stretching band in the 2600-2500 cm^{-1} region.[55]

Figure 4-1. FTIR spectra of (a) AET and (b) MUAm.

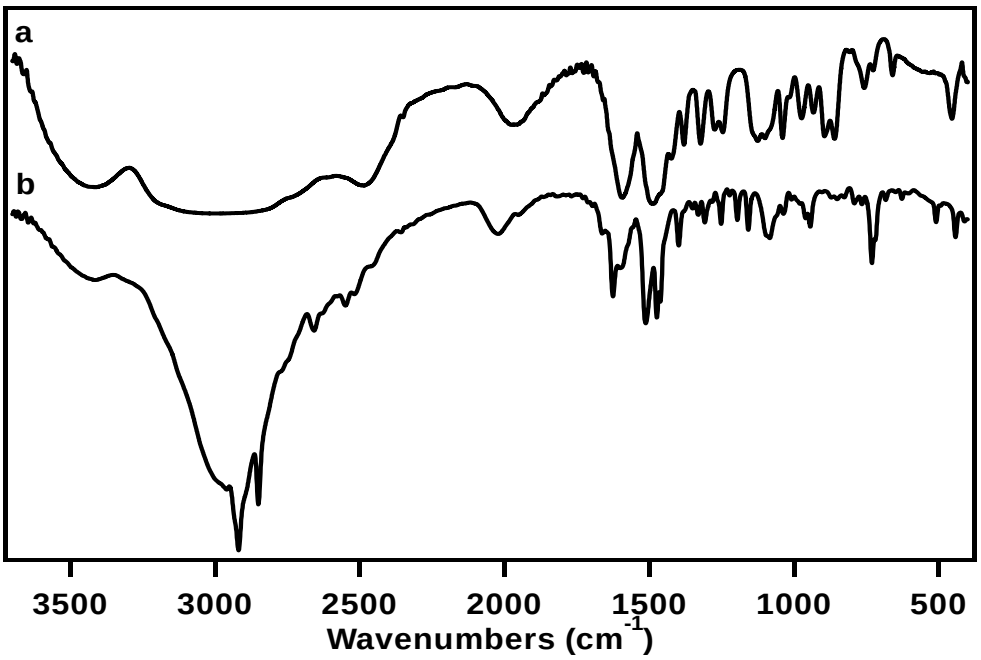

Table 4-1. Assignments of FTIR bands for MUAm and AET.

assignment	**MUAm (cm^{-1})**	**AET (cm^{-1})**
ν_s and ν_{as} NH_3^+	b, 3200-2800	b, 3200-2800
ν_{as} CH_2	2919	-----
ν_s CH_2	2850	-----
ν SH	2550	2490
ν_{as} NH_3^+ + ρ NH_3^+	2025	1973

δ_{as} NH_3^+	1600	1597
δ_s NH_3^+	1512	1490
δ_s CH_2	1461	1458
ν C-N	1085	1100
ρ CH_2	730	727
ν C-S	684	660
ρ NH_3^+	510	460

4.2.6 Preparation of Gold Superstructures.

In all cases Au-superstructures were obtained by addition of an aqueous 0.1M solution of 2-aminoethanethiol hydrochloride (AET) or 0.05M solution of (11-mercaptoundecyl)ammonium chloride (MUAm) to the colloidal gold solutions. Slow addition of the hetero-functional ligand results in the agglomeration of the colloidal gold, which could be isolated by centrifuge, washed with water and methanol, and dried under vacuum.

4.3 Results and Discussion.

4.3.1 Thermodynamic Forces of Assembly.

In the assembly of nanoparticles, a competition exists between the Van der Waals dispersion forces of the nanoparticle cores pulling the particles together and the steric forces of the surface passivating ligands pushing them apart. The steric repulsion energy (E_{steric}) between two nanoparticles surface stabilized with alkyl ligands scales directly with the particle diameter, the square of the ligand length, and inversely with the cube of the diameter of the surface area occupied by the head group on the particle surface, which should not change significantly with ligand length.[39,40] Other contributions to steric terms that modulate the magnitude of the interaction arise from inter-chain effects on the quantum dot surface arising from packing and tilting interactions similar to self-assembled

monolayers.[56] The Van der Waals attractive forces (E_{vdW}) between nanoparticles increases with the square of the ratio of the particle radius and center-to-center distance and can thus be expected to increase rapidly with increasing particle size and decreasing particle separation.[39,40] Thus by increasing the particle size and decreasing the length of the ligand connecting them, it is expected that E_{vdW} will dominate control over assembly and separation distance between particles should decrease. Steric and Van der Waals terms can be overcome by strong covalent interactions arising from ligand surface interactions (E_{cov}) in bifunctional assemblies.

Since the Van der Waals dispersion forces increase rapidly with increasing particle diameter and decreasing particle separation, this predicts a minimum favorable separation distance (C) for particles of a given size (R). For bifunctional assemblies this gives rise to two regimes: L (ligand length) > C or L < C. As L is reduced below C, the thermodynamic energy to form an assembly increases due to steric contributions, which may lead to particle coalescence and loss of individual properties. Recent MD simulations suggest particle coalescence gives rise to ramified structures in which partial coalescence of the particle is observed as necking of the structure at the Au-Au interface.[42-44,57] At a critical value, which is particle size dependent, this should lead to irreversible coalescence of the particles to minimize the total energy in the system.

Contributions from chain packing on the nanoparticle surface to steric energy are crucial to the final assembly. As illustrated in Figure 4-2, the chain length of the ligand controls the distance of particle separation and provides an insulating layer between the metallic cores. As the particles initially come into proximity. The particle separation is determined by twice the ligand length. As E_{cov} (covalent) forces become stronger, due to the binding affinity, the ligand length should determine the separation distance and the interparticle interaction potential between the two particles becomes solely dependent upon $E_{vdW} + E_{steric}$.[40] Illustrations of interparticle interaction potential ($E_{vdW} + E_{steric}$) calculations for nanoparticles with 3.0, 6.0 and 18.0 nm diameters and hetero-functional ligands 1.4 (MUAm) and 0.4 nm (AET) in length are given in Figures 4-3 to 4-6. Figures 4-3 and 4-4 compare the interparticle interaction potential where the distance separating the particles is L and 2L, respectively, for hetero-functional ligands 1.4 nm in length. Figures 4-5 and 4-6 compare the interparticle interaction potential where the distance separating the particles is L and 2L, respectively, for hetero-functional ligands 0.4 nm in length. From Figures 4-3 to 4-6 it is apparent that the steric terms tend to dominate the separation distance for MUAm, while Van der Waals terms dominates AET assemblies which may lead to particle coalescence, when the repulsive energy is greater than the energy required to drive surface reconstruction.

Figure 4-2. Illustration of the variables in equations 1 and 2.

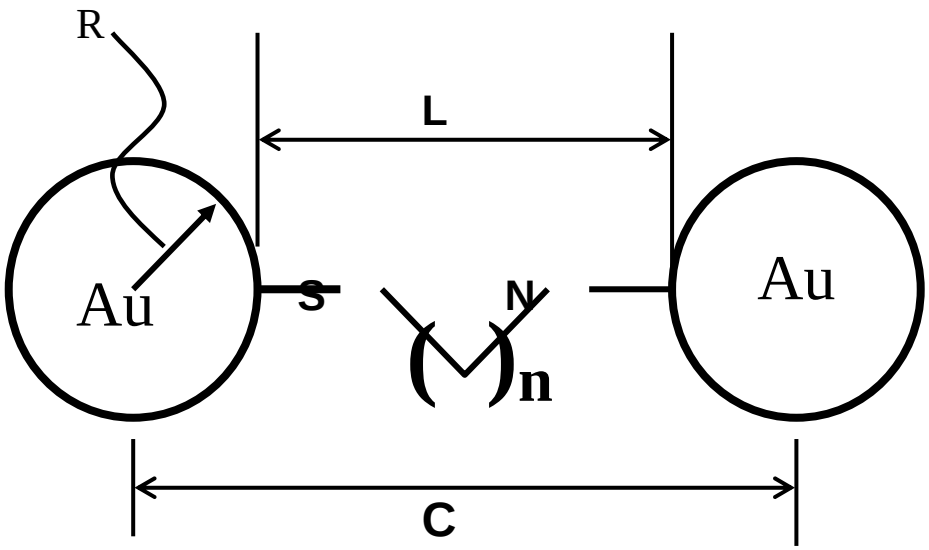

$$C = 2R + L$$

Figure 4-3. Interparticle interaction potential (E_{vdW} + E_{steric}) calculations for nanoparticles with (a) 3.0, (b) 6.0 and (c) 18.0 nm diameters and hetero-functional ligands 1.4 nm in length, with a particle separation of 2L. The inset shows the calculated values for these assemblies.

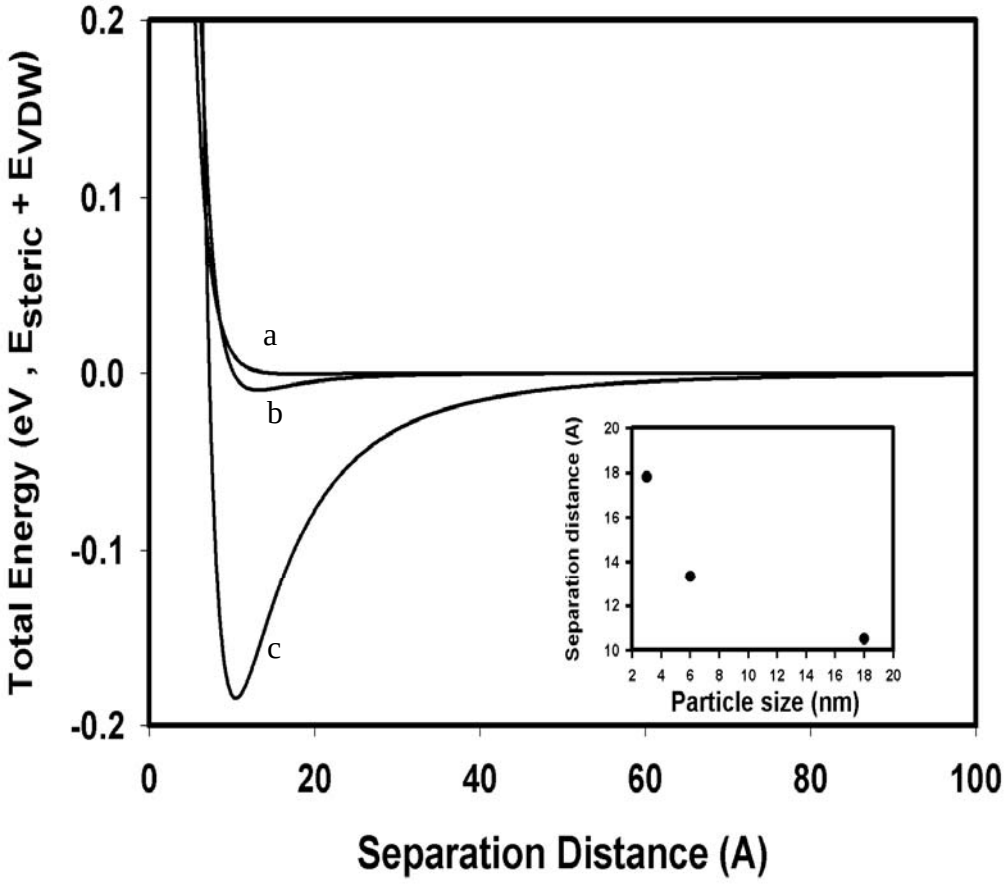

Figure 4-4. Interparticle interaction potential (E_{vdW} + E_{steric}) calculations for nanoparticles with (a) 3.0, (b) 6.0 and (c) 18.0 nm diameters and hetero-functional ligands 1.4 nm in length, with a particle separation of L. The inset shows the calculated values for these assemblies.

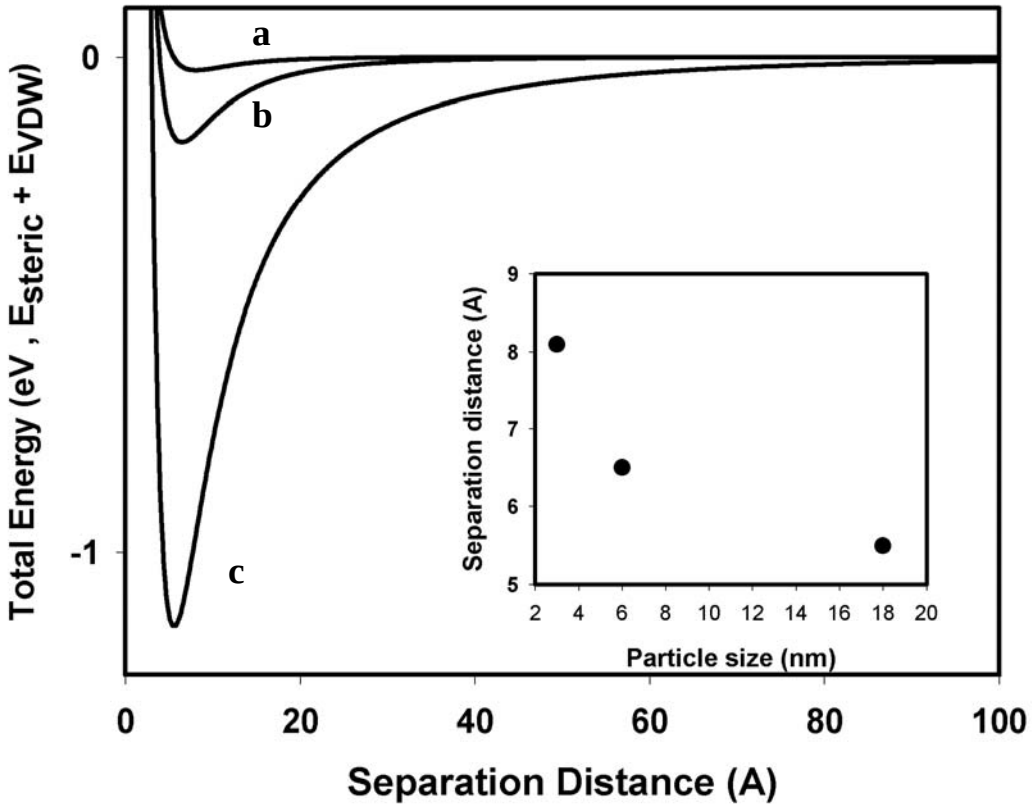

Figure 4-5. Interparticle interaction potential (E_{vdW} + E_{steric}) calculations for nanoparticles with (a) 3.0, (b) 6.0 and (c) 18.0 nm diameters and hetero-functional ligands 0.4 nm in length, with a particle separation of 2L.

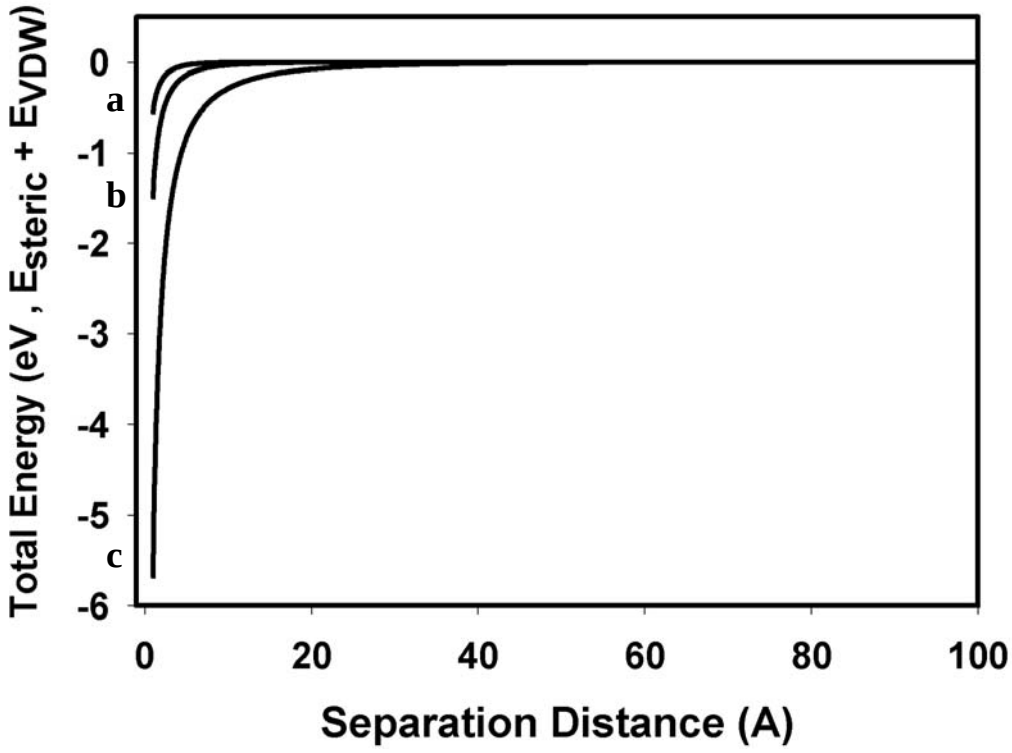

Figure 4-6. Interparticle interaction potential (E_{vdW} + E_{steric}) calculations for nanoparticles with (a) 3.0, (b) 6.0 and (c) 18.0 nm diameters and hetero-functional ligands 0.4 nm in length, with a particle separation of L.

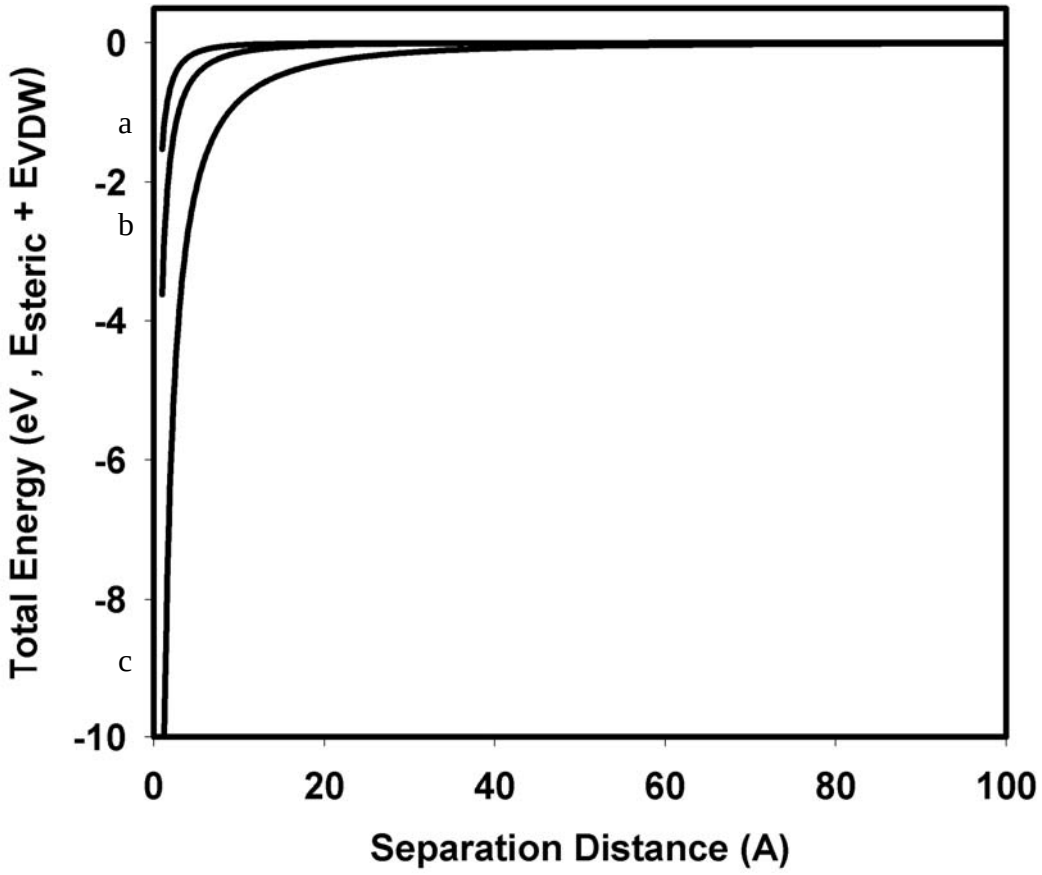

4.3.2 Chain Packing Contributions to E_{steric}

The steric energy term is modulated by the chain length and the chain packing on a surface.[40] Analogous to the packing model for self-assembled monolayers on gold surfaces, alkanethiols are observed to form domains of closely packed carbon chains oriented in an all trans configuration.[23,27,56,58-60] The competition between inter- and intra-ligand effects on a gold surface will compliment the contributions of E_{steric} to the total thermodynamic model. The length of the alkane portion, which depends on the number of gauche defects, dictates the packing of the chains on the surface of the nanoparticle. The methylene modes in FTIR spectroscopy are a convenient reporter of trans and gauche configurations in the chain packing and the degree of crystallinity within the system.[23,27,59,60] As the separation distance between nanoparticles in an assembly is decreased below the length of the passivating ligand ($C < L$) gauche defects should be observed in the IR spectra. With increasing particle size, a subsequent increase in E_{vdW} is expected, which may lead to an increase in gauche conformers. Conversely, changes in chain tilting relative to the metal surface or packing density can relieve the strain induced by Van der Waals attractions, which would result in $C < L$ without loss of all trans conformational order. The influence of these effects are evident by inspection of the vibrational data for the nanoparticle assemblies.

Figure 4-7 shows the FTIR spectra obtained for (a) 3.0, (b) 6.0, and (c) 18.0 nm gold assemblies formed with MUAm. Immediately observable is a loss of the broad ammonium band from 3200 to 1700 cm^{-1} and the thiol stretch at 2550 cm^{-1}, along with the emergence of a new band at 3350 cm^{-1} assigned to the asymmetrical stretch of NH_2.[55] This suggests that both functionalities are binding to the surface of gold nanoparticles with the N binding as an amine and not as an ammonium group. This is further supported by loss of the asymmetrical and symmetrical NH_3^+ bending vibrations for the ammonium group, observed at 1600 and 1512 cm^{-1}, respectively (Table 4-2), and the observance of a single band at 1550 cm^{-1}, assigned to the NH_2 bend of a primary amine.[55]

The location of the symmetrical and asymmetrical methylene stretching modes of adsorbed thiolates on nanoparticle surfaces has traditionally been an indicator of the packing of alkane chains on the surfaces.[27,59] Strong inter-chain effects and high packing density leads to crystalline motifs with observed methylene stretching bands at 2918 and 2848 cm^{-1}. Greater disorder or gauche defects in the chain leads to greater shifts of the methylene stretching bands to higher wavenumbers indicative of a liquid-like phase transition with methylene stretching modes at 2928 and 2856 cm^{-1}.[58,60] In the assemblies, the νCH_2 modes at 2918 and 2848 cm^{-1} are indicative of an all trans crystalline packing for the organic passivating layer. Supporting this assignment, the narrow line width and

the observation of the alpha carbon at 3937 and 2856 cm^{-1} indicates good crystallinity in the chain packing. The observation of single peaks at 1460 and 720 cm^{-1}, assigned to the methylene scissoring and rocking modes, indicate hexagonal packing of the chains.[27,58-60]

Limited information about chain tilting can be observed by inspection of the relative intensities of the νNH_3 and νCH_2 modes, as well as the νCN and νNH modes. Changes in packing of the chains are observed with increasing particle size for the MUAm assembly. The amine stretching band around 3350 cm^{-1} is observed to increase in intensity with increasing particle size, which is opposite of what is observed for the methylene stretching modes. This suggests that as the particles pack closer together the chains may become compressed and tilt towards the surface to alleviate strain. The increase in the intensity of the amine bands and decrease in intensity for the methylene bands is expected due to surface selection rules. This is coupled to a shift in the C-N bands to higher wavenumbers and a shift in the N-H bending modes to lower wavenumbers. It is expected that as the Au-N bond strength increases the C-N bond strength decreases and a shift to higher wavenumbers is observed.[27,59]

It should be noted in the 6 nm Au assembly that peaks associated with tannic acid and citrate are still present. This indicates that complete exchange of surface protecting groups is not necessary for assembly of the gold nanoparticles. The FTIR for AET assembly is not shown due to the small CH_2 contributions in the

two-carbon assembly. Analysis of the TEM patterns for the Au assemblies will provide further insight into the magnitude of E_{vdW} and E_{steric} contributions to the final assembly.

Figure 4-7. FTIR spectra of (a) 3nm, (b) 6 nm, and (c) 18nm gold nanoparticle assemblies formed by the addition of MUAm to the initial colloidal gold solutions.

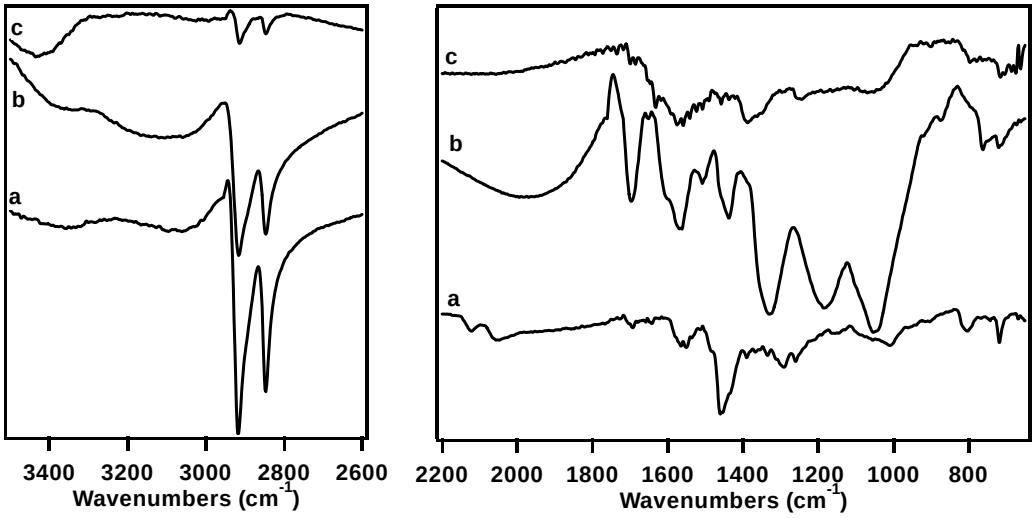

Table 4-2. Assignments for FTIR bands of (a) 3nm, (b) 6 nm, and (c) 18nm gold nanoparticle assemblies shown in Figure 4-7.

Assignment	**3 nm (cm^{-1})**	**6 nm (cm^{-1})**	**18 nm (cm^{-1})**
ν_{as} NH_2	3350	3352	3388
ν_{as} CH_2	2918	2916	2914
ν_s CH_2	2848	2846	2846
δ NH_2	1550	1550	1558
δ CH_2	1460	1460	1458
ν C-N	1083	1047	1055

$\rho\ CH_2$	720	720	717

4.3.3 Au-Au Separation in Nanoparticle Assemblies.

4.3.3.1 18 nm Au Assemblies.

Formation of gold assemblies by reaction with the hetero-functional ligand AET should produce structures separated by ~0.4 nm based on the AET ligand length. Drop-wise addition of a 0.1M AET solution to an 18.0 nm Au solution results in an immediate color change in the solution from wine red to blue with the formation of a black precipitate. The UV-vis absorption spectrum of the reaction as the AET solution is added is shown in Figure 4-8. As the concentration of the AET is increased, the absorbance spectrum shows the emergence of a new band around 640 nm with a concomitant decrease in intensity of the SPR band at 520 nm. The lack of isobestic behavior suggests a concurrent shift in energy and increase in band intensity occurs as the assembly forms. The band shift arises from both changes in the local dielectric field experienced by the Au particles and the onset of quantum mechanical coupling.[4,8,33]

TEM analysis of the solution after the addition of two drops of the AET solution, shown in Figure 4-9, indicates formation of gold assemblies, as well as remaining discrete nanoparticles. At higher magnification (Figure 4-10) the separation distances in the assembled gold nanoparticles are ≤ 0.6 nm. The observation of C < 0.6 nm is consistent with the expected particle separation distance based upon

the minimum separation distance using $E_{total} = E_{vdw} + E_{steric}$ for assemblies where C = 2R + 2L. The observance of particles touching suggests that as the particles come into greater proximity, E_{vdW} effects overcome the E_{steric} effects and the particles come into intimate contact with one another.

Figure 4-11 shows a TEM image of 18.0 nm Au after the addition of a larger molar ratio of AET to Au. In this image the gold nanoparticles show evidence of particle coalescence with no definable separation between particles. This observation suggests the lower surface energy of the larger dots lead to surface induced particle reconstruction in order to minimize interaction energies. The curvature of the interface arises from plastic deformation of the Au particles and formation of a single monolithic interface.[42,43,61] The assembly exhibits an absorption spectrum with complete absence of the SPR band at 520 nm, and a broad absorption band centered around 642 nm, due to a collective resonance oscillation of the electrons across the larger monolith.

Similar effects on the position of the SPR band can be seen as a function of the temperature of the reaction. Figure 4-12 shows a UV-vis spectrum of the 18 nm Au solution after the addition of one drop of a 0.1M AET solution at several temperatures. Initially at 30 ^{o}C a decrease in the intensity of the SPR band at 520 nm is mirrored by an increase in intensity of a new band at 635 nm. As the reaction is heated to 50 ^{o}C the band at 520 nm decreases further in intensity and the band at 635 nm shifts to 670 nm followed by an increase in intensity. The

band at 670 nm corresponds to the formation of a Au monolith structure, in which the individual particles have coalesced as in Figure 4-11. Further heating to 75 ^{o}C shows a decrease in intensity for both bands. The decrease in intensity of the SPR band with increasing temperature has also been observed for 18.0 nm Au solutions alone, as shown in Figure 4-13. The decrease in intensity is believed to be due to the change in the dielectric constant of the solution with heating, which has a strong influence on the intensity of the SPR of colloidal nanoparticles as dictated by the Mie theory.[62,63] As the solution is cooled the original peak intensity is recovered.

Figure 4-8. UV-vis absorbance spectrum following the drop-wise addition of a 0.1M solution of AET to a colloidal Au-cit solution. The arrows indicate the progression of the peak with subsequent additions of the AET solution. The spectra have not been corrected for changes in concentration.

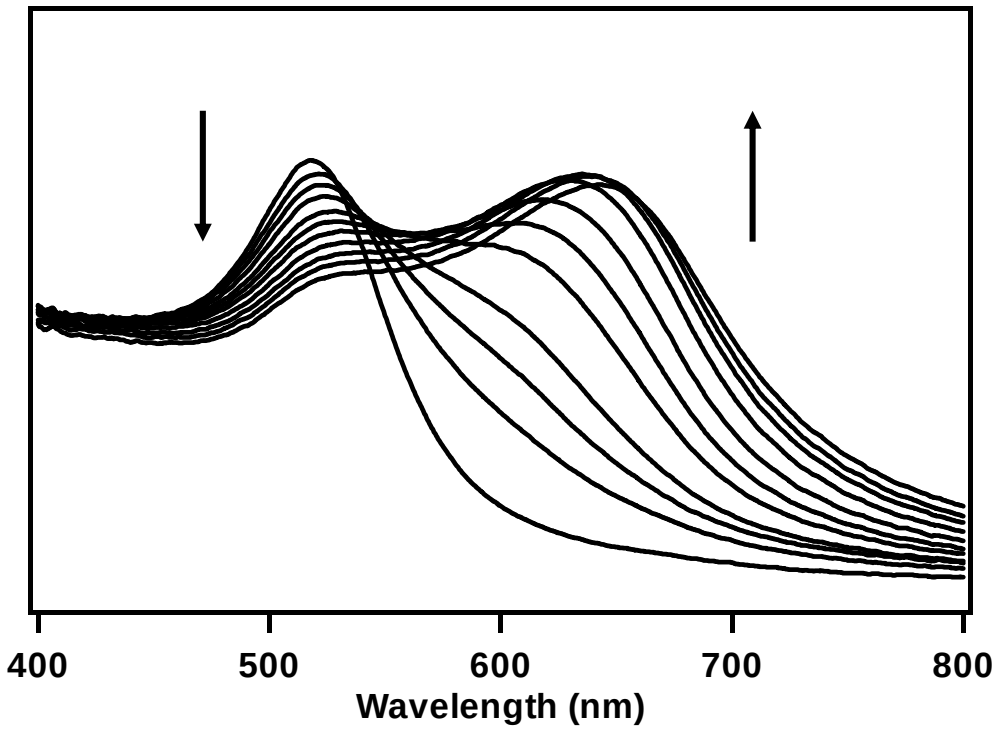

Figure 4-9. TEM image of the 18 nm Au solution after the addition of two drops of a 0.1M AET solution showing the formation of gold assemblies as well as the presence of individual nanoparticles remaining in solution. The image was taken at a magnification of x50k.

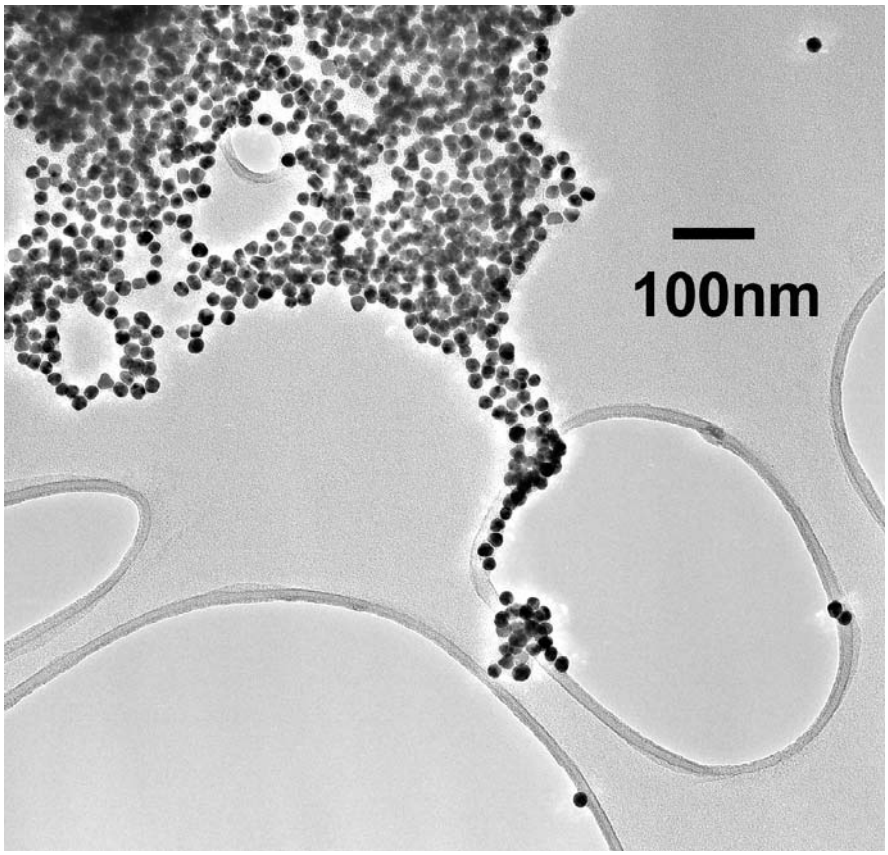

Figure 4-10. TEM image of an 18 nm Au assembly controlled by the addition of AET. A separation distance of 0.6 nm or less can be measured in the assembled gold nanoparticles and, in many cases, the nanoparticles are actually seen to be in contact and beginning to fuse, as indicated by the arrows. The image was taken at a magnification of x300k.

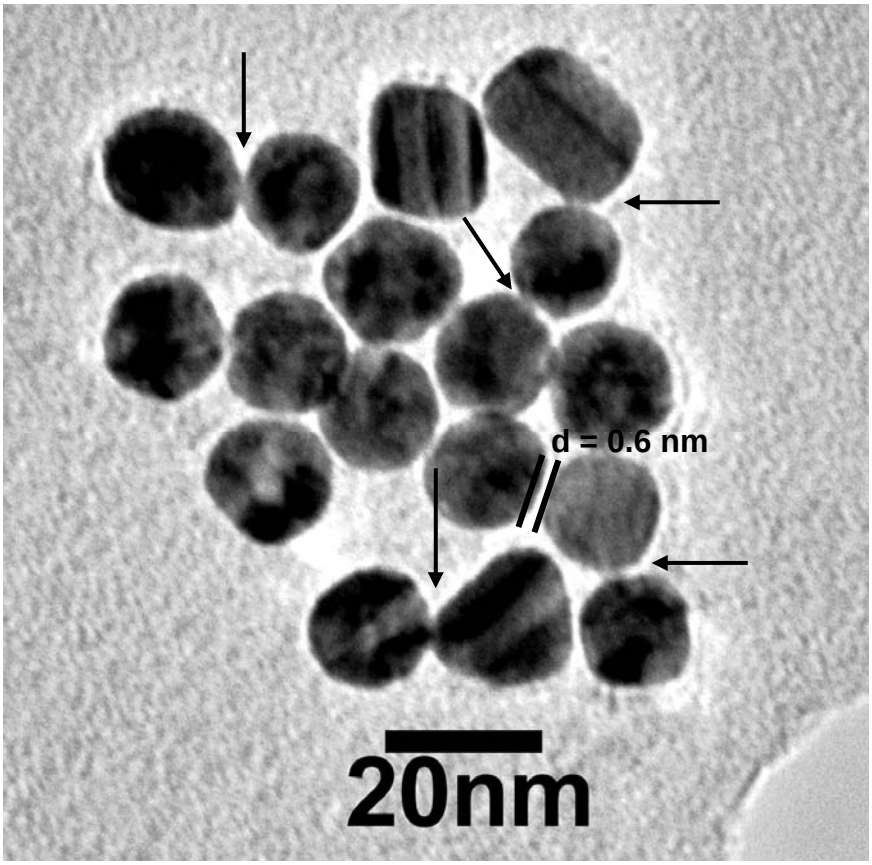

Figure 4-11. TEM image of an 18 nm Au assembly following the addition of excess amounts of AET showing coalescence of the nanoparticles into larger structures. The image was taken at a magnification of x120k.

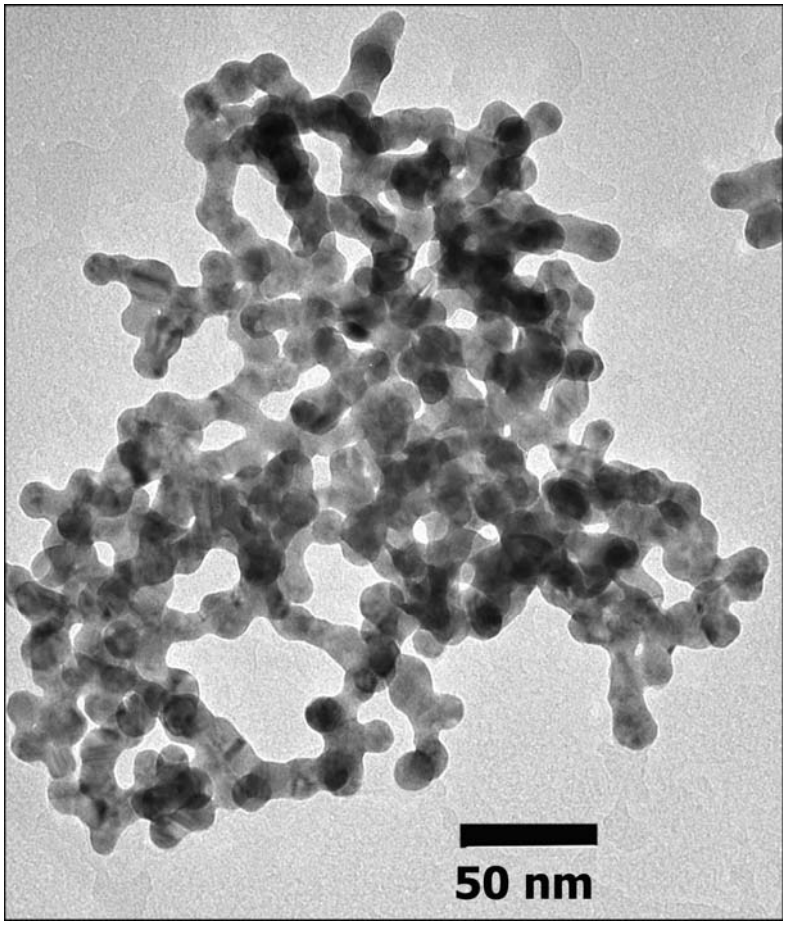

Figure 4-12. UV-vis absorption spectrum of an 18 nm Au solution at room temperature followed by addition of two drops of a 0.1M AET solution and heated to 30, 50 and 75 ^{o}C.

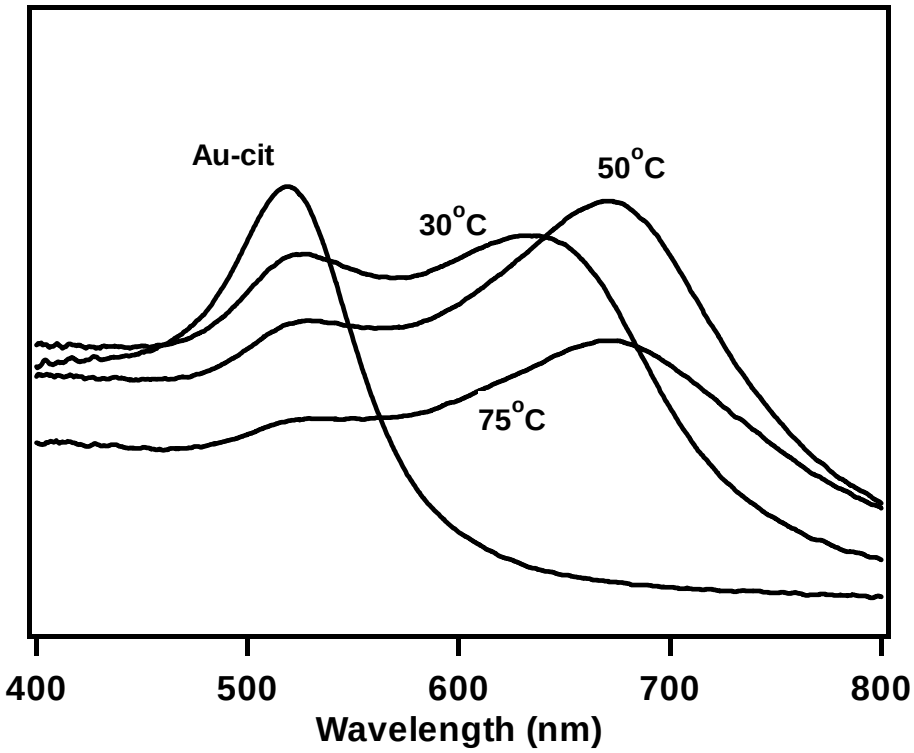

Figure 4-13. UV-vis absorption spectrum of an 18 nm Au solution as a function of heating the sample.

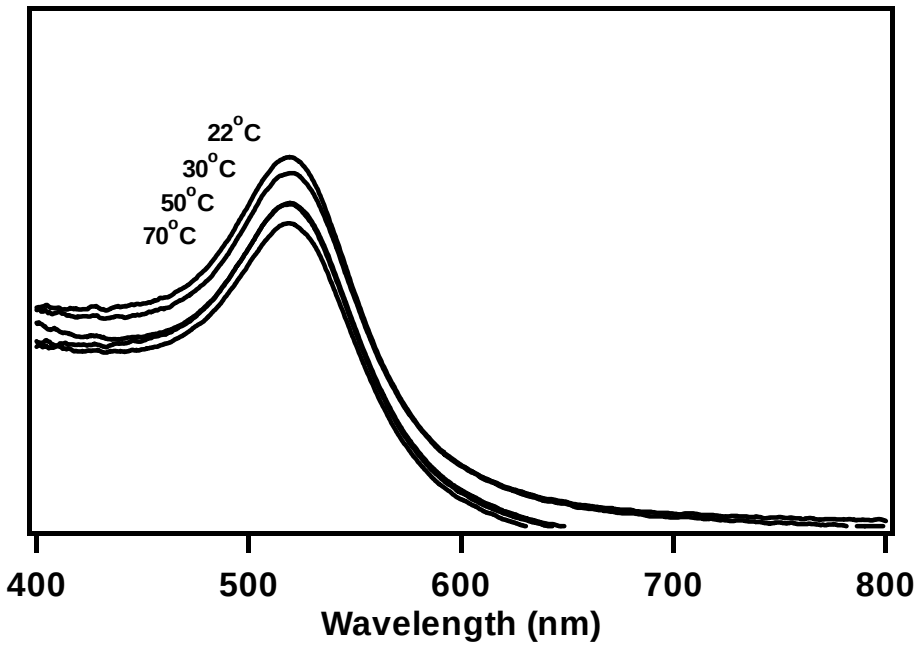

The bifunctional ligand MUAm is expected to produce assemblies with particles separated by ~1.4 nm based on the ligand length. Calculations of the minimum separation distance based on E_{vdW} and E_{steric} calculations predict a closest approach of 0.65 nm when C = 2R + L, and 1.25 nm when C = 2R + 2L. Addition of a 0.05M MUAm solution to the 18 nm Au solution results in the formation of a colored precipitate with a slight blue tint in the solution. Figure 4-14 shows the UV-vis spectrum of an 18 nm Au solution titrated with a solution of MUAm illustrating a gradual shift in the peak location from 520 nm to 607 nm with an initial increase in the absorbance maximum due to an increase in the base line arising from increased reflectivity, followed by a decrease in the intensity as the assembly flocculates out of solution. TEM analysis of the solution after the addition of only two drops of the MUAm solution, shown in Figure 4-15, indicate the formation of gold nanoparticle assemblies with few remaining individual nanoparticles in solution. The gold nanoparticles within the assemblies remain well differentiated from one another and at higher magnification the average separation distance is measured to be 1.2 nm (Figure 4-16). This separation distance indicates contributions from E_{elec}, arising from the amine groups, and E_{steric} contribute to the assembly. A separation distance less than twice the ligand length is due to steric ligand effects arising from the all trans close packing on the gold surface and chain tilting due to E_{vdW}, to offset the loss in energy as observed in the FTIR. This distance is on the order of the onset of quantum mechanical

coupling for the real part of the optical properties.[4] Consistent with this observation, the reflectivity increases and the SPR band shifts to 607 nm, rather than 670 nm typically observed for particle coalescence.

Similar to the temperature dependent shifts in the absorbance band observed in the 18 nm Au and AET reaction, addition of one drop of the MUAm solution followed by heating results in a shift in the absorption peak from 520 nm to 615 nm at 70 ^{o}C along with a decrease in intensity at higher temperatures, as shown in Figure 4-17. The decrease in intensity is due to a combination of flocculation of the product from solution and the temperature dependent peak intensity illustrated in Figure 4-13.

Figure 4-14. UV-vis absorbance spectrum following the drop-wise addition of a 0.05M solution of MUAm to an 18 nm colloidal Au solution. The spectra have not been corrected for changes in concentration.

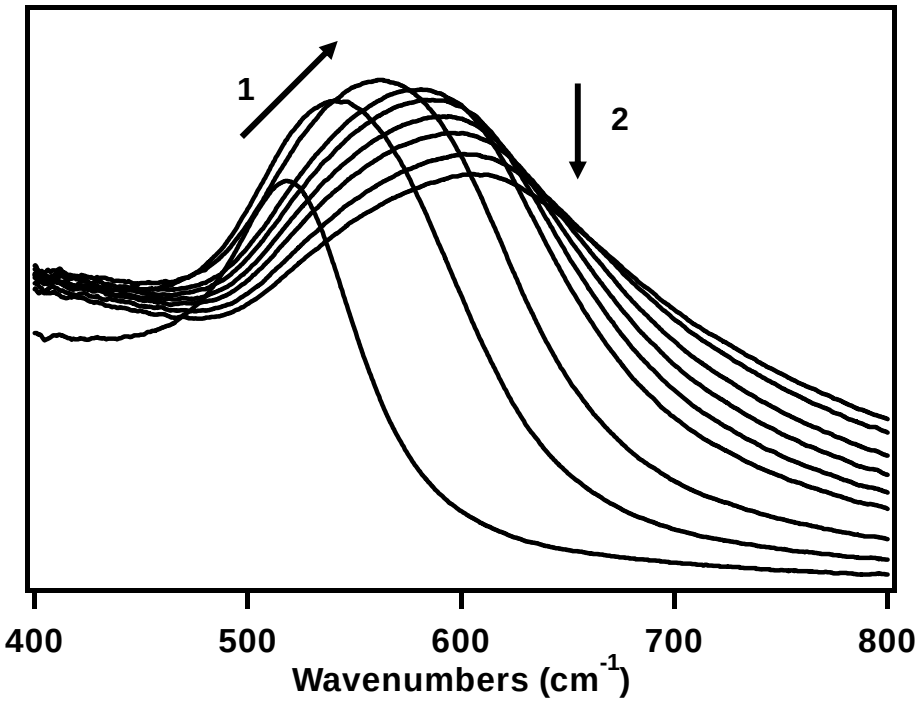

Figure 4-15. TEM image of gold assemblies formed after addition of two drops of a 0.05M solution of MUAM to an 18 nm Au solution. The images were taken at a magnification of x60k.

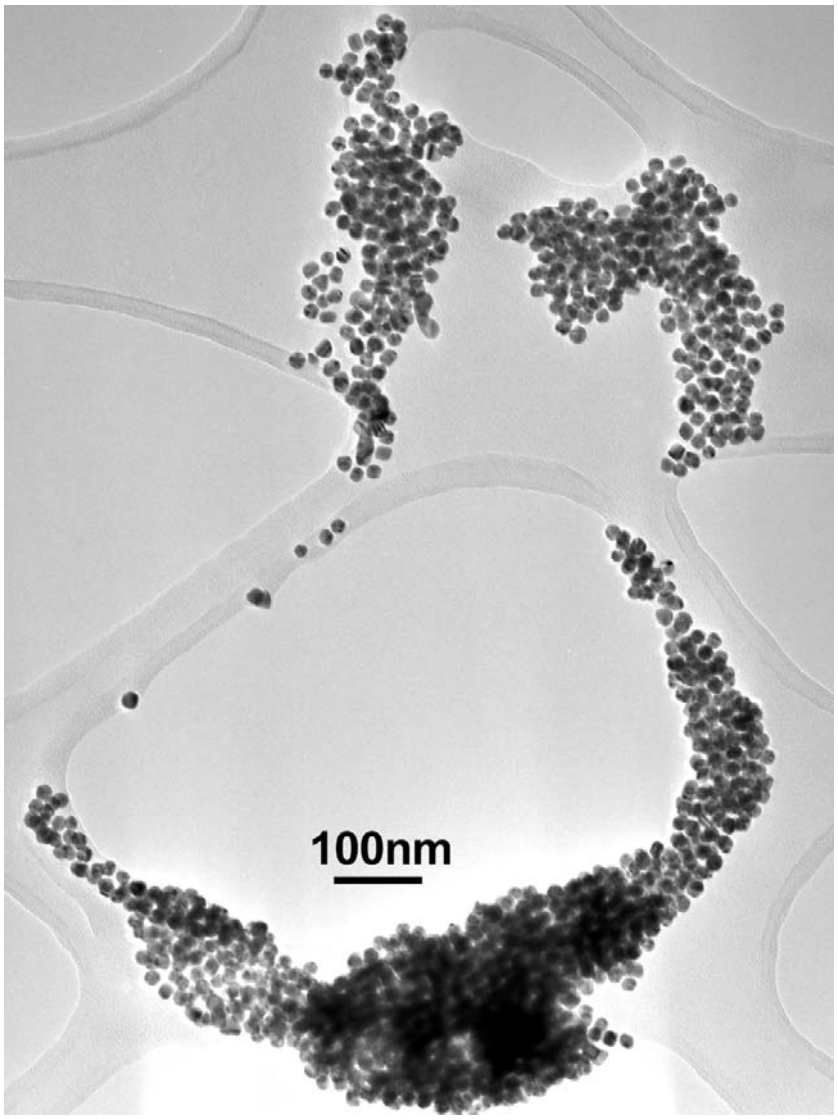

Figure 4-16. TEM image of gold assemblies at higher magnification illustrating an average particle separation distance of 1.2 nm. The images were taken at a magnification of x60k.

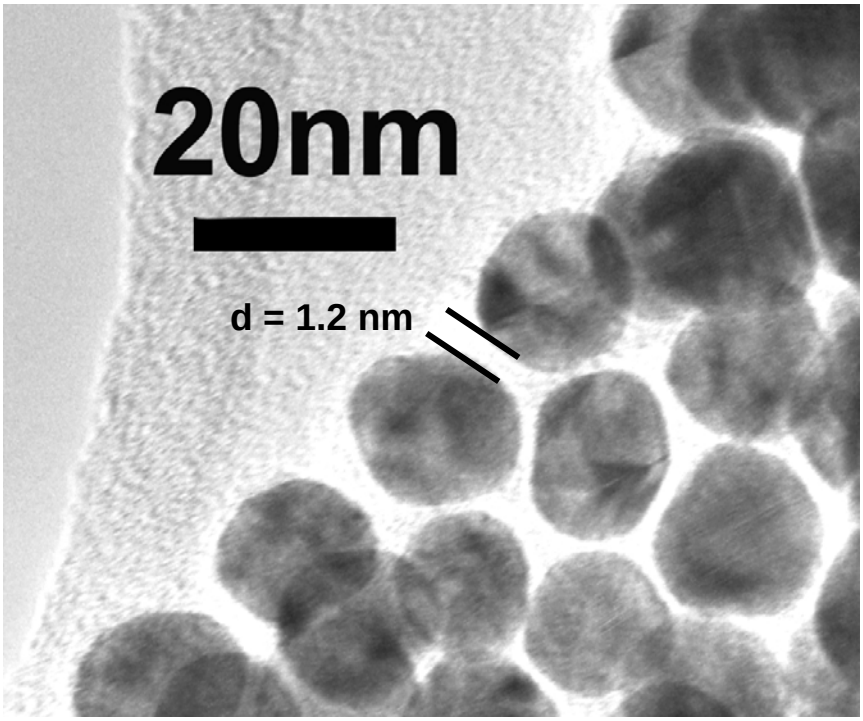

Figure 4-17. UV-vis absorption spectrum of an 18 nm Au solution at room temperature followed by addition of two drops of a 0.05M MUAm solution and heated to 30, 50 and 75 ^{o}C.

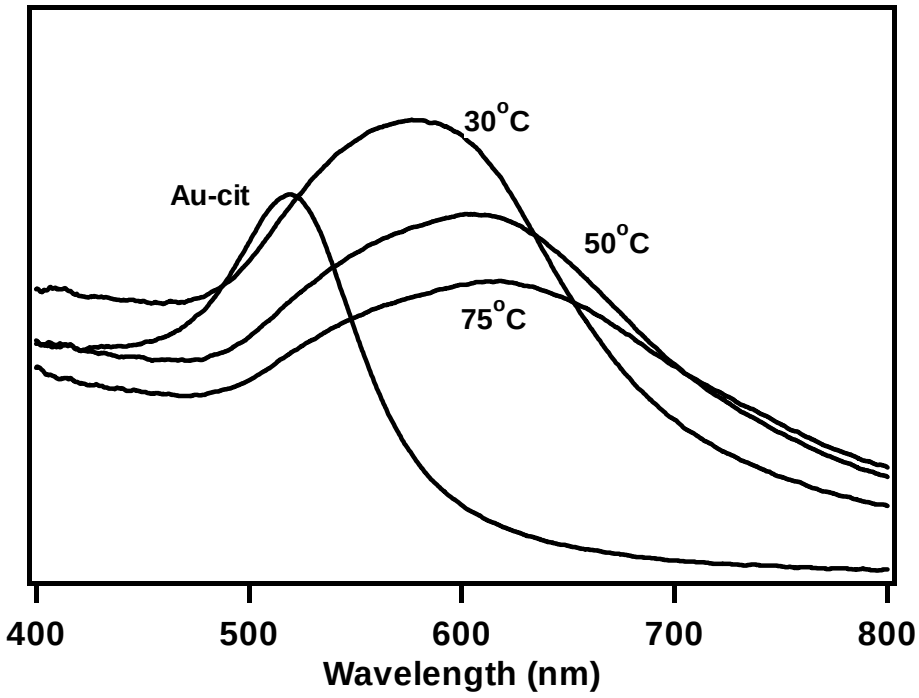

4.3.3.2 6.0 nm Au Assemblies.

Assemblies formed from the reaction of 6.0 nm Au nanoparticles with the bifunctional AET and MUAm ligands do not show as great a change in the absorption spectra as the larger 18 nm Au nanoparticles. Calculations of the minimum separation distances based on E_{vdW} and E_{steric} contributions predict a separation distance of < 0.5 nm in the case of AET and 1.2 nm or 0.55 nm in the case of MUAm when C = 2R + 2L or C = 2R + L, respectively. Drop-wise addition of a 0.1M AET solution to 6 nm Au solution results in a gradual change in the color of the solution from a clear wine red to a purple colored solution. The UV-vis absorption spectrum of the 6 nm Au solution as it is titrated with the AET solution is shown in Figure 4-18. The spectra illustrate a gradual shift in the absorption maximum from 525 nm to 557 nm with a decrease in band intensity as the assembly flocculates out of solution. The shift in the SPR band is indicative of changes in the local dielectric field with weak coupling of the wavefunctions. No evidence for particle coalescence is observed, consistent with the particle distance being greater than the predicted values based on E_{vdW} and E_{steric} contributions.

TEM analysis of the assembly formed after the addition of 1 drop of the AET solution, shown in Figure 4-19, shows large assemblies of non-fused close packed

gold nanoparticles. The average separation distance between nanoparticles, as measured on the fringes of the assembly, indicates a separation distance of 0.8 nm, which is greater than L. This suggests that E_{elec} effects control assembly due to the large steric effects from the ligands. With increased AET concentrations the distances separating the particles becomes shorter and changes in the morphological structure indicative of coalescence of the assemblies can be detected in the TEM, as illustrated in Figure 4-20. It is believed that a collective resonance peak in the absorption spectrum is not exhibited even in the fused nanoparticle assemblies because the agglomeration does not extend over the entire structure. Rather it is more likely that two or three nanoparticles under go surface reconstruction to form larger nanoparticles and not agglomerates.

Addition of a 0.05M MUAm solution to a 6 nm Au solution results in the formation of a precipitate that maintains the wine red color of the solution, even after drying as a thin film on a glass substrate. UV-Vis analysis of the colloidal gold solution as it is titrated with the MUAm solution is illustrated in Figure 4-21, and shows an initial shift in the peak location from 525 nm to 547 nm followed by a broadening of the peak and decrease in intensity as the assembly flocculates out of solution. Consistent with the SPR band indicating little coalescence, the TEM analysis of the assemblies as they form in solution, shown in Figure 4-22, indicate the formation of larger open structures with average separation distances of 1.6 nm between nanoparticles, which is larger than the predicted value and on the

order of partial ligand length dominated structures, consistent with the observation of less significant chain tilting in the FTIR. The shift in the SPR band suggests only weak coupling of the wavefunctions for these assemblies as expected for distances > 1.2 nm.

Figure 4-18. UV-vis absorption spectra of a 6 nm Au solution as it is titrated with a 0.1M AET solution. Many of the spectra have been removed to improve the clarity of the image. The spectra have not been corrected for changes in concentration.

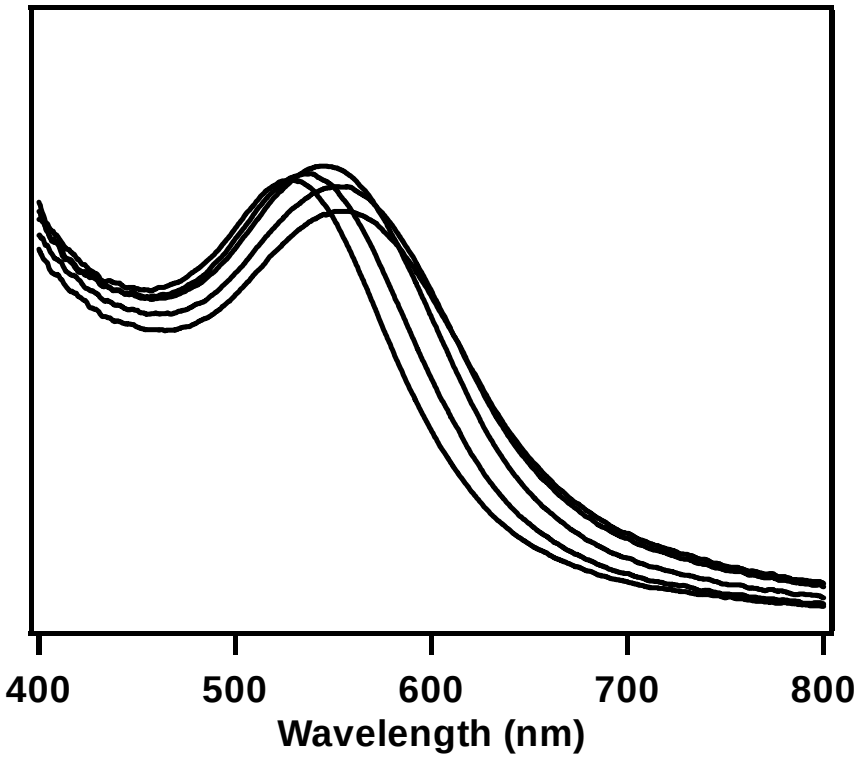

Figure 4-19. TEM analysis of the assembly formed after the addition of 1 drop of a 0.1M AET solution to a 6 nm Au solution. The image was taken at a magnification of x210k.

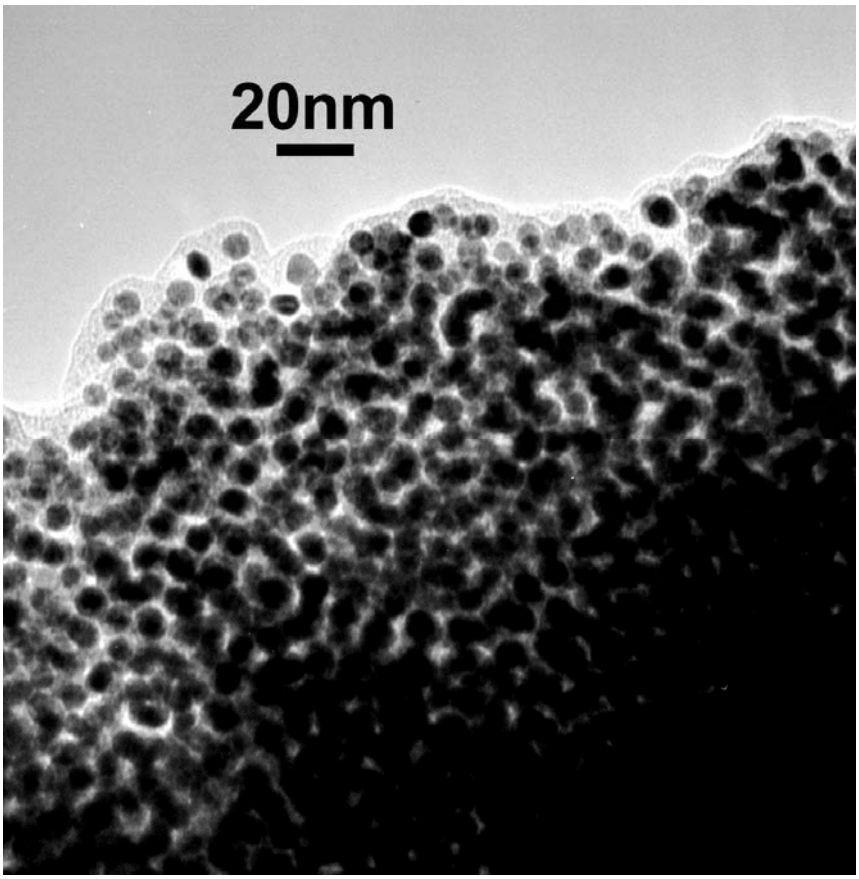

Figure 4-20. TEM image of a 6 nm Au assembly following addition of higher concentrations of the 0.1M AET solution showing particle coalescence (a). The image was taken at a magnification of x300k.

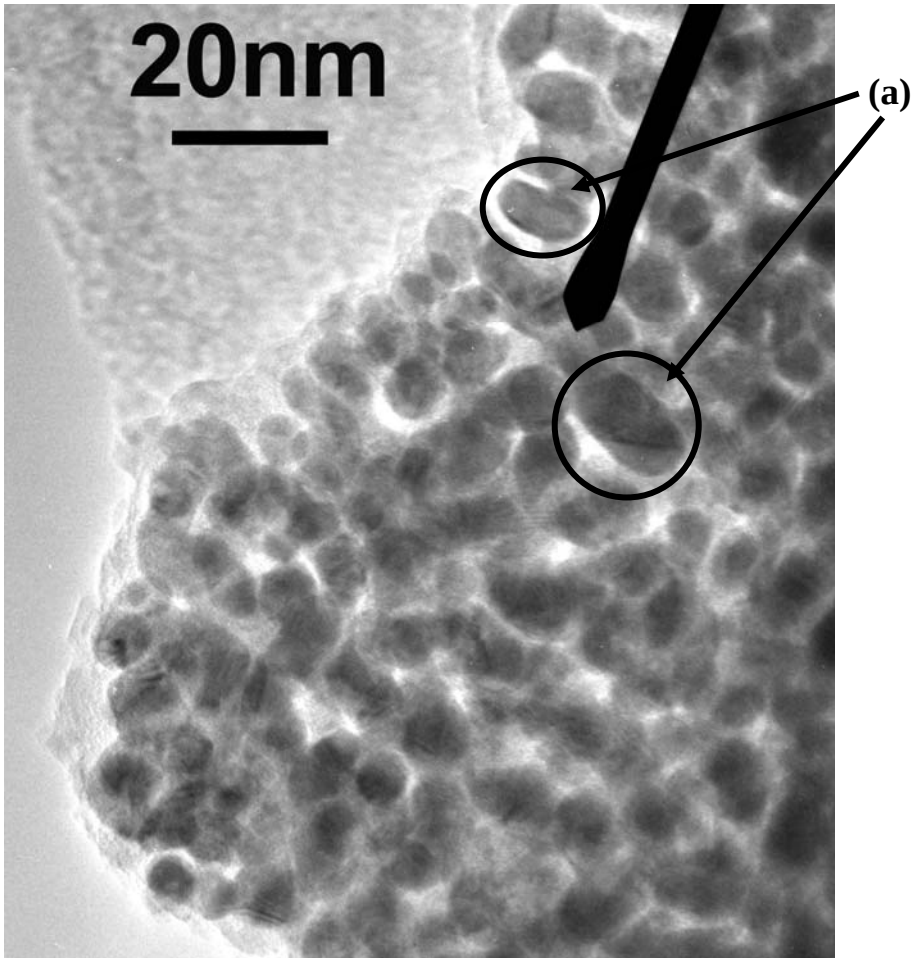

Figure 4-21. UV-vis absorbance spectrum following the drop-wise addition of a 0.05M solution of MUAm to a 6 nm colloidal Au solution. Many of the spectra have been omitted for clarity. The spectra have not been corrected for changes in concentration.

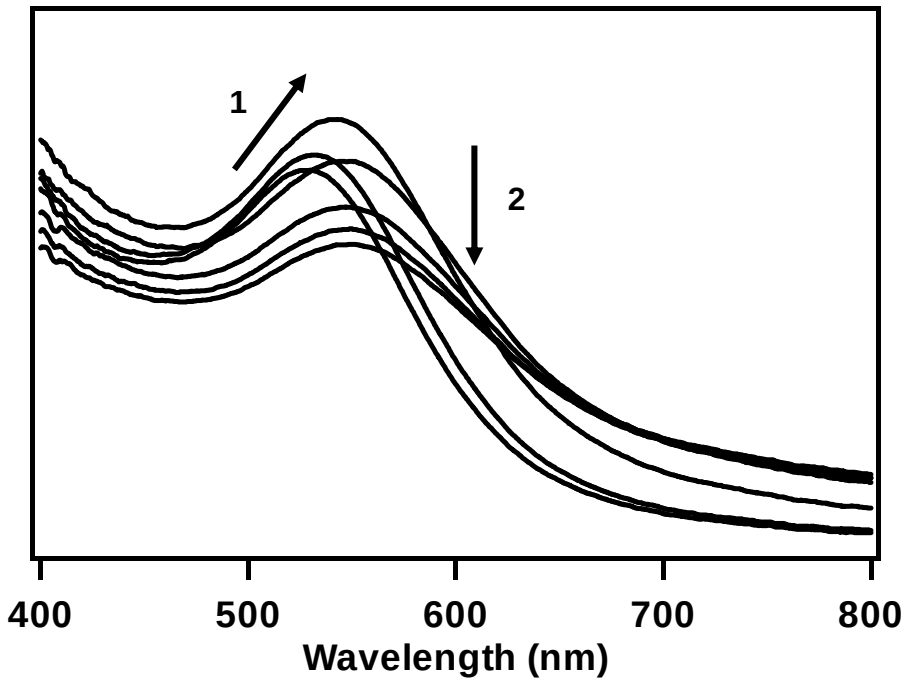

Figure 4-22. TEM image of gold assemblies formed from the addition of two drops of a 0.05M solution of MUAM to a 6 nm Au solution. The images were taken at a magnification of x170k.

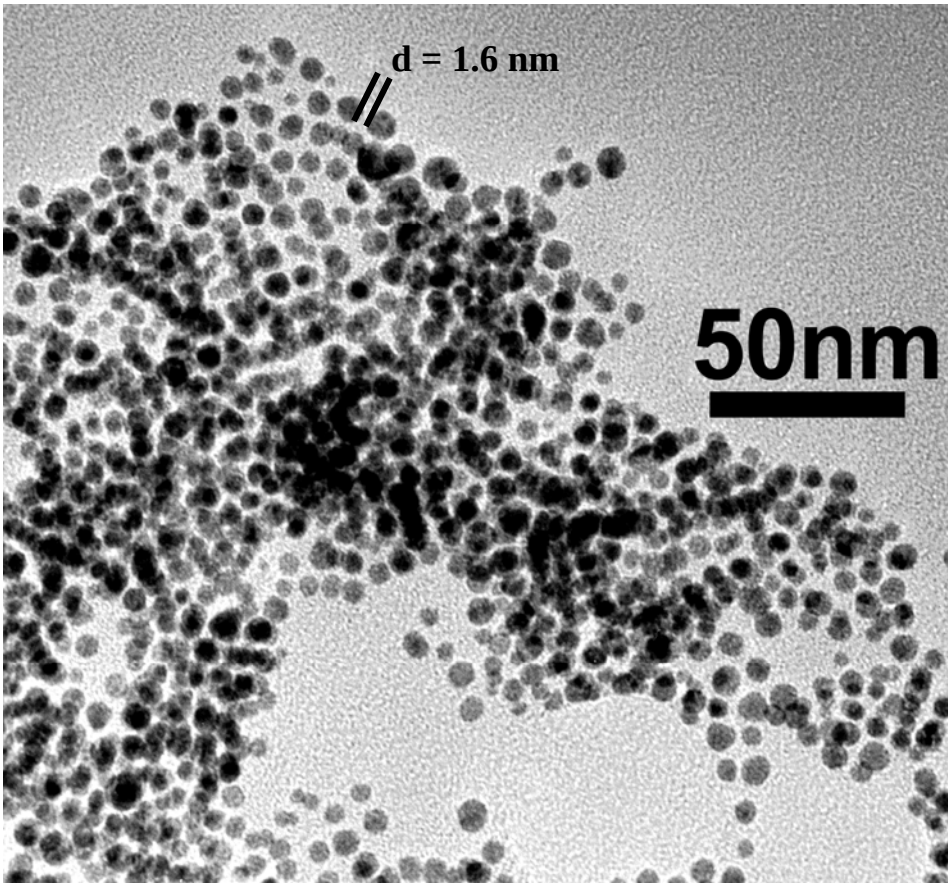

4.3.3.3 3 nm Au Assemblies.

Calculations of the minimum separation distance of 3 nm Au particles in these assemblies, based on E_{steric} and E_{vdW} equations, predicts a separation distance of <0.1 nm for AET-directed assemblies and 1.8 nm for MUAm-directed assemblies. Addition of either the 0.1M AET or the 0.05M MUAm solutions to the 3 nm Au solution results in the solution becoming opalescent. Since the size of the nanoparticles are too small to exhibit a SPR band, as illustrated in Figure 4-23, no change in the optical properties can be measured using UV-vis spectroscopy. TEM analysis of the collected precipitates at low magnification indicate the formation of large nanoparticle assemblies, yet the small nature of the nanoparticles makes them easily damaged by the electron beam and under higher magnification the assemblies can be seen to "melt" with subsequent formation of larger monolithic structures. The effect is more pronounced for the assemblies formed by reaction with AET than for assemblies formed with MUAm. This is attributed to the longer MUAm chain length serving to keep the small nanoparticles further apart. This phenomenon is illustrated in Figures 4-24, 4-25, and 4-26 showing TEM images of 3.0 nm Au, 3.0 nm Au assembled with AET taken at x17k magnification, and the same 3.0 nm Au/AET assembly taken at x85k magnification.

Figure 4-23. UV-vis absorption spectrum of a 3.0 nm Au solution exhibiting no SPR band.

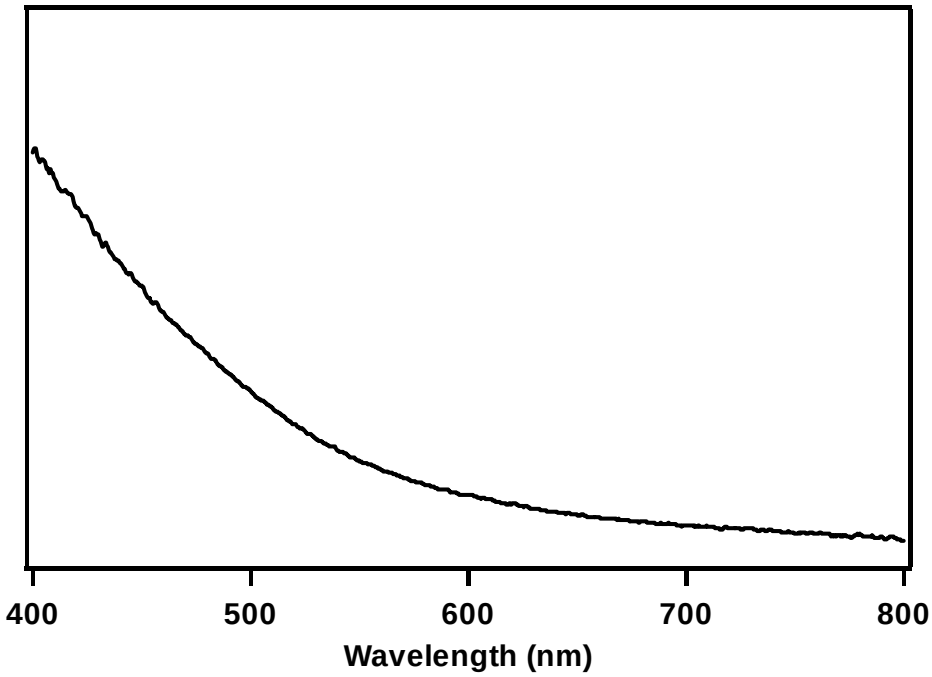

Figure 4-24. TEM images of 3.0 nm Au taken at a magnification of x500k.

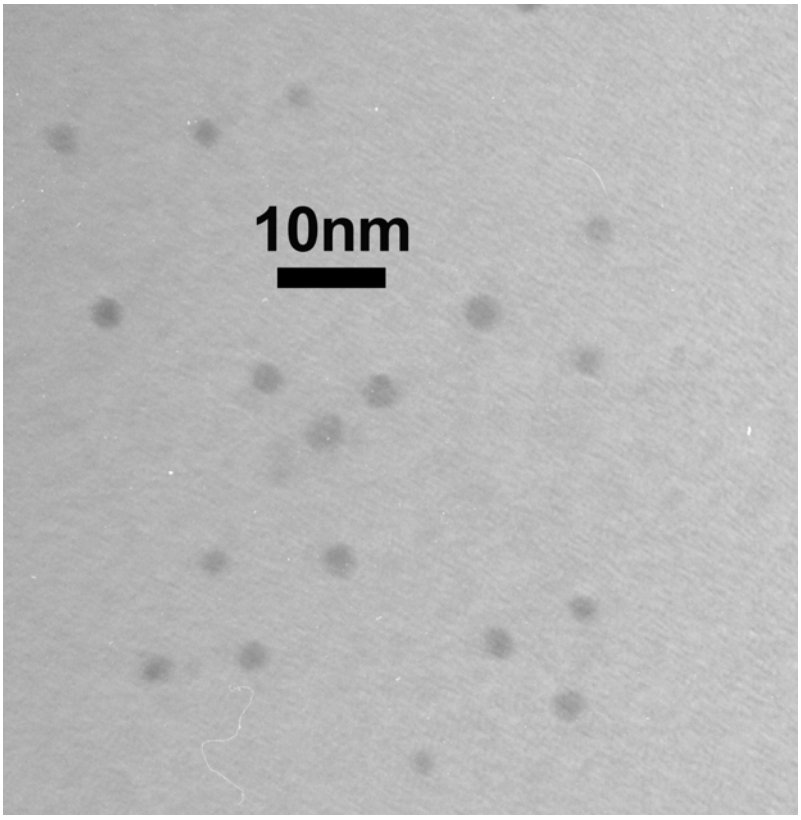

Figure 4-25. TEM image of 3.0 nm Au assembled with AET taken at x17k magnification illustrating the formation of large 3.0 nm Au assemblies.

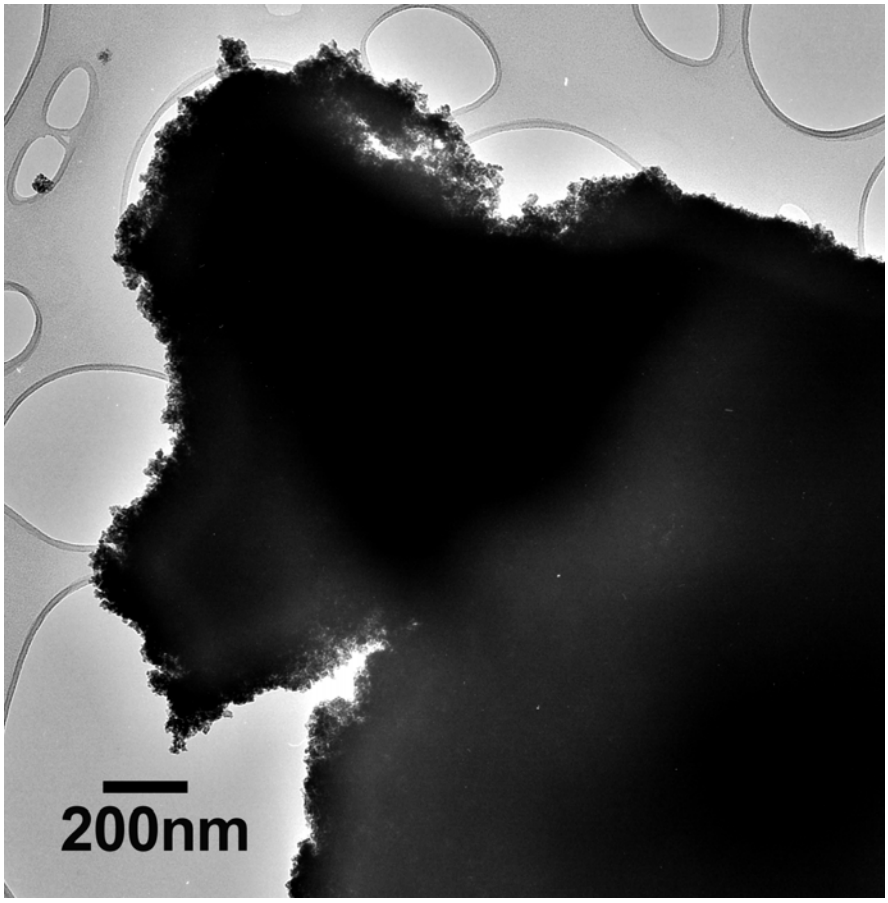

Figure 4-26. TEM image of 3.0 nm Au assembled with AET taken at x85k magnification illustrating the melting of the gold nanoparticles to form larger structures.

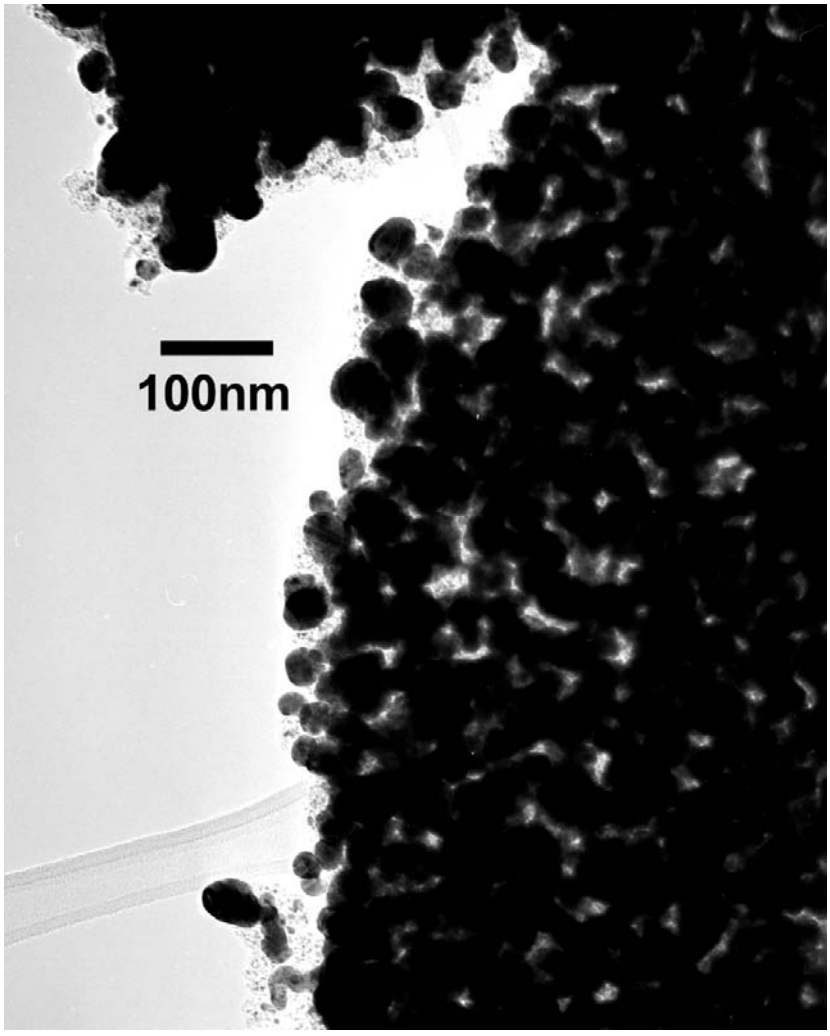

Figure 4-27. Plot of the shift in the SPR band as a function of D/2R.

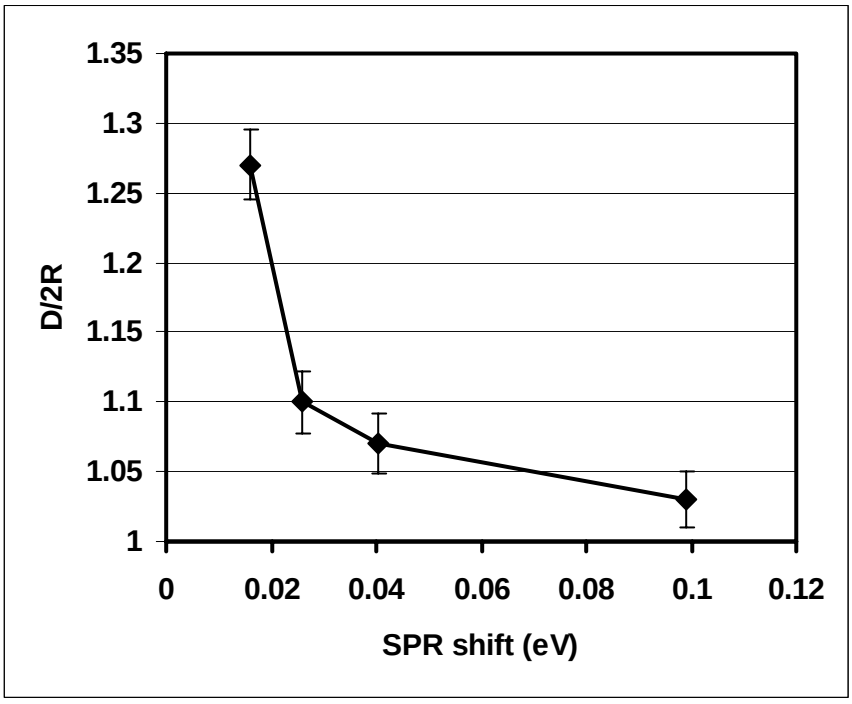

4.3.4 Summary

As illustrated by the interparticle interaction potential ($E_{vdW} + E_{steric}$) calculations for gold assemblies, with increasing particle size the separation distance between particles decreases due to greater E_{vdW} effects. What is initially observed is the expected particle separation distance for hetero-functional ligands with E_{elec} and E_{steric} effects dominating assembly formation ($C = 2R + 2L$) due to purely electrostatic interactions of the amine head groups and chain packing. What is eventually observed is a decrease of the particle separation distance as the covalent energy term leads to binding of the amine functionality to the particle surface ($C = 2R + L$) followed by particle coalescence ($C < 2R + L$) due to greater E_{vdW} effects as the particles come into closer proximity.

The analysis of the nanoparticle assemblies by TEM and the FTIR supports the belief that with decreasing nanoparticle size the Van der Waals effects are minimized and assembly is controlled by steric effects. In the TEM images, the particle separation distance of the larger gold assemblies is considerably smaller than that for the smaller gold assemblies of the same ligand length. In the IR, the greater crystalline nature of the carbon chains in the smaller gold nanoparticle assemblies is evidenced by the intense asymmetrical and symmetrical methylene stretching bands at 2918 and 2848 cm^{-1}, and the observance of single peaks at

1460 and 720 cm^{-1}, assigned to the methylene scissoring and rocking modes, indicating hexagonal packing of the chains.

UV-vis analysis of the assemblies as they form in solution exhibit a shift of the SPR to lower energies, which is attributed to the onset of collective interactions of the particles due to an overlap of the wavefunctions. This effect has been shown to be dependent upon the particle size and separation distance and can be characterized by the parameter D/2R, where D is the separation distance and R is the particle radius. Figure 4-27 illustrates the shift in the SPR band as a function of D/2R indicating an increase in the SPR band shift with decreasing D/2R. A deviation from the quasi-linear relationship is observed when the value of D/2R is greater than 1.2. This is consistent with similar shifts in the SPR band for compressed films of silver particles observed by Heath et al.[4] As the separation distance between nanoparticles was decreased, a red shift in the SPR band is observed for values of D/2R greater than 1.2. Below 1.2 the trend is reversed suggesting electron delocalization over several particles due to wave function overlap.

4.4 Conclusion.

In this chapter it has been demonstrated that the thermodynamic forces controlling the assembly of metal nanoparticles can be controlled by judicious choice of particle size and hetero-functional ligand length. Gold superstructures composed

of nanoparticles with 3.0, 6.0, and 18.0 nm diameters assembled with hetero-functional ligands 0.4 and 1.4 nm in length were analyzed by TEM, UV-vis, and FTIR analysis. As the particle size increases the contributions from E_{vdW} dominates control over assembly resulting in chain tilting of the ligands on the particle surface and eventually leading to irreversible particle coalescence. At smaller sizes a competition between E_{elec} and E_{steric} dominate assembly as illustrated by the crystalline nature of the ligand chains by FTIR analysis.

4.5 References.

1) Heath, J. R.; Shiang, J. J. *Chemical Society Reviews* **1998**, *27*, 65-71.

2) Shiang, J. J.; Heath, J. R.; Collier, C. P.; Saykally, R. J. *Journal of Physical Chemistry B* **1998**, *102*, 3425-3430.

3) Heath, J. R.; Knobler, C. M.; Leff, D. V. *Journal of Physical Chemistry B* **1997**, *101*, 189-197.

4) Collier, C. P.; Saykally, R. J.; Shiang, J. J.; Henrichs, S. E.; Heath, J. R. *Science* **1997**, *277*, 1978-1981.

5) Markovich, G.; Collier, C. P.; Henrichs, S. E.; Remacle, F.; Levine, R. D.; Heath, J. R. *Accounts of Chemical Research* **1999**, *32*, 415-423.

6) Freeman, R. G.; Hommer, M. B.; Grabar, K. C.; Jackson, M. A.; Natan, M. J. *Journal of Physical Chemistry* **1996**, *100*, 718-724.

7) Voisin, C.; Christofilos, D.; Fatti, N. D.; Vallee, F.; Prevel, B.; Cottancin, E.; Lerme, J.; Pellarin, M.; Broyer, M. *Physical Review Letters* **2000**, *85*, 2200-2203.

8) McConnell, W. P.; Novak, J. P.; Brousseau, L. C.; Fuierer, R. R.; Tenent, R. C.; Feldheim, D. L. *Journal of Physical Chemistry B* **2000**, *104*, 8925-8930.

9) Terrill, R. H.; Postlethwaite, T. A.; Chen, C. H.; Poon, C. D.; Terzis, A.; Chen, A. D.; Hutchison, J. E.; Clark, M. R.; Wignall, G.; Londono, J. D.; Superfine, R.; Falvo, M.; Johnson, C. S.; Samulski, E. T.; Murray, R. W. *Journal of the American Chemical Society* **1995**, *117*, 12537-12548.

10) Fishelson, N.; Shkrob, I.; Lev, O.; Gun, J.; Modestov, A. D. *Langmuir* **2001**, *17*, 403-412.

11) Hicks, J. F.; Zamborini, F. P.; Osisek, A.; Murray, R. W. *Journal of the American Chemical Society* **2001**, *123*, 7048-7053.

12) Wuelfing, W. P.; Green, S. J.; Pietron, J. J.; Cliffel, D. E.; Murray, R. W. *Journal of the American Chemical Society* **2000**, *122*, 11465-11472.

13) Sarathy, K. V.; Thomas, P. J.; Kulkarni, G. U.; Rao, C. N. R. *Journal of Physical Chemistry B* **1999**, *103*, 399-401.

14) Musick, M. D.; Pena, D. J.; Botsko, S. L.; McEvoy, T. M.; Richardson, J. N.; Natan, M. J. *Langmuir* **1999**, *15*, 844-850.

15) Ahmadi, T. S.; Wang, Z. L.; Green, T. C.; Henglein, A.; El-Sayed, M. A. *Science* **1996**, *272*, 1924-1926.

16) Bharathi, S.; Fishelson, N.; Lev, O. *Langmuir* **1999**, *15*, 1929-1937.

17) Henglein, A.; Giersig, M. *Journal of Physical Chemistry B* **1999**, *103*, 9533-9539.

18) Leff, D. V.; Brandt, L.; Heath, J. R. *Langmuir* **1996**, *12*, 4723-4730.

19) Muhlpfordt, H. *Experientia* **1982**, *38*, 1127-1128.

20) Slot, J. W., Geuze, H. J. *European Journal of Cell Biology* **1985**, *38*, 87-93.

21) Sun, S. H.; Murray, C. B. *Journal of Applied Physics* **1999**, *85*, 4325-4330.

22) Warner, M. G.; Reed, S. M.; Hutchison, J. E. *Chemistry of Materials* **2000**, *12*, 3316-3320.

23) Yee, C. K.; Jordan, R.; Ulman, A.; White, H.; King, A.; Rafailovich, M.; Sokolov, J. *Langmuir* **1999**, *15*, 3486-3491.

24) Murthy, S.; Bigioni, T. P.; Wang, Z. L.; Khoury, J. T.; Whetten, R. L. *Materials Letters* **1997**, *30*, 321-325.

25) Brust, M.; Walker, M.; Bethell, D.; Schiffrin, D. J.; Whyman, R. *Journal of the Chemical Society-Chemical Communications* **1994**, 801-802.

26) Connolly, S.; Fitzmaurice, D. *Advanced Materials* **1999**, *11*, 1202-1205.

27) Badia, A.; Cuccia, L.; Demers, L.; Morin, F.; Lennox, R. B. *Journal of the American Chemical Society* **1997**, *119*, 2682-2692.

28) Harfenist, S. A.; Wang, Z. L.; Whetten, R. L.; Vezmar, I.; Alvarez, M. M. *Advanced Materials* **1997**, *9*, 817.

29) Lin, X. M.; Sorensen, C. M.; Klabunde, K. J. *Chemistry of Materials* **1999**, *11*, 198-202.

30) Martin, J. E.; Wilcoxon, J. P.; Odinek, J.; Provencio, P. *Journal of Physical Chemistry B* **2000**, *104*, 9475-9486.

31) Mulvaney, P. *Langmuir* **1996**, *12*, 788-800.

32) Link, S.; El-Sayed, M. A. *Journal of Physical Chemistry B* **1999**, *103*, 4212-4217.

33) Link, S.; El-Sayed, M. A. *Journal of Physical Chemistry B* **1999**, *103*, 8410-8426.

34) Alvarez, M. M.; Khoury, J. T.; Schaaff, T. G.; Shafigullin, M. N.; Vezmar, I.; Whetten, R. L. *Journal of Physical Chemistry B* **1997**, *101*, 3706-3712.

35) Wilcoxon, J. P.; Williamson, R. L.; Baughman, R. *Journal of Chemical Physics* **1993**, *98*, 9933-9950.

36) Lyon, L. A.; Musick, M. D.; Smith, P. C.; Reiss, B. D.; Pena, D. J.; Natan, M. J. *Sensors and Actuators B-Chemical* **1999**, *54*, 118-124.

37) Brust, M.; Bethell, D.; Kiely, C. J.; Schiffrin, D. J. *Langmuir* **1998**, *14*, 5425-5429.

38) Quinten, M.; Kreibig, U. *Surface Science* **1986**, *172*, 557-577.

39) Ulman, A.; Eilers, J. E.; Tillman, N. *Langmuir* **1989**, *5*, 1147-1152.

40) Korgel, B. A.; Fullam, S.; Connolly, S.; Fitzmaurice, D. *Journal of Physical Chemistry B* **1998**, *102*, 8379-8388.

41) Doty, R. C.; Yu, H.; Shih, C. K.; Korgel, B. A. *Journal of Physical Chemistry B* **2001**, *105*, 8291-8296.

42) Lewis, L. J.; Jensen, P.; Barrat, J. L. *Physical Review B-Condensed Matter* **1997**, *56*, 2248-2257.

43) Yu, X.; Duxbury, P. M. *Physical Review B-Condensed Matter* **1995**, *52*, 2102-2106.

44) Zhu, H. L.; Averback, R. S. *Philosophical Magazine Letters* **1996**, *73*, 27-33.

45) Tranquada, J. M.; Buttrey, D. J.; Sachan, V.; Lorenzo, J. E. *Physical Review Letters* **1994**, *73*, 1003-1006.

46) Tranquada, J. M.; Sternlieb, B. J.; Axe, J. D.; Nakamura, Y.; Uchida, S. *Nature* **1995**, *375*, 561-563.

47) Hicks, J. F.; Templeton, A. C.; Chen, S. W.; Sheran, K. M.; Jasti, R.; Murray, R. W.; Debord, J.; Schaaf, T. G.; Whetten, R. L. *Analytical Chemistry* **1999**, *71*, 3703-3711.

48) Cumberland, S. L.; Strouse, G. F. *submitted to Langmuir* **2001**.

49) Brongersma, M. L.; Hartman, J. W.; Atwater, H. A. *Physical Review B* **2000**, *62*, R16356-R16359.

50) Kreibig, U.; Vollmer, M. *Optical properties of metal clusters*; Springer: Berlin ; New York, 1995.

51) Nolte, D. D. *Journal of Applied Physics* **1994**, *76*, 3740-3745.

52) Baschong, W.; Lucocq, J. M.; Roth, J. *Histochemistry* **1985**, *83*, 409-411.

53) Turkevich, J.; Stevenson, P. S.; Hillier, J. *Journal of Physical Chemistry* **1951**, 58.

54) Tien, J.; Terfort, A.; Whitesides, G. M. *Langmuir* **1997**, *13*, 5349-5355.

55) Silverstein, R. M.; Bassler, G. C.; Morrill, T. C. *Spectrometric identification of organic compounds*; 5th ed.; Wiley: New York, 1991.

56) Xia, Y. N.; Zhao, X. M.; Whitesides, G. M. *Microelectronic Engineering* **1996**, *32*, 255-268.

57) Bardotti, L.; Jensen, P.; Hoareau, A.; Treilleux, M.; Cabaud, B. *Physical Review Letters* **1995**, *74*, 4694-4697.

58) Templeton, A. C.; Hostetler, M. J.; Kraft, C. T.; Murray, R. W. *Journal of the American Chemical Society* **1998**, *120*, 1906-1911.

59) Meulenberg, R. W.; Strouse, G. F. *Journal of Physical Chemistry B* **2001**, *105*, 7438-7445.

60) Hostetler, M. J.; Stokes, J. J.; Murray, R. W. *Langmuir* **1996**, *12*, 3604-3612.

61) Corcoran, S. G.; Colton, R. J.; Lilleodden, E. T.; Gerberich, W. W. *Physical Review B-Condensed Matter* **1997**, *55*, 16057-16060.

62) Hodak, J. H.; Martini, I.; Hartland, G. V. *Journal of Physical Chemistry B* **1998**, *102*, 6958-6967.

63) Hartland, G. V.; Hodak, J. H.; Martini, I. *Physical Review Letters* **1999**, *82*, 3188.

Chapter 5

Au-CdSe Nano-Composites

5.1 Introduction

Recent synthetic developments allow materials below 100nm in size to be readily prepared as surface passivated, near monodisperse metal and semiconductor nanomaterials, whose physical and chemical properties can be systematically tuned by controlling size and surface passivation.[1-14] Non-lithographic assembly strategies using evaporative self-assembly or Langmuir-Blodgett methods allow for the formation of closely packed structures with homogenous materials, however, well-packed structures of mixed nanomaterials are rarely observed due to a propensity for phase segregation in composite nanomaterial assemblies.[15-19] The most significant contributor to phase segregation in composites is the difference in the polarizability of the nanomaterial, which is reflected in the magnitude of the Hamaker constant (A) for the material in the Van der Waals energy term (E_{VdW}) illustrated in eqn 4.[19-22] The influence of E_{VdW} on phase segregation has been observed for alloy composite structures of gold and silver nanoparticles evaporatively self-assembled from intimately mixed toluene

solutions.[15] In the gold/silver nanocomposite, in which the Hamaker constant for the two nanoparticles differ by a small amount (3.12×10^{-19} J for silver verses 1.0×10^{-19}J for gold[20,23]) only random alloy structures have been observed.

Overcoming the limitation of soft-sphere packing in nanomaterial composites can be achieved by inclusion of a ligand coordination event (templating) to compete with the E_{VdW} repulsion terms (eqn 5). E_{cov} represents the covalent interaction between the terminal functional group on a passivating ligand and the ligand-surface binding energy on a second nanomaterial.

$$E_{total} \sim E_{VdW} + E_{steric} + E_{cov} \qquad (5)$$

This term acts to improve the stability of the assembly allowing shorter particle separation distances (C) to be achieved in a composite, without the penalty of phase segregation arising from E_{vdw}. Since the gold colloids in these experiment are not surface stabilized by ligands containing charged functional groups, the E_{elec} term can be considered negligible and eliminated from the overall equation of the forces controlling assembly. If eqn 1 can be manipulated so that E_{cov} is stronger than E_{VdW} and E_{steric}, the assembly should be controlled by the binding interactions of the functional groups rather than the VdW or steric interaction potentials.

In analogy to recent efforts on self-assembled monolayers (SAM), surface group exchange with a ligand possessing a terminal functionality allows incorporation of surface charges or ligands capable of specific chemical interactions on a nanomaterial surface.[11,24-27] By judicious choice of the ligand, a systematic approach for assembly of individual nano-materials into nano-engineered composites can be derived, where the inter-dot connectivity can be both templated and modulated by the surface groups. These 3-dimensional superstructures composed of individual nano-materials hold promise for applications ranging from electronics, to catalysis, to non-linear opto-electronics.[9,10,18,20,28-36]

Reported here is the formation of a macroscopic, 3-dimensional self-supporting composite assembled from individual gold and CdSe nanomaterials. The structures can be described as flexible networks producing a non-statistical, glassy composite composed of a regular 1:6 Au:CdSe composition. The mechanism for the formation of the assembly is pH controlled via acid/base equilibria due to a proton exchange between the $R\text{-}NH_3^+$ group of 2-aminoethanethiol passivated CdSe and the $R\text{-}COO^-$ group of the citrate ions passivating the Au surface. Analysis of SAED (selected area electron diffraction) patterns in the TEM indicates the free standing composite exhibits a surprising degree of short-range ordering in the material.

This suggests these “flexible” composite materials may provide a paradigm for the design of electronic networks based on self-assembling lattices using the competition of VdW, steric, and covalent interactions to drive nano-structural motifs.

5.2 Experimental

5.2.1 Optical Measurements.

FT-IR analysis was conducted using pressed KBr pellets on a Perkin-Elmer Spectrum GX FT-IR between 370 – 7000 cm^{-1} with a resolution of 4 cm^{-1}. UV/Vis spectra were recorded using an Ocean Optics S2000 CCD spectrometer (resolution 0.1 nm). Atomic Absorption measurements of the composites were performed on a modified Varian Techtron flame atomic absorption instrument with the absorbance of gold taken at 267.6 nm and the absorbance of cadmium taken at 326.1 nm using an oxy-acetylene flame. A lock-in amplifier/PMT was coupled to the instrument to improve signal to noise.

Emission measurements were performed on a CCD based instrument utilizing the 458.0 nm Ar^{+} ion laser line for excitation (power < 2 mW) and dispersion on a 0.5M spectrometer. Laser line rejection was accomplished by use of a holographic notch filter.

5.2.2 Electron Microscopy.

TEM analysis was obtained on a JEOL 2010 or JEOL 2000 microscope operated at 200 kV in bright field mode using 400 mesh Ni or Cu grids coated with a ~5nm layer of holey carbon (SPI). Energy dispersive x-ray analysis (EDX) was performed on the JEOL 2000 instrument with an Oxford attachment and Inca software. SAED analysis in the TEM was achieved at a magnification of 50K with a camera length of 83.0 cm. SEM images were obtained using a JEOL 6300 FE-SEM instrument with EDS & CL capabilities. Elemental mapping in the SEM was accomplished using a LYNX collector with Inca software from Oxford instruments.

5.3 Synthesis.

5.3.1 Materials.

Au nanoparticles were prepared following a method developed by Mühlpfordt, as outlined in Chapter 2, using tannic acid as an additional reductant of auric acid in the presence of a sodium citrate buffer in an aqueous media producing gold nanoparticles with a 15% size distribution (Au-TA).[5] Figure 5-1 shows a TEM image of the gold colloids as prepared in solution. The images were obtained by setting a drop of the colloidal gold solution onto the TEM grid for ~1 minute then wicking away the solution and drying the grid under vacuum.

CdSe nanocrystals (5-6% distribution) capped with hexadecylamine (CdSe-HDA) were prepared by modification of a single source lyothermal technique, as outlined in Chapter 2.[3] Figure 5-2 shows a TEM image of a self-assembled monolayer of 6.0 nm CdSe-HDA evaporated on a TEM grid from a toluene solution. Size, size dispersity, and crystallinity of CdSe-HDA and Au nanoparticles were verified by optical measurements, TEM, and powder X-ray diffraction analysis.

Figure 5-1. TEM image of 6.0 nm colloidal gold nanoparticles as prepared in aqueous solution. The image was taken at a magnification of x210K.

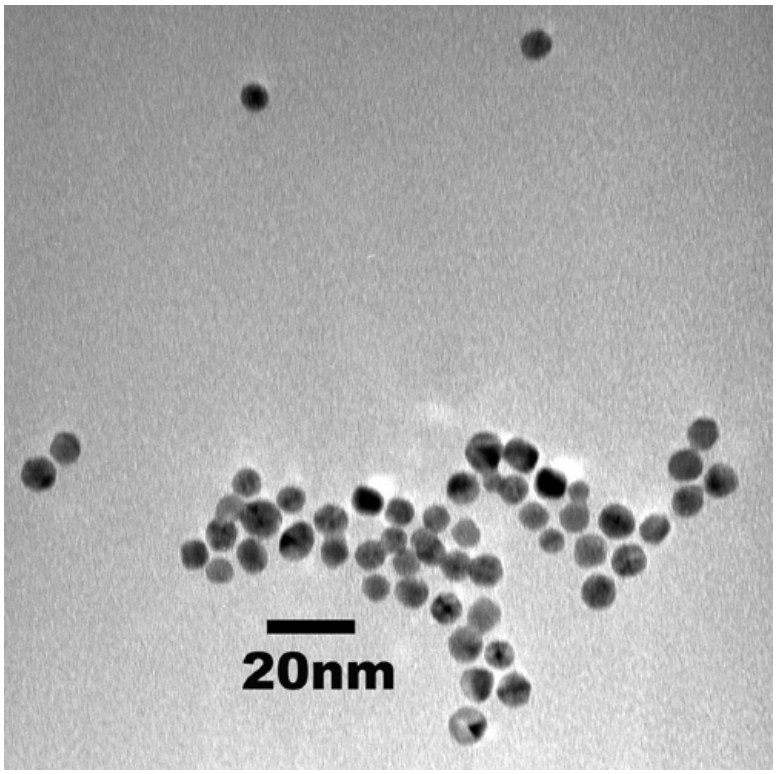

Figure 5-2. TEM image of 6.0 nm CdSe-HDA evaporated on a copper grid from a toluene solution. The image was taken at a magnification of x300K.

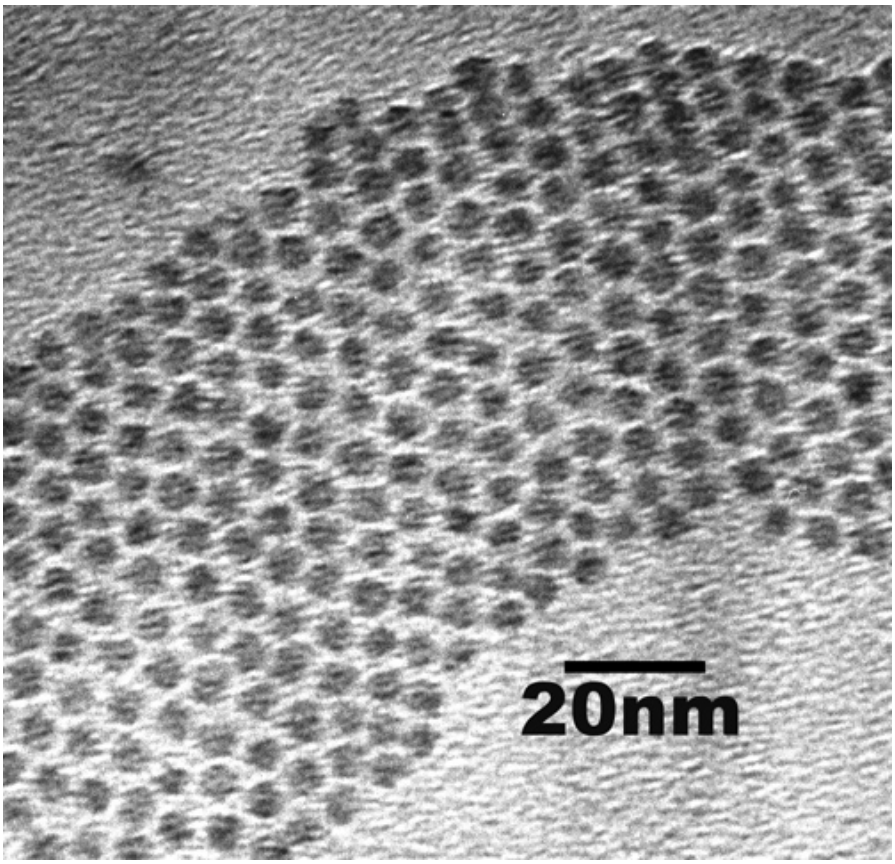

5.3.2 Preparation of CdSe-AET.

Surface ligand exchange of the hexadecylamine (HDA) passivant layer on CdSe-HDA for 2-aminoethanethiol (AET) was accomplished by dispersing 20mg of CdSe-HDA in 0.5ml of N,N-dimethylformamide with light sonication. An excess of 2-aminoethanethiol hydrochloride was added and the solution heated in an oil bath at 70 ^{o}C for 5 minutes with stirring. The product was isolated by selective precipitation via the addition of methanol and collected by centrifugation. The pellet was washed with methanol to remove trace impurities and dried under vacuum. This produces a water-soluble CdSe-AET material with a pH of ~5.5 in aqueous solution. FTIR analysis of water-soluble CdSe-AET suggests complete exchange of the HDA by AET (Figure 5-3). A TEM image of the CdSe-AET product cast on a copper TEM grid from an aqueous CdSe-AET solution is shown in Figure 5-4. In this image the lattice fringes characteristic of CdSe can be easily identified indicating that the CdSe maintains its crystallinity. The CdSe-AET does not self-assemble onto the TEM grid in a hexagonal packing motif, characteristic of nanoparticles surface-stabilized with long-chain alkyl thiols or amines (Figure 5-2).

Figure 5-3. FTIR spectra of water-soluble a) CdSe-AET and b) CdSe-HDA suggesting complete exchange of hexadecylamine by 2-aminoethanethiol.

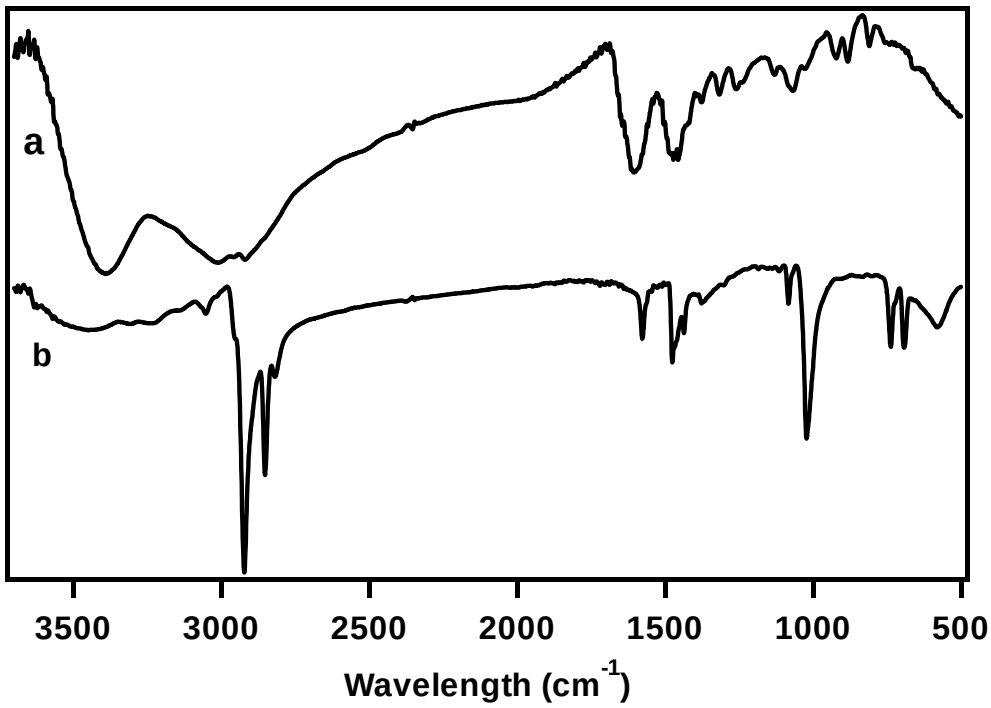

Figure 5-4. TEM image of CdSe-AET drop cast onto a copper grid from an aqueous CdSe-AET solution. The image was taken at x410k magnification.

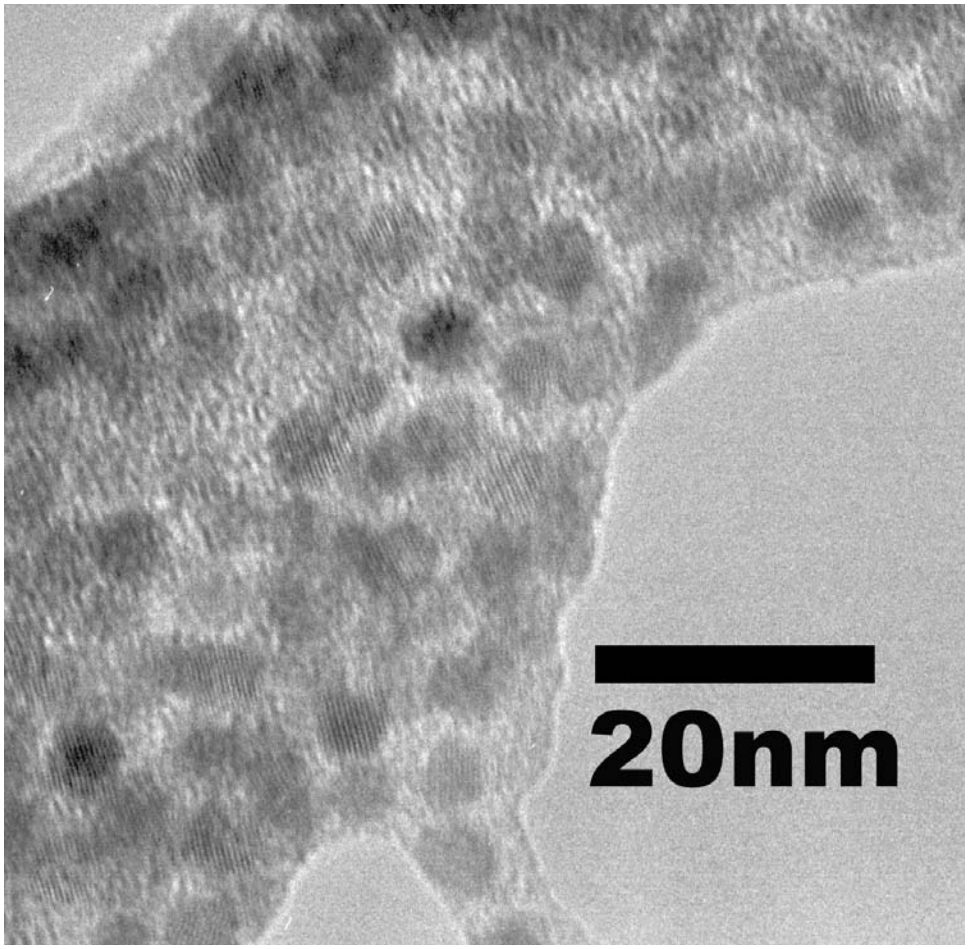

With shorter chain lengths functionalized with polar amine/ammonium groups the E_{steric} term influencing the self-assembly becomes negligible and E_{vdw} term dealing with the core-core interactions and the E_{elec} term dealing with the electrostatic interactions begin to dominate.

5.3.3 Preparation of Au-CdSe Composites.

Free-standing composites were prepared by the addition of an aqueous solution of 6.0 nm CdSe-AET (pH ~5.5) to a stirred aqueous solution of 6.0 nm Au buffered at pH 5.0 (sodium citrate: citric acid) at 298K. Upon mixing a colored particulate product forms immediately and is collected by centrifuge, washed several times with water and methanol, then dried under vacuum to give a 3-dimensional self-supporting structure. Thin films of the composite can be obtained by collecting the particulate as it falls out of solution and allowing it to dry on a solid substrate such as a copper grid or silicon substrate for TEM or SEM and elemental analysis.

Systematic controls to optimize the formation rate of the materials were investigated by controlling the pH of the nanomaterial solutions, mole ratios of the gold to CdSe nanoparticle solutions, and size ratios between the two nanoparticles. The pH of the gold and CdSe solutions were adjusted in a pH range from 3-6 by the addition of dilute solutions of either acetic acid or potassium carbonate. The Au/CdSe mole ratios were varied by measuring the

minimal amount of CdSe necessary to form a product and then by increasing that amount ten fold. The Au/CdSe size ratios were varied by reacting similarly prepared 6.0 nm Au-TA solutions with 3.0, 4.5, and 6.0 nm CdSe-AET solutions and by reacting an 18nm Au-cit solution with a 6.0 nm CdSe-AET solution.

5.4 Results

5.4.1 Reaction.

CdSe-AET is readily dissolved in water giving an optically clear aqueous solution, which is stable in the pH range from 3-7 for several days. In this pH range a sufficient percent of the amine functionalities are protonated (δ_{NH2} = 1650 cm^{-1}, δ_{NH3+} = 1600 and 1480 cm^{-1}), as shown by the FTIR data in Figure 5-5, which allows the CdSe to remain soluble in water. The δ_{NH2} and δ_{NH3+} ratio can be determined from the relative intensity ratios of the peaks at 1620 and 1600 cm^{-1}, respectively. As the pH of the CdSe-AET solution is increased to >7 the CdSe tends to aggregate and flocculate out of solution due to an increase in the NH_2/NH_3^+ ratio. The pH of the gold solution can be adjusted in the pH range of the CdSe-AET (pH = 3-7) by addition of dilute acetic acid or potassium carbonate without affecting the stability or quality of the Au nanoparticles. Upon mixing 6.0 nm gold and 6.0 nm CdSe-AET nanoparticle solutions together at room temperature with moderate stirring

and at pH levels less than 6.0, a particulate matter forms within a matter of seconds and flocculates out of solution leaving a colorless supernatant. The particulate color is a combination of the color of the Au and CdSe nanoparticles and not a black color characteristic of agglomerated gold. At solutions with a pH greater than or equal to 6.0, no reaction is observed.

To verify that the product formed is not influenced by the presence of citrate ions or tannic acid, a solution of sodium citrate and tannic acid was added to an aqueous solution of CdSe-AET with no formation of a particulate matter. Consequently, addition of an aqueous solution of 2-aminoethanethiol to the gold nanoparticle solution results in the immediate formation of a solution with a blue tint and a black precipitate arising from the agglomeration of the Au nanoparticles. TEM analysis of this product, shown in Figure 5-6, illustrates that as the gold colloids are brought into close proximity due to the binding affinity of the sulfur and amine groups of AET, the gold nanoparticles fuse together.

5.4.2 Infrared Analysis.

FTIR spectra of a) 2-aminoethanethiol, b) CdSe recapped with 2-aminoethanethiol, and c) the final product obtained from the reaction of aqueous gold and CdSe-AET solutions are shown in Figure 5-7 and summarized in Table 5-1. In the spectrum of CdSe-AET, the loss of the ν_{SH}

mode at 2500 cm^{-1} and the observation of ν_{NH2} and ν_{NH3+} modes at 2900 and 3400 cm^{-1} supports preferential thiol binding leaving a free amine/ammonium head group at the solution interface (Figure 5-7b). Preferential binding through the sulfur moiety is expected due to the stronger Lewis basicity of the thiol and the greater binding affinity of thiols to CdSe.[37,38]

Figure 5-5. FTIR spectrum of a) 2-aminoethanethiol and b) CdSe-AET indicating the amine/ammonium ratio of the AET on the surface of the CdSe-AET at pH 6.5.

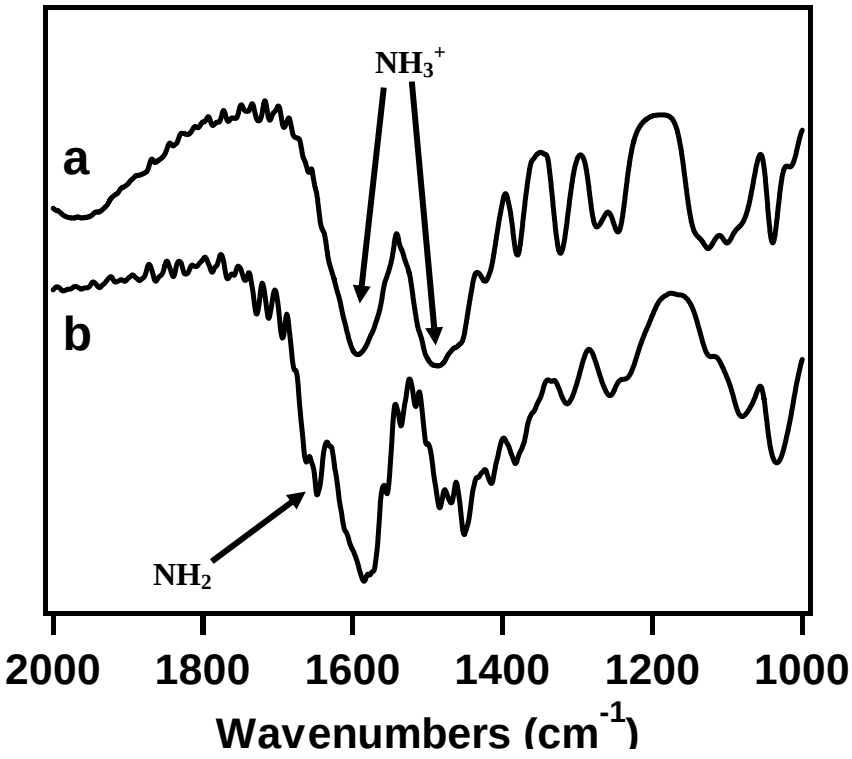

Figure 5-6. TEM image of product formed by the addition of an aqueous AET solution to an aqueous colloidal gold solution. The image was taken at a magnification of x150K.

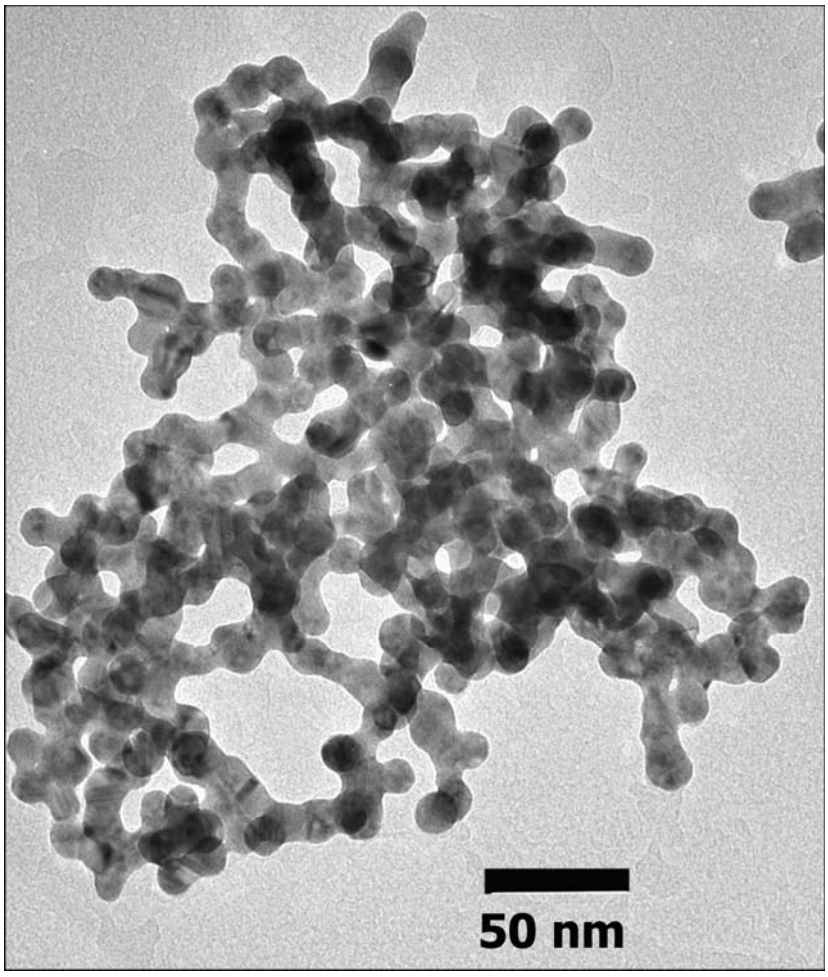

Figure 5-7. FTIR spectrum of a) 2-aminoethanethiol, b) CdSe-AET, and c) Au-CdSe illustrating preferential binding of the thiol to the CdSe surface and amine bounding to the gold surface.

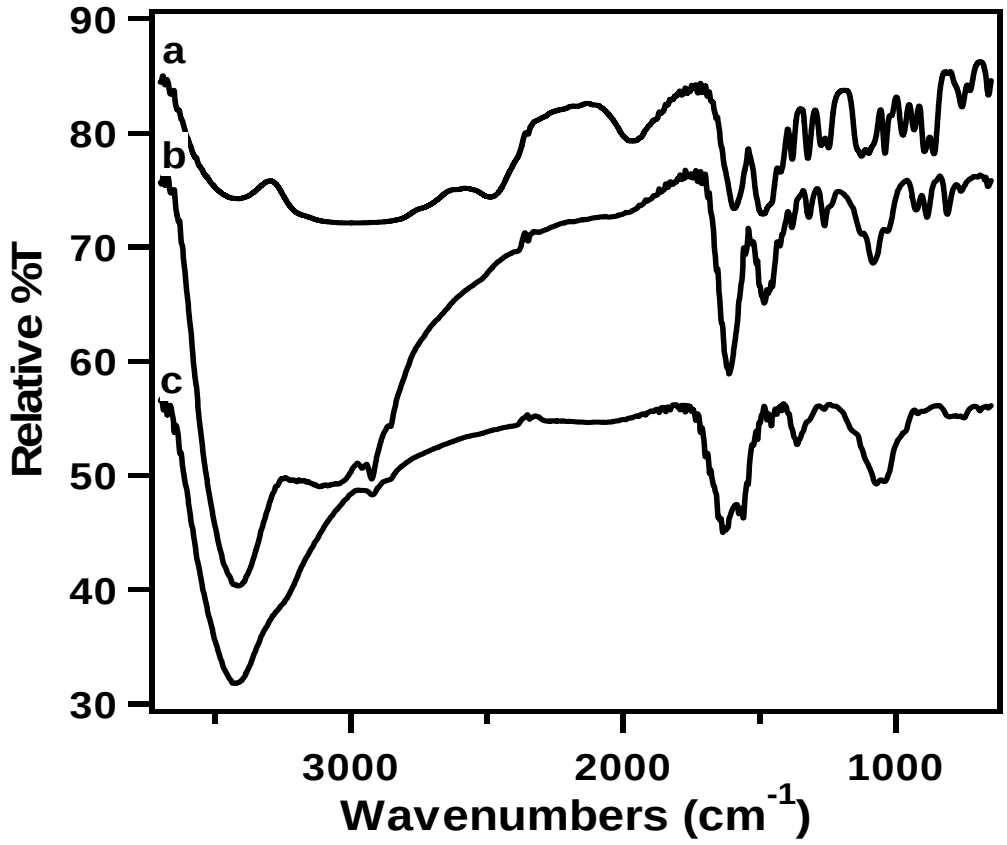

Table 5-1. Peak assignments for thiol and amine modes in 2-aminoethanethiol, CdSe-AET, and Au-CdSe.

Compound	Wavenumbers (cm^{-1})	Assignment
AET	2500	S-H stretch (νS-H)
	3425 s,b	NH_3^+ (N-H) stretch
	1595	NH_3^+ (N-H) bend (asym)
	1490	NH_3^+ (N-H) bend (sym)
	1100	C-N stretch (νC-N)
CdSe-AET	n.o.	S-H stretch (νS-H)
	3395 s,b	NH_3^+ (N-H) stretch
	1600	NH_3^+ (N-H) bend (asym)
	1480	NH_3^+ (N-H) bend (sym)
	1620	N-H bend (δNH_2)
	1068	C-N stretch (νC-N)
	810	N-H wag
Au-CdSe	3286	N-H stretch (asym)
	3148	N-H stretch (sym)
	1550	N-H bend (δNH_2)
	1050	C-N stretch (νC-N)
	757	N-H wag

Ammonium salts typically show strong, broad absorption in the 2800 to 3000 cm^{-1} region due to symmetrical and asymmetrical N-H stretching with a combination band in the 2000-1709 cm^{-1} region, as well as two strong bands near 1600-1575 cm^{-1} and 1550-1504 cm^{-1} from the symmetrical and asymmetrical NH_3^+ bending modes, respectively. The ammonium functionality of AET in Figure 5-7a has two bands at 1490 and 1600 cm^{-1} corresponding to the symmetrical and asymmetrical bending vibrations of the NH_3^+ group. The amine functionalities of the AET-bound CdSe in Figure 5-7b maintains these two peaks as well as an additional peak at 1640 cm^{-1} which corresponds to the N-H bending vibration of a primary amine.[39] The AET-bound CdSe displays a band at 806 cm^{-1} corresponding to the N-H wagging mode of an amine functionality as well as a broad band around 640 cm^{-1} due to the torsional N-H oscillation of an ammonium group. Amines typically display medium-to-strong absorption in the 900-700 cm^{-1} region arising from N-H wagging whereas the amine salts display a torsional N-H oscillation near 500 cm^{-1}, consistent with the above assignment.

Figure 5-8 compares the FTIR spectra of a) sodium citrate, b) Au-TA, isolated by the addition of sodium chloride to the gold nanoparticle solution, and c) tannic acid. From this comparison the gold nanoparticles are shown to be surface stabilized by a combination of sodium citrate and tannic acid.

Figure 5-8. FTIR spectra of a) sodium citrate, b) Au-TA, and c) tannic acid illustrating that the gold surfaces are stabilized by the presence of citrate ions and tannic acid.

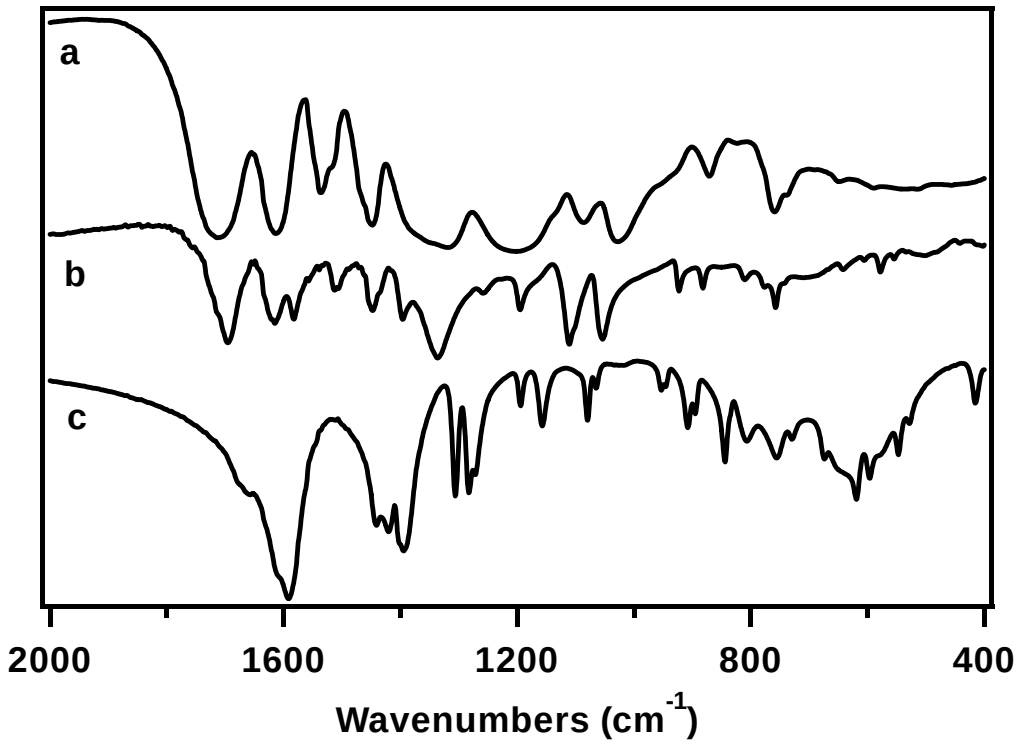

The carboxylate functionalities on the sodium citrate and tannic acid can be identified by C=O stretching, C-O stretching, and C-O-H bending modes. Due to strong hydrogen bonding between carboxylic acid groups on the citrate and tannic acid these functionalities often exist as dimers and display a very intense, broad O-H stretching absorption in the 3300-2500 cm^{-1} region as well as a strong C=O stretching mode at 1708 cm^{-1}. Two other bands due to C-O stretching and C-O-H bending modes appear at 1330 cm^{-1} and 1448 cm^{-1}, respectively. As a salt, the sodium citrate has two characteristic carboxylate absorbance peaks at 1582 cm^{-1} and 1394 cm^{-1} due to a strong asymmetrical and weaker symmetrical C-O stretching band, respectively.[39] The FTIR spectrum for Au-TA in Figure 5-8b shows a combination of all these modes indicating that the surface of the gold nanoparticle is stabilized by citrate ions and tannic acid.

5.4.3 TEM and SEM Analysis.

The morphology of the free-standing Au-CdSe nanocomposite materials can be imaged by transmission electron microscopy (TEM) and scanning electron microscopy (SEM). Figure 5-9 shows a TEM image of a macroscopic Au-CdSe assembly several microns in length composed of individual 6.0 nm Au and 6.0 nm CdSe nanoparticles, which are well differentiated. The CdSe nanoparticles do not image as well as the gold nanoparticles, but can be

readily identified by the characteristic fringe patterns of the CdSe under higher magnification as shown in Figure 5-10.

Figure 5-11 shows a selected area electron diffraction (SAED) image taken over a thinner area of the sample in Figure 5-9, which illustrates a contribution of diffraction rings arising from both Au and CdSe nanoparticles along with intense diffraction spots suggesting a polycrystalline material with preferential ordering of the nanomaterials in the assembly. The observed hexagonal pattern responds to stage tilting consistent with diffraction arising from a crystalline structure. Figure 5-12 shows the SAED image of a Au-CdSe composite with a corresponding intensity distribution curve contrasted against distribution curves of SAED images of gold and CdSe nanoparticles alone. The rings in the composite come from a contribution of both the CdSe and gold nanocrystal lattice planes, giving further evidence for the presence of both CdSe and gold nanoparticles within the composite.

Comparison of the initial TEM images of Au and CdSe nanoparticles illustrating their size distributions with a thin film composite, shown in Figure 5-13, suggests the composite seems to exclude poorly formed and large Au particles from the assembly, which is consistent with a thermodynamically driven assembly. Figure 5-14 shows the same Au-CdSe thin film at higher

magnification showing the Au and CdSe nanoparticles well mixed in the composite.

Figure 5-9. TEM image of Au-CdSe nanocomposite several microns in length formed from the reaction of aqueous solutions of 6.0 nm CdSe-AET and 6.0 nm Au-TA at room temperature with pH 5.0. The image was taken at a magnification of x17K.

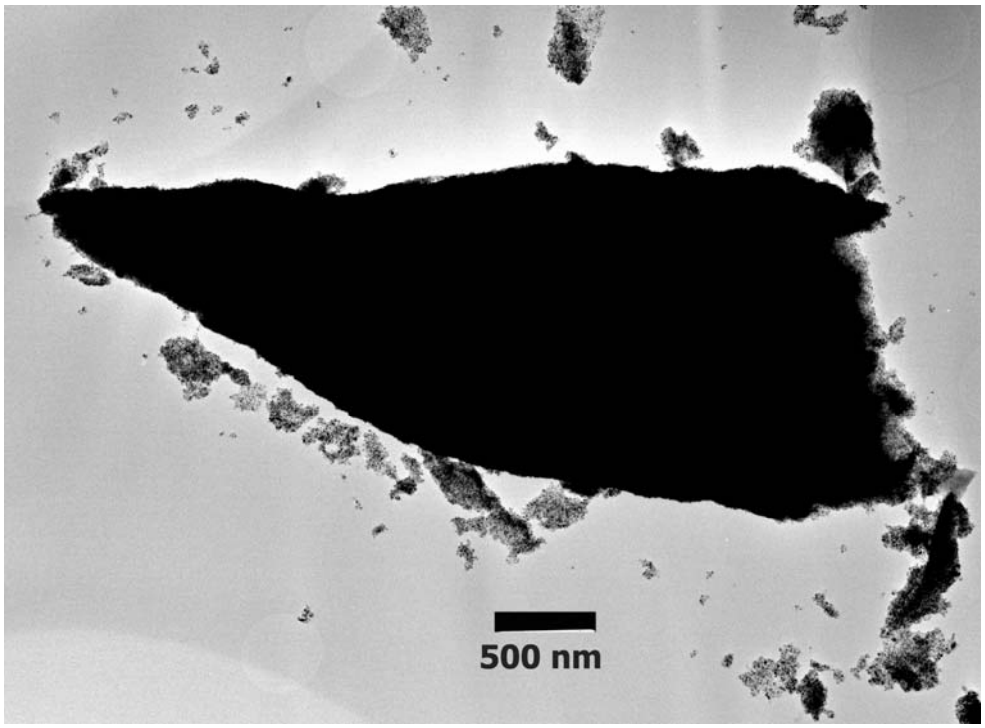

Figure 5-10. TEM image of an edge of the Au-CdSe nanocomposite shown in Figure 2-9 at higher magnification. Arrows point out some of the more easily seen CdSe nanoparticles, identified by their characteristic fringe patterns. The image was taken at a magnification of x410K.

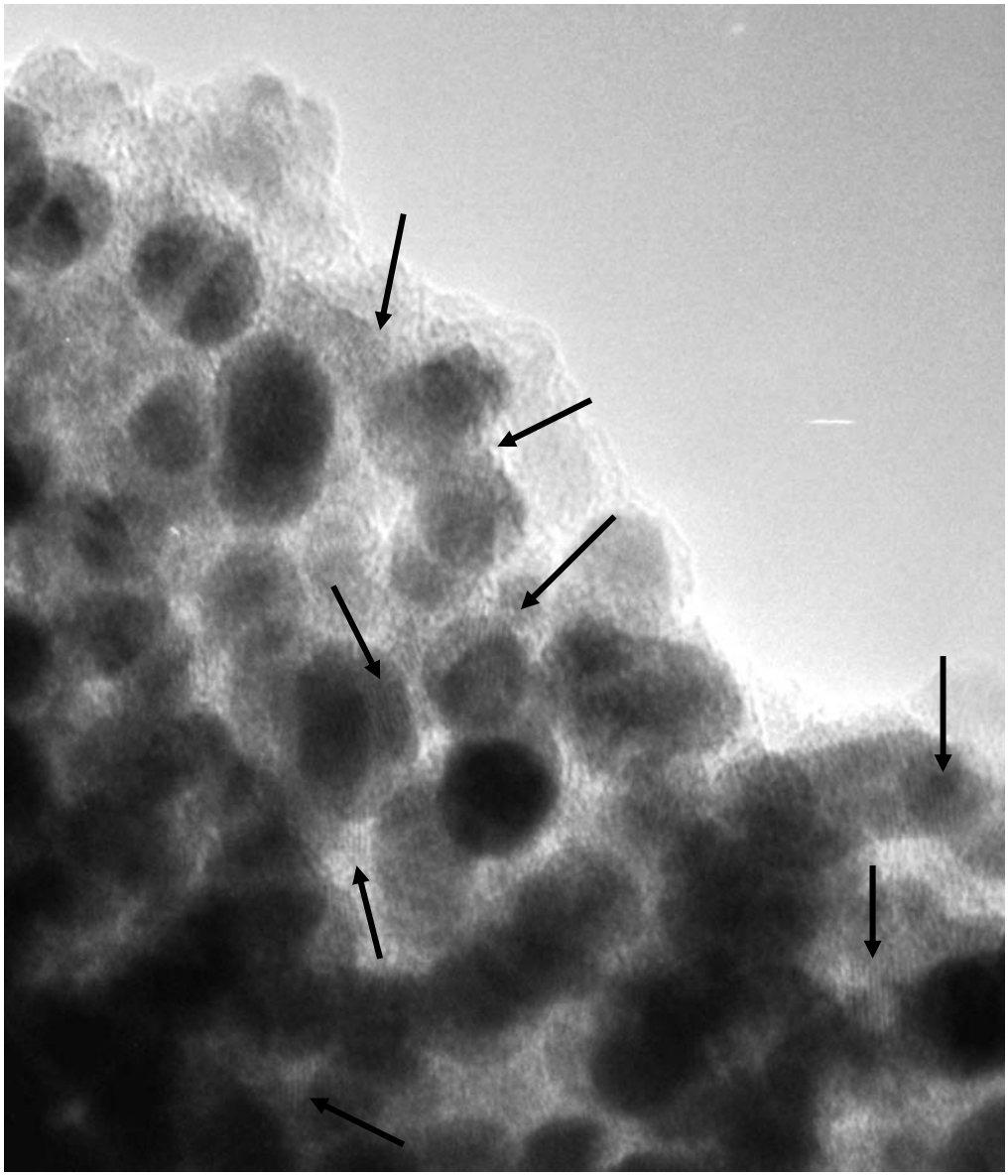

Figure 5-11. Selected area electron diffraction (SAED) pattern obtained from a thin section of the material at x50K magnification and with a camera length of 83.0 cm.

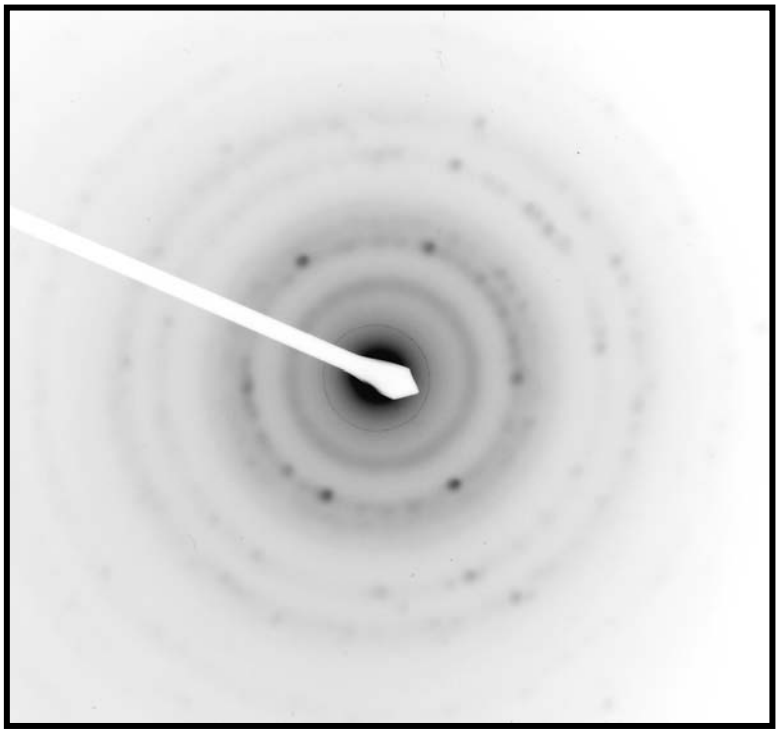

Figure 5-12. SAED pattern from a Au-CdSe composite with an intensity distribution curve taken from the SAED compared with distribution curves from the SAED pattern of 6.0 nm gold and 6.0 nm CdSe nanoparticles. The corresponding distances in angstroms are given to the left of the SAED pattern.

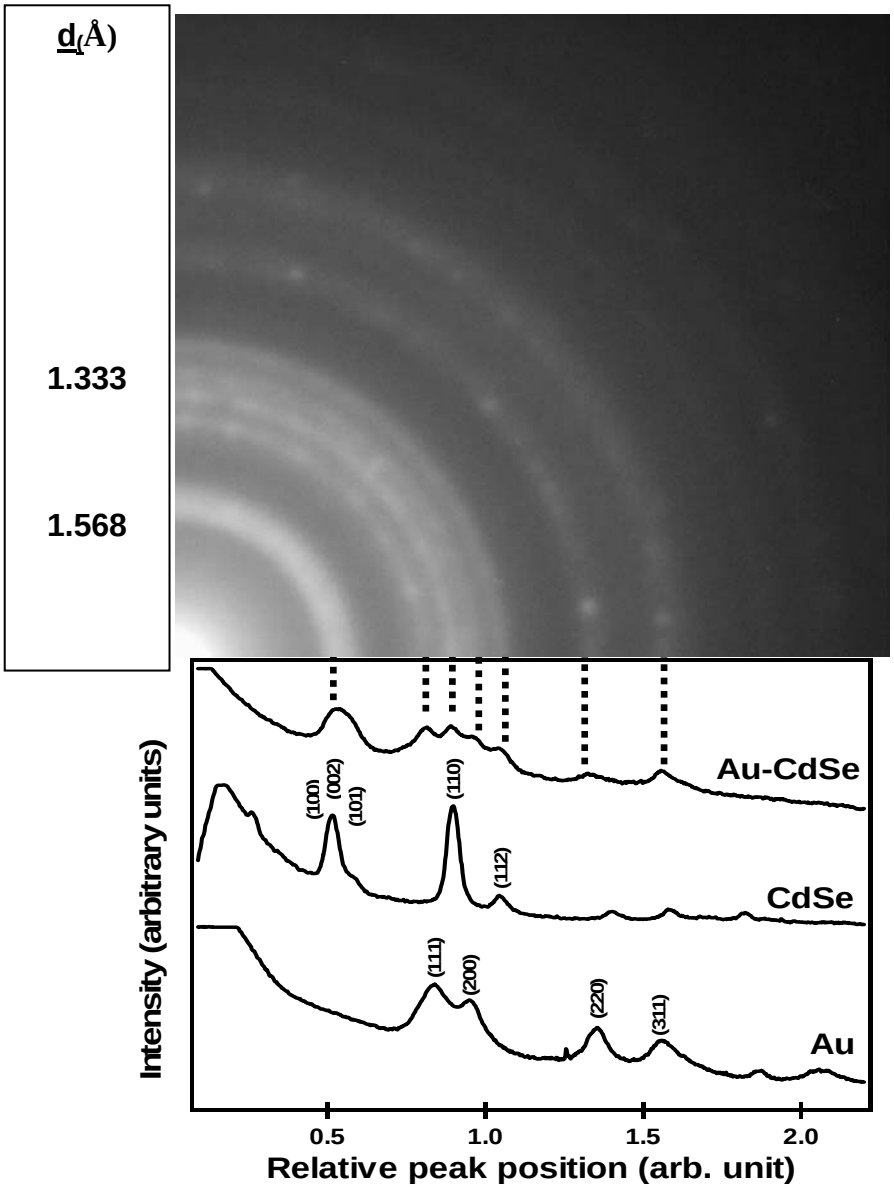

SEM analysis of the 3-dimensional free-standing composite formed at pH 5.5 shows a “glassy” type structure, as illustrated in Figure 5-15. At higher magnification the structure appears to have a granite-like appearance characteristic of the packing of hard spheres. The fact that the structure can be imaged as is in the SEM demonstrates the conductive nature of the material. Elemental analysis of the Au-CdSe nanocomposite was obtained using energy dispersive x-ray analysis (EDX) performed in the SEM on a silicon substrate with the results given in Table 5-2. The resulting spectrum and SEM image are shown in Figure 5-16. Confirmation of the CdSe/Au molar ratio was obtained by flame-AA. Interestingly, solutions prepared at pH > 6.0 show no indication of reaction. TEM analysis of a mixed solution of Au-TA and CdSe-AET nanoparticles at pH 6.0 evaporated onto a TEM grid from the reaction mixture shows only phase-segregated structures are achieved (Figure 5-17).

Evidence for CdSe-AET directed control of assembly is illustrated in Figure 5-18, which shows TEM images comparing the differences in the gold nanoparticle morphology obtained from mixing a gold nanoparticle solution with a solution of a) CdSe-AET and b) 2-aminoethanethiol. TEM analysis of the product from the reaction of Au colloids with 2-aminoethanethiol shows the gold nanoparticles to be agglomerated in such a manner as to be

indistinguishable from one another. In comparison, the gold nanoparticles reacted with CdSe-AET remain well differentiated.

Figure 5-13. TEM image of a Au-CdSe nanocomposite thin film from the reaction solution as the particles begin to form. The Au nanoparticles remain well separated from one another indicating no particle agglomeration. The image was taken at a magnification of x210K.

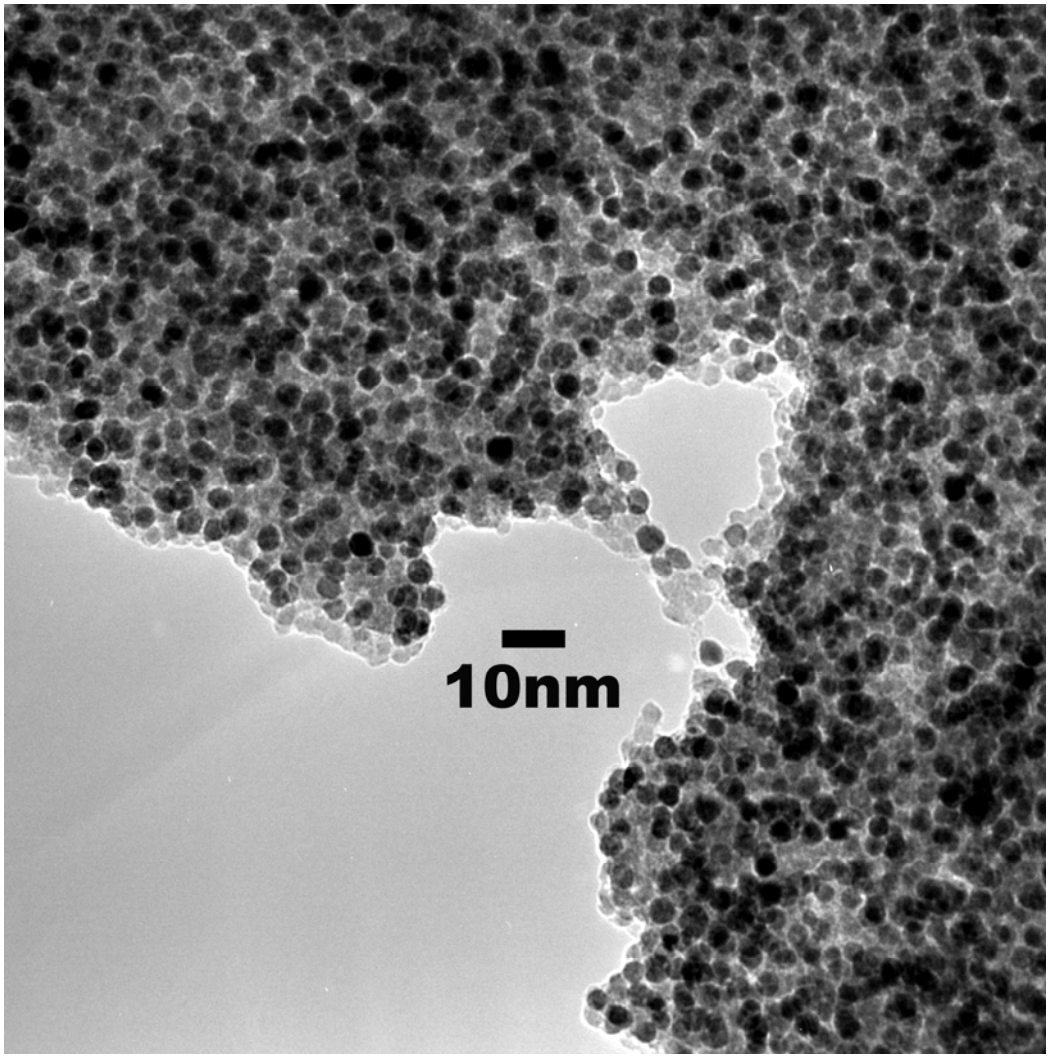

Figure 5-14. TEM image of Au-CdSe thin film in Figure 2-11 at x410K magnification showing CdSe well mixed with the Au nanoparticles.

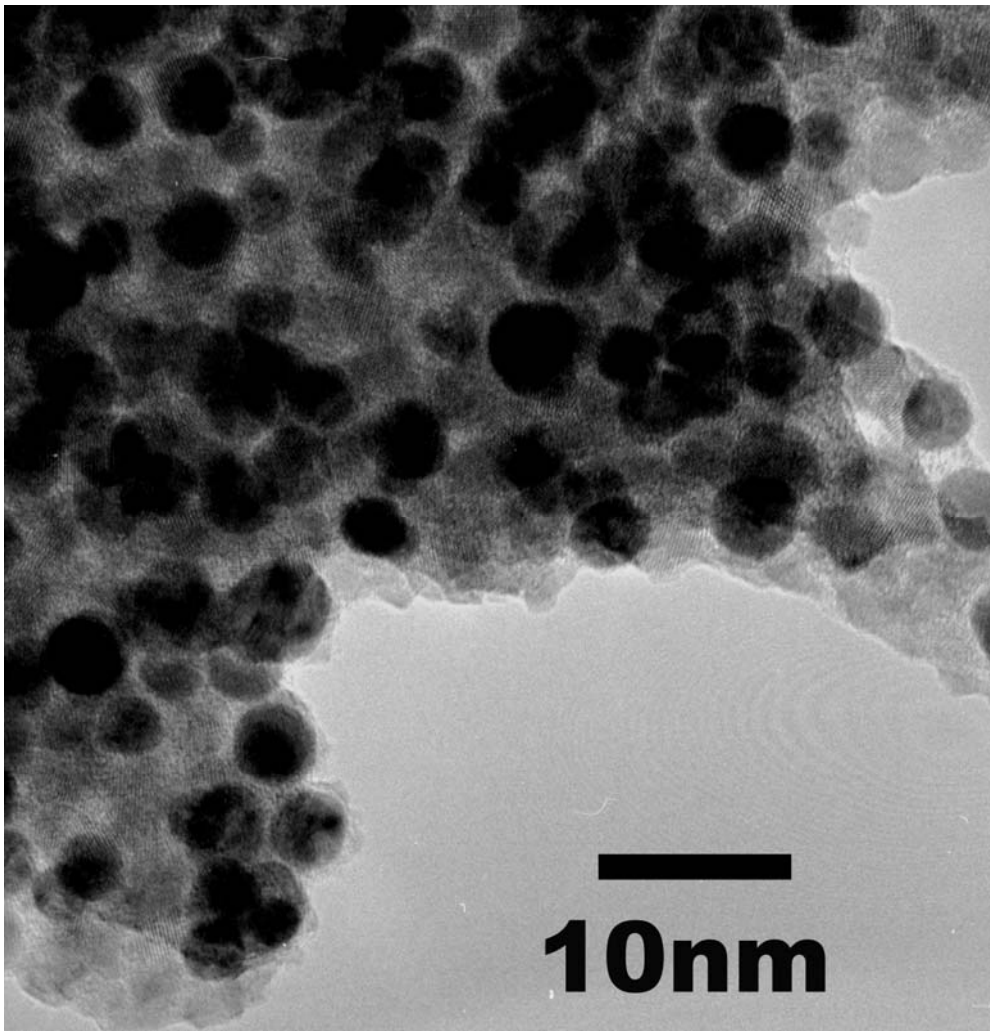

Figure 5-15. SEM image of a free-standing 3-dimensional Au-CdSe composite formed at pH 5.5 illustrating a "glassy" type structure at lower magnification (x10K)(a). At higher magnification the structure appears to have a granite-like appearance characteristic of the packing of hard spheres (x100K)(b).

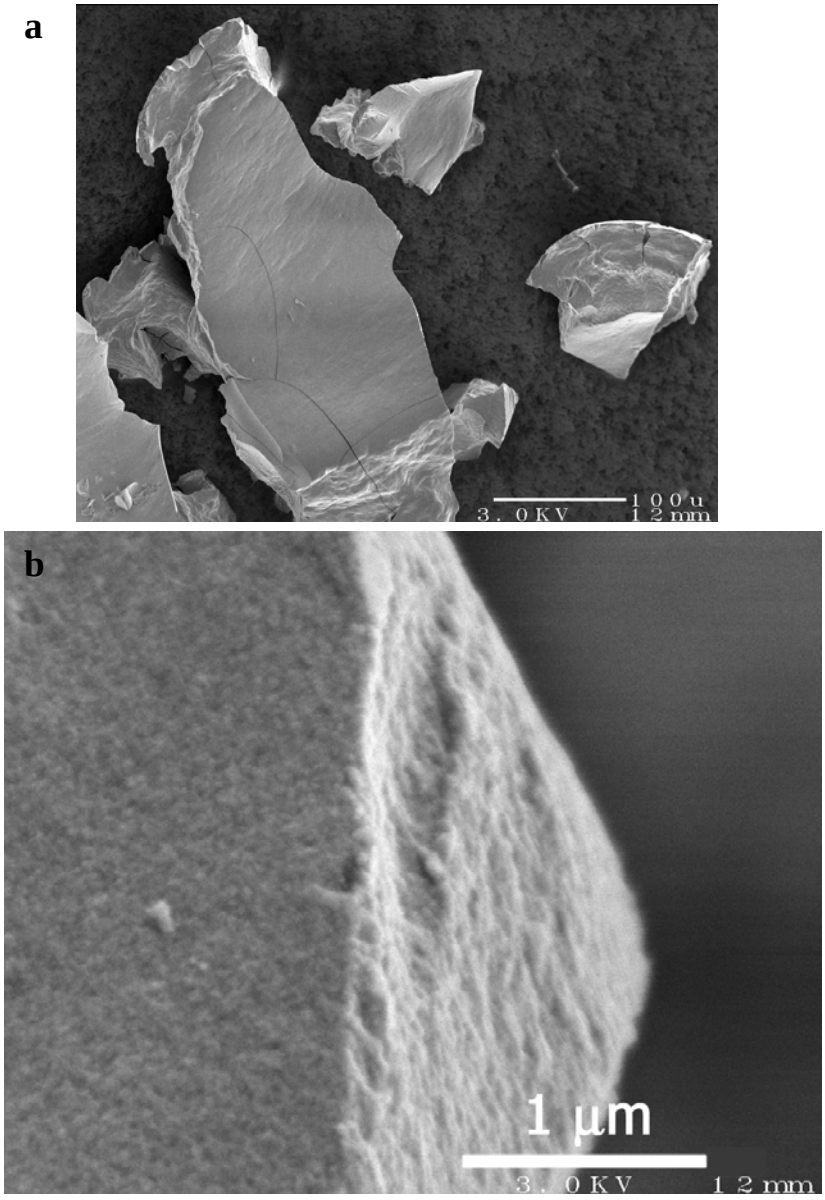

Table 5-2. Calculated and experimental weight percentages based on SEM-EDX Au-CdSe composites formed from the reaction of Au and CdSe-AET nanoparticles in a 1:6 molar ratio and a 1:60 molar ratio followed by washing with water to remove excess nanoparticles from the composite structure.

Reaction conditions	**Weight %**		
	Au	**Cd**	**Se**
Calculated [a] (6:1 CdSe:Au)	**36.2**	**34.6**	**29.2**
pH 4.5 (6:1)	**34.3**	**37.7**	**28.0**
pH 4.5 (60:1)	**34.7**	**37.8**	**27.5**

[a] Calculated weight percentages are based on molar concentrations calculated using the molecular weight of 6.0 nm Au and CdSe.

Figure 5-16. SEM-EDX image and corresponding spectrum of a Au-CdSe nanocomposite thin film on a silicon substrate.

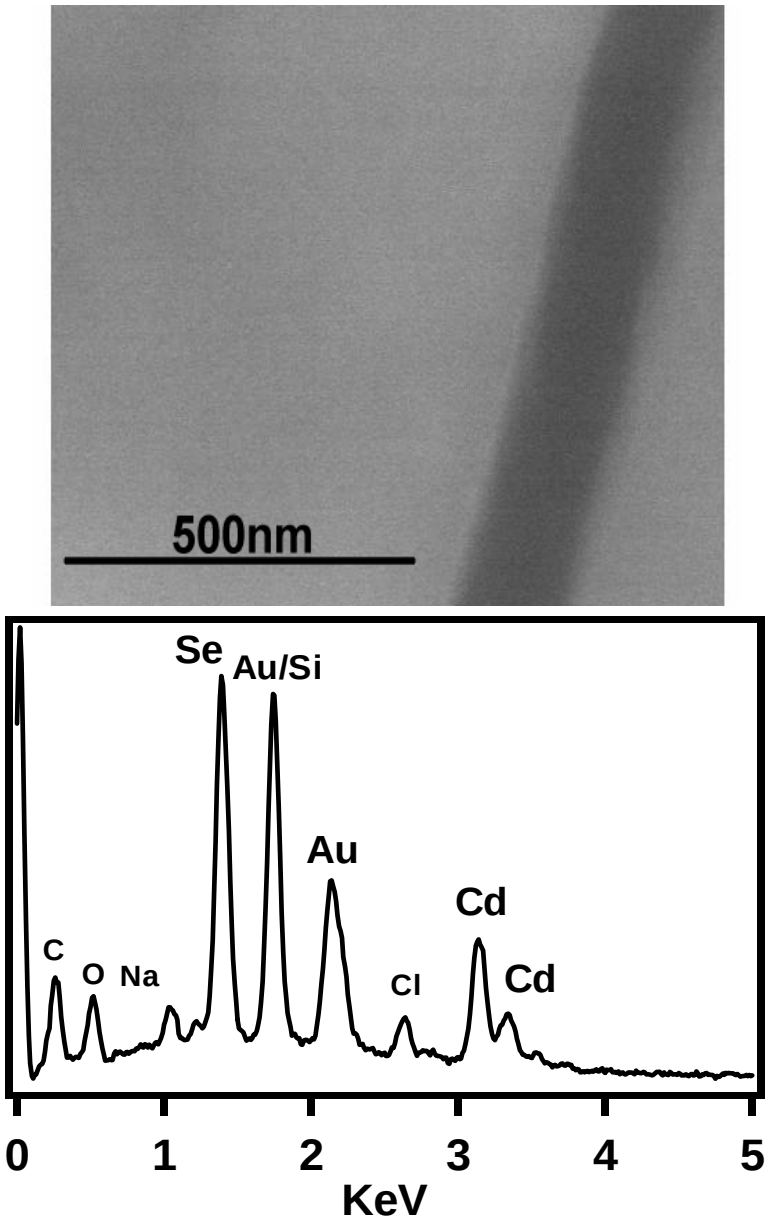

Figure 5-17. TEM image from Au/CdSe solutions reacted together at pH 6 illustrating phase segregated structures. The image was taken at a magnification of x340K.

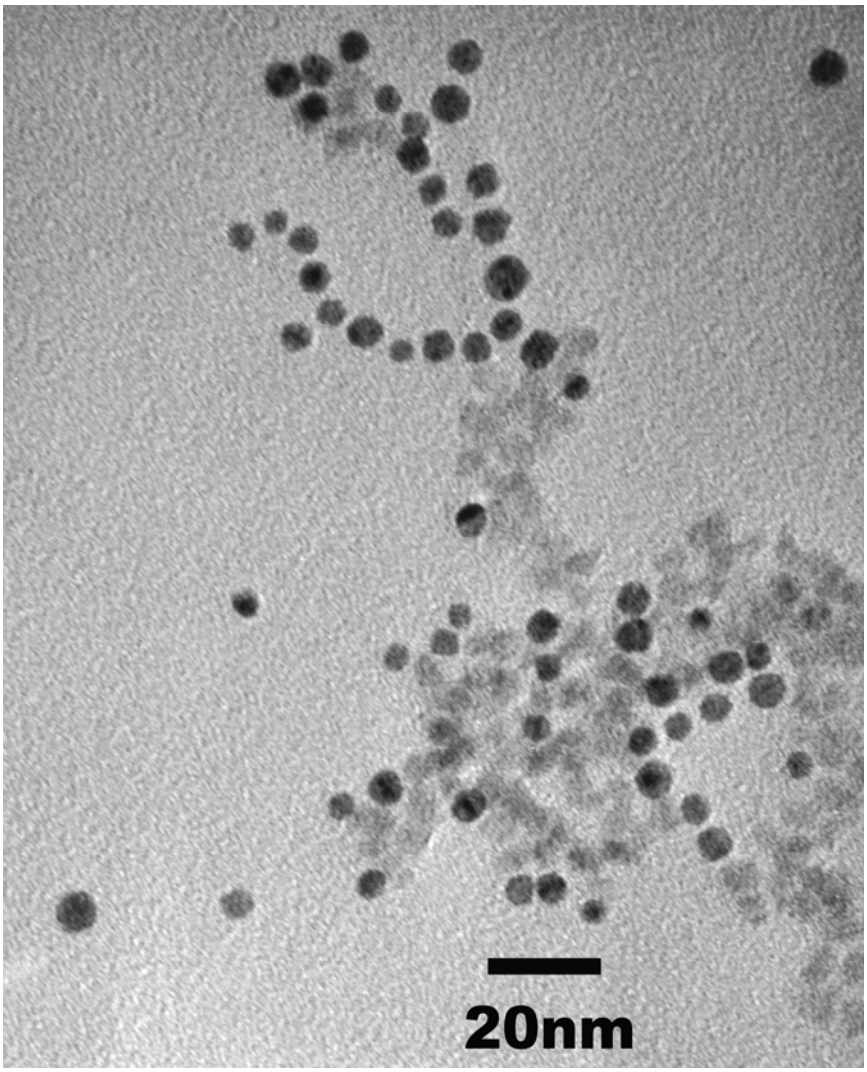

Figure 5-18. TEM comparison of gold nanoparticles reacted with a) CdSe-AET and b) a solution of 2-aminoethanethiol alone. The images were taken at a magnification of x350K and x150K, respectively.

a

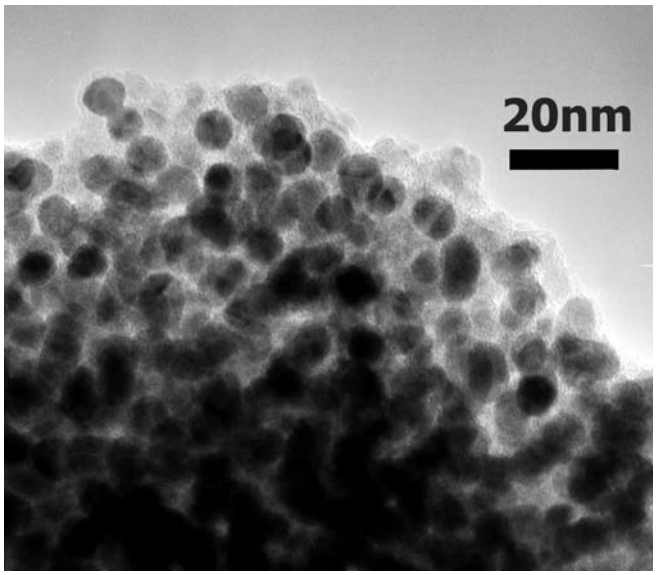

b

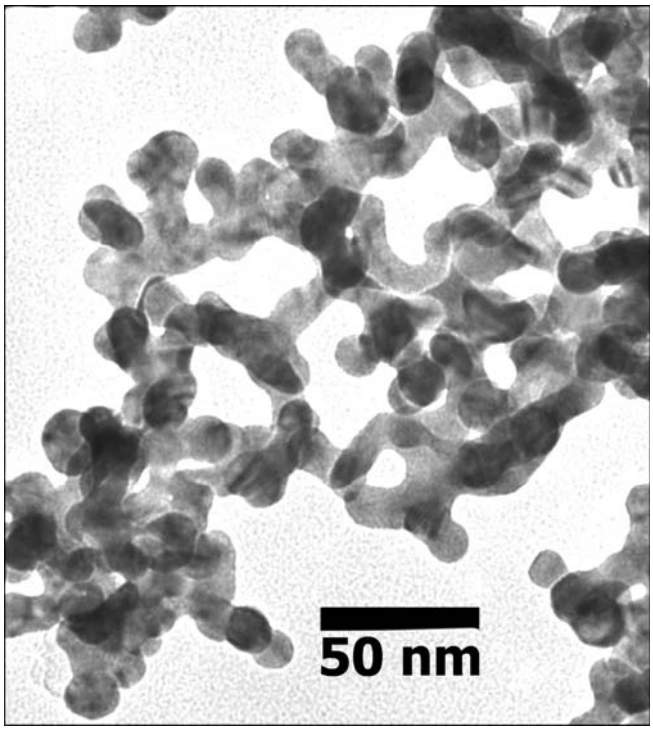

5.4.4 Absorbance.

Figure 5-19 illustrates a comparison of the absorption and emission properties of 6.0 nm gold nanoparticles, 6.0 nm CdSe, and a composite comprised of Au-CdSe. The gold nanoparticle surface plasmon absorption is observed at 520 nm and the CdSe exciton transition is observed at 610 nm.[6,40,41] Absorbance of the Au-CdSe nanocomposite material shows the combined absorption bands of the gold and the CdSe nanoparticles without a band due to agglomerated gold. There is no evidence for gold particle agglomeration in these composite materials as has been observed for citrate-stabilized Au nanoparticles upon drying.[42] Agglomerated gold nanoparticle structures give rise to a broad absorption band from 520 to 685 nm due to overlap of the dipole resonances between neighboring gold particles,[43,44] as illustrated in Figure 5-20. The absorption in Figure 5-20b represents a nano-composite material in which the Au nanoparticles remain well differentiated from one another as indicated by absorbance and TEM data. The absorption in Figure 5-20c was obtained from a thin film of Au nanoparticles formed from a colloidal gold solution prepared by the reduction of auric acid with sodium citrate and allowed to dry on a glass slide.

Figure 5-19. Absorbance (solid line) and emission (dotted line) spectra of an aqueous gold nanoparticle solution (Au), an aqueous CdSe-AET solution (CdSe-AET), and a thin film of the Au-CdSe nanocomposite material drop cast onto a glass slide.

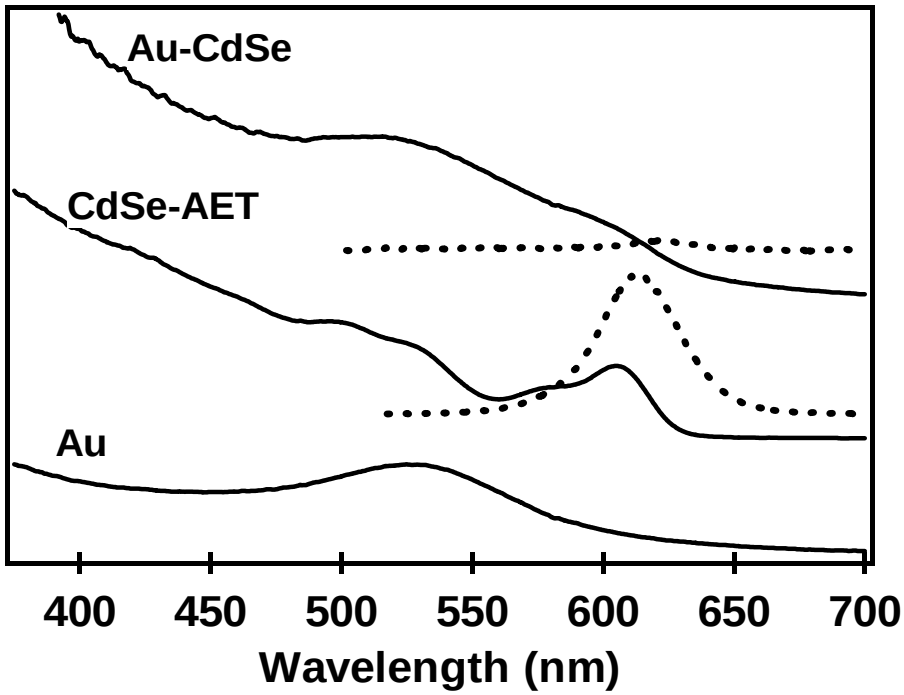

Figure 5-20. Absorbance spectra of a) gold nanoparticle solution, b) Au-CdSe thin film, and c) agglomerated Au nanoparticles.

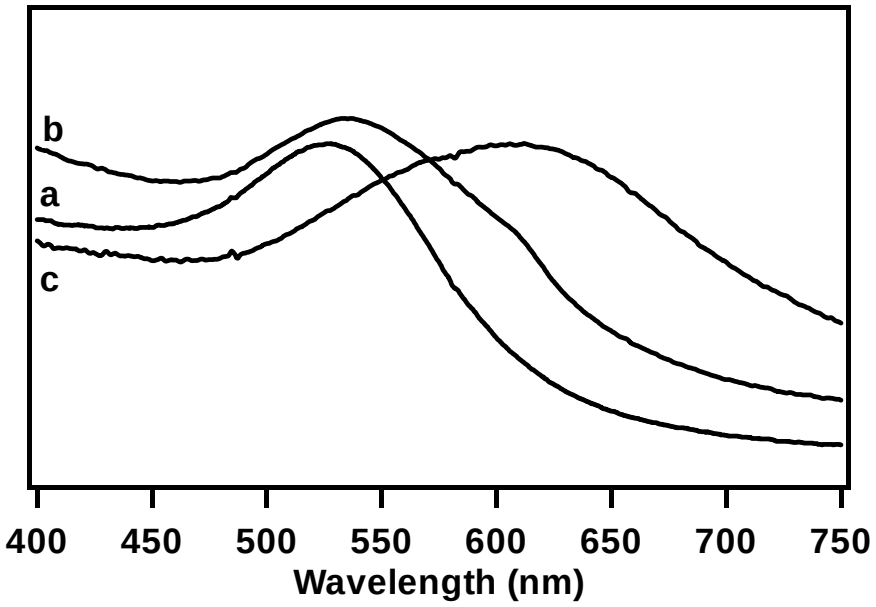

5.5 Discussion

5.5.1 Reaction Mechanism.

Controlled mixing of Au-TA and CdSe-AET solutions at pH 3-6 produces micron-scale, free-standing composite materials composed of individual Au-TA and CdSe nanomaterials separated by ~5Å due to the organic passivant AET. Several mechanisms for the formation of the composite structure are possible including self-assembly, electrostatic attraction, ligand exchange, or a coordination event. Based on the pH dependence and molar ratio behavior for assembly, the formation of the Au-CdSe composite appears to be driven by an acid-base equilibria, suggesting a thermodynamically controlled reaction mechanism modulated by the formation of a Au-NH_2 bond as proposed in Figure 5-21. Displacement of the carboxylate stabilizing functionality on the Au surface leads to formation of the composite modulated by a proton transfer from the ammonium functional group to the citrate passivating ligand. Control of the pH at 5.5 allows slow thermodynamic growth of the structure by buffering the solution, which controls the rate of exchange for the ammonium proton with the citrate group on the Au nanoparticles, providing a driving force for the amine functionality to bind the Au surface.

Figure 5-21. Proposed reaction mechanism for formation of Au-CdSe composite from CdSe-AET and Au-TA illustrating the predicted displacement of the citrate ions from the gold surface and proton exchange from the ammonium groups allowing for gold-amine bonding.

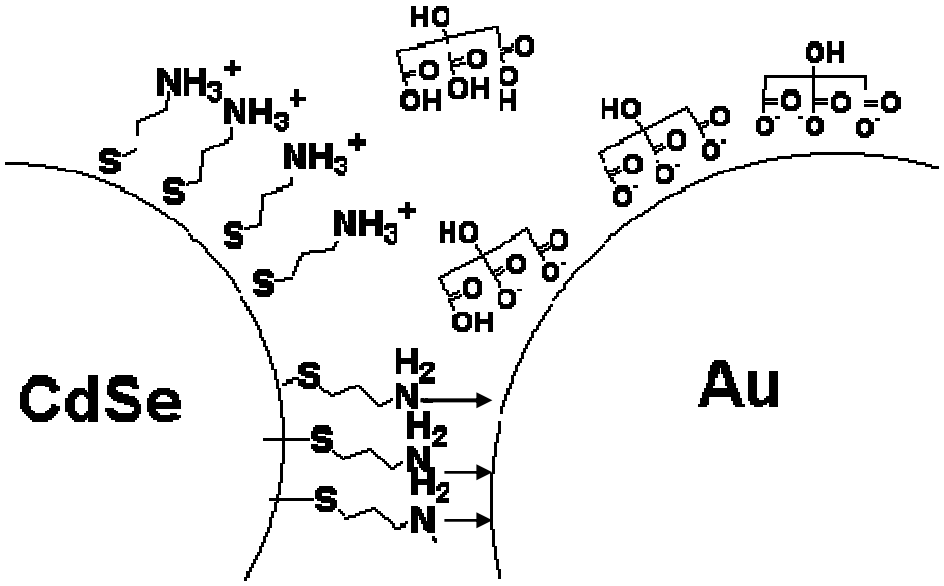

Displacement of citrate ions from gold surfaces by amines has been reported in the literature as being driven by the availability of the lone pair of electrons on the amine for the gold surface, as well as ionic interactions with the negatively charged particles.[45-47] Although the AET has a higher pKa than the citrate groups (~9.5 vs. 6.39 respectively), the solution equilibrium is driven by the bond formation of a Au-NH_2 coordination complex.

The proposed mechanism can be verified by inspection of the FTIR data from 3500 to 1400 cm^{-1} in Figure 5-22. Upon addition of the CdSe-AET to the Au-TA solution, there is an immediate loss of the ν_{COO-} at 1710 cm^{-1} and the ν_{NH3+} mode at 1485 cm^{-1}. The ν_{NH2} modes at 3400 cm^{-1} shifts to lower frequency in the 3100-3300cm^{-1} region and decreases in intensity, as expected for the formation of a metal-amine bond.[12,14] Similar shifts are observed for octylamine monolayers on gold surfaces, with a shift in the ν_{NH2} modes of octylamine from 3292 and 3370 cm^{-1} to 3220 and 3286 cm^{-1}, respectively, upon binding to gold (Figure 5-23, Table 5-3). The shift to lower frequency for ν_{NH2} in the Au-CdSe product is consistent with a metal-NH_2 interaction, and loss of the ammonium proton. Further evidence for binding can be seen in the δ N-H bending modes in the 1500-1600 cm^{-1} region. Upon formation of the free-standing composite, the ammonium vibrations disappear and the amine bending vibration shifts to 1550 cm^{-1}.

Figure 5-22. FTIR spectra of a) 2-aminoethanethiol, b) CdSe-AET, and c) Au-CdSe nanocomposite illustrating the effect of product formation on the amine stretching modes in the region from 3500 to 1400 cm^{-1}.

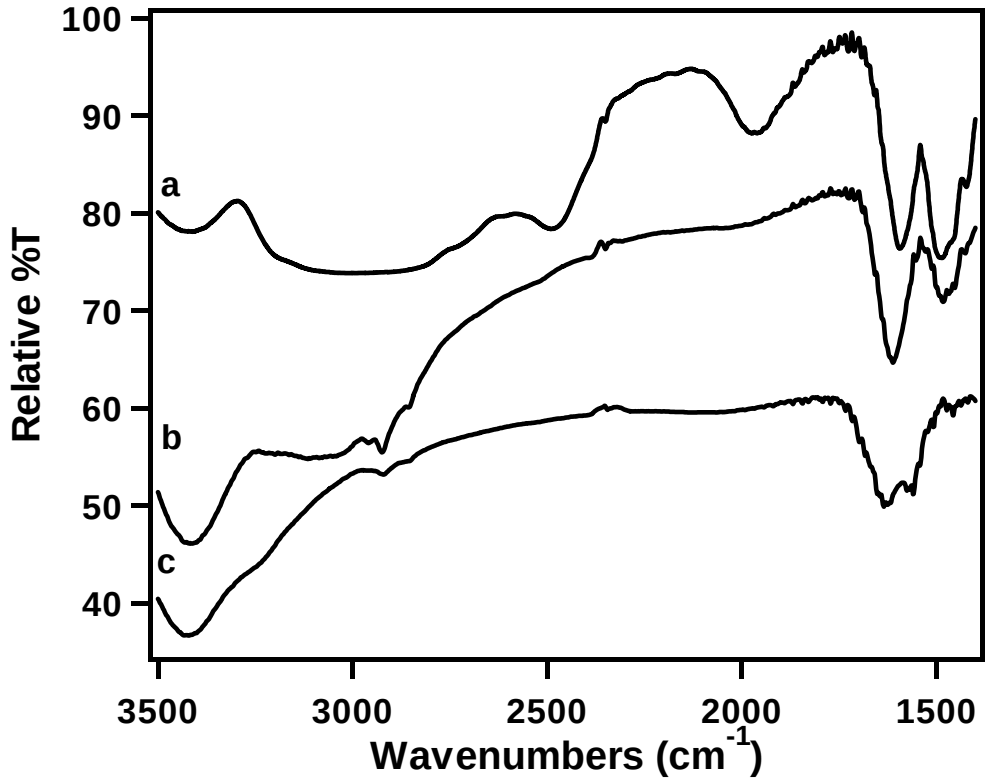

Figure 5-23. FTIR spectra of a) octylamine and b) octylamine-capped gold nanoparticles illustrating the shift in frequencies and decrease in intensity for the amine stretching frequencies upon bonding onto gold surfaces.

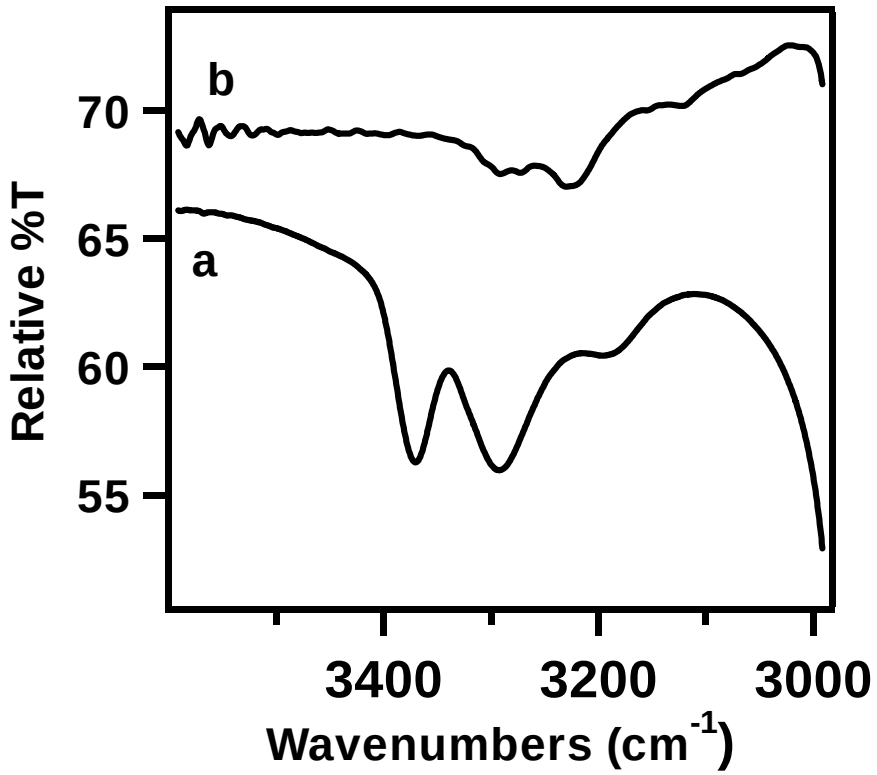

Table 5-3. Peak assignments for amine stretching frequencies for octylamine and Au-octylamine.

Compound	Wavenumbers (cm^{-1})	Assignment
Octylamine	3372	N-H stretch (asym)
	3295	N-H stretch (sym)
	1610	N-H bend (δNH_2)
	1073	C-N stretch (νC-N)
	796	N-H wag
Au-octylamine	3286	N-H stretch (asym)
	3221	N-H stretch (sym)
	1556	N-H bend (δNH_2)
	1037	C-N stretch (νC-N)
	800	N-H wag

Shifts consistent with the formation of a Au-NH_2R bond are also observed in the IR region from 1200 to 700 cm^{-1} illustrating the N-H wagging mode (810 cm^{-1} in CdSe-AET shifts to 800 cm^{-1} in the composite), and the C-N stretching mode (1100 cm^{-1} shifts to 1050 cm^{-1}), as shown in Figure 5-24. The shift in these peaks and the loss of intensity in the amine bands, as well as a gain in intensity of the C-N bands, further supports the binding of the amine functionalities to the gold surface. Similar changes in intensity and frequency of these bands relative to the free amines have been reported for gold and CdSe nanoparticles functionalized with alkanethiols and alkylamines.[14,48,49]

Figure 5-24. FTIR spectra of a) 2-aminoethanethiol, b) CdSe-AET, and c) Au-CdSe nanocomposite in the region from 1200 to 700 cm^{-1}.

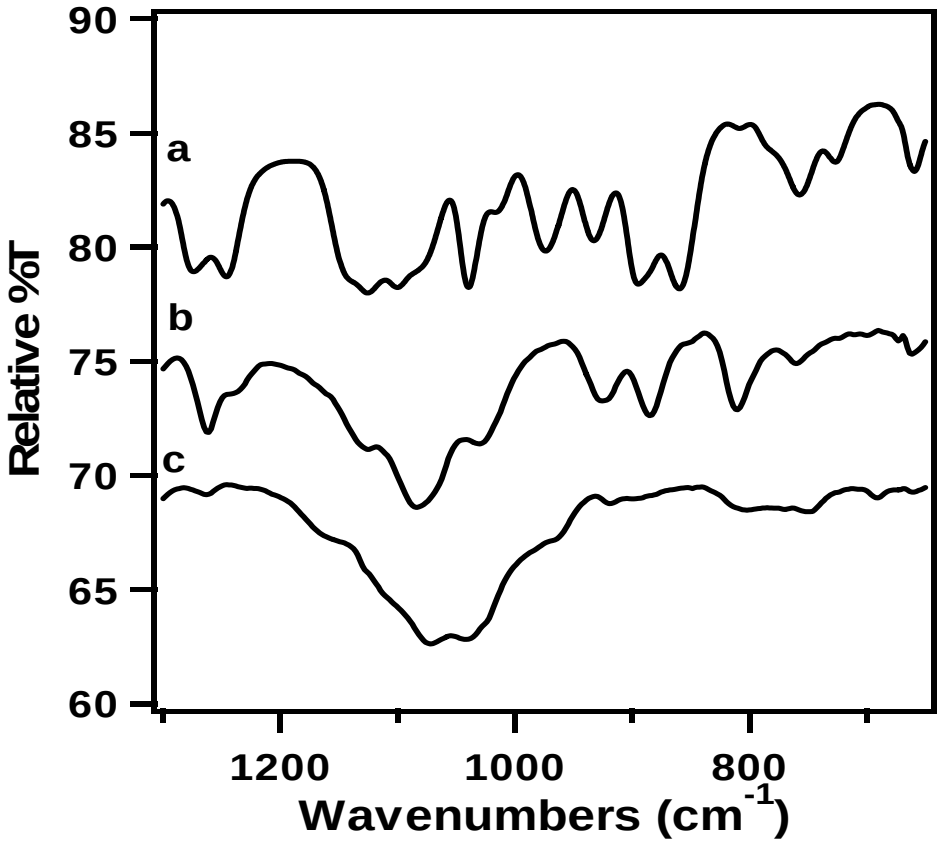

Direct self-assembly appears to be a minor contributor to the formation of the composite. Non-templated, evaporatively self-assembled structures prepared by the intimate mixing of a toluene solution with a 1:1 molar ratio of 5.0 nm CdSe capped with hexadecylamine and 5.0 nm Au capped with hexadecanethiol produces phase-segregated materials as illustrated in the TEM images shown in Figure 5-25. As demonstrated in equation 1 through equation 4, composites are predicted to form non-crystalline, phase-segregated structures due to differences in E_{vdw} arising from the Hamaker term. Since the Hamaker constant scales directly with the particles' polarizability and the cube of the particle radius, the polarizability of the nanoparticle is proportional to the magnitude of the induced electric dipole at the surface, which is experimentally observed as a surface plasmon resonance band.[49] Effectively, the surface plasmon resonance band is an indirect measure of the magnitude of the Hamaker constant.[50] Although the Hamaker constant for CdSe is unknown, the Hamaker constant for semiconductors, such as Ge (-4.6 x 10^{-23}), have been calculated to be significantly smaller than for metals, such as Au, in bulk materials (0.85 x 10^{-21} J),.[51] Consistent with the lower value for A in semiconductors, no observable plasmon resonance arises in Ge or CdSe. This suggests that the Au nanoparticles would dominate the

contribution to E_{VdW}, and drive phase segregation in a composite assembly formed from Au and CdSe.

Figure 5-25. TEM images of 2-dimensional evaporatively self-assembled structures of gold and CdSe nanoparticles from a mixed toluene solution of 50Å CdSe-HDA and 50Å Au-HDT drop cast onto a TEM grid. The darker images are Au-HDT and the lighter images are the CdSe-HDA. The image was taken at a magnification of x250K.

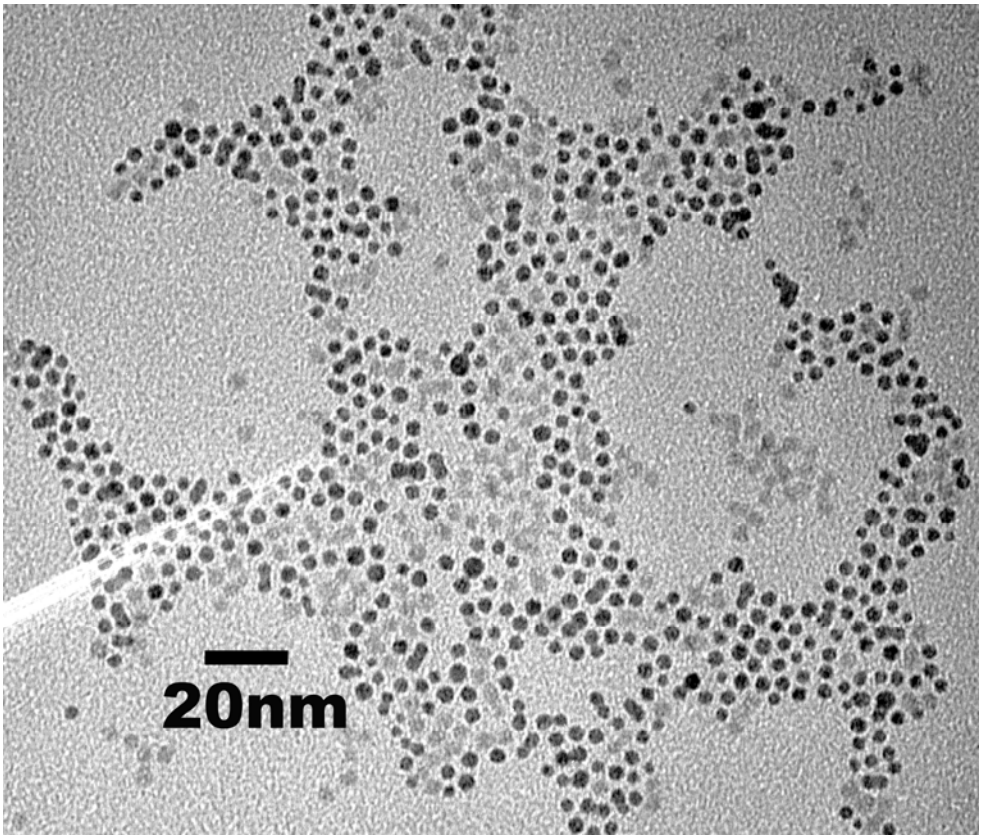

The lack of phase segregation in the assembly of aqueous Au and CdSe-AET nanoparticles of similar size illustrates the fact that the E_{cov} term dominates the assembly in these structures.

The proposed mechanism in Figure 5-21 is consistent with the belief that negligible contributions arise from an electrostatic interaction between citrate/tannic acid-stabilized gold and ammonium-functionalized CdSe in these composites. This observation is not surprising since it has been observed that complexation of gold nanoparticles with proteins is largely unaffected by the electrostatic interactions and that surface stabilizing citrate ions are easily displaced.[8] Although it is possible that citrate or tannic acid is bound up in the Au-CdSe structure, loss of modes for tannic acid at 1700 cm^{-1} and citrate at 1395 cm^{-1}, 1285 cm^{-1}, and 1300 cm^{-1} suggests that less than 5% of the structure is contaminated by excess tannic acid or sodium citrate in the final product. Removal of citrate and tannic acid surface-stabilizing ligands from the colloidal gold, as described in Chapter 3, results in a gold nanoparticle with labile passivating groups that are easily displaced by the amine functionalities of CdSe-AET. These gold-salts react readily with CdSe-AET to form similar 3-dimensional Au-CdSe structures without the threat of tannic acid being bound up within the super-structure. Figure 5-26 shows a TEM image of a Au-CdSe nanocomposite thin film formed from the reaction

of Au-CO_3 and CdSe-AET. Figure 5-27 shows a SAED pattern from the TEM image in Figure 5-26 indicating the presence of Au and CdSe within the structure and preferential ordering of the nanoparticles illustrated by the diffraction spots within the diffraction rings. Figure 5-28 shows an area of the image in Figure 5-26 under higher magnification showing the fringe patters characteristic of CdSe indicating the presence of CdSe within the gold nanoparticles. These results support the belief that the Au-CdSe composite formation is most likely largely controlled by acid-base equilibria and the Au-N vs. Au-citrate bond strength (E_{cov}).

Contributions from ligand exchange to assembly can also be eliminated as a primary driving force for the composite formation based on the reactivity of the starting materials and final product. If a solution of sodium citrate and tannic acid is added to the CdSe-AET solution alone, no reaction is observed. In fact the CdSe-AET appears to be even more stable under these conditions and remains in solution longer than without the citrate and tannic acid. Conversely, as shown in Figure 5-16, if a solution of AET is added to the gold solution alone, a black precipitate of agglomerated gold nanoparticles falls out of solution resulting in an agglomeration of the gold nanoparticles in which the gold particles appear to be melted together, and exhibit a broad absorbance band centered around 620 nm, as illustrated in Figure 5-19. Formation of gold

agglomerates has been observed for precipitation of citrate stabilized gold nanoparticles.[42,44]

Figure 5-26. TEM image of a Au-CdSe nanocomposite thin film formed from the reaction of Au-CO_3 and CdSe-AET. The image was taken at a magnification of x50K.

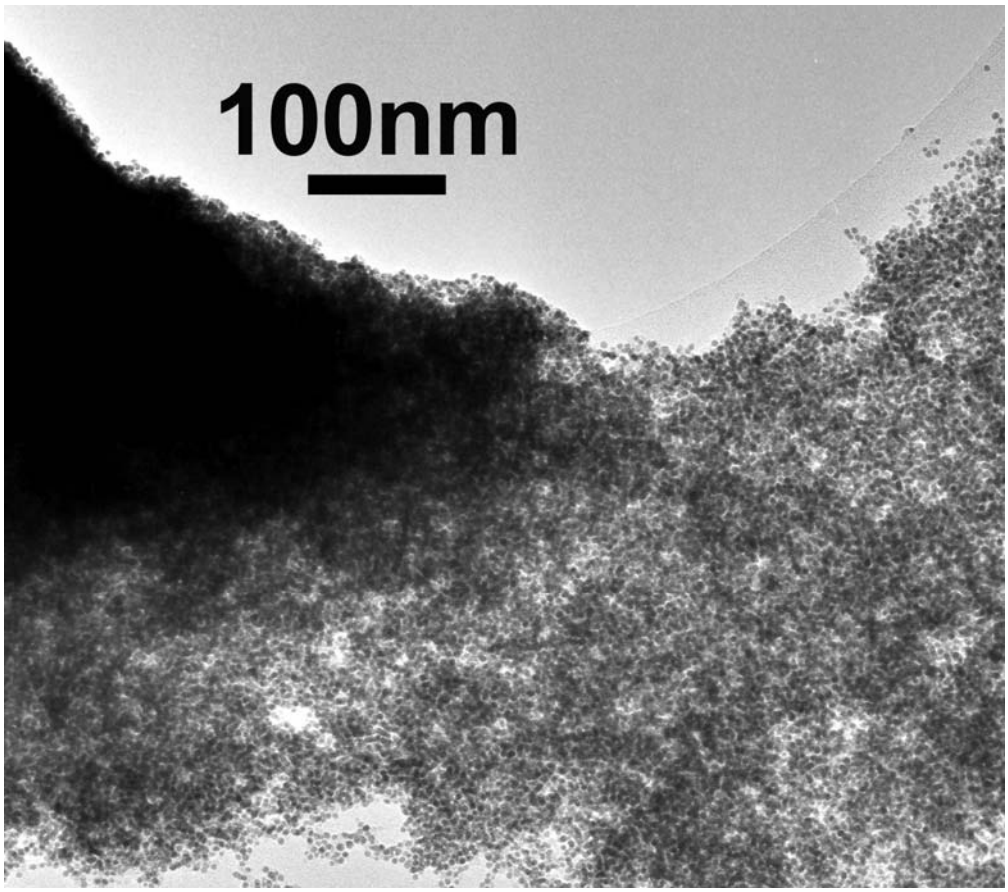

Figure 5-27. SAED pattern from the TEM image in Figure 5-30 taken at a magnification of x50K and a camera length of 50.0 cm.

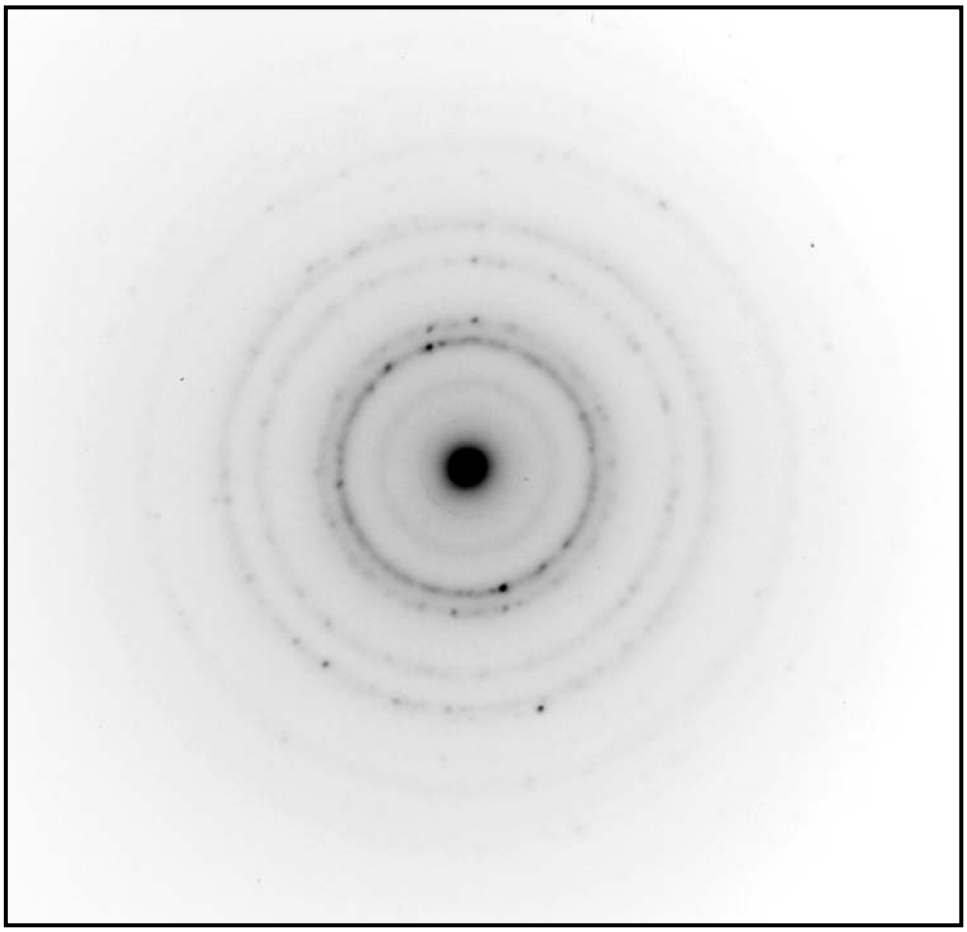

Figure 5-28. TEM image of an area of the image in Figure 5-30 under higher magnification showing the fringe patters characteristic of CdSe with arrows indicating the presence of the more easily seen CdSe within the gold nanoparticles. The image was taken at a magnification of x340K.

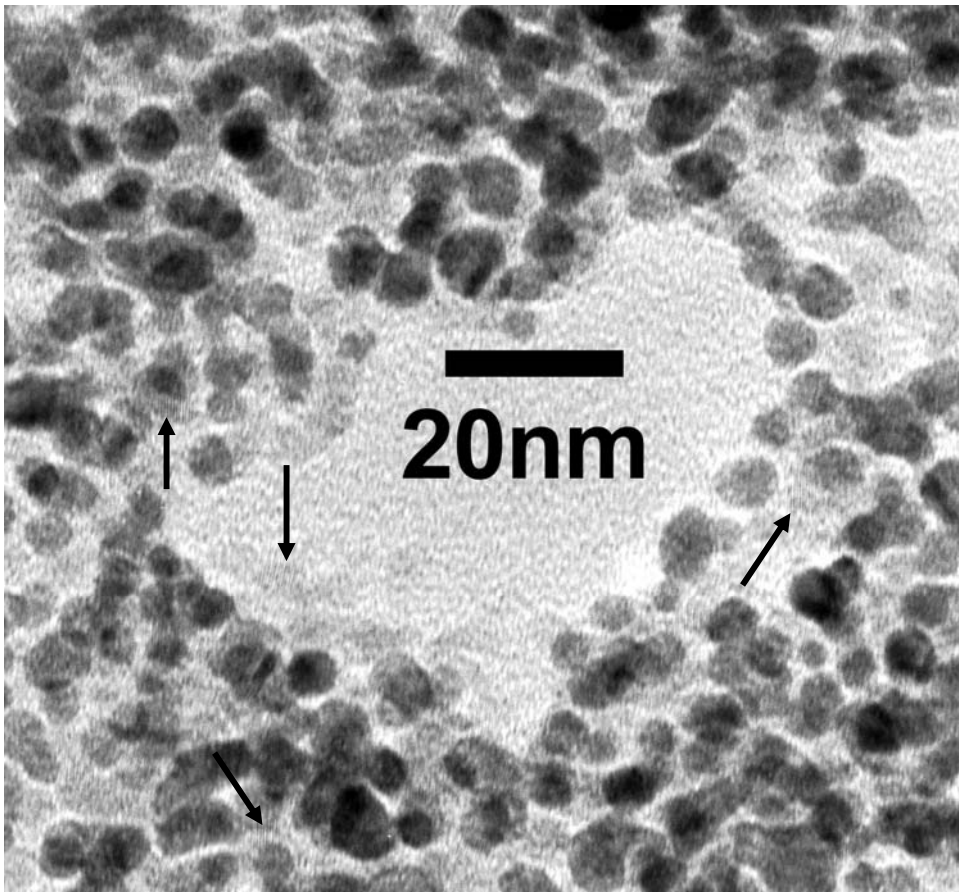

5.5.2 Size-Dependent Assembly.

Au-CdSe composites formed by varying the size ratios of the Au and CdSe nanoparticles exhibit regions of phase-segregation with the degree of phase segregation increasing with increasing differences in the sizes of the nanoparticles. Figure 5-29 shows a TEM image of a Au-CdSe nanocomposite prepared from the reaction of 3.0 nm CdSe-AET with 6.0 nm Au-TA. The large difference in sizes between the two nanoparticles results in the formation of a product with regions of phase segregated Au and CdSe nanoparticles. The corresponding SAED pattern from phase segregated composites illustrated in Figure 5-30 shows ring patterns arising from contributions from both the nanocrystalline Au and the nanocrystalline CdSe. Unlike the SAED pattern from well-formed Au-CdSe nanocomposite, the rings are broadened with dominant ring patterns arising from the nanoparticle predominantly in that area of the sample.

Figure 5-29. TEM image of a Au-CdSe nanocomposite formed from 6.0 nm Au-TA and 3.0nm CdSe-AET illustrating the degree of phase segregation between nanoparticles with a large difference in sizes. The images were taken at a magnification of x340K.

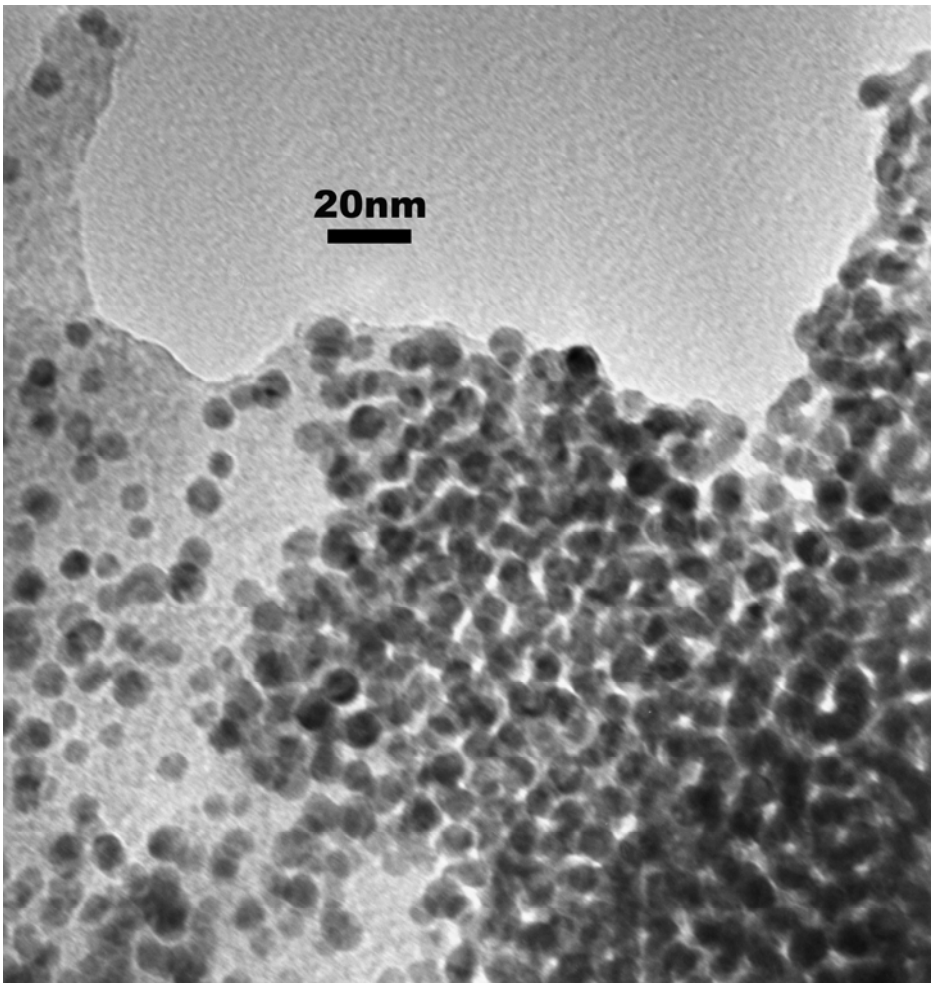

Figure 5-30. SAED pattern of Figure 5-26 taken at a magnification of x50K and a camera length of 83.0 cm.

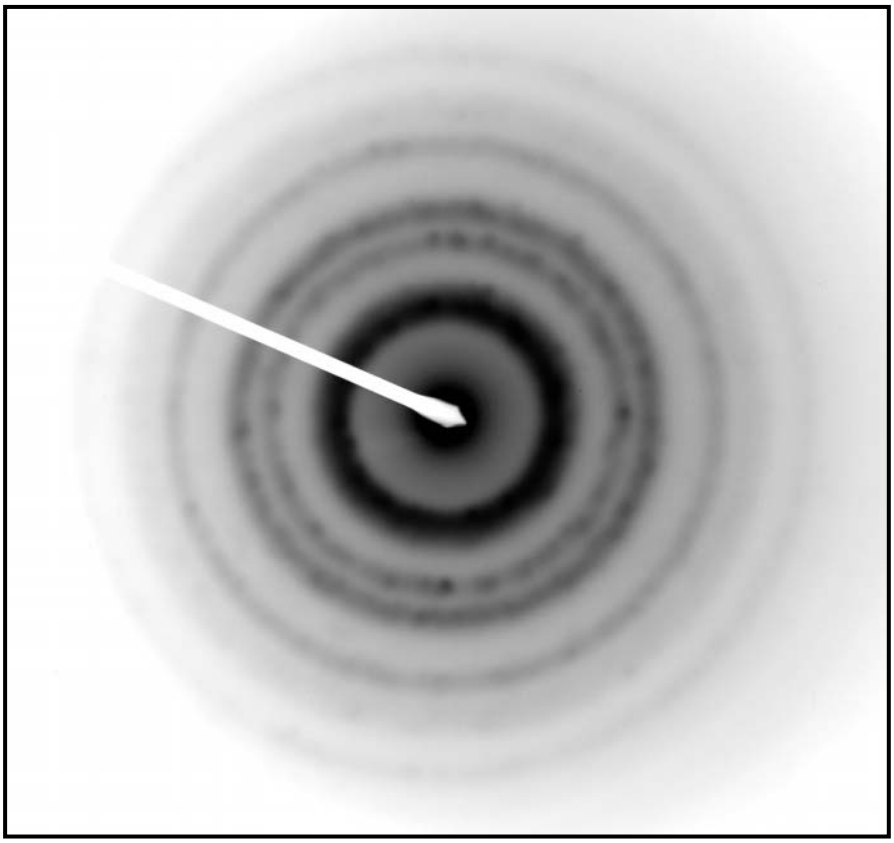

Figure 5-31 shows an image of a product obtained from the reaction of 6.0 nm Au-TA with 4.5 nm CdSe-AET. Although the degree of phase segregation between the Au and CdSe nanoparticles is less than that seen in the previous sample, and the nanoparticles appear well mixed, areas of phase segregated CdSe nanoparticles can be seen.

Reaction of 18 nm Au-cit and 6.0 nm CdSe-AET produces large structures composed predominantly of phase-segregated gold nanoparticles, as illustrated in Figure 5-32. In these structures phase segregation is due in part to large differences in sizes of the nanoparticles, but more so to the greater influence of the Hamaker term for the larger Au nanoparticles. As stated above, the Hamaker term increases with particle radius, and thus as the Hamaker constant increases so does the influence of the E_{VdW} for phase segregation of composite assemblies. This is supported by the increase in phase segregation with increasing Au/CdSe size ratio.

Evidence for the lack of an electrostatically controlled assembly is apparent in the FTIR spectra in Figures 5-7, 5-22, and 5-24, in which no citric acid, tannic acid, or ammonium IR modes are observed in the final structure. Although these mechanisms are minor contributors to the final assembly, it is expected they play a role in the initial reaction mechanism as postulated in equation 5.

Figure 5-31. TEM image illustrating an image of a product formed from the reaction of 6.0 nm Au-TA with 4.5 nm CdSe-AET. The image was taken at a magnification of x340K.

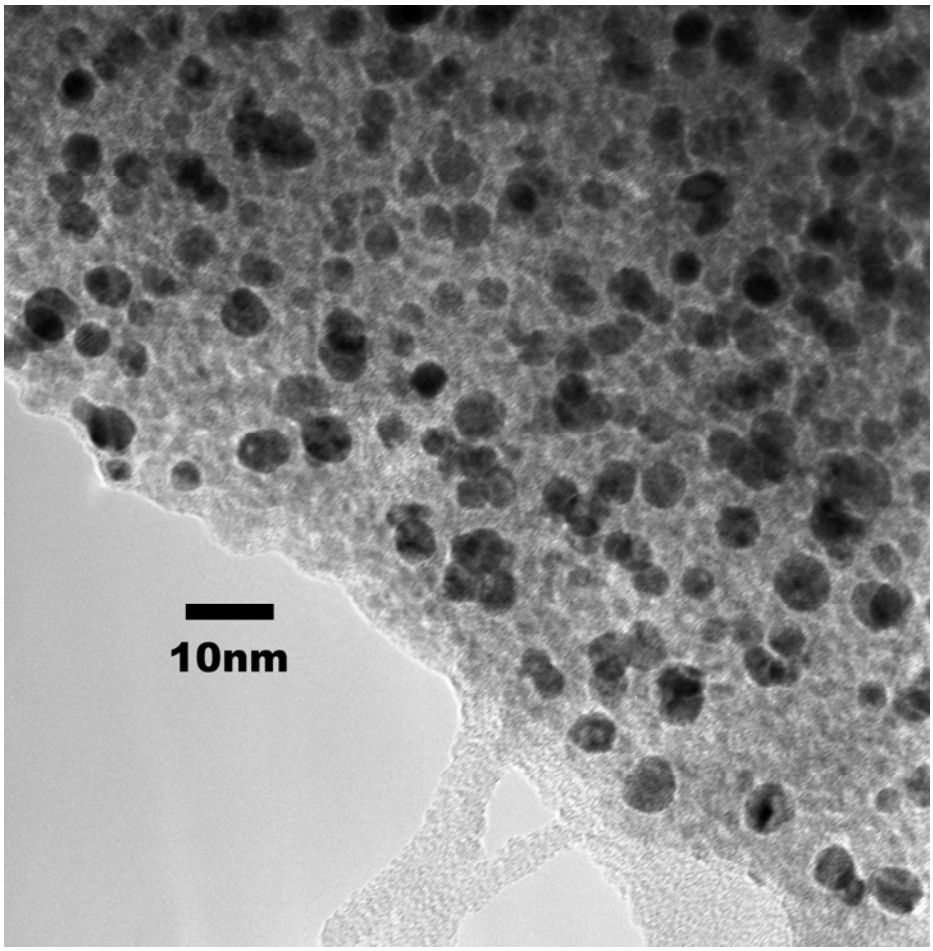

Figure 5-32. TEM image of a Au-CdSe nanocomposite composed of 18 nm Au-cit and 6.0 m CdSe-AET illustrating the phase segregation of the gold nanoparticles due to a large difference in nanoparticle sizes. The images were taken at a magnification of x34k.

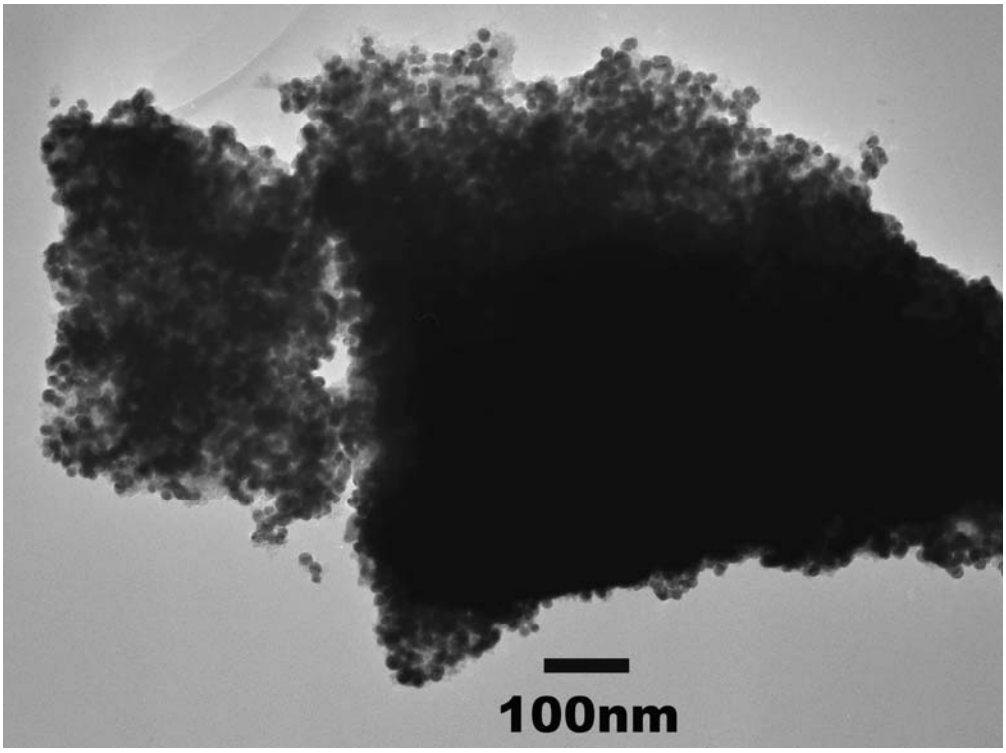

5.5.3 Composite Morphology.

The effect of buffering the solution on the structure can be analyzed by inspection of the pH dependent TEM data. There are 3 regimes observed in the pH-dependent analysis. TEM analysis of the solution at pH>6 showed no formation of a Au-CdSe composite (Figure 5-18). In the pH range 3.0-4.5 an immediate reaction is observed with formation of a "glassy" structure with a 1:6 ratio of Au:CdSe, as determined by SEM-EDX and Flame AA. Figure 5-33 illustrates the morphology of a Au-CdSe structure formed at pH 3.0 and Figure 5-34 shows the SAED pattern arising from this structure suggesting a "glassy" composite. In the pH range 5.0-6.0, well-formed structures are observed giving rise to a hexagonal pattern in the SAED-TEM. Figure 5-35 shows an image of a Au-CdSe composite formed at pH 5.5 and Figure 5-36 shows the SAED from this structure suggesting greater ordering of the nanoparticles in the composite.

Figure 5-33. TEM image of a Au-CdSe composite formed at pH 3.0. The images were taken at a magnification of x68K.

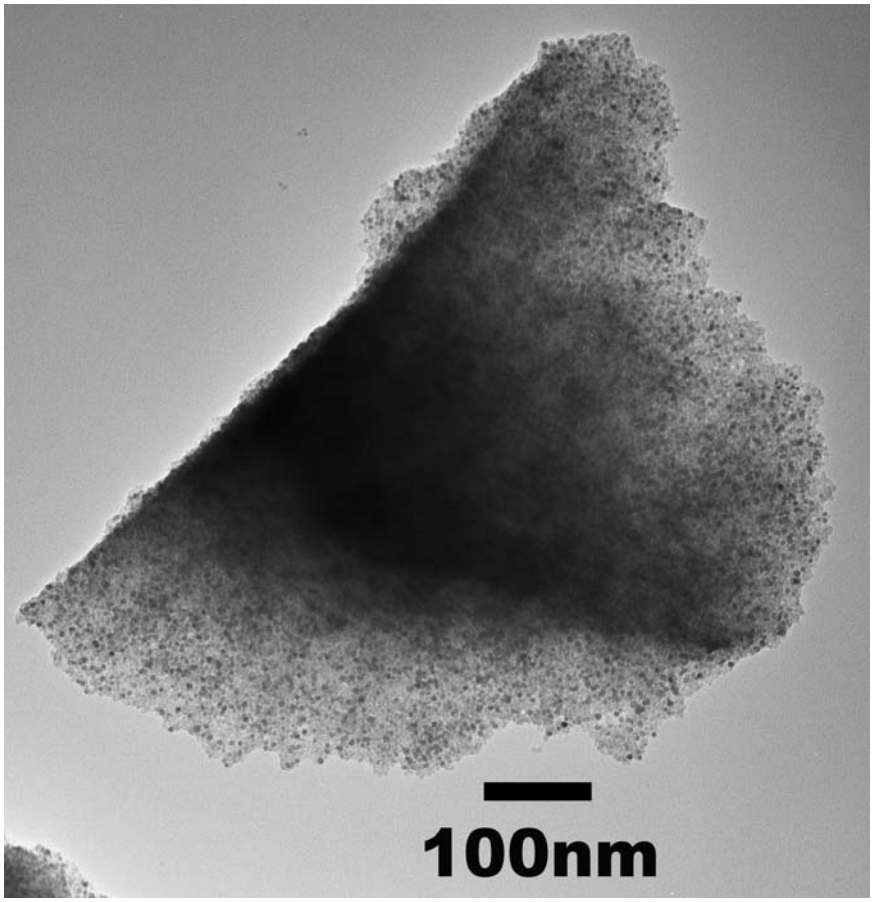

Figure 5-34. SAED pattern from a Au-CdSe composite illustrated in Figure 5-33.

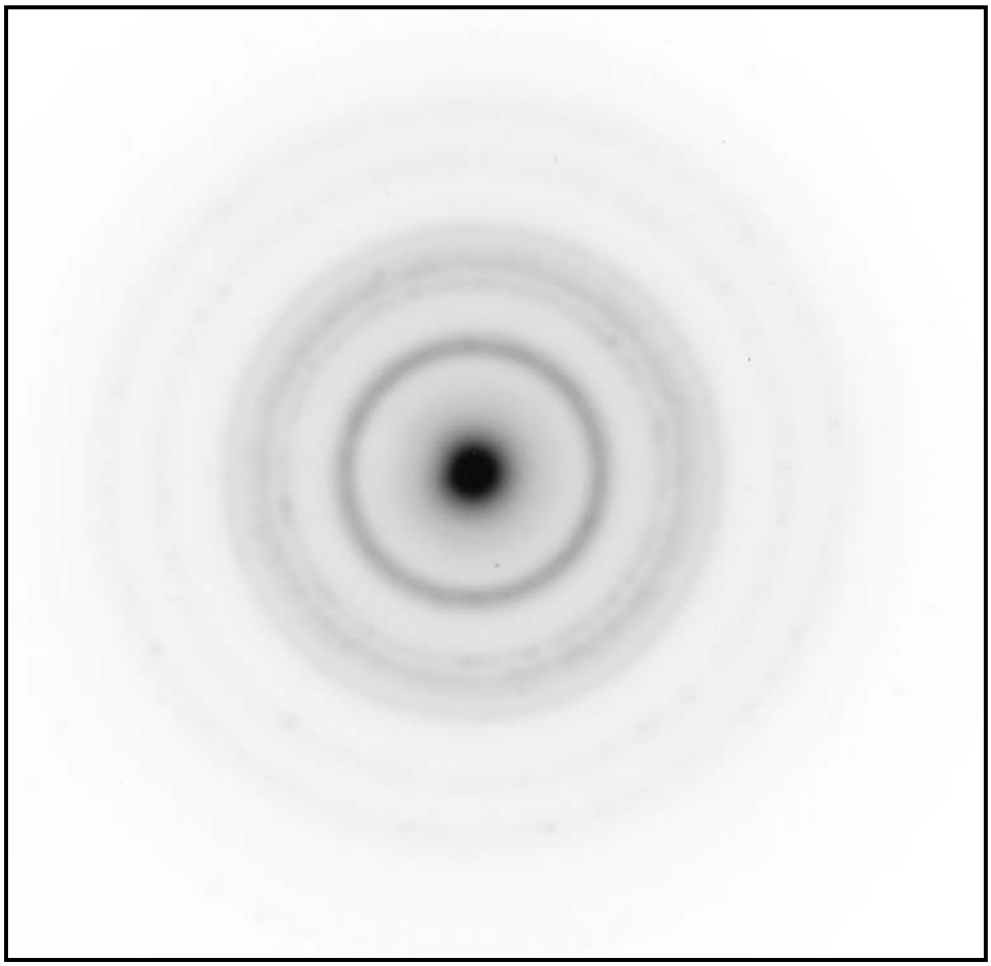

Figure 5-35. TEM image of an edge of a Au-CdSe composite structure formed at pH 5.5. The images were taken at a magnification of x100K.

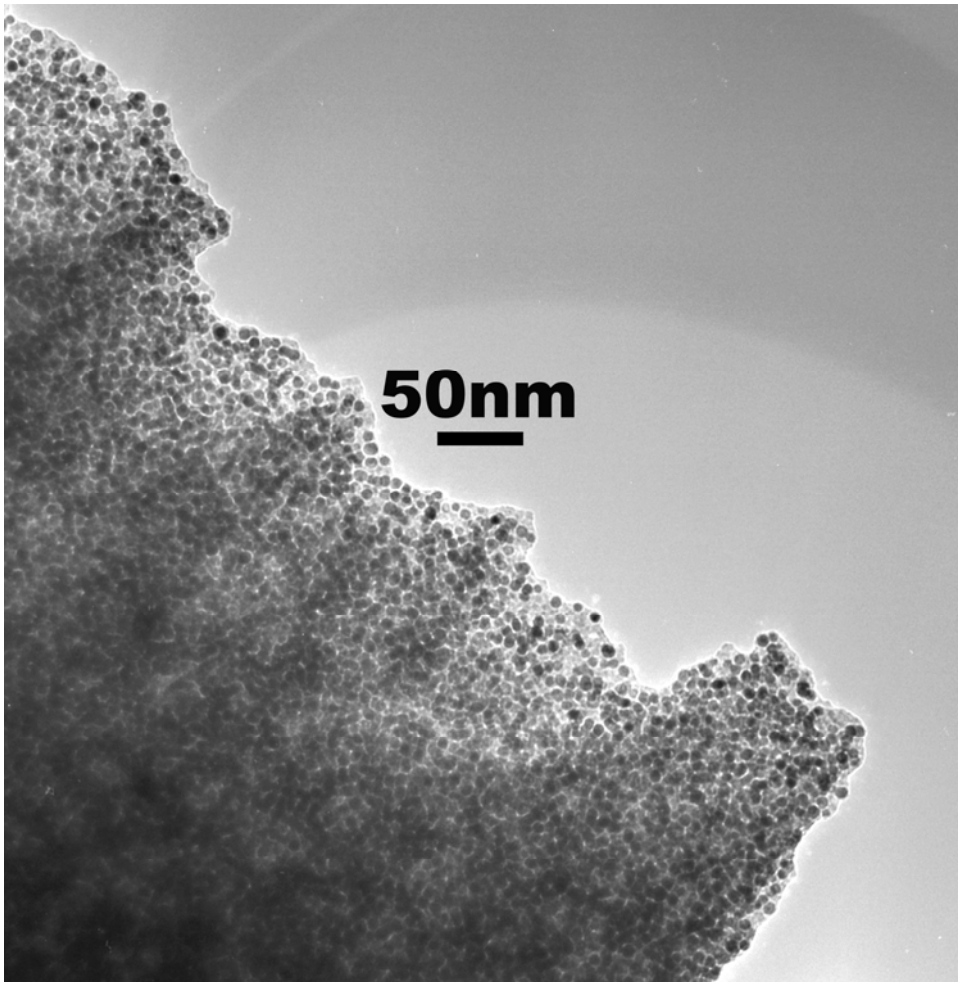

Figure 5-36. SAED pattern from Au-CdSe composite structure illustrated in Figure 5-35.

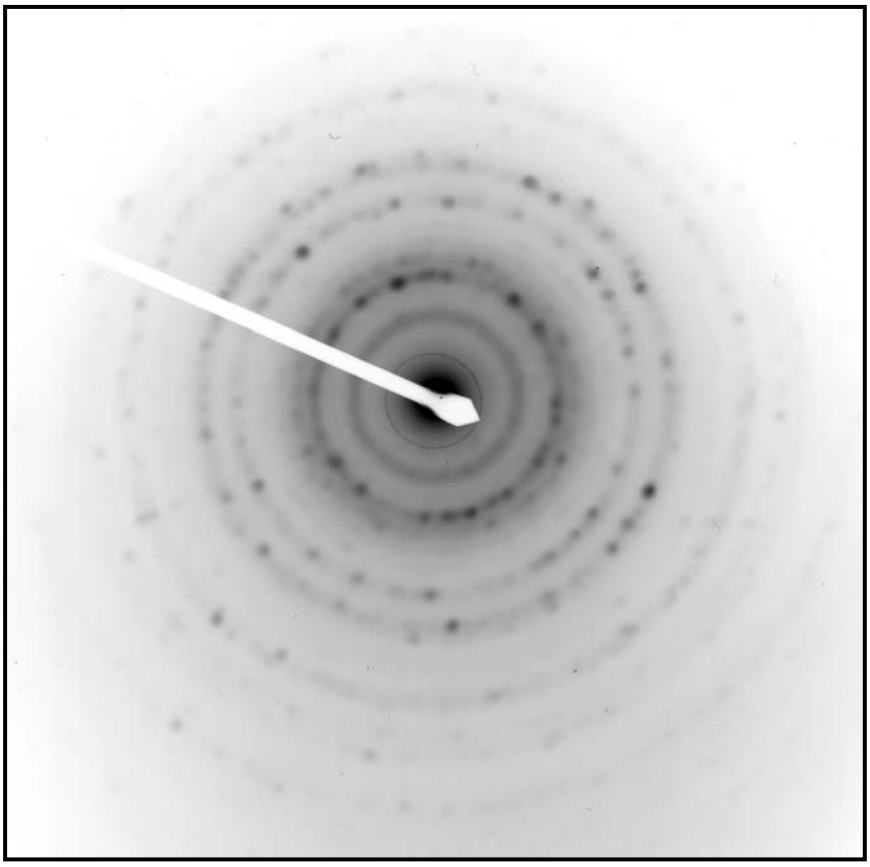

The intensity distribution curve for the TEM-SAED image on a thin section of the Au-CdSe composite (Figure 5-37) provides further structural insight into the nature of the composite. The Debye-Scherrer rings originating in the composite can be assigned to contributions of the individual components and correspond to lengths of 2.877, 2.557, 2.332, 2.1666, 1.999, 1.568, and 1.333 Å. Peak position assignments can be made by comparison against powder x-ray diffraction patterns for gold and CdSe nanoparticles surface stabilized with long chain alkyl groups, shown in Figures 5-33 and 5-39, and reported in the literature.[28,52,53] The rings at 2.557 and 2.166 Å are solely from the Au nanoparticles and correspond to the <111> and <200> planes of the gold nanoparticles, respectively. The rings at 2.877, 2.332, and 1.999Å correspond to lattice fringes assigned in the CdSe spectrum. The ring at 2.877 corresponds predominately to the <002> plane of the CdSe but is broadened due to contributions from the <100> and <101> planes. The rings at 2.332 and 1.999 Å correspond to the <110> and <112> planes of the CdSe, respectively, with the greatest contribution from the <110> plane suggesting a preferential ordering of the CdSe nanocrystals in the composite structure along the c-axis. The rings at 1.568 and 1.333 Å are a combination of peaks from both the CdSe and gold but have only been assigned to the <220> and <311> planes of the gold nanoparticles, respectively.[28,52,53]

Figure 5-37. SAED pattern from a thin portion of a Au-CdSe nanocomposite with an intensity distribution curve taken from the SAED compared with distribution curves from the SAED pattern of 6.0 nm gold and 6.0 nm CdSe nanoparticles. The corresponding distances in angstroms are given to the left of the SAED pattern.

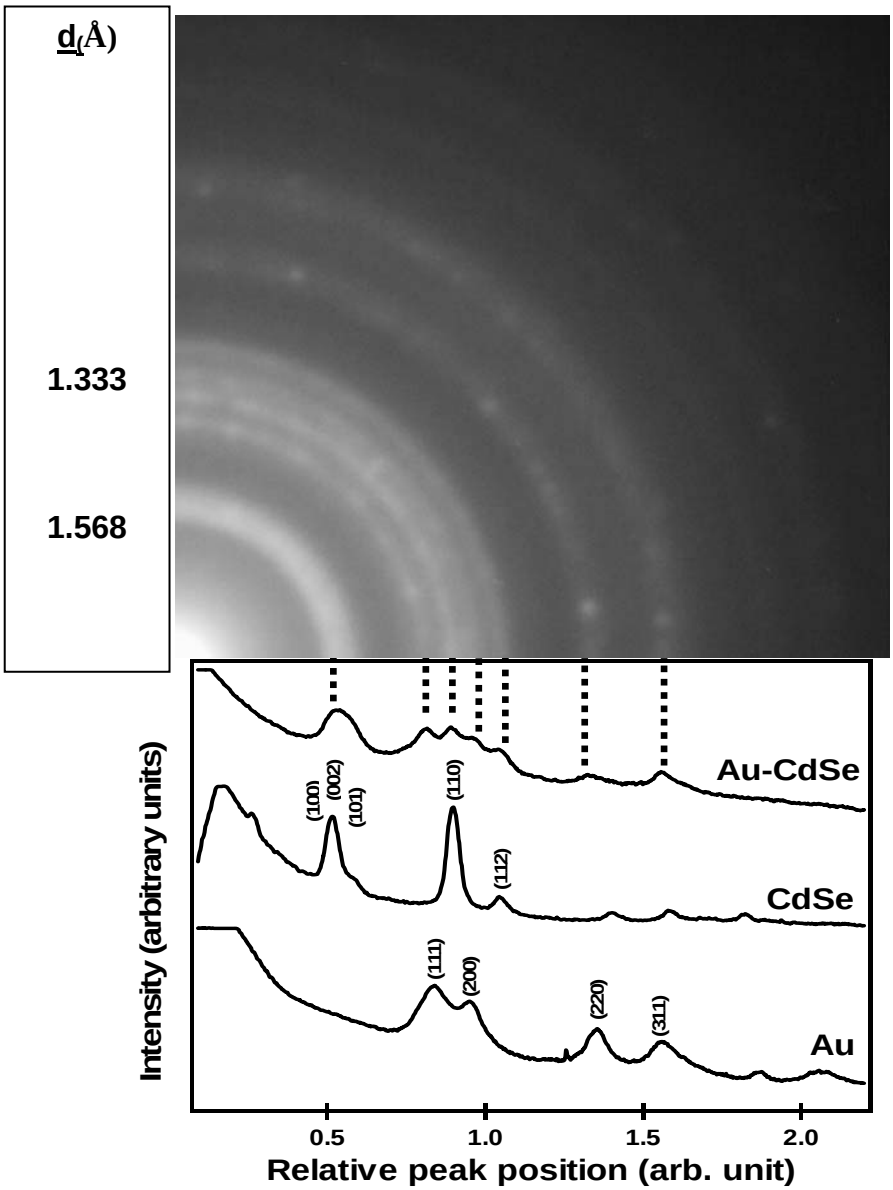

Figures 5-38. Powder x-ray diffraction pattern for 6.0 nm gold nanoparticles surface passivated with hexadecanethiol (Au-HDT).

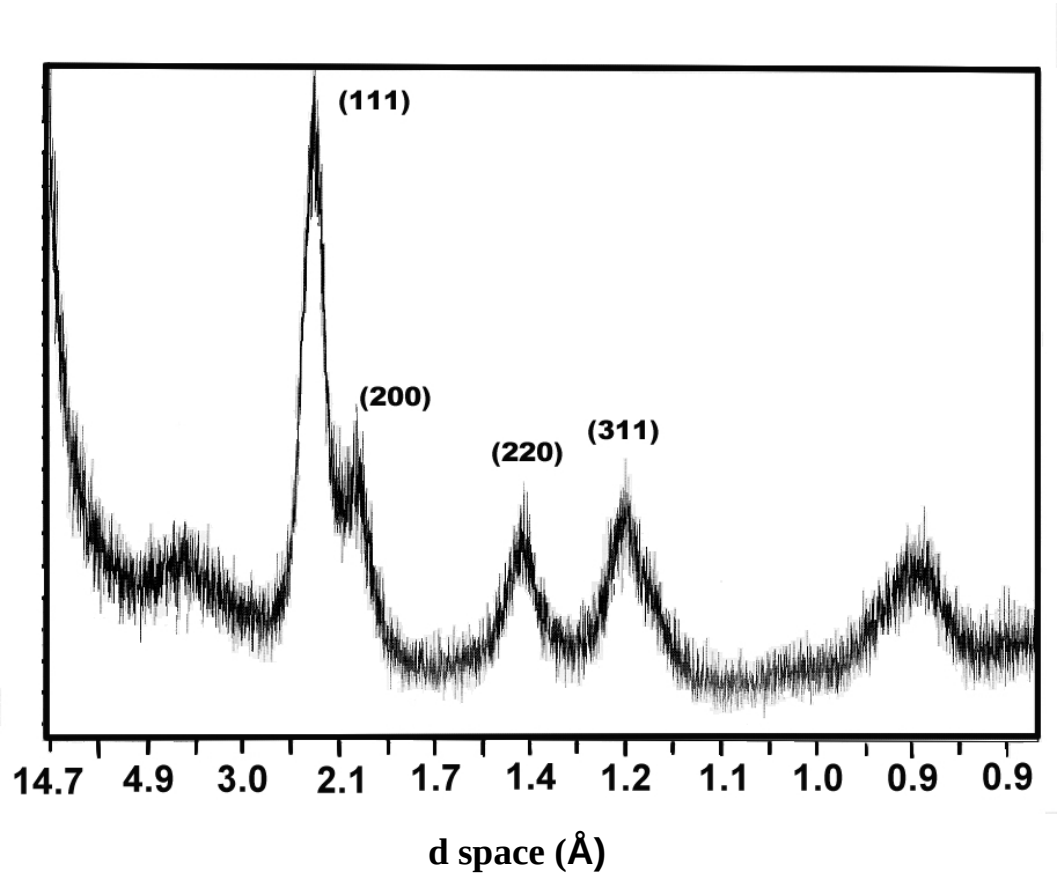

Figures 5-39. Powder x-ray diffraction pattern for 6.0 nm CdSe nanoparticles surface passivated with hexadecylamine (CdSe-HDA). The nanocrystals exhibit a wurtzite structure.

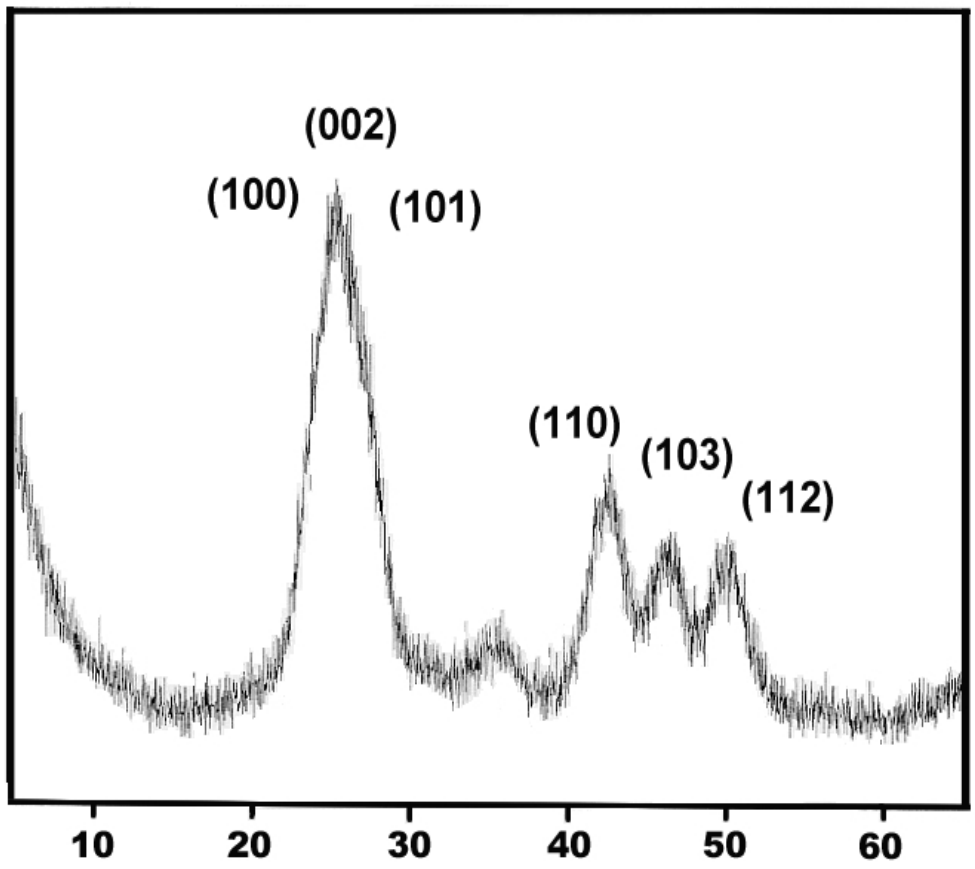

Due to limited distances in the SAED, no lattice peaks can be directly assigned in the composite structure, however the observation of a well-defined, intense, hexagonal spot pattern in the SAED image, shown in Figure 5-11, supports either a polycrystalline or, more likely, a "glassy" composite, exhibiting short-range order. As the electron beam is passed over thicker areas of the sample the spots wash out to give only ring patterns, suggesting a more "glassy" order exists over longer-range in these materials. Similar electron diffraction results have been observed in self-assembled CdSe, Au, and Ag superstructures, and interpreted as arising from preferential ordering of the nanomaterial lattice planes in the composite superstructure.[16,18,31,33,54] The observation of intense patterns over several lattice planes for the composite suggests preferential ordering of the nanomaterials, perhaps arising from local ordering of the individual nanomaterials or a limited degree of crystallinity.

5.5.4 Stoichiometric Control.

Consistent with a thermodynamic assembly, the final product of a reaction of either 6 equivalents of CdSe with 1 equivalent Au or 60 equivalents CdSe with 1 equivalent Au produces a composite with a 6:1 CdSe:Au molar ratio, regardless of reaction conditions (Table 5-2). Compositional analysis of the composite probed by energy dispersive X-ray analysis (EDX) in the SEM (Figure 5-40) as well as in the TEM (Figure 5-41) confirms a 6:1 CdSe:Au molar ratio (at pH 3.0 and 4.5) (Table 5-2).

Mapping and line scan analysis in the SEM-EDX demonstrates the composition is uniform over a several micrometer length scale (Figure 5-42). The molar ratio observed in the SEM EDX corresponds to the experimentally determined minimal amount of CdSe needed to produce a composite structure upon addition of a CdSe solution to a gold colloid solution followed by washing to remove any unreacted nanoparticles or surface passivating groups. The observed local ordering in the SAED pattern is consistent with the observation of a 1:6 packing ratio observed in the SEM-EDX mapping of the final composite.

Figure 5-40. Compositional analysis of a Au-CdSe thin film composite probed by energy dispersive X-ray analysis (EDX) on a silicon substrate in the SEM.

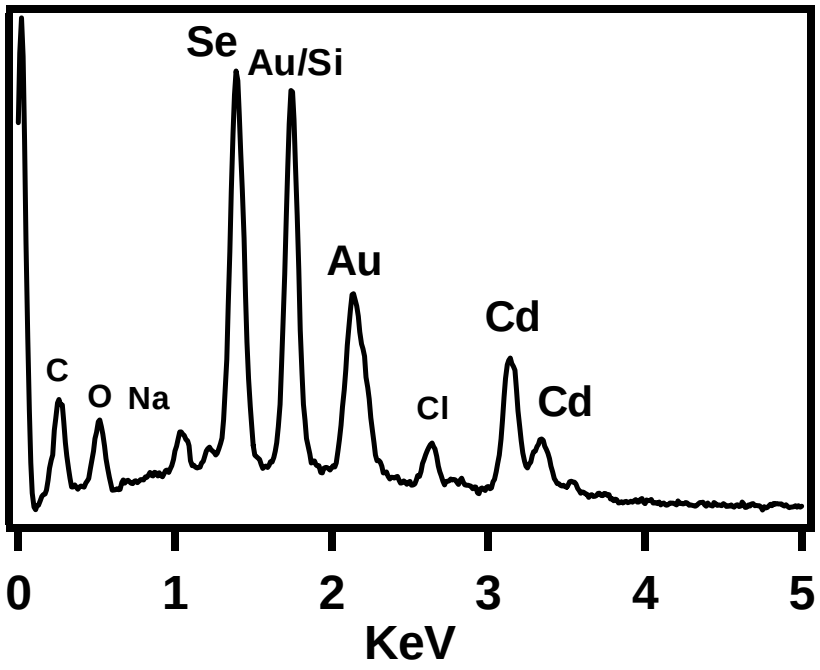

Figure 5-41. Compositional analysis of a 3-dimensional self-supporting Au-CdSe composite probed by energy dispersive X-ray analysis (EDX) in the TEM on a copper grid.

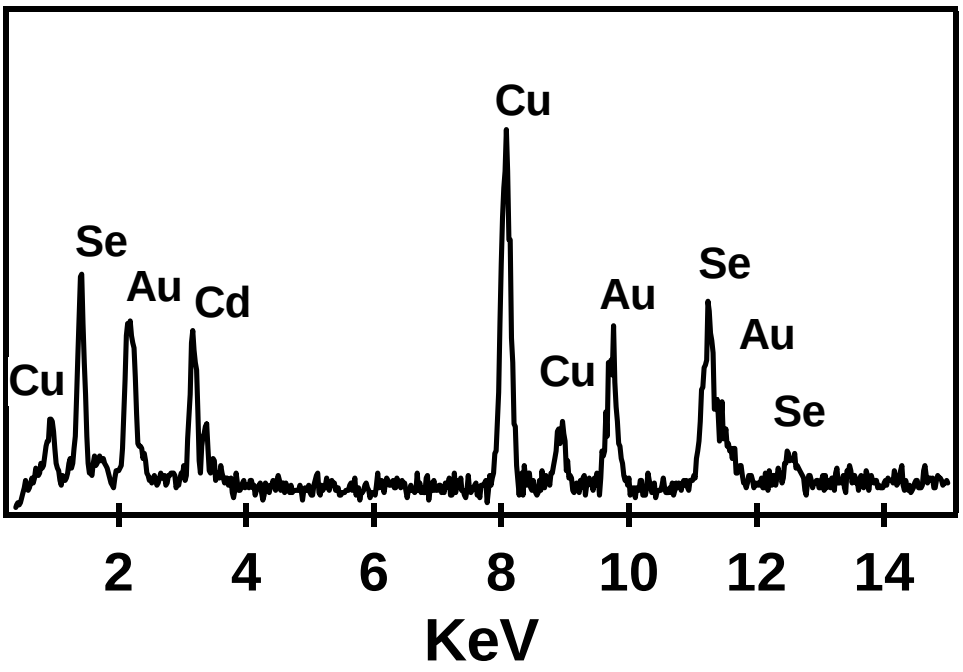

Figure 5-42. SEM image of Au-CdSe thin film on a silicon substrate with EDX line scan analysis of the individual Au, Cd, Se, and Si components. The scale bar on the side of the image equals 5 μm.

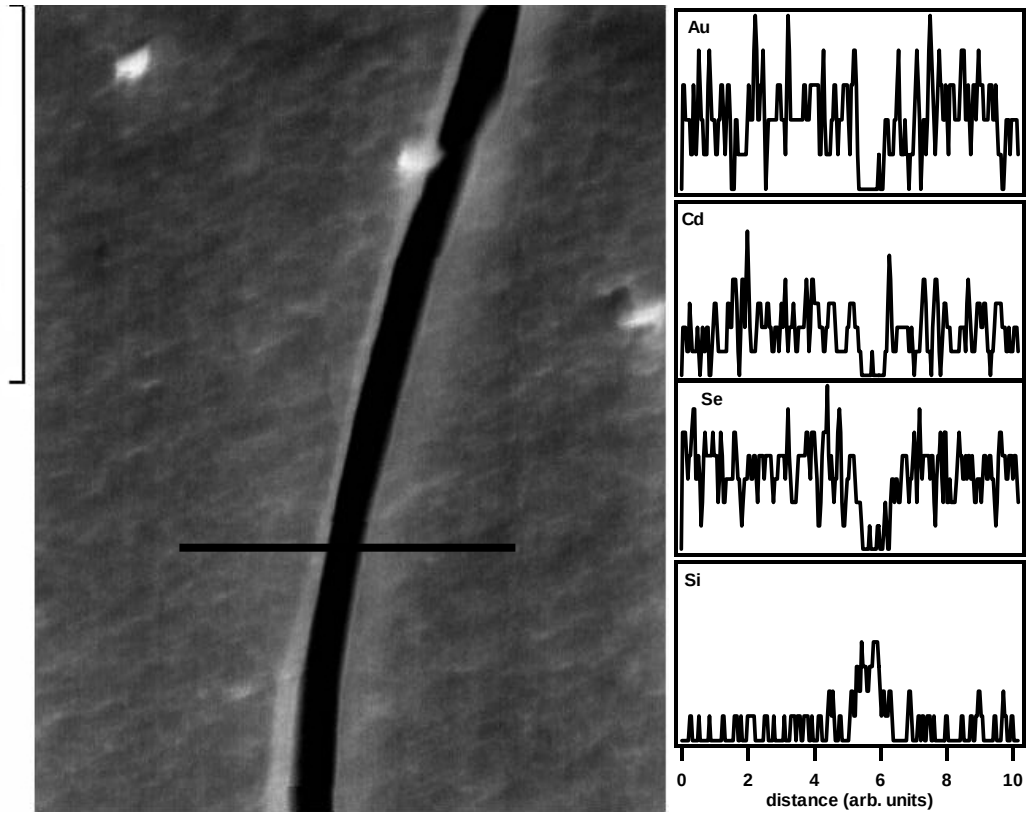

5.5.5 Optical Properties.

Further evidence for the formation of a composite that has short-range uniformity is gained by inspection of the optical spectra. The optical absorption and emission spectra of a Au-CdSe thin film on a glass substrate is shown in Figure 5-43. The intensities of the absorption components supports a 1:6 molar ratio of Au:CdSe in the final product. The observation of both the gold surface plasmon resonance at 520 nm and the CdSe exciton at 610 nm suggests the Au and CdSe are intimately mixed in the composite lattice. Excitation into the exciton transition for CdSe leads to rapid quenching of the CdSe presumably by photo induced electron injection into the Au nanoparticle (Figure 5-43). The observation of CdSe emission in phase-segregated composites formed by self-assembly without a covalent ligand interaction supports the postulate that electron injection arises when Au is proximal to the CdSe excited state molecule.

Figure 5-43. Optical absorption (solid line) and emission (dotted line) spectra of a Au-CdSe thin film on a glass substrate suggesting a 1:6 molar ratio of the two components, respectively. Quenching of the CdSe emission suggests intimate contact of the CdSe with the Au.

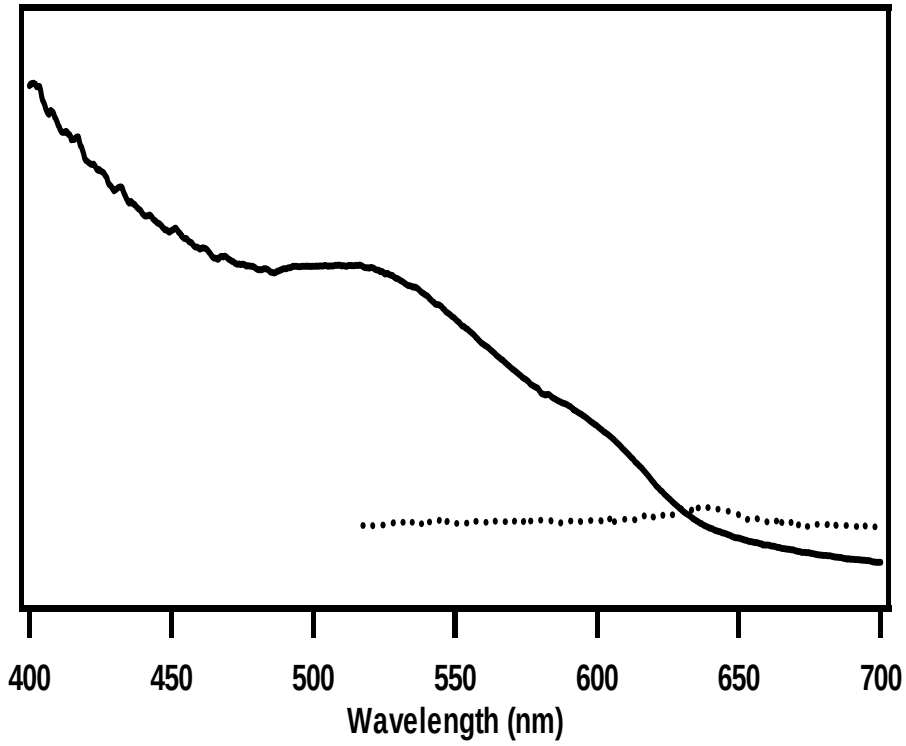

5.6 Conclusions.

Development of nano-scale composites may provide potential new systems for a wide range of material applications. Control over the 3-dimensional assembly of these nanoscale composites can be controlled by thermodynamic equilibria reactions, in essence a competition between the thermodynamic interaction potentials for steric, van der Waals, and covalent energy terms. The magnitude of the covalent energy term contribution should be manipulated by the choice of the terminal functional group on the passivating layer of one nanomaterial and the energetics of coordination on the surface of a second nanomaterial. By application of acid/base equilibrium control, glassy assemblies composed of a 6:1 ratio of two different nanomaterials can be achieved which exhibit short-range order. Further analysis of this mechanism, by control of chain length, terminal functional group, and nanomaterial may allow tailored composite 3-dimensional structures to be designed.

5.7 References.

1) Ahmadi, T. S.; Wang, Z. L.; Green, T. C.; Henglein, A.; El-Sayed, M. A. *Science* **1996**, *272*, 1924-1926.

2) Ahmadi, T. S.; Wang, Z. L.; Henglein, A.; El-Sayed, M. A. *Chemistry of Materials* **1996**, *8*, 1161.

3) Cumberland, S. L.; Hanif, K.; Khitrov, G. A.; Raola, O. E.; Simburger, J. T.; Yun, C. S.; Woessner, S.; Strouse, G. F. *in prep* .

4) Danek, M.; Jensen, K. F.; Murray, C. B.; Bawendi, M. G. *Journal of Crystal Growth* **1994**, *145*, 714-720.

5) Muhlpfordt, H. *Experientia* **1982**, *38*, 1127-1128.

6) Murray, C. B.; Norris, D. J.; Bawendi, M. G. *Journal of the American Chemical Society* **1993**, *115*, 8706-8715.

7) Murthy, S.; Bigioni, T. P.; Wang, Z. L.; Khoury, J. T.; Whetten, R. L. *Materials Letters* **1997**, *30*, 321-325.

8) Slot, J. W., Geuze, H. J. *European Journal of Cell Biology* **1985**, *38*, 87-93.

9) Sun, S. H.; Murray, C. B. *Journal of Applied Physics* **1999**, *85*, 4325-4330.

10) Sun, S. H.; Murray, C. B.; Weller, D.; Folks, L.; Moser, A. *Science* **2000**, *287*, 1989-1992.

11) Zamborini, F. P.; Gross, S. M.; Murray, R. W. *Langmuir* **2001**, *17*, 481-488.

12) Leff, D. V.; Brandt, L.; Heath, J. R. *Langmuir* **1996**, *12*, 4723-4730.

13) Henglein, A.; Giersig, M. *Journal of Physical Chemistry B* **1999**, *103*, 9533-9539.

14) Bharathi, S.; Fishelson, N.; Lev, O. *Langmuir* **1999**, *15*, 1929-1937.

15) Kiely, C. J.; Fink, J.; Zheng, J. G.; Brust, M.; Bethell, D.; Schiffrin, D. J. *Advanced Materials* **2000**, *12*, 640-643,612.

16) Whetten, R. L.; Shafigullin, M. N.; Khoury, J. T.; Schaaff, T. G.; Vezmar, I.; Alvarez, M. M.; Wilkinson, A. *Accounts of Chemical Research* **1999**, *32*, 397-406.

17) Wang, Z. L.; Yin, J. S. *Materials Science and Engineering a-Structural Materials Properties Microstructure and Processing* **2000**, *286*, 39-47.

18) Murray, C. B.; Kagan, C. R.; Bawendi, M. G. *Science* **1995**, *270*, 1335-1338.

19) Ohara, P. C.; Leff, D. V.; Heath, J. R.; Gelbart, W. M. *Physical Review Letters* **1995**, *75*, 3466-3469.

20) Korgel, B. A.; Fullam, S.; Connolly, S.; Fitzmaurice, D. *Journal of Physical Chemistry B* **1998**, *102*, 8379-8388.

21) Takagahara, T. *Journal of Luminescence* **1996**, *70*, 129-143.

22) Israelachvili, J. *Intermolecular and Surface Forces*; Academic Press: San Diego, 1985.

23) Kane, V.; Mulvaney, P. *Langmuir* **1998**, *14*, 3303-3311.

24) Chen, S. W.; Murray, R. W. *Journal of Physical Chemistry B* **1999**, *103*, 9996-10000.

25) Warner, M. G.; Reed, S. M.; Hutchison, J. E. *Chemistry of Materials* **2000**, *12*, 3316-3320.

26) Schreiber, F. *Progress in Surface Science* **2000**, *65*, 151-256.

27) Xia, Y.; Kim, E.; Whitesides, G. M. *Journal of the Electrochemical Society* **1996**, *143*, 1070-1079.

28) Murray, C. B.; Kagan, C. R.; Bawendi, M. G. *Annual Review of Materials Science* **2000**, *30*, 545-610.

29) Wang, Z. L.; Harfenist, S. A.; Whetten, R. L.; Bentley, J.; Evans, N. D. *Journal of Physical Chemistry B* **1998**, *102*, 3068-3072.

30) Mitchell, G. P.; Mirkin, C. A.; Letsinger, R. L. *Journal of the American Chemical Society* **1999**, *121*, 8122-8123.

31) Kagan, C. R.; Murray, C. B.; Bawendi, M. G. *Physical Review B-Condensed Matter* **1996**, *54*, 8633-8643.

32) Kagan, C. R.; Murray, C. B.; Nirmal, M.; Bawendi, M. G. *Physical Review Letters* **1996**, *76*, 1517-1520.

33) Harfenist, S. A.; Wang, Z. L.; Whetten, R. L.; Vezmar, I.; Alvarez, M. M. *Advanced Materials* **1997**, *9*, 817.

34) Harfenist, S. A.; Wang, Z. L.; Alvarez, M. M.; Vezmar, I.; Whetten, R. L. *Journal of Physical Chemistry* **1996**, *100*, 13904-13910.

35) Bigioni, T. P.; Harrell, L. E.; Cullen, W. G.; Guthrie, D. E.; Whetten, R. L.; First, P. N. *European Physical Journal D* **1999**, *6*, 355-364.

36) Takagahara, T. *Surface Science* **1992**, *267*, 310-314.

37) Seker, F.; Meeker, K.; Kuech, T. F.; Ellis, A. B. *Chemical Reviews* **2000**, *100*, 2505-2536.

38) Wilcoxon, J. P.; Martin, J. E.; Provencio, P. *Langmuir* **2000**, *16*, 9912-9920.

39) Silverstein, R. M.; Bassler, G. C.; Morrill, T. C. *Spectrometric identification of organic compounds*; 5th ed.; Wiley: New York, 1991.

40) Whetten, R. L.; Khoury, J. T.; Alvarez, M. M.; Murthy, S.; Vezmar, I.; Wang, Z. L.; Stephens, P. W.; Cleveland, C. L.; Luedtke, W. D.; Landman, U. *Advanced Materials* **1996**, *8*, 428.

41) Alvarez, M. M.; Khoury, J. T.; Schaaff, T. G.; Shafigullin, M. N.; Vezmar, I.; Whetten, R. L. *Journal of Physical Chemistry B* **1997**, *101*, 3706-3712.

42) Park, S. J.; Lazarides, A. A.; Mirkin, C. A.; Brazis, P. W.; Kannewurf, C. R.; Letsinger, R. L. *Angewandte Chemie-International Edition* **2000**, *39*, 3845-3848,3729.

43) Lin, X. M.; Sorensen, C. M.; Klabunde, K. J. *Chemistry of Materials* **1999**, *11*, 198-202.

44) Storhoff, J. J.; Mirkin, C. A. *Chemical Reviews* **1999**, *99*, 1849-1862.

45) Sato, T.; Hasko, D. G.; Ahmed, H. *Journal of Vacuum Science & Technology B* **1997**, *15*, 45-48.

46) Larson, I.; Chan, D. Y. C.; Drummond, C. J.; Grieser, F. *Langmuir* **1997**, *13*, 2429-2431.

47) Lyon, L. A.; Pena, D. J.; Natan, M. J. *Journal of Physical Chemistry B* **1999**, *103*, 5826-5831.

48) Brittain, S.; Paul, K.; Zhao, X. M.; Whitesides, G. *Physics World* **1998**, *11*, 31-36.

49) Tian, F.; Klabunde, K. J. *New Journal of Chemistry* **1998**, *22*, 1275-1283.

50) Kimura, K. *Journal of Physical Chemistry* **1994**, *98*, 11997-12002.

51) Chen, X. J.; Levi, A. C.; Tosatti, E. *Nuovo Cimento Della Societa Italiana Di Fisica D-Condensed Matter Atomic Molecular and Chemical Physics Fluids Plasmas Biophysics* **1991**, *13*, 919-937.

52) Akamatsu, K.; Deki, S. *Journal of Colloid and Interface Science* **1999**, *214*, 353-361.

53) Revaprasadu, N.; Malik, M. A.; O'Brien, P.; Wakefield, G. *Chemical Communications* **1999**, 1573-1574.

54) Wang, Z. L.; Harfenist, S. A.; Vezmar, I.; Whetten, R. L.; Bentley, J.; Evans, N. D.; Alexander, K. B. *Advanced Materials* **1998**, *10*, 808-812.